Hydro-environmental Modelling and Interaction of Tidal Lagoons around the UK Coast

Bin Guo

Hydro-environmental Research Centre

School of Engineering, Cardiff University, Cardiff CF24 3AA, U.K.

A thesis submitted to Cardiff University

in candidature for the degree of

Doctor of Philosophy

March 2022

Weakness and ignorance are not barriers to survival, but arrogance is

--- *Cixin Liu*

Abstract

Despite the great advantages of tidal lagoons, such as predictable renewable energy generation and flood risk reduction, tidal lagoons are expected to have an impact on the coastal and riverine environment. The uncertainties regarding the environmental impacts can potentially affect the development and influence the design of tidal lagoons. Therefore, it is desirable to fully assess their environmental impacts to evaluate the potential impacts associated with lagoons, and to mitigate any adverse impacts by improving the construction design and operation methods where necessary. A comprehensive study regarding the environmental impact of lagoons and their operation should be undertaken at the preliminary design stage and beyond. Furthermore, it is important to explore the accumulative impacts and the interaction of the conjunctive operation of the lagoons in different locations around the coast, which is regarded as an integrated potential effective tidal range energy scheme to provide continuous power.

This research study involves developing a refined two-dimensional hydrodynamic model to provide an accurate assessment of the hydro-environmental impact and the interaction of tidal lagoons. Improvements are made through simulations of island wakes, which provides a similar scenario to the flow patterns around obstacle, such as lagoons, in a macro-tidal environment. Innovative refinements are also made to enhance the modelling accuracy of the hydro-environmental process within and outside of a lagoon, including full momentum conservation between the subdomains and the independent operation of the turbines and sluice gate blocks. Three state-of-the-art tidal lagoon proposals, namely: West Somerset Lagoon (WSL), Swansea Bay Lagoon (SBL) and North Wales Tidal Lagoon (NWTL), are used as case studies in this research to investigate their impacts and hydro-environmental interactions.

The results show that the operation of the West Somerset Lagoon slightly reduces the tidal range in the Bristol Channel and Severn Estuary. The changes in tidal elevation caused by the WSL and NWTL resulted in a loss of intertidal mudflats of up to 20 km^2 in the Bristol Channel and Severn Estuary, while the decrease in the peak water elevations reduces the coastal flood risk. The maximum velocity in the inner Bristol Channel increases by about 0.25-0.75 m/s with the operation of WSL, which improves the water renewal capacity and increases the maximum suspended sediment concentration in the Bristol Channel and Severn Estuary, and consequently reduces the risk of hypernutrification and eutrophication. In contrast, the current designs for the SBL and NWTL schemes as modelled in thisstudy showed a decrease in the water residence

time by 4% and 45.7% in the lagoon area, respectively. The bed shear stress study and the indicative morphological modelling demonstrated potential erosion in the turbine wake region, influencing the general morphodynamics during lagoon operation. Furthermore, the presence of WSL is likely to cause sediment deposition at two sides of the lagoon impoundment, while increasing slightly the risk of scouring the seabed in the inner Bristol Channel.

In the study of the conjunctive operation of WSL and NWTL, as well as WSL and SBL, the interactions between the lagoons were investigated, but they were found to be minor. The interactions between the lagoons are associated with the lagoon scale, location, tidal phase, et al., therefore a general conclusion could not be obtained. However, the feasibility of relatively continuous tidal power output is presented for the conjunctive operation of WSL and NWTL.

Acknowledgements

I would like to express my deepest gratitude to my supervisors Dr Reza Ahmadian and Professor Roger Falconer, for giving me the opportunity to work in an excellent research environment and for their supervision, support, and guidance throughout my PhD study.

I would like to thank Professor Shunqi Pan for useful discussions during the study. Thanks also go to all my colleagues at Hydro-environmental Research Centre (HRC), particularly Christ, Giovanni, Ken, Shahla, JingJing, Nejc, Jonathan, and Amyrhul, for their continued support. It was a great pleasure to work with you. I would also like to thank my examiners, Professor Thomas Adcock and Dr Zhihua Xie, for their constructive comments and suggestions, which have greatly improved the work.

I gratefully acknowledge the financial support from China Scholarship Council and Cardiff University. In addition, I give my thanks to the Supercomputing Wales (SCW) and Advanced Research Computing at Cardiff (ARCCA) for the supercomputing facility and technical support offered throughout the research period. I would also like to express my gratitude to Dr Paul Evans for providing the moored ADCP data, and Prof Chris Binnie and Mr David Kerr for their extensive experience and instructive suggestion.

I would like to say thank you to Xiangyu Li, Yujue Wang, Min Gan, Hongyu Ji, Xindong Chen, Min Chen, Yiqing Gong, Hao Yu etc. for their company and support. I will miss the happy time in past years.

I send deep gratitude to my family (Dad, Mum and Sister, Brother-in-law) for their unconditional support, encouragement to me. Finally, to Jing, my wife, your unending love, support and patience over the course on my study was immeasurable. The PhD study becomes a wonderful journey with you.

Table of Contents

Abstract ..... **i**

Acknowledgements ..... **iii**

Table of Contents ..... **iv**

List of Figures ..... **viii**

List of Tables ..... **xvi**

Acronyms ..... **xviii**

Nomenclature ..... **xx**

List of Publications ..... **xxii**

Chapter 1 Introduction **1**

1.1 Research Background 1

1.2 Hydro-environmental Impacts of Tidal Range Scheme 3

1.3 Research Aim and Objectives 6

1.4 Novelty and Contribution 7

1.5 Thesis Structure 8

Chapter 2 Literature Review **9**

2.1 Tide Theory 9

2.2 Tidal Energy 11

2.2.1 Tidal Stream Devices 12

2.2.2 Tidal Range Structures (TRS) 13

2.2.3 Global TRS Development 14

2.2.3.1 United Kingdom 15

2.2.3.2 France 17

2.2.3.3 Canada 18

2.2.3.4 South Korea 19

2.2.3.5 China 21

2.2.4 Features of TRS 22

2.3 Numerical Modelling of TRS 24

2.3.1 Preliminary Assessment Models 24

2.3.2 TRS Structure Modelling 25
2.4 Environmental Impacts of TRS 27
2.4.1 Hydrodynamic Impacts of Individual TRS 28
2.4.2 Combined Hydrodynamic Impacts of Multiple TRSs 32
2.4.3 Other Environmental Impacts of TRS 33
2.5 Summary 36

Chapter 3 Hydrodynamic Model Development 38

3.1 Numerical Modelling 38
3.1.1 Hydrodynamics 39
3.1.1.1 Source/Sink terms 40
3.1.1.2 Treatment of Tidal Flats and Dry Zones 42
3.1.2 Turbulence 42
3.1.3 Tracer Transport 45
3.1.4 Suspended Sediment Transport 45
3.1.5 Solution Algorithm 47
3.1.6 Boundary Conditions 49
3.1.7 Momentum Conservation through Tidal Lagoon 50
3.2 Severn Estuary and Bristol Channel Model 51
3.2.1 Model Setup 51
3.2.2 Model Validation 53
3.2.3 Mesh Convergence Test 60
3.3 Continental Shelf Model 62
3.3.1 Model Setup 63
3.3.2 Model Validation 66
3.4 Summary 70

Chapter 4 Island Wake Modelling and Further Model Calibrations 71

4.1 In-Situ Data Collection 72
4.2 Model Comparison with ADCPs Data 75
4.3 Evolution of Island Wake 76
4.4 Options for Turbulence Model 82
4.5 Summary 85

Chapter 5 Lagoon Modelling 86

5.1 Implementations of Lagoons and Operations 86
5.1.1 Idealised Lagoon Model 86
5.1.2 Operation Schemes 90
5.1.2.1 One-way Generation 90

5.1.2.2 Two-way Generation 92
5.1.2.3 Pumping Function 93
5.1.2.4 Flexible Generation and 0D model 94
5.1.3 Turbine and Sluice Gate 95
5.1.4 Embankments 100
5.1.5 Other Lagoon Modelling Setups 103
5.1.5.1 Water Level Representation 103
5.1.5.2 Ramp Function 104
5.2 Case I: West Somerset Lagoon (WSL) 104
5.2.1 Introduction and Modelling Setup 104
5.2.2 Operation Schemes and Energy Output 109
5.2.3 Momentum Conservation and Velocity Field 112
5.3 Case II: Swansea Bay Lagoon (SBL) 115
5.3.1 Introduction 115
5.3.2 Operation Schemes and Energy Output 118
5.3.3 Momentum Conservation and Velocity Field 122
5. 4 Case III: North Wales Tidal Lagoon (NWTL) 125
5.4.1 Introduction 125
5.4.2 Operation Schemes 128
5.5 Summary 131

Chapter 6 Environmental Impact of Tidal Lagoons 134

6.1 Impacts on Tide Constituents 136
6.2 Impacts on Water Level and the Intertidal Flat 140
6.2.1 Case I: WSL 140
6.2.2 Case II: SBL 144
6.2.3 Case III: NWTL 147
6.3 Impacts on Maximum Velocity Magnitude 149
6.3.1 Case I: WSL 149
6.3.2 Case II: SBL 150
6.3.3 Case III: NWTL 153
6.4 Bed Shear Stress Study 154
6.5 Impacts on Water Renewal Time 160
6.5.1 Case I: WSL 161
6.5.2 CaseII: SBL 168
6.5.3 Case III: NWTL 170
6.6 Suspended Sediment Transport Study 173
6.6.1 GAIA Settings and model validation 175

6.6.2 Impact on Maximum Suspended Sediment Concentration 176
6.6.3 Morphological Changes 180
6.7 Impacts on Phytoplankton Biomass - WSL 186
6.7.1 Phytoplankton Biomass 186
6.7.2 Eutrophication Potential 190
6.8 Summary 192

Chapter 7 Interactions of Lagoons 197
7.1 Effect of Open Boundary Location 197
7.2 Interaction between WSL and SBL 202
7.3 Interaction between the WSL and NWTL 204
7.3.1 Hydrodynamic Interaction 204
7.3.2 Impacts on Power Generation 207
7.4 Summary 211

Chapter 8 Conclusions and Recommendations 213
8.1 Conclusions 213
8.1.1 Hydrodynamic Modelling of Tidal Lagoons 213
8.1.2 Environmental Impact of Tidal Lagoons 215
8.1.3 Interaction between Lagoons 219
8.2 Recommendations for Future Study 219

References 221

Appendix A: TELEMAC Settings for Hydrodynamic Model and TRS Modelling 250

Appendix B: Validation Result for Continental Shelf Model 256

Appendix C: Typical Mesh Resolution Presentation 261

Appendix D: Morphological Evolution Modelling 263

List of Figures

Figure 2.1: Relationship between the position of the Moon and the tidal range. 9

Figure 2.2: Classification of tidal power technologies (Elliott et al., 2018). 12

Figure 2.3: Conceptual graphs of a tidal barrage and a tidal lagoon (Elliott et al., 2018). 14

Figure 2.4: Summary of tidal range resource of the UK (Sustainable Development Commission, 2007b). 15

Figure 2.5: Configuration of STPG Barrage (Severn Tidal Power Group, 1989). 16

Figure 2.6: The Rance River Barrage, Brittany, France (Wikipedia, 2021). 17

Figure 2.7: Annapolis station, on the Bay of Fundy in Nova Scotia, Canada (Brad, 2013). 18

Figure 2.8: Schematisation of offshore and coastal lagoons (Cousineau et al., 2012). 19

Figure 2.9: (a) Lake Sihwa Dam (Park, 2007) and (b) Lake Sihwa Tidal Barrage Plant (Aggidis, 2010). 20

Figure 2.10: Jiangxia Tidal Power Plant (Zhang et al., 2014) 21

Figure 2.11: Maximum water elevation changes due to the Severn Barrage operation (Čož, 2019). 29

Figure 2.12: Cumulative Impact of Swansea Bay Lagoon on (a) maximum velocities and (b) maximum water levels (Angeloudis and Falconer, 2017). 31

Figure 3.1: Correction of the gradient of the free surface to semi-wet element (Hervouet, 2007). 42

Figure 3.2: Shape of the low head bulb turbine housing and measured velocity distribution in the outer turbine diffuser (Wilhelm et al., 2016) 51

Figure 3.3: SEBC Model domain and the validation data measured points. 53

Figure 3.4: Water level comparison of model predictions and BODC measured data at Avonmouth. 55

Figure 3.5: Water level comparison of model predictions and BODC measured data at Hinkley Point. 55

Figure 3.6: Water level comparison of model predictions and BODC measured data at Mumbles. 56

Figure 3.7: Water level comparison of model predictions and BODC measured data at Newport. 56

Figure 3.8: Water level comparison of model predictions and L1 ADCP measurement points. 56

Figure 3.9: Current speed comparison of model predictions and L1 ADCP measurement points. 57

Figure 3.10: Current direction comparison of model predictions and L1 ADCP measurement points. 57

Figure 3.11: Water level comparison of model predictions and L3 ADCP measurement points. 57

Figure 3.12: Current speed comparison of model predictions and L3 ADCP measurement points. 58

Figure 3.13: Current direction comparison of model predictions and L1 ADCP measurement points. 58

Figure 3.14: Water Level comparison with different meshes at Hinkley points during (a) spring and (b) neap tides. 61

Figure 3.15: Velocity comparison with different meshes at ADCP measurement point L3, (a) velocity magnitude; (b) Velocity direction. 62

Figure 3.16: Computational domain of the CS model and the bathymetry where the areas of higher resolution data are indicated in the yellow rectangle highlight zone. 64

Figure 3.17: Mesh resolution in the CS model, with refined mesh resolution in the Severn Estuary and Bristol Channel, and the Colwyn Bay. 65

Figure 3.18: The tide gauges used to validate CS model prediction (In UTM 30 coordinate system). 66

Figure 3.19: Predicted amplitude (left) and the phase (right) of the M2 tidal constituent from the CS model. 68

Figure 3.20: Predicted amplitude (left) and the phase (right) of the M2 tidal constituent from Young et al. (2000). 68

Figure 3.21: Predicted amplitude (left) and the phase (right) of the S2 tidal constituent from the CS model. 69

Figure 3.22: Predicted amplitude (left) and the phase (right) of the S2 tidal constituent from Young et al. (2000). 69

Figure 4.1: Flat Holm Island and the ADCPs measurement transect lines. 73

Figure 4.2: Sontek ADCP unit mounted on a swing arm during the survey (Guo et al., 2020). 74

Figure 4.3: Comparison of observed and modelled current speed. 76

Figure 4.4: Streamlines nearby to Flat Holm Island at date 11/07/2011: (a) High water (slack tide); (b) HW+1.7h (c) HW+3.25h (peak ebb); (d) Low water (slack tide); (e) LW+1.7h; (e) LW+3.25h (peak flood) 77

Figure 4.5: Streamlines nearby to Flat Holm Island at date 05/07/2011: (a) High water (slack tide); (b) HW+0.5h (c) HW+1.0h; (d) HW+1.5h (e) HW+2.0h; (e) HW+3.0h (peak ebb). 79

Figure 4.6: Streamlines nearby to Flat Holm Island at date 05/07/2011: (a) Low water (slack tide); (b) LW+0.5h; (c) LW+1.0h; (d) LW+1.5h; (e) LW+2.0h; (e) LW+3.0h (peak flood). 80

Figure 4.7: The comparison of different solvers in k-epsilon model. 84

Figure 5.1: The outline and dimension of the idealised lagoon model. 87

Figure 5.2: Internal barrier and the turbine and sluice gate points..... 88

Figure 5.3: (a) the water level change in subdomain I and II; (b) the discharge of turbines and sluice gates; (c) the water volume change inside of lagoon basin..... 89

Figure 5.4: The flow structure during the operation of the idealised lagoon during (a) flooding generation; (b) ebb generation. 90

Figure 5.5: Diagram of ebb generation (Cousineau, 2011)..... 91

Figure 5.6: Diagram of two-way generation of tidal lagoons (Cousineau et al., 2012). 93

Figure 5.7: The key elements of a conventional hydro double regulated bulb turbine (Tidal Lagoon Plc, 2013). 96

Figure 5.8: Q-H relationships of a typical Andritz Hydro Hill chart for a double-regulated bulb turbine (Aggidis and Feather, 2012)..... 97

Figure 5.9: Turbine Q-H and P-H comparison for the diameters of 7.2 m and 9 m, respectively (Xue, 2021). 97

Figure 5.10: Turbine efficiency (Xue et al., 2019a)..... 98

Figure 5.11: Cross-section of a sluice caisson proposed for the Lake Sihwa tidal power plant (Bae et al., 2010) 99

Figure 5.12: The mesh of the lagoon test model with (a) domain decomposition method; (b) bed-level rise method..... 101

Figure 5.13: The water jets through the turbines in the idealised models with (a) (c) mesh with domain decomposition method; (b) (d) mesh with bed-rise method. 102

Figure 5.14: Water level oscillations inside and outside of lagoon basin. 103

Figure 5.15: Location of West Somerset Lagoon, and the geography division of Severn Estuary and Bristol Channel. 105

Figure 5.16: (a) The computational domain of the model; (b) layout of the turbine housing and sluice gate blocks around West Somerset Lagoon. 106

Figure 5.17: A typical tide level distribution in the Bristol Channel during the operation of WSL. .. 108

Figure 5.18: Flow chart of the two-way operation scheme in which each block of turbines and sluice gates is operated by its judgement routine (HW/LW = High/Low water level, ΔHi = water level inside

lagoon - outside, H_start = Desired head difference for turbine operation (m), H_end = minimum head difference for turbine operation (m)). 109

Figure 5.19: (a) Water level variations for WSL operation; (b) discharge through a single turbine; (c) power output for a single turbine. 110

Figure 5.20:(a) Water level variations for WSL operation; (b) discharge through a single turbine; (c) power output of a single turbine in two-way operation with pumping function. 111

Figure 5.21: Instantaneous velocity fields of WSL for peak discharges during flood and ebb generation, for a typical spring tide and with different momentum source term formulations: (a) and (b) model without momentum source term; (c) and (d) model with momentum source using velocity at the end of the turbine diffusor; and (e) and (f) model with momentum using velocity taken at the turbine blade location. 114

Figure 5.22: Turbine jet comparisons between momentum with depth-averaged source velocity (m/s) (colour contour) and depth-integrated momentum (dotted line) during (a) flooding generation and (b) ebb generation. 115

Figure 5.23: The horseshoe shape of the SBL proposal and its location in Swansea Bay (Tidal Lagoon Plc, 2016). 116

Figure 5.24: Mesh resolution in the whole model domain and around the Swansea Bay Lagoon. 117

Figure 5.25: Locations of the turbine and the sluice gates of SBL and the dredging area, the points used to calculate the water level change. 118

Figure 5.26: Predicted water levels on both sides of the SBL and the corresponding total water discharge of turbines for the ebb generation method. 119

Figure 5.27: Predicted water levels on both sides of the SBL and the corresponding total water discharge of turbines for the ebb/pumping generation method. 119

Figure 5.28: Predicted water levels on both sides of the SBL and the corresponding total water discharge of turbines for the two-way generation method. 120

Figure 5.29: Predicted water levels on both sides of the SBL and the corresponding total water discharge of turbines for the two-way/pumping generation method. 120

Figure 5.30: Predicted water levels on both sides of the SBL and the corresponding total water discharge of turbines for the flexible two-way generation method. 121

Figure 5.31: Instantaneous velocity fields of SBL for peak discharges during flood and ebb generation, for a typical spring tide and with different momentum source term formulations: (a) and (b) model without momentum source term; (c) and (d) model with momentum source using velocity at the end of

the turbine diffusor; and (e) and (f) model with momentum using velocity taken at the turbine blade location.....124

Figure 5.32: Comparison of the turbine jets with depth-averaged source velocity (colour contour) and depth-integrated momentum (dotted line) during (a) ebb generation; (b) flood generation. 125

Figure 5.33: The preliminary planned location and scale of the NWTL, as shown in the red area (North Wales Tidal Energy, 2020) 126

Figure 5.34: Bathymetry of the North Wales coastline and main rivers in this area (bathymetry data refers to MSL).....127

Figure 5.35: The mesh resolution around the NWTL and the distribution of turbine and sluice gate blocks. 128

Figure 5.36: (a) Water level variations during the NWTL lagoon operation, (b) discharge through a single turbine and (c) power output for a single turbine. (The yellow line indicates the flexible two-way generation scheme and the blue line indicates the flexible two-way generation scheme with pumping for each panel.).....130

Figure 5.37: Typical instantaneous flow pattern during the two-way operation of the NWTL at (a) ebb generation, (b) emptying phase, (c) flood generation and (d) filling phase. 131

Figure 6.1: Comparison of cotidal charts for M2, N2, S2 before and after the construction of WSL. (a),(c) and (d) the amplitude of M2, N2 and S2; (e), (d) and (f) the phase of M2, N2 and S2. (The colour contour represents the tidal constituents for pre-lagoon construction and the purple line with a label refers to post-lagoon scenario).....137

Figure 6.2: Comparison of cotidal charts for M2, N2, S2 before and after the construction of SBL. (a),(c) and (d) the amplitude of M2, N2 and S2; (e), (d) and (f) the phase of M2, N2 and S2. 138

Figure 6.3: Comparison of cotidal charts for M2 before and after the construction of NWTL. (The colour contour represents the tidal constituents for pre-lagoon construction and the dot line with a label refers to post-lagoon). 139

Figure 6.4:Comparison of cotidal charts for N2 before and after the construction of NWTL.....139

Figure 6.5: The cumulative effect of WSL on maximum water level during a spring-neap tidal cycle. 140

Figure 6.6: Envelope curves of high water levels for pre- and post-WSL and maximum predicted model deviation.....142

Figure 6.7: Change in intertidal mudflat areas before and after the construction of WSL, (a) the area of tidal flat area for pre- and post-WSL; (b) the change in tidal flat area with WSL.....144

Figure 6.8: The loss of low intertidal zone after the operation of WSL. 144

Figure 6.9: The cumulative effect of SBL on maximum water level during a spring tidal cycle. 145

Figure 6.10: Predicted changes to mean high water level of spring tide (MHWS) (Tidal Lagoon Plc, 2013). 146

Figure 6.11: The loss of low-level intertidal mudflats after the construction of SBL. 147

Figure 6.12: Cumulative effect of NWTL on maximum water level during a spring-neap tidal cycle. 148

Figure 6.13: The loss of low level intertidal mudflats after the construction of NWTL..... 148

Figure 6.14: The cumulative effect of WSL on (a) maximum current speed and (b) averaged current speed for a spring-neap tidal cycle. ΔVmax is the difference in the maximum current speed and ΔVmean refers to the average current speed difference during the spring-neap tidal cycle. 150

Figure 6.15: The cumulative effect of SBL on maximum velocities magnitude during a spring-neap tidal cycle. 151

Figure 6.16: The cumulative effect of SBL on maximum velocities magnitude and averaged velocities during a spring-neap tidal cycle. 152

Figure 6.17: Predicted difference in mean spring tidal flow (Tidal Lagoon Plc, 2013). 152

Figure 6.18: Top, regional maximum velocity deviation between pre- and post-NWTL simulations; bottom, close-up of inset rectangle from the top panel. 154

Figure 6.19: Variation in (a) maximum and (b) averaged bed shear stress with the operation of WSL. 156

Figure 6.20: Distribution of sand and rock outcrops (toned zone) at the sea bed in the Bristol Channel and Severn Estuary (Kirby, 2010; British Geological Survey, 1986). 157

Figure 6.21: Variation in maximum (a) and averaged (b) bed shear stress with the operation of SBL. 158

Figure 6.22: Variation in maximum (a) and averaged (b) bed shear stress with the operation of NWTL. 159

Figure 6.23: Median grain size (d50) distribution map of Liverpool Bay (Christie, 2014; HR Wallingford, 1991). 160

Figure 6.24: Instantaneous tracer flushing distribution after 21.7 hours of release: (a) without lagoon; (b) with lagoon and mass balance only; (c) with lagoon and momentum using realistic source; (d) with lagoon and momentum using simplified source. 163

Figure 6.25: Concentration variations of tracer in the initial release area for pre-WSL, and post-WSL with different momentum term settings. 163

Figure 6.26: Instantaneous tracer flushing distribution at the end of renewal time: (a) without lagoon; (b) with lagoon and mass balance only; (c) with lagoon and momentum using realistic source; (d) with lagoon and momentum using simplified source. 164

Figure 6.27: The release area of tracer, in (a) Severn Estuary and Bristol Channel; (b) Severn Estuary and inner Bristol Channel; (c) Severn Estuary..... 165

Figure 6.28: Residence time distribution for tracer release in (a) Severn Estuary and Bristol Channel without WSL; (b) Severn Estuary and Bristol Channel with WSL; (c) Severn Estuary and inner Bristol Channel without WSL; (d) Severn Estuary and inner Bristol Channel with WSL; (e) Severn Estuary without lagoon; (f)Severn Estuary with WSL..... 167

Figure 6.29: Concentration variations of tracer in the initial release area for pre-SBL, and post-SBL with different momentum term settings. 169

Figure 6.30: Instantaneous tracer concentration distribution at (a) initial releasing moment with release area of SBL impoundment; (b) end of renewal time in natural condition; (c) end of renewal time in post-SBL condition. 169

Figure 6.31: Instantaneous tracer concentration distribution at (a) initial releasing moment with release area of Swansea Bay and Porthcawl; (b) end of renewal time in natural condition; (c) end of renewal time in post-SBL condition. 170

Figure 6.32: Concentration variations of tracer in the tracer release area, i.e, The NWTL impoundment area, for pre- and post-NWTL scenarios. 171

Figure 6.33: The residence time distribution with the threshold taken as 1/e, (a) the natural condition, (b) the scenario for the post-NWTL..... 171

Figure 6.34: The typical discharges of a turbine block and sluice gates block in NWTL. 172

Figure 6.35: Distribution of suspended sediments in Bristol Channel and Severn Estuary observed from a satellite image (Parsons Brinckerhoff Ltd, 2010). 173

Figure 6.36: Sand transport pathways for the inner Bristol Channel and outer Severn Estuary (Otto, 1998) 174

Figure 6.37: The comparison of predicted and measured suspended sediment concentration at (a) Minehead and (b)Trecco Bay..... 176

Figure 6.38: The predicted suspended sediment concentration at spring flood tide across the (a) inner Bristol Channel and (b) Swansea Bay..... 177

Figure 6.39: The predicted suspended sediment concentration at spring flood tide for (a) post-WSL and (b) post-SBL scenarios. 179

Figure 6.40: Seabed evolution in the inner Bristol channel for the pre- and post-WSL scenarios after a spring-neap cycle, with the critical deposition shear stress (τcd) equal to 0.1 N/m^2 and the critical erosion shear stress (τce) equal to (a) (b) 2 N/m^2; (c) (d) 2.5 N/m^2; (e) (f) 3 N/m^2; (g) (h) 3.5 N/m^2. 182

Figure 6.41: Seabed evolution in the Swansea Bay for the pre- and post-SBL scenarios after a spring-neap cycle, with the critical deposition shear stress (τcd) equal to 0.1 N/m^2 and with the critical erosion shear stress (τce) equal to (a) (b) 2 N/m^2; (c) (d) 2.5 N/m^2; (e) (f) 3 N/m^2; (g) (h) 3.5 N/m^2, respectively. 185

Figure 7.1: The impact of the WSL on maximum water level during a spring-neap tidal cycle in the CS model. 199

Figure 7.2: The impact of the WSL on maximum tide speed in the CS model during a spring-neap tidal cycle. 200

Figure 7.3: The water level comparison on the location of Bristol Channel mouth in CS model, for pre- and post-WSL. 201

Figure 7.4: The accumulative impact of SBL and WSL on maximum water level. 203

Figure 7.5: The accumulative impact of SBL and WSL on maximum velocities. 203

Figure 7.6: Water level change at Swansea Bay for the pre- and post-WSL conditions. 204

Figure 7.7: The accumulative impact of the NWTL and WSL on maximum water level during a typical spring-neap tidal cycle. 205

Figure 7.8: The accumulative impact of the NWTL and WSL on maximum tide speed during a typical spring-neap tidal cycle. 206

Figure 7.9: Water level change in North Wales coast area for pre- and post-WSL scenarios. 208

Figure 7.10: Water level change in West Somerset coast for pre- and post-NWTL scenarios. 208

Figure 7.11: The power output of WSL and NWTL with the conjunctive two-way operation. 210

Figure 7.12: The power output of WSL and NWTL with the conjunctive operation. 210

List of Tables

Table 2.1: Tidal constituents at the mouth of the Severn Estuary (Vazquez and Iglesias, 2015). 11

Table 2.2: Levelized cost estimates for electricity with different sources (Astariz et al., 2015; Poyry Consultants, 2014). 13

Table 2.3: The main TRSs of the past in China (Li and Pan, 2017). 21

Table 3.1: Validation statistics of BODC gauge data and Swansea Bay ADCP data. 59

Table 3.2: Amplitude and phase for M2, S2 and N2 tidal constituents at 5 Tidal Gauges. 60

Table 3.3: The validation statistics of model results with different meshes. 60

Table 3.4: Water level validation statistics of the 12 BODC tide gauges. 67

Table 4.1: Time and transect lines of each ADCPs measurement. 75

Table 4.2: Island wake parameters at a point located northeast of Flat Holm Island during ebb tide. . 81

Table 4.3: Island wake parameters at a point located southwest of Flat Holm Island during flood tide. 82

Table 4.4: The statistical data of different turbulence schemes 83

Table 4.5: MAE and RMAE for different k-ε model solvers 84

Table 5.1: Pseudocode of the genetic algorithm (Xue et al., 2020). 95

Table 5.2: Summary of the energy output of WSL with different operation schemes. 110

Table 5.3: The energy output of SBL with different operation schemes. 121

Table 5.4: The electricity generation from the NWTL for a typical spring-neap tidal cycle. 129

Table 6.1: High and low water level differences with WSL at selected sites in the Bristol Channel and Severn Estuary. (DHWS: Difference in water level at high spring tide; DLWS: Difference in water level at low spring tide; DHWN: Difference in water level at high neap tide; DLWN: Difference in water level at low neap tide) 141

Table 6.2: Critical bed shear stress (τ_c) conditions and the critical flow velocity for the entrainment by particle-size classification (Haverson et al., 2018; Berenbrock and Tranmer, 2008). 157

Table 6.3: The spatially averaged residence time in the study area. 167

Table 6.4: A summary of the main sediment inputs from the tributaries in the Bristol Channel and Severn Estuary (Cannard, 2016). 175

Table 6.5: input variable and parameters for the screening model. 189

Table 6.6: Range of dissolved nutrients and chlorophyll concentrations in the research area and the model predictions for pre- and post- WSL..... 191

Table 7.1: Typical energy outputs for the WSL and SBL with and without interaction between the two. 204

Table 7.2: The water level change for pre-and post-lagoon scenarios..... 208

Table 7.3: Energy outputs of the WSL and NWTL, respectively, with and without interaction between the two..... 209

Acronyms

ADCPs	Acoustic Doppler Current Profilers
ARCCA	Advanced Research Computing at Cardiff
BICGSTAB	Biconjugate stabilized gradient method
BODC	British Oceanographic Data Centre
BSS	Bed shear stress
CDOM	Coloured dissolved organic matter
CFL	Courant–Friedrichs–Lewy
CS	Continental Shelf
CSTT	Comprehensive studies task team
DAIN	Dissolved available inorganic nitrogen
DAIP	Dissolved available inorganic phosphate
DGPS	Global Positioning System
DHWN	Difference in water level at high neap tide
DHWS	Difference in water level at high spring tide
DLWN	Difference in water level at low neap tide
DLWS	Difference in water level at low spring tide
GMRES	Generalised minimum residual
H_end	Water head when turbine ends generation
H_pump	Water head when turbine finish pumping
H_start	Water head when turbine starts generation
HPC	High-performance computing
HW	High water
LW	Low water
MAE	Mean absolute error
MSL	Mean sea level
NWTL	North Wales Tidal Lagoon
PAR	Photosynthetically available radiation
R^2	Coefficient of determination
RMAE	Relative mean absolute error
RMSE	Root mean squared error
RT	Residence time

SBL	Swansea Bay Lagoon
SCW	Supercomputing Wales
SEBC	Severn Estuary and Bristol Channel
SPM	Suspended particulate matter
SS	Suspended sediment
TRS	Tidal Range Structure
UTM	Universal Transverse Mercator
UWWTD	Urban waste water treatment directive
WL	Water Level
WSL	West Somerset Lagoon
WwTW	Wastewater treatment work

Nomenclature

Symbol	Unit	Definition
$\vec{n}_f$	---	Vector normal to the bottom
C_{Zref}	*g/l*	Near-bed concentration of suspended sediment
C_d	---	Bottom drag coefficient
C_{eq}	*g/l*	Equilibrium near-bed concentration of suspended sediment
C_{eq}	*g/l*	Equilibrium near-bed concentration of suspended sediment
C_f	--	Dimensionless quadratic friction coefficient
F_x, F_y	m/s^2	Source/sink in the momentum equation
F_x^c, F_y^c	m/s^2	Coriolis force
K_l, K_t	m/s^2	Viscosity for longitudinal and transverse Diffusion
R_h	*m*	Hydraulic radius
S_h	*m/s*	Source/sink term in the continuity equation
T_s	*g/l*	Depth-averaged suspended sediment concentration
T_s	*g/l*	Depth-averaged suspended sediment concentration
T_{sce}	---	Source value of the racer
T_{sce}	---	Source value of the racer
Z_f	*m*	Bottom elevation
Z_s	*m*	Free surface elevation
a_i	*m*	Amplitude of tide harmonic component
u^*	*m/s*	Shear velocity
u_{*mud}^{cr}	*m/s*	Critical shear velocity for sediment deposition
u_i'	*m/s*	Temporal fluctuation of velocity
u_s, v_s	*m/s*	Flow velocity components at the source points
v_e	m^2/s	Momentum diffusion coefficient
α_l, α_t	---	Longitudinal and transversal diffusion coefficients
ε_S	m^2/s	Turbulent diffusivity of the sediment
η_t	---	Turbine efficiency
η_ρ	---	Pumping efficiency
θ_{cr}	---	Critical Shields parameter
ρ_s	Kg/m^3	Density of sediment
τ_{cd}	N/m^2	Critical bed shear stress for deposition
τ_{ce}	N/m^2	Critical bed shear stress for erosion

τ_{xz}, τ_{yz}	N/m^2	Bed shear stress at the bottom in the x and y Directions
υ_T	m/s^2	Dispersion coefficient of tracer
ω_i	*deg/h*	Angular frequency of tide harmonic Component
ω_s	*m/s*	Settling velocity of suspended sediment
ω_s	*m/s*	Sediment settling velocity
ϕ_i	*degree*	Phase of tide harmonic component
Δt	*s*	Time step
Δx	*m*	Spatial interval
D	$Kg/m^2/s$	Sediment deposition rate
d_{50}	*m*	Mean grain diameter
E	$Kg/m^2/s$	Sediment erosion rate
h	*m*	Water depth
K	$m^{1/3}/s$	Strickler coefficient
P	---	Island wake parameter
Q	m^3/s	Discharge
T	--	Value of tracer
V	m^3	Water volume
C	$m^{1/2}/s$	Chézy coefficient
Z	*m*	Free surface level
k	m^2/s^2	Turbulence kinetic energy
u	*m/s*	Depth-averaged horizontal velocities Flow velocity in the x-direction
v	*m/s*	Depth-averaged horizontal velocities Flow velocity in the y-direction
α	*degree*	Bottom slope
ε	m^2/s^3	Dissipation of turbulence kinetic energy
κ	---	Von Kármán constant
λ	*degree*	Latitude
ρ	Kg/m^3	Water density
σ	---	Energy transform coefficient
ω	*rad/s*	Angular velocity of the Earth
θ	---	Discharge coefficient

List of Publications

Journal Articles and Book Chapter

Guo, B., Ahmadian, R. and Falconer, R.A., 2021. Refined hydro-environmental modelling for tidal energy generation: West Somerset Lagoon case study. *Renewable Energy*,179, pp.2104-2123.

Guo, B., Ahmadian, R., Evans, P. and Falconer, R.A., 2020. Studying the Wake of an Island in Macro-tidal Estuary. *WATER*, *12*(5), pp.1225.

Falconer, R.A., Guo, B., and Ahmadian, R., 2019. Coastal Reservoirs and their Potential for Urban Regeneration and Renewable Energy Supply; In: Sitharam, T.G. ed. *Sustainable Water Resource Development Using Coastal Reservoirs*, pp.182-194.

Guo, B., Ahmadian, R. and Falconer, R.A., 2022. The Conjuctive Operation of Tidal Lagoons on The West Coast of UK and the Interactions in the System. *Renewable Energy*. (Under Review)

Conference proceedings

Guo, B., Ahmadian, R. and Falconer, R.A., 2019. Influence of Different Momentum Sources on Modelling Tidal Lagoons. Proceedings of the 38th IAHR World Congress, Panama City. pp.3946-3956.

Guo, B., Ahmadian, R. and Falconer, R.A., 2018. Modelling the Different Operation Scheme of Swansea Bay Lagoon by TELEMAC-2D. Proceedings of the 5th IAHR Europe Congress, Trento, Italy.

Guo, B., Ahmadian, R. and Falconer, R.A., 2018. Modelling Tidal Range Structures Using Delft3D and TELEMAC-2D and the Hydro-Environmental research of tidal lagoon. 2nd PRIMaRE Conference, Bristol, UK, 3-4 July 2019. (Poster presentation

Chapter 1 Introduction

1.1 Research Background

Climate change and extreme weather events linked with the rise of global temperatures have occurred around the world. It has been demonstrated that global temperature has risen more than 1°C since the pre-industrial period (1720-1800) (Hawkins et al., 2017), and this rise will accelerate in the future on long timescales. Furthermore, the latest research has indicated that meeting the established international goal set by the Paris Agreement of limiting temperature change to well below 2 °C is already challenging. Pursuing efforts towards limiting change to 1.5 °C would require a more rapid and deeper energy system decarbonisation action in the next two decades (Gambhir et al., 2019).

There is substantial evidence that a key driver of global warming is the rising level of atmospheric carbon dioxide (CO_2), which could modulate the global temperature via the 'greenhouse effect' (Visser et al., 2016; Intergovernmental Panel on Climate Change (IPCC), 2012). Since the First Industrial Revolution, human activity has generated large volumes of greenhouse gas by combusting fossil fuels. It is estimated that the main sources of greenhouse gas emissions (CO_2) are electricity generation (26%), industry (19%), forestry (17%) and agriculture (14%) (Metz et al., 2007). Therefore, using renewable energy to replace fossil fuels is key to restricting the temperature rise to under the established limit (United Nations, 2012).

Besides the environmental benefits, renewable energy also has a number of advantages for future development. First, the price competitiveness of renewable energy keeps growing: with the development of more energy-efficient equipment, better engineering work and part design, and the maturity of the market, the price of renewables is rapidly dropping. Second, renewable energy provides long-term certainty for its relatively long service life; last, national energy security could be strengthened with a diversified portfolio of energy assets, avoiding influences from market fluctuations and political factors.

As the most populated country, China aims to reduce its carbon emissions per unit gross domestic product (GDP) by 60-65% by 2030 from the level of 2005; the target for the non-fossil fuel share in total energy demand is 20% by 2030 (NDRC, 2016). In September 2020, the Chinese President announced the nation's plan to hit peak emission before 2030 and carbon neutrality by 2060 (McGrath, 2020).

As one of the leading global promoters on reducing carbon emissions and deploying renewable energy, the United Kingdom (UK) government has set a series of ambitious targets for clean energy systems. In June 2019, the UK committed to reducing the UK's net emissions of greenhouse gases by 100% relative to 1990 levels by 2050, which is the first net zero emissions commitment among major economies in the world (UK Government, 2019a). Prior to this target, the UK was aiming to reduce net greenhouse gas emissions by at least 80% of their 1990 levels, also by 2050 (UK Government, 2019b). To achieve this target, the UK would need to take quick action to develop renewable energy that is efficient, economically viable and reliable. In the past decade, the proportion of renewable energy has kept rising. In 2017, renewables made up 27.9% of domestic electricity production (BEIS, 2018c), with wind power providing 50% of the utilised renewable resources (BEIS, 2018b).

Developed countries have led the way in developing, promoting and deploying renewable energy, aiming at sustainable development and decarbonisation of their economies (Baldwin et al., 2017). For example, in June 2018, the EU established a new binding renewable energy target for 2030 of at least 32% of its total energy needs, while this target was 27% in 2014 (EU, 2018). As one of the leaders in the EU, the Energiewende in Germany has declared that the whole country will abandon nuclear power and decrease green gas emissions by 80% by 2050 (Renn and Marshall, 2016; Morris and Jungjohann, 2017). In recent years, lower-income countries have begun to express increased interest in and commitment to renewable energy (Gielen et al., 2019). The Indian government has increased its renewable energy target to 227 GW by 2027, from a previous target of 175 GW by 2022 set several years ago (Gielen et al., 2019).

However, one of the noticeable features of currently developed renewable energy is the stochastic nature of its sources, that the power output is weather dependent (Uqaili and Harijan, 2011). For example, a so-called 'wind drought' was caused by an exceptionally calm anti-cyclonic weather system during July 2018 in the United Kingdom, which resulted in the overall wind power capacity dropping to less than half the normal annual capacity percentage in 2017 (Vaughan, 2018). For national energy security, a diversified renewable energy portfolio is desirable to protect the country from disruptions and outages in any one sector.

One of the most unexploited and vast renewable energy resources for the UK is tidal energy. Tidal energy could potentially produce up to 50 TWh/year in the UK, accounting for 48% of the total European tidal energy resource potential (Burrows et al., 2009b), which can supply up

to 29% of the UK demand relative to 2013 (DECC, 2014; Todeschini, 2017). Furthermore, the potential tidal energy development schemes in the UK are some of the few sites worldwide that are close to electricity users and the transmission grid (Burrows et al., 2009b). Tidal range energy, created by the rising and falling of tides, is regarded as one of the renewable sources that have the most prospective application potential. One significant advantage of tidal range energy over many other forms of renewables, e.g. wind and solar, is its almost perfect predictability over long time horizons. It is also more predictable than other kinds of marine energy such as wave energy which is partly a consequence of wind energy (Bahaj, 2011; Fraenkel, 1999). Therefore, incorporating power generated by tidal ranges into the power grid should be less challenging than incorporating less predictable sources.

A Tidal Range Scheme (TRS) is capable of generating predictable energy from tides by utilizing a water head difference artificially generated by impounding water throughout a tidal cycle. Traditionally, tidal barrages have been the main focus of tidal range schemes due to their lower wall to basin size ratio, thereby reducing the civil engineering costs of the scheme (Xia et al., 2010b). However, the environmental impact of the tidal barrage is regarded as its greatest disadvantage (Rourke et al., 2010). By blocking the entire estuary, the operation of a tidal barrage can have adverse effects on a large area of the ecosystem by modifying water circulation, sediment behaviour, water quality, bird habitats and fish migratory passage (Hooper and Austen, 2013; Burrows et al., 2009a). In the alternative forms, tidal lagoons, which share the same well-developed construction and operation techniques as the tidal barrages, while having less environmental impacts, have attracted considerable attention. As tidal lagoons generally do not block major estuaries to the same extent as barrages, they tend to have reduced impacts on the estuarine environment, and potentially offer multifunctional features, such as flood risk reduction and significant amenity or leisure opportunities etc. (Hendry, 2016; Angeloudis and Falconer, 2017).

1.2 Hydro-environmental Impacts of Tidal Range Scheme

Most of the suitable locations for proposed lagoons are sites in complex ecosystems, so even a well-designed tidal lagoon would inevitably have an impact on the surrounding environment. For example, the La Rance barrage has been shown to have the effects such as enhanced muddiness on the seabed and raised productivity of the foreshore (Kirby and Retière, 2009). Although a tidal lagoon is different from a tidal barrage in the level of blockage, these two

forms of TRS generally share the same working principles and operation mode and thus produce comparable impacts. The operation of the lagoon will decrease the tidal range in the water impoundment area, which consequently reduces the water volume entering or leaving the planned lagoon area during each tidal cycle. These fundamental hydrodynamic changes will then profoundly affect the hydro-environmental conditions in the broadest sense for the surrounding region.

A tidal lagoon affects sea levels within and around the impounded area due to its significant water volume storage, usually reducing the tidal range, which can lead to the shrinking of intertidal habitats and a decrease in flood risk (Xia et al., 2010b). For example, the proposed Severn Barrage could reduce the tidal range by 10% in the near-field downstream (Frau, 1993), and could continue to affect tidal elevation as far as 100 km seaward (Parsons Brinckerhoff Ltd, 2008b). The estimated potential loss of intertidal habitat area caused by the Severn Estuary Barrage ranges from 14,428 hectares (Sustainable Development Commission, 2007a) to 20,000 hectares (Parsons Brinckerhoff Ltd, 2008b). Estuaries and coasts with large tides usually form an important component in the migration patterns of a wide variety of wading birds and waterfowl. Any pronounced loss of intertidal habitats can significantly restrict feeding opportunities for birds post-development (Kirby, 2010; Adcock et al., 2015). The specific impact on bird populations depends on the remaining size of the feeding area and the available feeding time, along with the abundance of prey. This impact might be crucial as the loss of feeding and breeding grounds associated with a tidal lagoon is detrimental to affected birds, and competition at the remaining intertidal habitats increases the mortality rate (Burton et al., 2006; Goss-Custard et al., 2002).

The tidal flow pattern and residual flows will also be modified around the tidal lagoon, and even minor changes in velocity magnitude may have a noticeable influence because the energy with the flow is proportional to the cube of the velocity (Hooper and Austen, 2013). The high-energy water flows exiting from the turbines and sluice gates may cause local scouring in the outflow region (Wolf et al., 2009). In principle, alterations to the tide flow can significantly affect the suspended sediment transport and movement of bottom sediments in the estuary, thereby affecting the region's geomorphology, turbidity and benthic environments (Kadiri et al., 2012; Gao et al., 2013; Ahmadian et al., 2014a; Xia et al., 2010c).

Water quality would be affected by many aspects of a TRS. For tidal barrages, a reduced tidal flushing rate is expected in the upstream area (Hooper and Austen, 2013), followed by

increased concentrations of dissolved nutrients (Parsons Brinckerhoff Ltd, 2008c) and dissolved oxygen levels (Kirby and Retière, 2009), and decreased salinity (Wolf et al., 2009). A reduced tidal flushing rate also means a lower water renewal capacity, which would hinder the dilution, transport and dispersal of nutrients and contaminants, probably failing to meet water quality standards (Evans, 2017). Phytoplankton biomass and primary production would be affected by the construction of the tidal lagoon; the increased dissolved nutrients would consequently benefit phytoplankton growth while changing water turbidity would also have an impact on phytoplankton production by influencing photosynthesis (Underwood, 2010). The change in phytoplankton biomass and production would in turn affect the food supply for the benthos and so influence the carrying capacity of intertidal areas for feeding shorebirds (Warwick and Somerfield, 2010).

The tidal lagoon industry is still in a nascent stage, and there is a lack of environmental regulatory guidance specific to tidal lagoons. It is essential for developers to fully understand the impact of the scheme on the environment where the tidal lagoon is deployed and eliminate any doubt from influential stakeholders such as government bodies, regulators and conservationists to prevent further issues. However, the current modelling tools available to forecast the potential results of a tidal lagoon on the hydro-environment have been found to work less well than desired. This is due to the lack of experimental data on one hand, and needs of developing better-performing models on the other hand, as an environmental impact assessment would need a full consideration of a range of potential impacts of the proposed lagoons.

1.3 Research Aim and Objectives

This research aims to enhance hydro-environmental modelling of tidal range structures, in order to more accurately assess their impacts and their interactions. The main aims of this research will be achieved by the following specific objectives:

- To improve the representation of tidal lagoons in numerical models and apply the improved model to the West Somerset Lagoon (WSL), North Wales Tidal Lagoon (NWTL) and Swansea Bay Lagoon (SBL). Improvements include full momentum conservation between the subdomains and the independent operation of blocks of turbines and sluice gates.
- To investigate the flow pattern around an obstacle in a macro-tidal environment to improve the understanding of lagoon modelling.
- To develop and validate two-dimensional hydrodynamic models for Severn Estuary and Bristol Channel (SEBC) and Continental Shelf (CS) to provide the baseline hydro-environmental parameters.
- To explore the effects of an open boundary location on the hydrodynamic impact of the tidal lagoon.
- To study the accumulative hydrodynamic impacts and the interaction of tidal lagoons.
- To investigate the hydro-environmental impacts of tidal lagoons, including assessments of the intertidal mudflats, water renewal capacity, sediment transport, nutrient concentration and phytoplankton biomass.

1.4 Novelty and Contribution

The novelty and contributions of this research are mainly concentrated in the following aspects:

1. Modelling tidal lagoons with multi-blocks of turbines where every block is operated independently. Using individual operation schemes for each turbine block in the modelling and optimisation of the lagoon has led to a closer match between the power output predicted by the 0D and 2D models.

2. Improved momentum conservation was included and tested in the model. This refinement is particularly important for the design of lagoons and identifying the interaction of the jets and lagoon structure, and studying morphological changes and water renewal capacity.

3. This thesis provides a comprehensive study on the hydro-environmental impact of two new proposed tidal lagoons in the UK, i.e., WSL and NWTL. For example, the investigation of water renewal capacity evolution for the water outside of a tidal lagoon and the spatial distribution of the residence time inside the lagoon basin provides a comprehensive understanding of the water renewal exchange throughout the lagoon's operation. Furthermore, although some research has used the screening model to study the influence of TRSs on phytoplankton biomass exchange etc., this study provides a more accurate prediction about phytoplankton biomass exchange. This is because the quantitative change of water residence time and the suspended particulate matter concentration changes were assessed based on the residence time and the suspended sediment predicted changes carried out as a part of this research.

4. The modelling of the lagoon was improved by modelling an island, as a natural obstruction, and using the turbulence model that showed the best performance for modelling the island.

1.5 Thesis Structure

This thesis is organised into eight chapters as detailed as follows:

Chapter 1 introduces the research background and motivation for this research study.

Chapter 2 provides an overview of previously published research related to this thesis, studying the tidal range scheme (TRS) both as a commercial industry and as an area of academic research. The background of tidal energy is discussed, followed by a review of TRS development around the world. A comprehensive investigation is conducted for the state-of-the-art numerical modelling method of TRS and its environmental impacts.

Chapter 3 describes the governing equations and associated numerical methods used in the hydrodynamic model, TELEMAC-2D. The developments and validations of two hydrodynamic models, namely the SEBC and CS models, are also presented in this chapter.

Chapter 4 investigates the island wake evolution in the macro-tidal environment to provide the necessary knowledge of flow structures around the tidal lagoon and improve hydrodynamic modelling.

Chapter 5 explains the parameterisation methodology of the lagoon structure components and their operation schemes, which are applied to three lagoon cases: West Somerset Lagoon (WSL), Swansea Bay Lagoon (SBL) and North Wales Tidal Lagoon (NWTL).

Chapter 6 presents the hydrodynamics impacts of lagoons on the surrounding waters, including the lagoon operation on the tidal harmonic constituents, tidal elevation and tide speed change. This chapter then explores the hydro-environmental impact assessments of tidal lagoons, including the intertidal mudflat area, renewal capacity of surrounding water, phytoplankton biomass study and the suspended sediment transport study.

Chapter 7 investigates the effects of open boundary location on the far-field hydrodynamics of tidal lagoon and the interaction between lagoons.

Chapter 8 presents the conclusions from this research and recommends the areas for future research.

Chapter 2 Literature Review

2.1 Tide Theory

Tide is defined as the oscillation of the sea level relative to the land. The physics and driving force of tides have long been understood - the tide-generating forces encompass the rotation of the earth and the gravitational force of the Sun and the Moon (Charlier and Finkl, 2009). Most tides oscillate twice a day, called semidiurnal tides; diurnal tides occur in some geographical areas, involving one high and low tide daily. The tidal day for the semidiurnal tide is 1.035 times as long as the solar day, i.e., each tidal cycle typically takes an average of just over 12 hours. The period of a full cycle of semidiurnal tides is over 14 days, with the highest water level, or spring tide, occurring a few days after either a new or a full moon; the lowest water level appears at a neap tide, which occurs shortly after the first or last quarter moon. The spring-neap tide is controlled by the complex superimposed impact of the Earth-Moon-Sun system, with the spring tide occurring when the Moon and the Sun align their gravitational forces; when the Moon and Earth are aligned vertically relative to the Sun and Earth, the superimposed tidal forces partially offset each other resulting in the neap tide, as shown in Figure 2.1.

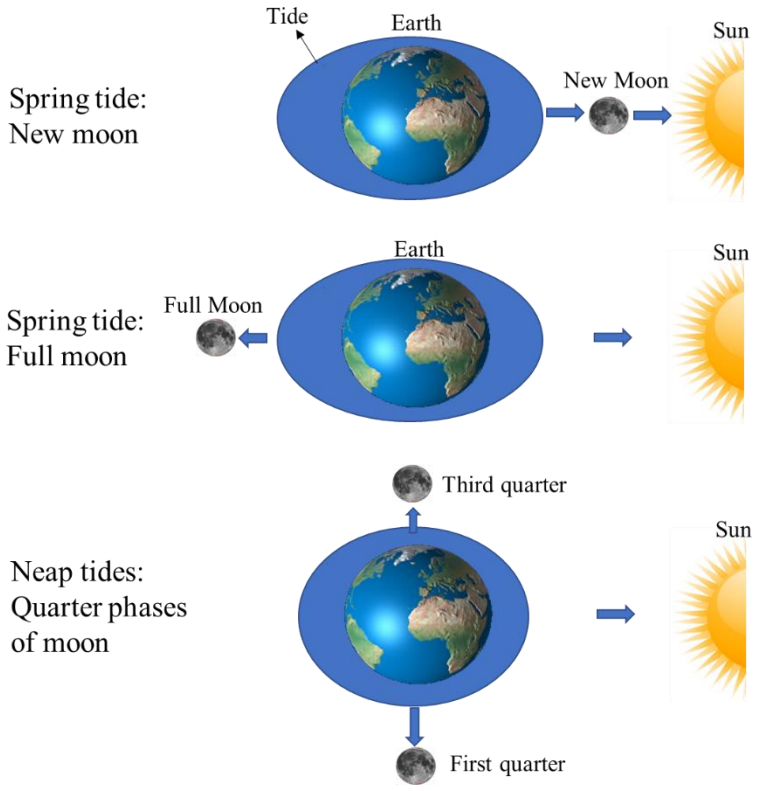

Figure 2.1: Relationship between the position of the Moon and the tidal range.

However, the distribution of global tide shows a noticeable spatial difference. The tide is driven by astronomical forces but is also significantly affected by the coastal geomorphology, coastal water depth and ocean floor topography. For example, the tidal range in the open ocean is relatively small but will grow near the shore, especially in the region of semi-enclosed seas and estuaries, because of the resonance and convergence effect of coastline (Pugh, 1996). For example, The tidal range in the Bay of Fundy, Canada, could reach 16.3 m during the spring tide, which is the largest tidal range in the world; the second largest tidal range occurs in Bristol Channel, UK, approaching 14.2 m (Greaves and Iglesias, 2018). A coast is classified based on the tidal range as microtidal, mesotidal and macro-tidal if the tidal range is below 2 m, 2-4m and exceeding 4 m, respectively (Charlier and Finkl, 2009).

The analysis of observed tide records and the harmonic analysis has been used to make accurate predictions of sea water levels (Pugh, 1996). Harmonic constants can be calculated through the analysis of periodic sea-level change data collected at a location. The tide predictions can be described mathematically as:

$$Z(t) = \sum_i a_i \cos(\omega_i t + \phi_i), \tag{2.1}$$

where Z is the free surface level at time t, and a_i, ω_i, ϕ_i are the amplitude, angular frequency and phase of the ith harmonic component, respectively. More harmonic components accounted for in the Fourier analysis result in more accurate water level predictions. Doodson (1921) identified 388 different harmonics components. However, seven or eight components are sufficient in most cases. For example, Table 2.1 lists the main tidal constituents at the mouth of the Severn Estuary (Vazquez and Iglesias, 2015).

Table 2.1: Tidal constituents at the mouth of the Severn Estuary (Vazquez and Iglesias, 2015).

Constituent	Description	Amplitude (cm)	Phase (Degree)
M_2	Principal lunar semidiurnal	235.24	156.87
S_2	Principal solar semidiurnal	84.17	201.21
N_2	Larger lunar elliptical semidiurnal	44.79	138.48
K_2	Lunisolar semidiurnal	24.45	195.80
K_1	Lunar diurnal	6.77	127.34
O_1	Lunar diurnal	6.70	351.17
P_1	Solar diurnal	2.23	121.81
Q_1	Larger lunar elliptical diurnal	1.95	305.66
M_4	Shallow water overtides of principal lunar	3.69	290.99

For any marine site, the time series of tide elevation could be decomposed into the tidal harmonics using harmonic analysis. However, a portion of the tidal signal is beyond the range of astronomical tide because of meteorological forcing and other non-linear effects. The meteorological tide includes the tide level oscillations caused by winds and atmospheric alteration. During storms, high air pressure exerts a force on the surroundings and corresponds to low sea level, while low atmospheric pressure can cause a rise in tidal level higher than the normal astronomical tidal range, which causes storm surge (Wadey et al., 2015). For this reason, pre-treatment should be carried out on the time series of tide levels before harmonic analysis to remove the non-astronomical factors (Thomson and Emery, 2014).

2.2 Tidal Energy

Tidal energy is the power produced by the surge of sea waters during the rise and fall of tides, or the energy from moving tidal currents. The significant advantage of tidal energy is the predictability over the other types of renewable energy, such as wind energy or solar power, which allows the future energy-generating potential to be accurately assessed, regardless of unexpected surges and other meteorological impacts (Rourke et al., 2010). There are two major

categories of tidal energy: tidal stream energy and tidal range energy, which correspond to different methods of energy harnessing, as seen in Figure 2.2.

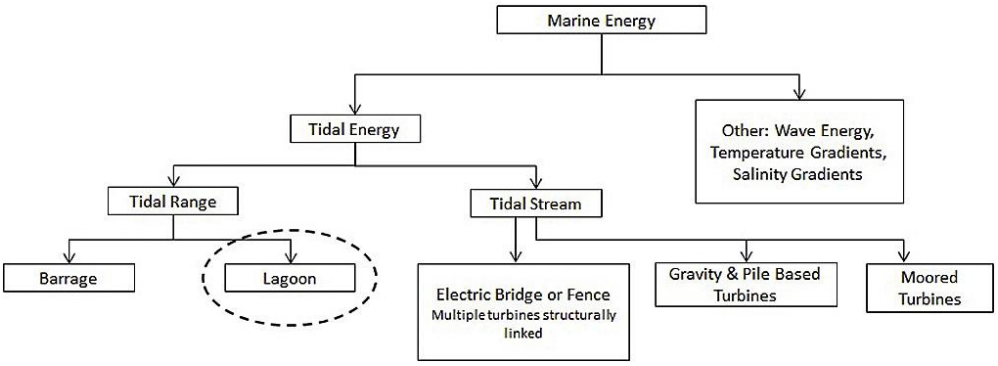

Figure 2.2: Classification of tidal power technologies (Elliott et al., 2018).

However, compared to the rapid growth of wind-turbine and solar energy applications, the development of tidal energy schemes is much slower because of the relatively high capital cost of a tidal energy project (Hendry, 2016). Thus, tidal power is still approaching commercial maturity. However, with the fast-growing commercial investments and exploratory deployments, the economic and environmental costs of tidal energy projects are expected to be mitigated in the future.

2.2.1 Tidal Stream Devices

A tidal stream generator takes advantage of the Kinetic energy of moving water to drive the generator, in a similar way to wind turbines that use wind for power. However, the ten times higher dynamic pressure in tidal flow and the unsteadiness flow in the marine environment lead to the different designs in the tidal turbine and wind turbine (Adcock et al., 2021). Additionally, locations where the flow is restricted, e.g. narrow channels, the tip of peninsulas, contain higher energy density, which is beneficial for energy extraction (Adcock et al., 2015).

The kinetic tide stream energy through a cross-section perpendicular to the flow direction per unit time is given by the following equation:

$$P_{\Omega} = \frac{1}{2}\sigma\rho V^3 A, \tag{2.2}$$

where V is the magnitude of the flow velocity averaged over the section, A is the surface area of the cross-section, ρ is the density of seawater, and σ is the energy transform coefficient (Carballo et al., 2009).

A tidal stream turbine operates with the same working principles as a wind turbine; thus, most of the fundamental technology used in the early development phases of a tidal stream turbine is derived from the wind turbine industry. The tidal turbine blades are shaped with an aerofoil cross-section (Roberts et al., 2016). When the tidal flow passes across the blade, a pressure gradient across the two surfaces of the blade occurs to drive the generator.

The successful deployment of tidal stream turbines is related to many factors, including local tide velocity, turbulence, bathymetry, water column velocity profile and depth, seabed mounting, shipping route and marine animals. Different from the tidal range energy schemes, the tidal stream turbines do not block the whole passage of the tide flow. Thus, the environmental influence from tidal stream turbines is assumed to be easier to control, compared with the tidal range energy structure. However, the higher energy cost of tidal stream energy is one of the key challenges for further development of TRSs, as shown in Table 2.2.

Table 2.2: Levelized cost estimates for electricity with different sources (Astariz et al., 2015; Poyry Consultants, 2014).

Source	Levelized cost estimates (€/MWh)
Tidal lagoon	105 - 175
Tidal stream	190
Offshore wind	165
Wave	325
Nuclear (pressurized water reactor)	49.96
Combined cycle gas turbine	43.17
Coal	36.59 - 55.76

Furthermore, it is understood that the profitability of ocean energy projects is heavily reliant on the site conditions, e.g. the upstream tide velocity and the bathymetry (Bahaj, 2011; Greaves and Iglesias, 2018), and also technological advancements and maturity of the type of energy project.

2.2.2 Tidal Range Structures (TRS)

Tidal range energy refers to the gravitational potential energy that exhibits a large difference in water height between the high tide and low tide (Baker, 1991). To utilise this kind of energy, a semi-enclosed construction, like a tidal barrage or lagoon, is required in the region to establish a water head difference between the two sides of the embankment as the tidal level rises and falls outside of the impoundment area. Eventually, the artificial water head difference forces the tide to flow through the turbine tunnel and drive the turbine-generator groups. The potential

energy yield that is extracted from the tidal range schemes is proportional to the plan impoundment area and the square of the water head difference:

$$E = \frac{1}{2}\rho A g h^2, \tag{2.3}$$

where ρ is the density, A is the area of the basin, g is the acceleration due to gravity, and h is the water head difference (Tousif and Taslim, 2011). Equation (2.3) demonstrates that the key to harnessing the tidal range energy is to contain large volumes of water with a large impounding area and high tidal range.

A barrage usually stretches across the estuary (Sustainable Development Commission, 2007b), while a tidal lagoon is an artificial coastal impoundment that is attached to the coastal line or is completely offshore, as seen in Figure 2.3. The primary difference between them is whether the estuary is completely or partially blocked. Tidal range schemes have proven successful in different countries (Waters and Aggidis, 2016a). This could support the development of coastally attached tidal or offshore tidal lagoons. Offshore tidal lagoon which is completely self-contained and independent of the shoreline, is thought by researchers to have less environmental impacts (Cousineau et al., 2012).

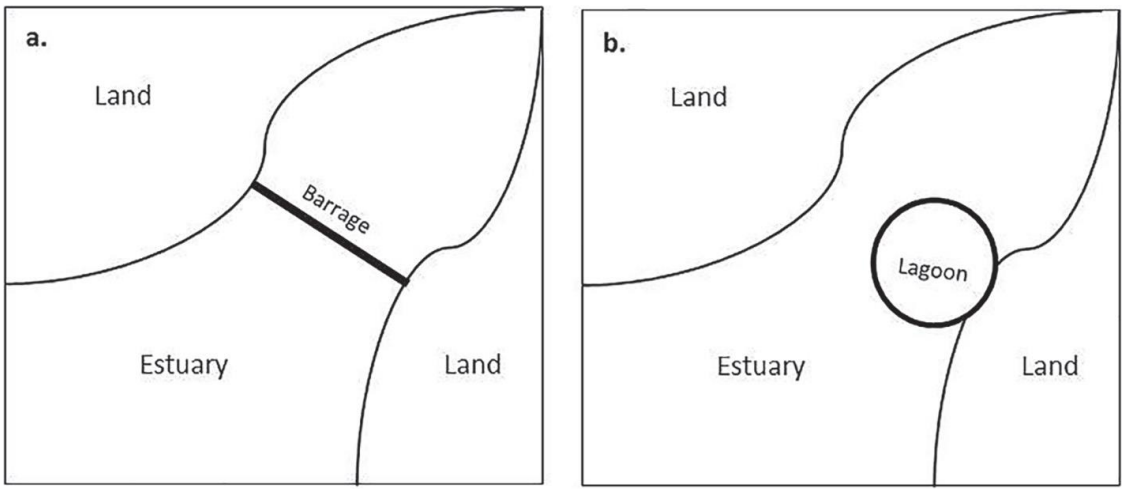

Figure 2.3: Conceptual graphs of a tidal barrage and a tidal lagoon (Elliott et al., 2018).

2.2.3 Global TRS Development

The primary requirements in TRS development are adequate tidal range and suitable coastal lines, which lead to a cost-effective site. Furthermore, environmental impact and easy power grid absorption should also be considered. Thus, not every site with sufficient tidal range is a potentially ideal location for TRS deployment. To gain a general picture of the TRS

development, the existing and potential TRS designs and the developing strategy in different countries are discussed as follows:

2.2.3.1 United Kingdom

Despite no commercial development of TRS yet in the United Kingdom (UK), its research on TRS has been at the forefront worldwide. The available tidal range energy in the UK that can be harnessed by both tidal barrages and tidal lagoons is 121 TWh/year (Estate Crown, 2012), which accounts for 35.7% of the total electricity production in 2015 (BEIS, 2018a). Thus, the UK has the potential to generate a reasonable proportion of renewable electricity from tidal range energy, as shown in Figure 2.4.

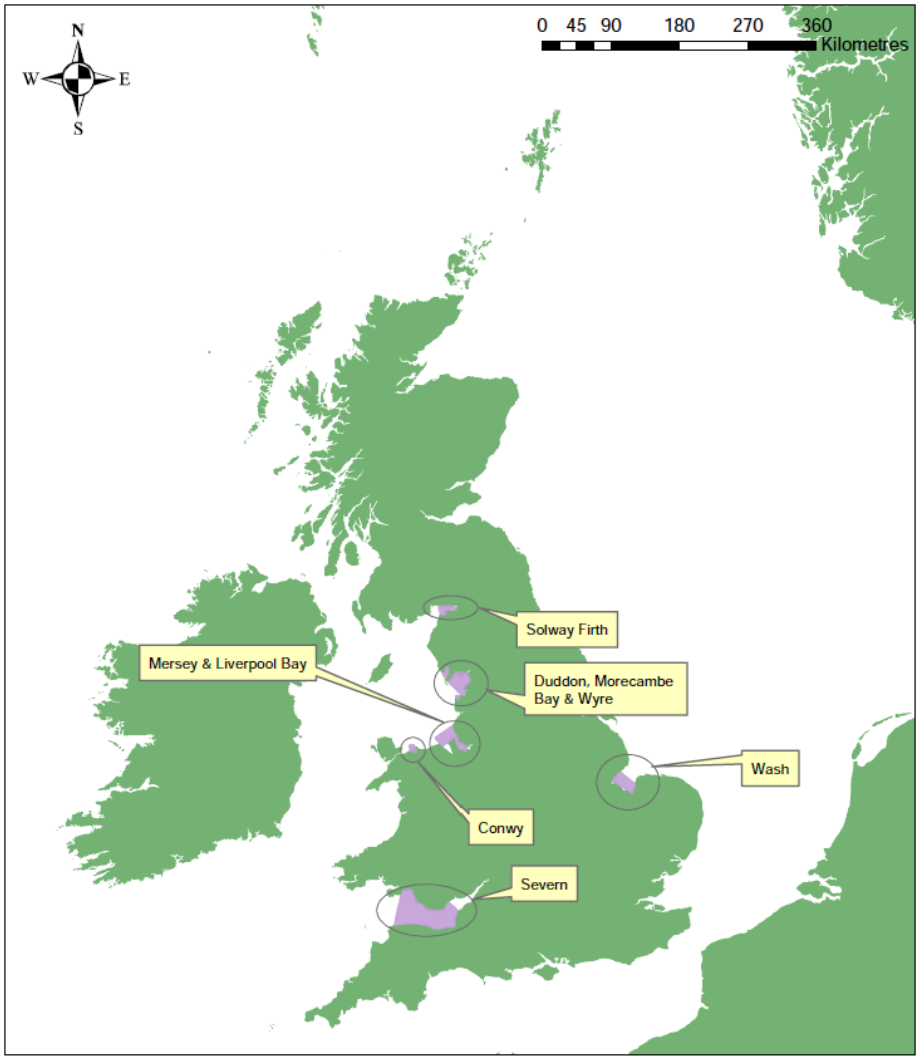

Figure 2.4: Summary of tidal range resource of the UK (Sustainable Development Commission, 2007b).

The Bristol Channel and Severn Estuary comprise the area most thoroughly investigated regarding TRS development (Charlier and Finkl, 2009), commonly referred to as the Severn Barrage. Implementing a tidal barrage in the Severn Estuary has been debated for many years, with numerous feasibility studies. The Bondi Committee investigated six possible barrage locations, proposing concrete powerhouse spans from Brean Down to Lavernock Point with a length of 16 km (Bondi, 1981). The Shoots Barrage (or Hooker Barrage) was published by Parsons Brinckerhoff in 2006 and discusses a smaller barrage located just below the Second Severn Crossing. In 1989, the Bondi Committee's 1981 plan was supported by the Severn Tidal Power Group (STPG), but with an enlarged turbine installation. The STPG plan is the most scrutinised Severn Barrage proposal and, thus, is usually regarded as the original Severn Barrage (Falconer et al., 2009), the configuration of which is given in Figure 2.5. The barrage would contain 216 40-MW turbines, achieving a total of 8,640 MW during the peak flow and providing power of 17 TWh/year. This design is expected to have a long lifespan, ranging from minimum 120 to 200 years with maintenance (Severn Tidal Power Group, 1989).

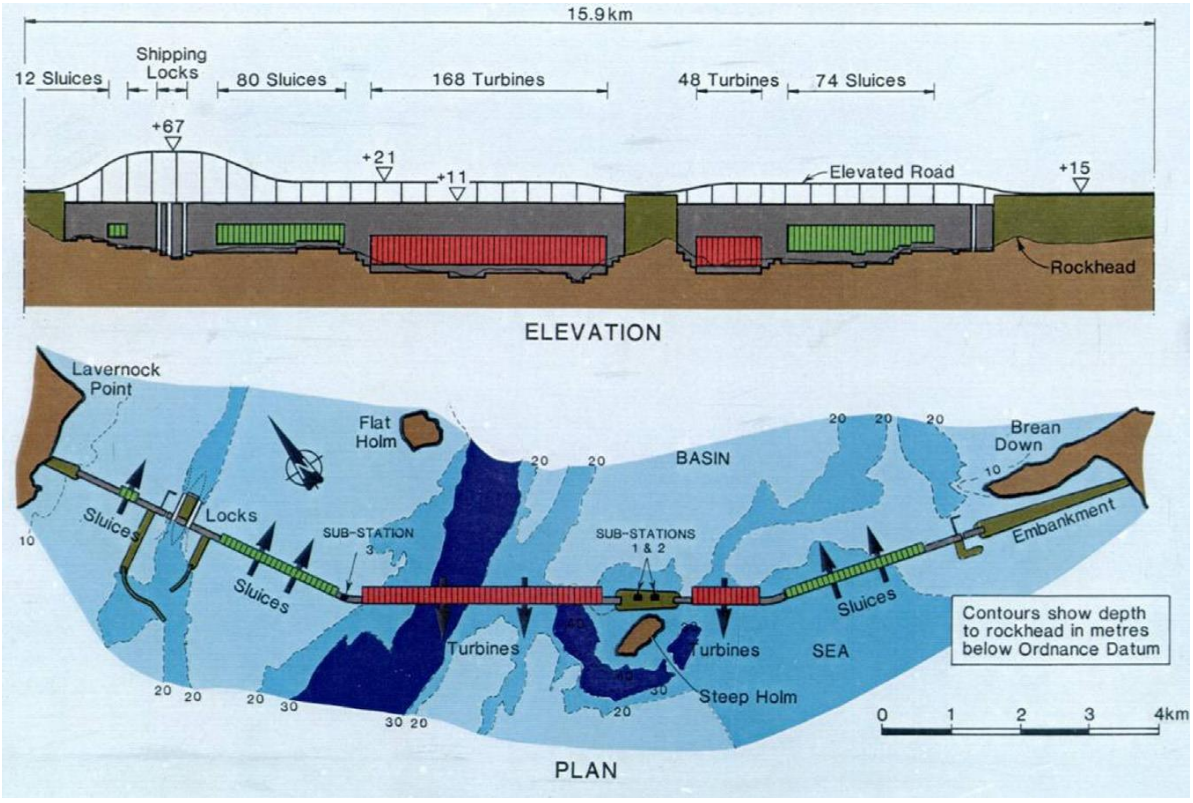

Figure 2.5: Configuration of STPG Barrage (Severn Tidal Power Group, 1989).

Even with the predictable and huge source of sustainable energy from Severn Barrage, the potential disadvantages include high costs of construction and produced energy and environmental risk. The Severn Barrage proposals have then fallen out of favour, and the

attention of the public and academia has shifted towards the tidal lagoons for their smaller hydro-environmental impact and larger output power per unit area enclosed (Waters and Aggidis, 2016a). Tidal lagoons have been considered in the east side of the Irish sea and the Bristol Channel, including the Swansea Bay Lagoon, Newport Lagoon, Cardiff Lagoon, Newport Lagoon, Bridgewater lagoon, West Somerset lagoon and North Wales tidal lagoon, etc.

2.2.3.2 France

The Rance Tidal Power Station located on the estuary of the Rance River in Brittany, France, is the first such project that has been successfully deployed in the world. A 720 m long barrage blocks the Rance river, capturing a 22 km^2 basin area (Rtimi et al., 2021). Twenty-four 10-MW Kaplan bulb turbines contribute to a total output of 240 MW and annual production roughly 480 GWh (Andre, 1976). The turbines operate on a bidirectional cycle, producing power on both the ebb and flood tides, and can also be used as pumps to enhance the water head difference (Waters and Aggidis, 2016a). Furthermore, the embankment also works as a road linking the sides of the river, improving local transportation and introducing a valuable tourist attraction.

Figure 2.6: The Rance River Barrage, Brittany, France (Wikipedia, 2021).

The barrage has been in operation for more than 50 years without requiring significant repair on the turbines (Charlier, 2007), and the electricity generation remains stable meeting

expectations. However, the environmental impacts have gotten progressively worse since its construction. The estuary was completely blocked for three years during construction, damaging the local marine ecosystem. In operation, a strong water jet near the turbine and sluice gates results in scour near the barrage (Charlier and Finkl, 2009).

The Rance River Barrage was regarded as a pathfinder in France to explore the future energy policy. Although the barrage is considered a success, France's energy strategy was re-oriented towards nuclear power.

2.2.3.3 Canada

With the largest tidal range in the world of 16 m during spring tide (Etemadi et al., 2011), the Bay of Fundy is an attractive location for potential TRS projects due to its natural advantage and proximity to the fast-developing New England market. In 1984, the Annapolis power plant was constructed in this area (Pelc and Fujita, 2002). This scheme hosts the largest Straflo turbine in the world with unit power of 20 MW, producing 50 GWh of electricity per year with ebb generation (Todeschini, 2017). In addition, the plant acts as a flood defence and provides a vital transport link (Waters and Aggidis, 2016a).

Figure 2.7: Annapolis station, on the Bay of Fundy in Nova Scotia, Canada (Brad, 2013).

After the implementation of the Annapolis power plant, interest in tidal lagoons in the Bay of Fundy has risen. Delta Marine Consultants (DMC) have assessed the feasibility of constructing

tidal lagoons in the upper Bay of Fundy in 2006 (Delta Marine Consultants, 2007). Various plant layouts were investigated by DMC, and two types of lagoons were chosen for further study, as shown in Figure 2.8. One option is an offshore lagoon with an 11.9 km long embankment detached from the shore that encloses 12 km^2 circular embankment; another is a coastal lagoon, which has a 24 km^2 impoundment formed between the 10.2 km long embankment and the existing shoreline (Cornett and Cousineau, 2011; Cornett et al., 2013).

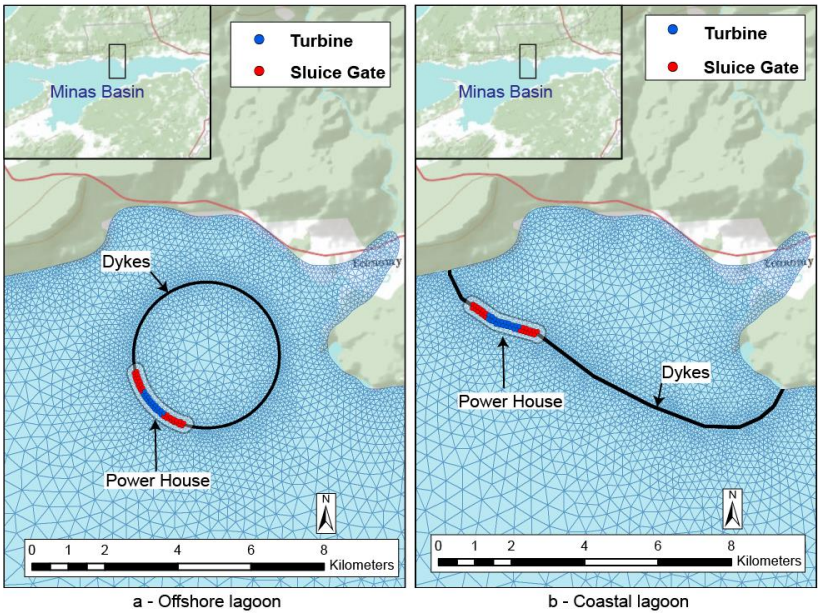

Figure 2.8: Schematisation of offshore and coastal lagoons (Cousineau et al., 2012).

2.2.3.4 South Korea

The Sihwa Tidal Barrage of South Korea is the latest large TRS in the world, although the initial purpose of this project is not for renewable energy generation. In 1994, the South Korea government constructed Sihwa Lake as a land reclamation project. The 43.8 km² artificial lake has a 12.7 km long seawall at Gyeonggi Bay. The purpose of Sihwa Lake was to reclaim land for the nearby metropolitan area, flooding defences and secure irrigation water (Bae et al., 2010). However, water quality deteriorated greatly once the project finished as a result of the cut-off of tidal currents and the pollution from nearby industries (Park, 2007). To improve the water quality, authorities began in 1997 to periodically open the sluice gates to flush the basin with circulating seawater. However, seawater circulation through the sluice gates alone was not sufficient. After a feasibility study, the government decided to build a tidal power plant at the site, which was estimated to double the seawater circulation (Cho et al., 2012).

The Sihwa tidal barrage, constructed in 2004, is shown in Figure 2.9. Ten optimised bulb turbines that only operate during the flood phase were installed with a total capacity of 254 MW. The Sihwa tidal barrage is considered a great success - The water quality has improved by the enhanced seawater exchange rate; vast clean energy is generated, and tourism and the environment have benefited. Therefore, the South Korea government is exploring the possibility of additional tidal energy plants, with the most promising being the bays of Gerolim and Incheon (Kim et al., 2012).

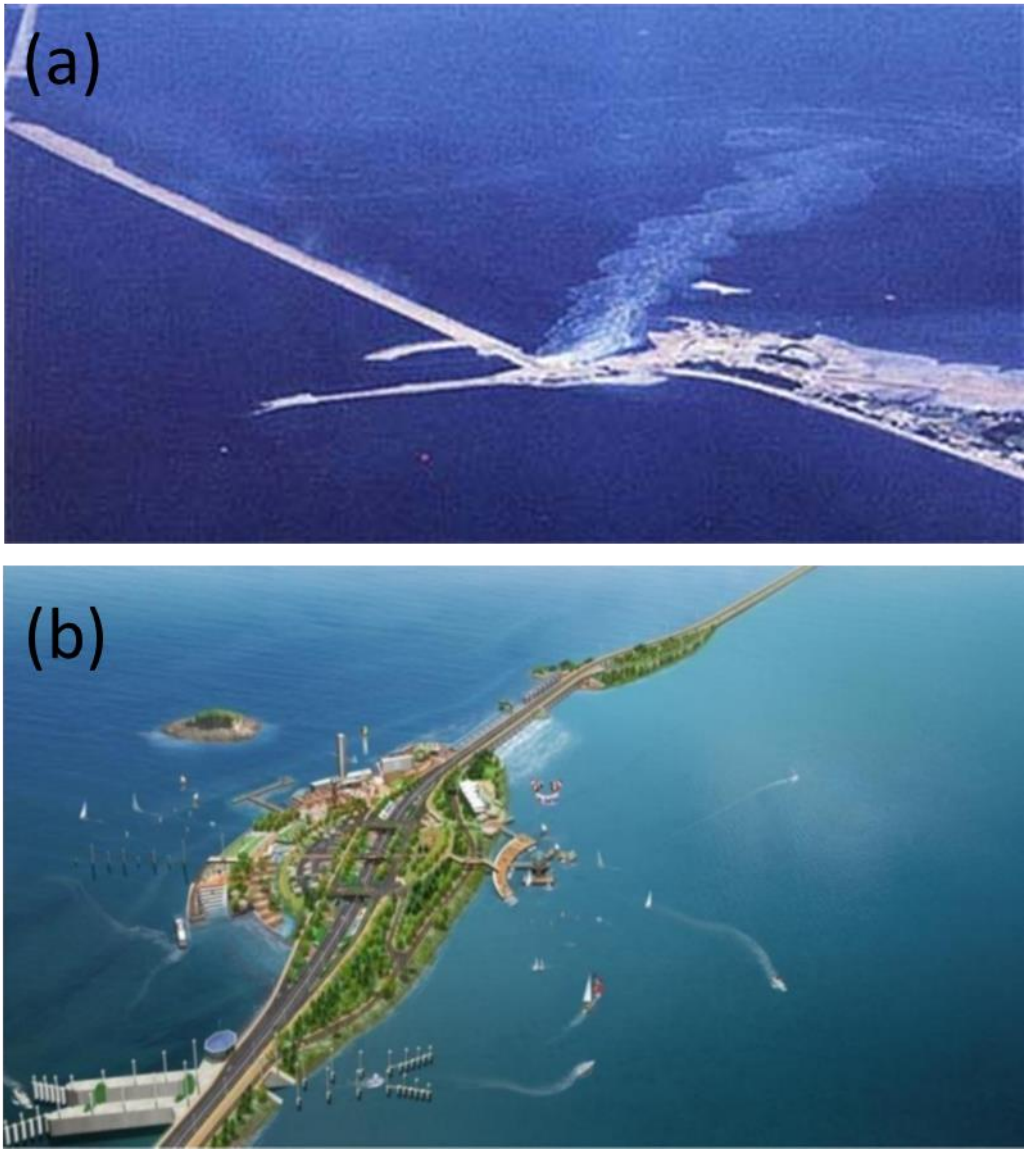

Figure 2.9: (a) Lake Sihwa Dam (Park, 2007) and (b) Lake Sihwa Tidal Barrage Plant (Aggidis, 2010).

2.2.3.5 China

China has been highly active in the exploration of tidal range energy extraction technologies. Since 1959, many tidal range plants have been constructed for research and testing (Li and Pan, 2017). However, with the limited technologies, most tidal range plants were discarded owing to the unreasonable locations and flawed turbine construction, as seen in Table 2.3.

Table 2.3: The main TRSs of the past in China (Li and Pan, 2017).

Name	Location	Basin storage (10^4 m^3)	Installed capacity (kW)	Design annual energy output (10^4 kWh)	Operation time	Operation condition
Xunqiao	Linhai	6.1	2×30	22	1959	Discarded in 1963
Shashan	Wenling	4	1×40	72	1959	Discarded in 1984
Gaotang	Xiangshan	30	1×50+2×75	50	1972	Discarded in 1980
Yuepu	Xiangshan	40	4×75	60	1972	Discarded in 1981
Jigang	Xiangshan	-	1×30	-	1972	Discarded in 1975
Bingying	Xiangshan	15	2×75	15	1976	Discarded in 1979
Haishan	Yuhuan	26+2.6	2×75	38	1975	Run up to now
Jiangxia	Wenling	514	1×600+5×700	720	1980	Run up to now

The most successful Chinese tidal range plant is the Jiangxia power station (Figure 2.10), which was constructed last but is the largest. The Jiangxia power plant has six bulb turbines that operate bi-directionally, with a total installed capacity of 4.1 MW (Wang et al., 2011).

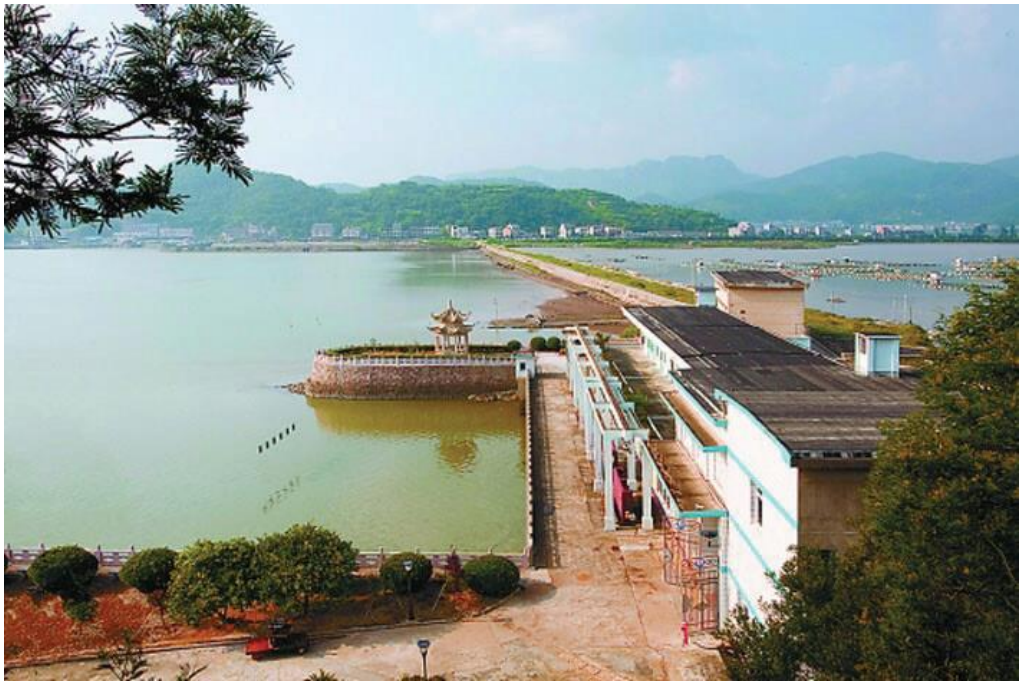

Figure 2.10: Jiangxia Tidal Power Plant (Zhang et al., 2014)

Although no other tidal range plant was constructed after the Jiangxia tidal barrage, China is still making progress in the development of tidal energy. After realising the importance of site selection, a new investigation has been carried out: 426 potential sites were selected in the preliminary stage, 242 of which were chosen for potential TRS construction with installed capacities ranging from 200 to 1000 kW (Shi et al., 2011).

2.2.4 Features of TRS

In addition to the clean and renewable energy output, TRSs have other advantages compared to other mature renewable energy technology like solar and wind energy. One advantage of TRSs is continuity and predictability. National energy security requires a steady and abundant energy source. However, the most developed renewable energy is often intermittent and unpredictable, causing fluctuations in the power grid. Wind and solar energy are more dependent on the weather. As weather conditions are often homogenous over large areas of the UK, Germany and other countries, heavy dependency on wind or solar power may lead to a large variation in energy output. For example, from 26 May to 3 June 2018, the UK experienced nine days with practically zero wind power generation, during which the power generated from UK wind farms fell from more than 6,000 MW to less than 500 MW (Morison, 2018). Different from solar or wind energy, the power output from TRSs relies on the continuous surge of sea waters and the rise and fall of tides, so the power output is known before construction (Neill et al., 2018).

Another noticeable advantage of tidal energy is its longevity of equipment and land space conservation. TRSs have a potential lifespan of approximately 120 years with turbine replacement occurring every 40 years (Kelly et al., 2012), three to four times the longevity of wind and solar farms. The longer lifespan of tidal power also contributes to cost efficiency. Compact space occupation is a significant benefit typically overlooked, especially in countries facing a shortage of available land like the Netherlands and Singapore. Large wind farms usually occupy hundreds of square meters, and solar farms take dozens of square meters. The TRSs are in the ocean, saving land space.

Furthermore, the TRSs could combine with other functions, such as the tourism industry, flooding control and freshwater storage. The initial proposal of the Swansea Bay lagoon emphasised the value of tourism. The early proposals of the Severn Barrage were designed with a double-track railway across the barrage. The management of coastal erosion and flood

risk is vital. In the UK, for instance, the central government has committed over £5bn to coastal management since 2005. The mean sea level is rising roughly 3 mm per year (Woodworth et al., 2009) from climate change, which will bring about an increased frequency and intensity of storms (Chini et al., 2010; Wadey et al., 2014) and a corresponding increase in extreme storm surge water levels. These factors will progressively degrade the standard of protection currently afforded by existing coastal defences (Buijs et al., 2007). Research indicates that the TRSs could reduce the flood risk of the impounded coastal areas (Ahmadian et al., 2014b; Ma et al., 2019). For example, the North Wales Tidal Lagoon is considered able to provide flood defence to the local community that has suffered from flooding (Hendry, 2016). These additional functions allow TRSs to be more than an energy generation project, also dispersing cost and risk.

However, TRSs have some recognised faults that caused several TRS proposals to be controversial, hindering their development. The high construction cost is one main reason to slow down the construction of TRSs (Waters and Aggidis, 2016b). For example, the proposed Swansea Bay lagoon was estimated to cost £1.3bn ($1.67bn) in 2015 with a total capacity of 320MW, while the Roscoe Wind Farm cost roughly $1bn for an output of 781 MW, and the Tengger Desert Solar Park cost approximately $530m for a total installed capacity of 850 MW. The high initial cost results in a relatively less competitive unit cost of power at the first 40 years (Parsons Brinckerhoff Ltd, 2008a). However, the cost comparison between these energy schemes does not usually consider the different lifespans of the scenarios, ignoring the income from the remaining 80 years of TRSs operation. Overall, the true limit of any TRS is that the energy output does not sufficiently provide a return on the investment of the development and running costs (Neill et al., 2018).

Moreover, due to the existence of minimum generation head of bulb turbine and the periodic changes of sea level, intermittent power production is inevitable in a TRS. The intermittency varies from the variations of the tides during a day and through the variations as a part of the spring-neap cycle which is observed fortnightly. This will increase grid congestion management costs and the exacerbating balancing challenges (Neill et al., 2016; Adcock et al., 2015; Mackie et al., 2020). The intermittency operation of TRSs and the periodic variation output of electricity should be taken into consideration in the design stage.

Another key concern of TRS construction is the potential effects on the environment from modifying the tidal elevation, flow structure, sediment transport, water quality and habitats

(Hooper and Austen, 2013). The TRS could cause the loss of intertidal mudflats and salt-marshes (Wolf et al., 2009), where nationally and internationally protected areas for some bird species may exist. The altered flow structure and bottom stress would introduce uncertainties to the local benthic communities. TRS operation would also impact the water renewal capacity, which consequently affects the transport and dispersion of dissolved pollutants and nutrients.

2.3 Numerical Modelling of TRS

Numerical modelling is a rapidly developing sector that has a crucial role in all stages of TRS development (Greaves and Iglesias, 2018). The primary advantage of this technique is the low-cost comparison with the physical model testing; furthermore, numerical modelling can begin earlier, at the stage of resource assessment and feasibility evaluation. In contrast, physical modelling can introduce uncertainties and is often limited to a scaled size of the experimental device based on the laws of dynamic similarity (Payne, 2008).

The complexity of the TRS development can involve a wide range of numerical modelling techniques related to the different aspects. The simplified preliminary modelling of TRS can identify the overall performance and provide an early project assessment. The hydrodynamic simulations of the water flow, such as currents and tides, and their interaction with the TRS are essential in the modelling process; the environmental impact modelling carried out from the preliminary stage of the TRS design mitigates the detrimental influence by optimising the construction (Prandle, 1984).

2.3.1 Preliminary Assessment Models

The optimal TRS design is site-specific because of the unique nature of each coastal environment. Therefore, the evaluation of the TRS before development relies on the models that simulate, predict and optimise TRS operation (Mejia-Olivares et al., 2020; Angeloudis et al., 2019). At this stage, preliminary assessment models such as zero-dimensional (0D) and one-dimensional (1D) models are commonly used. The zero-dimensional (0D) model, also known as flat-estuary or two-tank model, has been extensively applied to synthesise TRS operation for preliminary assessments and optimisation analyses (Burrows et al., 2009b; Aggidis and Benzon, 2013; Mejia-Olivares et al., 2020).

Given the input of tide conditions and the numerical representation of the constituent performance of hydraulic structures, predictions of the TRS configuration and operation space are feasible, providing an informed resource assessment (Angeloudis and Falconer, 2017). The key advantage of such a simple model is the high computational efficiency, making the optimisation of the TRS design and operation relatively straightforward (Adcock et al., 2015). In recent years, 0D modelling tools have been utilised in TRS design to optimise the operation (Angeloudis et al., 2018; Aggidis and Benzon, 2013; Xue et al., 2019b).

Many candidate TRSs are located on estuaries, thus one-dimensional (1D) model can be used to capture the variations in water level across the TRS and along the estuary (Adcock et al., 2015). 1D models could provide more physical information than 0D models, including tidal elevation changes as a result of the lagoon construction, TRS location optimisation and power output prediction. However, studies using 1D models show that they are grossly insufficient to model large scale TRSs. Therefore, 1D models are only recommended for the preliminary assessment of TRSs due to their computational efficiency (Angeloudis et al., 2019).

Although 0D and 1D models are deemed sufficient in predicting the performance of a small-scale TRS (Yates et al., 2013a; Burrows et al., 2009b; Neill et al., 2018), neglecting tidal level oscillations and the interference of TRS on regional tide flow can result in poor accuracy in the 0D model for some cases (Yates et al., 2013b), and the limitations of 1D model on large scale TRS (Neill et al., 2018). Such drawbacks in the 0D/1D approach have led to the development and applications of multi-dimensional (2D, 3D) hydrodynamic models (Lewis et al., 2017; Angeloudis et al., 2020). Therefore, a 2D or even 3D numerical models may be necessary to study the complexities of the regional hydrodynamics surrounding the TRS.

2.3.2 TRS Structure Modelling

Hydrodynamic modelling of TRS structure plays a significant role from an engineering perspective that can provide valuable understanding about the resource evaluation, interactions between the tidal flow and the proposed TRS, and minimisation of any potential detrimental impact through design optimisation (Neill et al., 2018).

In recent years, a variety of modelling tools have been applied to model the hydrodynamics for TRSs, including EFDC (Zhou et al., 2014a; Bray et al., 2016), Delft3D (Čož et al., 2019; Evans, 2017), ADCIRC (Burrows et al., 2009b; Ma and Adcock, 2020), TELEMAC (Carroll et al., 2009; Cousineau et al., 2012), Thetis (Angeloudis et al., 2020), and some in-house software

used by Ahmadian et al. (2010a), Xia et al. (2010c). Most hydrodynamic models for regional TRS study are 2D, while full 3D modelling of TRS is typically limited to laboratory-scale flows. For example, some blade-scale models, such as the full 3D RANS simulation and large-eddy simulation (LES), have also been applied to the study of flow structure in a TRS turbine tunnel, focusing on the performance of the bulb turbine (Wilhelm et al., 2016; Ahn et al., 2020) and the hydrodynamics of the flow through the turbine (Ahn et al., 2017a). These blade-scale models found that the flow passing through a turbine is noticeably influenced by the sudden expansion and contraction cross-section area at the turbine inlet and outlet, respectively (Ahn et al., 2017b; Wilhelm et al., 2016). The flow pattern in locations near the turbines and sluice gates is undoubtedly 3D (Wilhelm et al., 2016; Ahn et al., 2020), and is highly non-uniformity both vertically and horizontally (Ahn et al., 2017b). However, previous experimental research indicates the 3D flow pattern will extend to a distance of 20D from the exit of the turbine, where D is the diameter of the turbine throat area (Jeffcoate et al., 2011). Swirl generated by the stators and rotors will affect the jet mixing and circulation within 5-duct diameters downstream of TRS, which will subsequently result in cross-stream circulation further downstream (Jeffcoate et al., 2017). Results also found that the bed shear stresses were magnified by swirl, which suggests that the bed shear stress might be considerably underestimated in the near field of TRS by a 2D model (Jeffcoate et al., 2013).

Čož et al. (2019) indicated that a 3D model could increase the accuracy of the predicted velocity field in the vicinity of TRS, particularly in terms of the vertical velocity distribution, compared to a 2D model. However, there is no significant advantage in using a 3D model beyond the point where jets have fully dissipated in a macro-tidal basin. Thus, for the investigation of flow behaviour beyond the immediate near-field of TRS turbines, the 2D model is generally sufficient for most of TRS modelling applications (Neill et al., 2018).

In the regional-scale hydrodynamic model, blade-scale behaviour in the flow is not directly modelled. Typically, the performance characteristics of bulb turbines are simply represented by design charts or the manufacturer's specification, i.e. a Hill chart (Adcock et al., 2015). The flow through hydraulic structures, including the discharge of turbines and sluice gates in a TRS hydrodynamic model, is calculated by the Hill chart and added as a source/sink term or an internal boundary condition in the model.

In early studies, turbines were modelled simply by solely considering the mass-balance through the impoundment wall (Ahmadian et al., 2010a; Xia et al., 2010a). However, recent research

has indicated that the accurate representation of the lagoon boundary and momentum conservation of flow through the turbines can significantly impact the wake hydrodynamic characteristics. This approach is critical in studying the hydro-environmental impact within the near-field outside of a lagoon or barrage (Angeloudis et al., 2016b; Čož et al., 2019). For example, the deteriorated water quality in the Sihwa Lake has been improved with the operation of Sihwa tidal power plant, by increasing the tidal currents and higher seawater circulation through tidal barrage, which indicates the importance of accurately predicting the water flow through the turbines (Park, 2007).

Therefore, the momentum fluxes through the turbines require specific model inputs to ensure momentum conservation, based on the characteristics of the structure (Sanders, 2002). Early studies modelling the momentum flux through the turbines have involved refining the cross-sectional area of the grid cell wall normal to the turbine efflux, thereby ensuring the velocity expected from the turbine cell interface leads to mean momentum conservation (Angeloudis et al., 2016b). The latest momentum conservation approach, adapted by Čož et al. (2019), represented the momentum of the discharged water as an additional external force in the momentum equation, accurately predicting the velocity of the discharged jets, as confirmed by the measurements.

2.4 Environmental Impacts of TRS

When TRSs extract tidal energy from the marine environment, the impact of this anthropogenic activity is bound range from beneficial to harmful, from the physical to the biological. Many estuaries are in a protected status or part of a conservation area for the international Ramsar Convention and the EU Habitats and Birds Directives, e.g. the Severn, Mersey, Morecambe Bay, Dee and Solway Firth (JNCC, 2019). Any abrupt intervention may have considerable consequences for biota in these established stable abiotic conditions. Thus, any forms of construction need to consider conservation issues and existing legislation (Wolf et al., 2009), especially the EU Habitats and Birds Directives.

The unique nature and complexity of coastal and estuarine ecosystems make it difficult to apply the findings from one TRS to another (Pethick et al., 2009). For example, although La Rance Barrage provides a mode for installation and operation of the TRS, the available experience from La Rance Barrage that can guide the specific barrage proposals for the UK is limited

because La Rance is a steep-sided ria and cannot be directly compared with sediment-laden coastal plain estuaries, such as the Severn (Hooper and Austen, 2013).

Thus, a complete investigation regarding the environmental impact of TRS operation should be undertaken from the preliminary design stage. The environmental impact study of a TRS should include both the hydrodynamic and hydro-environmental impact: the source and principle of the specific influence, the affected aspect and consequences, and the component availability and status within the total natural resource.

2.4.1 Hydrodynamic Impacts of Individual TRS

One of the most well-studied TRS is Severn Barrage Scheme. Although variations in predictions exist among the hydrodynamical impact research of the Severn Barrage, the general hydrodynamic impact predictions are similar. In the studies, the operation of the Severn Barrage decreases the high water level by up to 1 m in the near-field downstream of the barrage (Sustainable Development Commission, 2007a), and a further high water level reduction appears in the upstream region, ranging from 0.5-2.0 m (Falconer et al., 2009), 0.5-1.5 m (Xia et al., 2010a), approximately 1 m (Ahmadian et al., 2010a; Čož, 2019) as shown in Figure 2.11, and up to 4.38 m during a storm surge event (Ma, 2020). The different water level changes upstream of Severn Barrage are the results of different operation head and model settings.

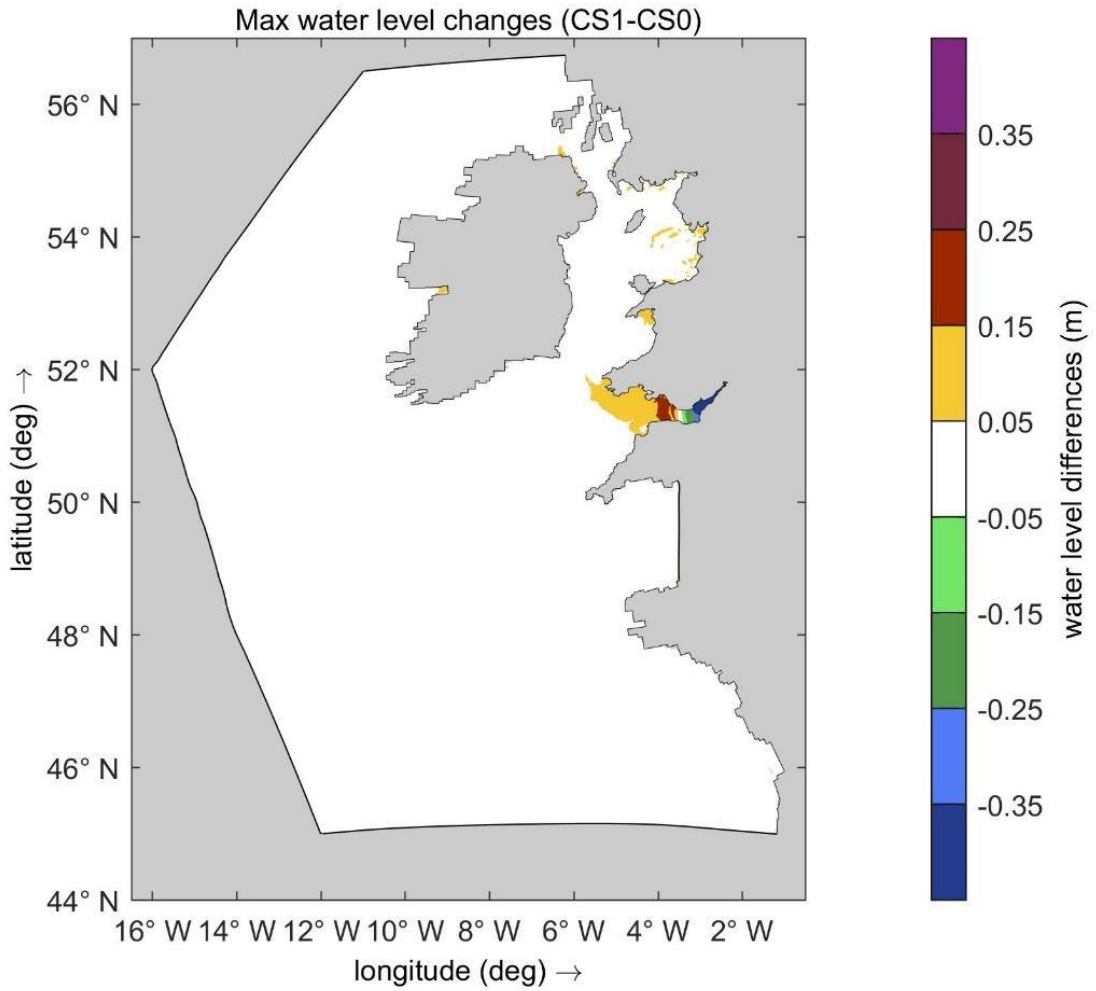

Figure 2.11: Maximum water elevation changes due to the Severn Barrage operation (Čož, 2019).

The immediate effect of the sea surface level change is the alteration of the inter-tidal area. A critical attribute of the tidal mudflats over the Severn estuary is its low and concave cross-sectional profile, offering restricted feeding opportunities for birds (Kirby, 2010). The rising low water level upstream of a tidal barrage will permanently submerge a considerable portion of the intertidal mudflat area. The estimated loss of area ranges from 14,428 hectares (Sustainable Development Commission, 2007a) to 20,000 hectares (Parsons Brinckerhoff Ltd, 2008b) in the upstream of Severn Barrage. Although the exact ecological impact of the potential loss of intertidal habitat depends on the specific biota living in the affected regions (Hooper and Austen, 2013), certain negative impacts are expected. A main concern of the Severn Barrage is the loss of birds habitats in Severn Estuary (Clark, 2006). The most influential conservation legislation for the proposed Severn Barrage is the EU Directives on

Birds and Habitats (Sustainable Development Commission, 2007b), which aims to protect birds against biodiversity loss by conserving at-risk habitats.

The Severn Barrage will also affect the tide velocity magnitude significantly; reduction of tidal current speed in the upstream area was expected (Burrows et al., 2009a; Sustainable Development Commission, 2007a). A reduction of 70-80% in the maximum discharge at the M4 bridge would occur with the operation of Severn Barrage, resulting in a 26-45% decrease of the predicted maximum velocities (Xia et al., 2010b). It was argued that the altered flow pattern in the impoundment basin could not only increase the stratification and reduce flushing rates (Burrows et al., 2009a) but also block the connectivity of fish migration and larval dispersal (Bulleri and Chapman, 2010).

As the most studied tidal lagoon, Swansea Bay Lagoon's hydrodynamic influence is well understood. Negligible influence of SBL on the hydrodynamic characteristics in the Bristol Channel was found owing to its relatively small size (Ma and Adcock, 2020; Waters and Aggidis, 2016b). The changes in the surrounding tide level and velocity were distributed in Swansea Bay, as shown in Figure 2.12. In the lagoon basin, the highwater level decreased by approximately 0.65 m, while the low water level increased by roughly 0.35 m (Angeloudis and Falconer, 2017); a large counter-rotating vortex was generated in the eastside of the water jets induced by the turbines during the flood generation (Čož et al., 2019), which occupied 27% of the plan impoundment area (Angeloudis et al., 2016b). The noticeable size of the recirculation zone combined with the low velocity in the centroid increased the likelihood of the accumulation of scalar quantities, e.g. pollution and sediment.

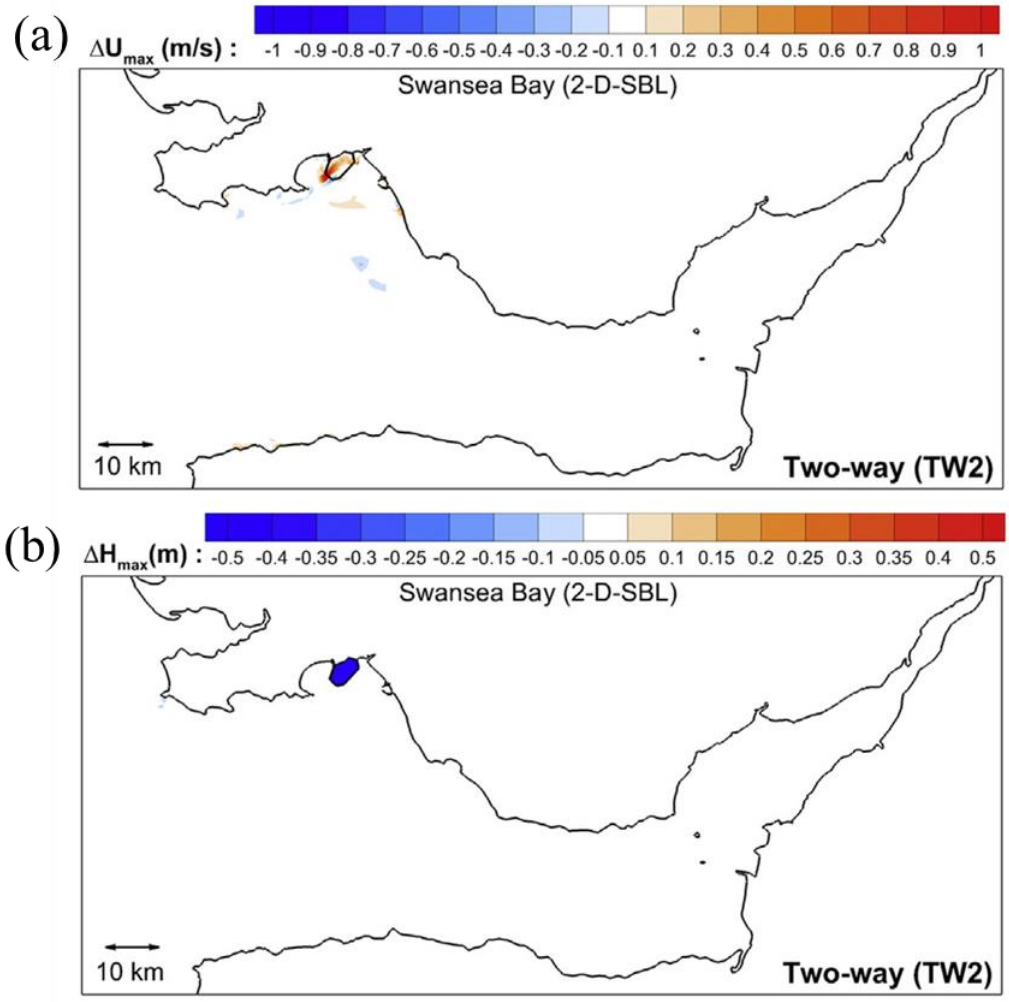

Figure 2.12: Cumulative Impact of Swansea Bay Lagoon on (a) maximum velocities and (b) maximum water levels (Angeloudis and Falconer, 2017)

There are many other TRSs located in Bristol Channel and Severn Estuary that have been studied, including Fleming Lagoon (Xia et al., 2010c; Falconer et al., 2009), Cardiff Lagoon, Newport Lagoon (Angeloudis and Falconer, 2017), Bridgewater bay lagoon (Bray, 2017), Clwyd tidal lagoon (Angeloudis et al., 2016a; Ahmadian et al., 2010b). Other TRSs are located in Mersey Estuary, UK (Carroll et al., 2009), and in the Bay of Fundy, Canada (Cornett et al., 2013; Cousineau et al., 2012). The general hydrodynamic impact is similar among all TRS operations. The tidal range in the surrounding area decreases when the tidal range energy is extracted by TRS. The increased low water level and decreased high water level in the impoundment basin may have a knock-on effect on the loss of intertidal area and reduce the flood risk in the upstream (or the basin) of the TRS. The influenced flow structure might cause a reset of the geomorphology and benthic environment.

2.4.2 Combined Hydrodynamic Impacts of Multiple TRSs

Up to now, the existing TRS and the well-studied TRS are all operated individually, without conjunctive operation with other TRSs or other renewable energy projects. However, with appropriate natural conditions, e.g., complementary tidal phases, and with an optimised operation scheme, a TRS system is considered to have great potential in providing continuous power and easier power grid absorption (Neill et al., 2018; Mackie et al., 2020). However, combined hydrodynamic impacts will also be expected from TRS system, which could affect the environment and the electricity generation performance of the individual lagoon. This becomes particularly apparent if joint TRSs are located in the same channel or estuary.

Angeloudis and Falconer (2017) modelled the joint operation of Swansea Bay Lagoon, Cardiff Lagoon and Newport Lagoon and assessed the combined environmental impact. A cumulative hydrodynamic impact can be observed in the proximity of Swansea bay lagoon and in the Severn Estuary. Consequently, the power output is influenced. For instance, the annual energy output of the Swansea Bay Lagoon is expected to be reduced by approximately 1.5-2.1% after the construction of the Cardiff Lagoon, and this power will be reduced by another 0.3-0.4% if both Cardiff Lagoon and Newport Lagoon operate. The eastern Irish Sea has also drawn attention for TRS development, having the next highest tidal range in the UK after the Severn Estuary. Wolf et al. (2009) introduced tidal barrages on the top five major estuaries along the west coast of the UK, including the Severn, Dee, Mersey, Morecambe Bay and Solway estuaries. An insignificant far-field impact was observed, except the potential 10% increase in tidal range along the east coast of Ireland, increasing the coastal flood risk. In the Bay of Fundy, Cornett and Cousineau (2011) modelled the joint operation of three offshore lagoons and three coastal lagoons. It was found that considerably larger hydrodynamic change was induced by multiple lagoons. These six lagoons would induce approximately a 5.5 cm increase in the high water level of the Boston tides, while one coastal lagoon would cause a 1.4 cm increase.

The modelling of joint tidal lagoons operation still lacks sufficient research, especially of tidal lagoons with complementary tidal phases, which can partially offset the power output variability. Considering the potential benefit, the conjunctive operation of multiple-TRSs system deserves further study from resource optimization and environmental impact assessment (Cornett et al., 2013).

2.4.3 Other Environmental Impacts of TRS

Others environmental impact study of a TRS are usually carried out following the hydrodynamic modelling because the basic information of flow, e.g. flow structure and water depth, are the fundamental inputs to any further environmental impact analysis (Hooper and Austen, 2013). Many coastal hydro-environmental modelling tools follow the causal chain approach, which models cause-effect relationships in a series of steps. The approach is used to investigate how hydrodynamics change affects the chain reaction of water renewal capacity, sediment transport, water quality and the potential implications on ecological influence (Spiteri et al., 2011).

The water quality alteration, especially within the impoundment of a TRS is attracting considerable attention. The physical impacts of a TRS on water levels, tidal currents and water volume exchange will also affect water quality. Most studies have shown that the TRS operation reduces the local tidal flushing rate (Hooper and Austen, 2013). In the Rance Estuary, the water volume exchanged with the ocean dropped by 30% after the construction of the Rance Barrage (Kirby and Retière, 2009). Xia et al. (2010b) predicted a 45% reduction in flow rate into the Severn Estuary after the construction of the Severn Barrage; the deterioration flow rate resulting in approximately a 60% decreased water exchanged volume (Prandle, 2009). For a TRS, the water exchange volume, and the recirculation zone formed by the water jet through the turbines and sluice gates, could impact the dispersion of dissolved nutrients, salinity, contaminants and particulate organic matters (Matta et al., 2018; Monsen et al., 2002).

One potential implication of water renewal capacity is the alteration of upstream salinity. The study of the Rance Estuary shows that the upstream salinity increased after the closure of the Rance Barrage (Kirby and Retière, 2009). The changes in salinity as a result of the proposed Severn Barrage is debatable mainly because of the uncertainty of the evolution of the flushing rate in the estuary (Wolf et al., 2009; Kirby and Retière, 2009). The operation of Swansea Bay Lagoon (SBL) was also studied and found the salinity in the lagoon basin would be increased to a certain degree, while salinity outside SBL is closely related to the local river discharge and distribution (Evans, 2017). Overall, the changes of salinity in Swansea Bay are not noticeable and may not have an adverse impact. Radford (1987) predicted that the operation of the Severn Barrage would increase the nutrient concentrations in the Severn Estuary because of reduced tidal flushing and increased residence time. The research from Kadiri et al. (2014a) showed that the phytoplankton primary productivity increases noticeably in the Severn Barrage

scenario, which was believed to be due to the increased water residence time behind the barrage. Moreover, a TRS may directly introduce contaminants into the surrounding water system with the antifouling coatings from the hydraulic structures or the chemical leakage from gearbox (The Robert Gordon University, 2002).

However, there are some studies that clearly show that the water quality benefits from the operation of a TRS. The goal of the Lake Sihwa lagoon is, without a doubt, to improve the polluted freshwater reservoir by increasing seawater circulation, and the reduced heavy metals and toxic organic contamination proved this feasibility (Kim et al., 2017; Bae et al., 2010). The presence of Swansea Bay Lagoon was predicted to enhance the water exchange rate in the adjacent Swansea Bay, generally reducing the nitrogen concentrations and having little effect on dissolved oxygen levels (Evans, 2017).

The operation of TRSs also has knock-on impacts on sedimentary processes due to the decrease in tidal forcing (Kadiri et al., 2012).). Understanding the influence of TRS on sediment transport process is vital in many research, including the regional benthic ecology, biogeochemistry, marine geology and long-term TRS basin water storage (Jay et al., 2007; Kim et al., 2021). After the construction of a TRS, equilibrium in the new sediment regime will not be achieved quickly; however, an enhanced sediment transport will appear for months or even years after barrage construction (Burrows et al., 2009). But in the long run, significant suspended sediment occurs due to the reduction of current speed (Kim et al., 2017; Kirby and Retière, 2009). A short-term in-situ observational study of sediment transport processes of Sihwa barrage showed a heavily unbalanced sediment fluxes during the operation of Sihwa barrage, that much higher suspended sediment concentration occurs during the turbine generating comparing with sluicing, which results in 78.28 tons m^{-1} of suspended sediment transport into embankment area over 18 days operation (Kim et al., 2021).

Research showed that the sediment transport and the geomorphology in the vicinity of TRSs are dominated by the artificial discharge through TRSs (Kim et al., 2017). Variations in velocity magnitude induce changes in sand transport flux - the water jet at the exit of turbines and sluice gates might cause scour and erosion; the recirculation zone appears with the water jet leading to sediment deposition (Angeloudis et al., 2016b). The study on the Mersey Estuary Barrage showed that the jet flow through the turbine and sluice gates caused strong erosion and deposition in the vicinity of the embankment, and increased the erosion risk in the narrows (Carroll et al., 2009). Research showed that the Severn Barrage would have a significant effect

on sedimentary flux by reducing the tidal force significantly on the seabed outside the vicinity of the barrage. This has the potential to decrease the suspended sediment concentrations in the upstream region by 83% (Ahmadian et al., 2010a). The reduction in suspended sediment levels might, in turn, reduce the bacteria level adsorbed to the sediments and decrease the turbidity, which will then strengthen the light penetration through the water column as well as bacteria decay rates (Gao et al., 2013; Ahmadian et al., 2014a; Xia et al., 2010c). Furthermore, the reduced bed shear stress will permit a greater bio-diversity in the benthic habitat owing to the higher solar radiation (Wolf et al., 2009).

Ahmadian et al. (2010a) and Gao et al. (2013) used different in-house models to predict the change of suspended sediment and faecal bacteria concentrations with the construction of Severn Barrage. In their models, the bacterial level was dynamically linked with the resuspension or deposition of sediment concentration. Carroll et al. (2009) presented the morphodynamic impacts of Mersey Estuary Tidal Barrage by coupling a hydrodynamic model (TELEMAC-2D) with the sediment transport model (Sisyphe) and the wave propagation model (Tomawac).

There was also research conducted on the ecological influence of TRS operations. Evans (2017) combined the Delft3D model and Intertek company's STORM-OPTIMISER modelling system to predict the impacts of Swansea Bay Lagoon on urban drainage and pollutant dispersion. Kadiri et al. (2014a) abstracted the available information from the previous Severn Barrage study and then applied the data into a steady-state model to predict the nutrient concentrations and phytoplankton biomass. Baker et al. (2020) examined the impact of a proposed Severn tidal barrage on 14 species via the linking of a hydrodynamic model (Thetis) to species distribution models.

Overall, most of the existing hydro-environmental modelling research on TRS operation only covers one or two indicators of hydro-environmental change. The existing modelling tools cannot provide a clear case for or against TRS, so a better model for decision-making is required.

2.5 Summary

For every TRS proposal, environmental impacts assessment should be carried out by the developer for planning and governmental consent. This is to evaluate the environmental impacts associated with the introduction of the scheme and to alleviate these man-made impacts by improving the construction design and considering mitigating measures. The fundamental changes introduced by a TRS will have profound effects on the environment in its broadest sense. It is a relatively straightforward path to quantitatively predict the tidal range changes and other basic hydrodynamic influences. However, the assessment of the potential alteration in water quality and then on through the ecosystem is less explored (Elliott et al., 2019).

Although previous studies have been conducted to understand the impact of TRS operation on the regional environment, most of the research was focused on basic effects of TRSs, such as tidal elevation and tide current. Few in-depth and comprehensive environmental impact assessments have been performed for the TRS development, owing to the limited study tools and lack of development plans. Therefore, it is clear that more research for environmental impact assessments of TRS is required to improve the understanding and assessment of hydrodynamics, and environmental and ecological implications of potential impacts in a given area. Extensive quantitative analysis should be conducted on the most direct and noticeable hydro-environmental changes caused by TRS operation, e.g. intertidal mudflat area, water renewal capacity, sediment transport and phytoplankton growth, etc.

This review has also identified a lack of research about the conjunctive operation of the TRSs, which is regarded as a potential advantageous TRSs option. Characterising the interactions between TRSs is essential for the development of multiple schemes.

The power output prediction and environmental impact assessment of a TRS are all underpinned by its modelling, which requires a robust numerical model to provide reliable and accurate predictions. Special attention has to be given to local hydrodynamics effects deriving from the TRS operation, i.e., the accelerated flow caused by turbines. Certain studies have identified the critical function of momentum transfer in regard to the accelerated flow. However, the review of the existing numerical TRS models has shown that the majority of previous studies ignored the conservation of momentum through the hydraulic structures, let alone the environmental impact investigation of TRS with the consideration of momentum conservation. Moreover, almost all research have regarded the operation of TRS as one unit

and overlooked the tide difference between turbine blocks. Thus, a refined TRS hydrodynamic modelling development is required with additional consideration being given to momentum conservation and the differences in tides between different blocks of turbines.

Chapter 3 Hydrodynamic Model Development

This chapter focuses on developing and calibrating hydrodynamic models used for natural hydrodynamic condition study and further implementation of TRS. Based on the location of the TRSs and the objectives in this research, two hydrodynamic models were developed and validated: the Severn Estuary and Bristol Channel (SEBC) model and Continental Shelf (CS) model. Furthermore, the relevant governing equations and background of the numerical modelling associated with TRS study are presented. However, as TELEMAC is a widely used hydrodynamic model, there is a great many of literature that covers the derivation of Saint-Venant equations and numerical solution of the hydrodynamic model. Thus, only the information deemed essential for this research is included to avoid repetition.

This chapter is organised as follows: Section 3.1 provides the general overviews of the relevant governing equations and other associated numerical approaches provided in the TELEMAC model. Section 3.2 presents the model domain and the model setup of SEBC model. The model performance is then validated against available measurements of tidal elevation and current magnitudes and directions. Furthermore, a mesh convergence test is carried out to validate the dependency of the model prediction. Section 3.3 offers the development and validation of the CS model, with the differences between SEBC and CS model highlighted specifically.

3.1 Numerical Modelling

Different hydro-environmental models, including EFDC, Delft3D, Telemac-2D/Telemac-3D MIKE, FVCOM, OpenFOAM, and in-house DIVAST etc. (Carroll et al., 2009; Rahimi et al., 2014; Čož et al., 2019; Guerra et al., 2017; Chu and Chong, 2018; Ahmadian et al., 2010a; Zhou et al., 2014c) had been used for tidal energy modelling. Each model has advantages and disadvantages. Unstructured TELEMAC developed by EDF and widely used globally, was selected for this project for the following reasons: (1) wide range of applications including in simulating tidal range schemes (Rtimi et al., 2021); (2) unstructured nature of the model enables achieving high-resolution mesh in the vicinity of the TRS where more information is required and low-resolution where farther from the schemes and less sensitive; (3) The open-access code provides the possibility of further development as described in before; (4) TELEMAC is highly scalable and efficient on High-Performance Computers (HPC) enables running computationally extensive simulations.

Since the water column at the modelling sites in this study is considered to be well mixed (Uncles and Radford, 1980; Evans et al., 1990), and the main focus of this study is preliminary on the far-field environmental assessment rather than the vertical profile of water flow near the structure. The 2D model was sufficient to meet the accuracy requirement while maintaining a high computational efficiency (Čož et al., 2019; Bray et al., 2016).

The TELEMAC-MASCARET is an integrated open-source modelling tool for use in the field of free-surface flows (www.opentelemac.org). The model was originally developed by EDF R&D and has been used in a wide range of applications and by many organisations. In addition to the TELEMAC-2D and TELEMAC-3D modules for hydrodynamic modelling, the TELEMAC system contains multiple modules which are used to represent various physical processes, including: MASCARET for simulating one-dimensional flow; GAIA/SISYPHE for sediment transport and morphodynamics modelling; TOMAWAC for wave propagation in the coastal zone; WAQTEL for water quality modelling; NESTOR for modelling sediment dredging; and ARTEMIS for wave agitation in harbours. These modules are powerful tools that can enable potential future research.

3.1.1 Hydrodynamics

TELEMAC-2D uses the Saint-Venant equations for hydrodynamics, which are in the depth-averaged forms of non-hydrostatic Navier-Stokes equations, including continuity and momentum along the x and y directions. They are provided below for completeness, while further details can be found in Hervouet (2007).

$$\frac{\partial h}{\partial t} + \frac{\partial (uh)}{\partial x} + \frac{\partial (vh)}{\partial y} = S_h, \tag{3.1}$$

$$\frac{\partial u}{\partial t} + u\frac{\partial u}{\partial x} + v\frac{\partial u}{\partial y} = -g\frac{\partial Z}{\partial x} + \frac{1}{h}\nabla \cdot (hv_e \nabla u) + F_x, \tag{3.2}$$

$$\frac{\partial v}{\partial t} + u\frac{\partial v}{\partial x} + v\frac{\partial v}{\partial y} = -g\frac{\partial Z}{\partial y} + \frac{1}{h}\nabla \cdot (hv_e \nabla v) + F_y, \tag{3.3}$$

where h is the depth of water below datum; Z is the free surface elevation relative to datum; u, v are the depth-averaged velocity components in the x and y directions; t is time; g is the acceleration due to gravity, v_e is the momentum diffusion coefficient, also referred to as the coefficient of turbulent viscosity or the eddy viscosity; S_h is the source term; F_x, F_y are the source/sink terms representing external forces such as wind shear, the Coriolis Force, bottom friction, sources of momentum and others.

3.1.1.1 Source/Sink terms

Source and sink terms can be added into the continuity equation or momentum equation to allow external input of mass or momentum. In scenarios that water intake or discharge exist in the model, or rainfall, evaporation and infiltrations that need to take into consideration, then the right side of Equation (3.1) is set to the value which represents the intake or release of a water body shown as 'S_h'. S_h represents 'Source' or 'Sink', with the real discharge expressed on a unit area. The unit of S_h is m/s, with a positive value signifies an injection and a negative value signifies an extraction.

The introduction of a water source or sink will affect the local flow structure, so a component vector with an equal values for $u_s S_h$ and $v_s S_h$ is added to the source terms of the momentum Equations (3.2) and (3.3), where u_s and v_s is the flow velocity components at the source or sink point. In order to include the momentum terms in the external force source terms F_x and F_y, momentum terms are included in an expression of $(u_s - u)\frac{S_h}{h}$ and $(v_s - v)\frac{S_h}{h}$. However, the momentum terms are zero when the velocity at the source is the same as that of the local current.

Friction on the bottom surface is also included in the source/sink terms in TELEMAC, which is one of the major sources of energy loss in environmental flow. The friction equations are mostly empirical, so numerical models need to be calibrated to estimate the relevant friction coefficient. The drag force due to the friction of flow exerted on the bed is parallel to the flow direction and is expressed by the classical quadratic friction equation (Dorfmann, 2017). The friction stress τ in each direction can be calculated as:

$$\begin{aligned} \tau_x &= -\frac{u}{2}\rho C_f \sqrt{u^2 + v^2}, \\ \tau_y &= -\frac{v}{2}\rho C_f \sqrt{u^2 + v^2}, \end{aligned} \tag{3.4}$$

where τ_x and τ_y are the friction stress in the *x* and *y* directions, and C_f is the dimensionless quadratic friction coefficient. The calculation of bottom friction *F* in Saint-Venant equations is equal to $\frac{1}{\rho h}\tau\vec{n}_f$. The $\vec{n}_f$ is the vector normal to the bottom, which is the reciprocal of the cosine of the steepest slope ($cos(\alpha)$). The coefficient C_f is usually replaced by other well-studied friction equations. One of the popular used is the law of Chézy, which provides the Chézy coefficient: $C = \sqrt{\frac{2g}{C_f}}$ (dimension: $m^{1/2}/s$). Taken the friction stress τ, Chézy coefficient *C* and

vector $\vec{n}_f$ into the expression of bottom friction *F*, then the Chézy law is achieved, expressed as:

$$\begin{aligned} F_x^f &= -\frac{u}{cos\,(\alpha)}\frac{g}{hC^2}\sqrt{u^2+v^2}, \\ F_y^f &= -\frac{v}{cos\,(\alpha)}\frac{g}{hC^2}\sqrt{u^2+v^2}, \end{aligned} \tag{3.5}$$

where F_x^f and F_y^f are bottom friction in the *x* and *y* directions. It should be noted that the Chézy coefficient is not a constant; dimensional analysis and experimental investigations indicate that it is a function of the bottom roughness and water depth. The introduction of the empirical law of Manning and Strickler could solve the problem of the non-constant Chézy coefficient.

The empirical friction equation of Strickler is related to the Chézy law via the Strickler coefficient *K*. The Chézy coefficient is expressed as $C = Kh^{1/6}$ where *K* ($m^{1/3}/s$) is the Strickler coefficient.

Then the Strickler's law is achieved and expressed as the following:

$$\begin{aligned} F_x^f &= -\frac{u}{cos\,(\alpha)}\frac{g}{h^{4/3}K^2}\sqrt{u^2+v^2}, \\ F_y^f &= -\frac{v}{cos\,(\alpha)}\frac{g}{h^{4/3}K^2}\sqrt{u^2+v^2}. \end{aligned} \tag{3.6}$$

The Strickler coefficient is independent of the water depth and is only a function of bottom roughness.

The manning formula is a simple variant of the Strickler's formula, with a coefficient *m*, the inverse of *K*, as:

$$\begin{aligned} F_x^f &= -\frac{u}{cos\,(\alpha)}\frac{gm^2}{h^{4/3}}\sqrt{u^2+v^2}, \\ F_y^f &= -\frac{v}{cos(\alpha)}\frac{gm^2}{h^{4/3}}\sqrt{u^2+v^2}. \end{aligned} \tag{3.7}$$

The source and sink terms also contain the Coriolis force, as the following:

$$\begin{aligned} F_x^c &= 2\omega\, sin(\lambda)\, u = fu, \\ F_y^c &= 2\omega\, sin(\lambda)\, v = -fv, \end{aligned} \tag{3.8}$$

where ω is the angular velocity of the Earth, equal to 7.292×10^{-5} rad/s, and λ is the latitude. The Coriolis force is necessary when a large water body is modelled. It should be noted that in TELEMAC, the Coriolis coefficient would be calculated automatically when the model uses the spherical coordinate. Otherwise, it is set as a constant average value throughout the computational domain. Thus, it is necessary to use spherical coordinates to model a large water body using TELEMAC system.

3.1.1.2 Treatment of Tidal Flats and Dry Zones

A threshold of water depth is usually adopted to distinguish uncovered beds or dry zones. This method, however, may cause the mass conservation problem for ignoring partially dry elements, and create unrealistic higher velocity on a fine film of water. Different from the above solution, two other methods could be applied in TELEMAC to the numerical treatment of dry (or partially dry) elements.

The first method abandons the minimum threshold criterion to distinguish the wet and dry element which is unfriendly to half-dry, half-wet elements. It simply decreases the dry node's free-surface elevation with the difference between its bottom elevation and the free surface elevation of the wet node, as shown in Figure 3.1. This specific treatment is only to calculate the free surface gradient to prevent flow between dry elements.

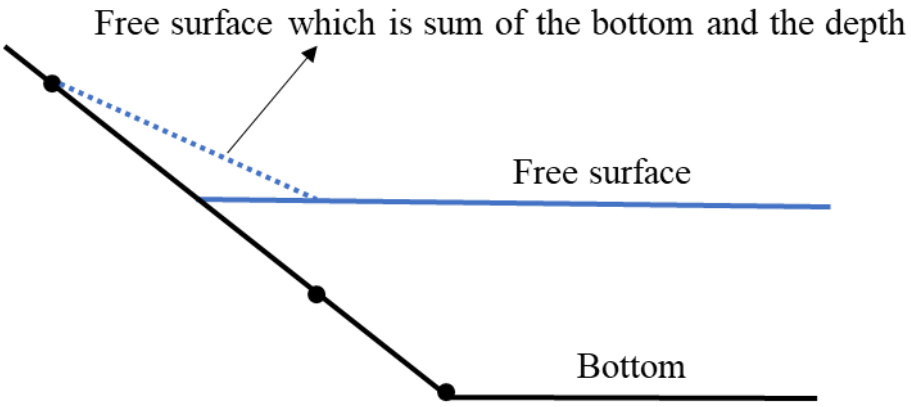

Figure 3.1: Correction of the gradient of the free surface to semi-wet element (Hervouet, 2007).

The second method excludes the elements that are not entirely wet from the computation. However, the second method can result in mass conservation errors and is not well suited to tidal flat problems. Thus, in modelling regions that with large tidal flats, it is recommended to use the former method.

3.1.2 Turbulence

TELEMAC-2D offers four different models for turbulence. The first involves using a constant viscosity coefficient that includes molecular viscosity and turbulence viscosity throughout the model domain, with a velocity diffusivity value of 10^{-4} m^2/s being suggested in various studies (Jourieh, 2013; Matta, 2018).

The second is the Elder model, which offers the possibility of specifying two different viscosity values for the longitudinal diffusion, i.e., K_l, and the transverse diffusion, i.e., K_t . Those two viscosity values are expressed as follows:

$$K_l = \alpha_l \cdot u^* \cdot h, \tag{3.9}$$

$$K_t = \alpha_t \cdot u^* \cdot h, \tag{3.10}$$

where u^* is the shear velocity (or friction velocity), h is the water depth, and α_l and α_t are dimensionless empirical coefficients that represent the longitudinal diffusion coefficients and transversal diffusion coefficients respectively. Elder has defined α_l and α_t as a constant value of 5.9 and 0.23 respectively based on the velocity profile in the logarithmic layer (Elder, 1959). Fischer et al. (1979) further proposed a transverse turbulence diffusion, α_t, value of about 0.6 in irregular natural streams with weak meanders. More recently, Wu et al. (2004) applied values for α_t in the range from 0.6 to 1.0; Steffler and Blackburn (2002) set α_t to 0.5 with recommended values from 0.2 to 1.0. Different values could be used for α_l and α_t due to the anisotropic features of turbulence structure in the horizontal and vertical directions. For this study, considering the finding of Elder and latter researchers, α_l and α_t are assigned values of 6 and 0.6, respectively, following the advised value of TELEMAC-2D manual.

The third is the classic *k-ε* model which is based on the calculation of physical quantities representing turbulence kinetic energy (*k*) and its dissipation (*ε*) in the flow. The eddy viscosity ν_t is calculated by:

$$\nu_t = C_u k^2/\varepsilon, \tag{3.11}$$

where C_u is an empirical constant and k and ε represent the turbulent kinetic energy and its dissipation rate, respectively, as defined after averaging over the vertical to give:

$$k = \frac{1}{h}\int_{Z_f}^{Z_s}\frac{1}{2}\overline{u_i' u_j'}dz, \tag{3.12}$$

$$\varepsilon = \frac{1}{h}\int_{Z_f}^{Z_s}\nu\overline{\frac{\partial u_i'}{\partial x_j}\frac{\partial u_i'}{\partial x_j}}dz, \tag{3.13}$$

where Z_s is the free surface elevation, Z_f is the bottom elevation, u_i' is the temporal fluctuation of velocity and the $\overline{u_i'}$ corresponds to the average value of u_i' overtime.

The k and ε are determined from the following model transport equations:

$$\frac{\partial k}{\partial t} + U\frac{\partial k}{\partial x} + V\frac{\partial k}{\partial y} = \frac{1}{h} div\left(h\frac{\nu_t}{\sigma_\kappa}\overrightarrow{grad}(k)\right) + P - \varepsilon + P_{kv}, \tag{3.14}$$

$$\frac{\partial \epsilon}{\partial t} + U\frac{\partial \epsilon}{\partial x} + V\frac{\partial \epsilon}{\partial y} = \frac{1}{h} div\left(h\frac{\nu_t}{\sigma_\epsilon}\overrightarrow{grad}(\epsilon)\right) + \frac{\epsilon}{k}[C_{1\varepsilon}P - C_{2\epsilon}\epsilon] + P_{\epsilon v}, \tag{3.15}$$

where production terms $P = \nu_t\left(\frac{\partial u_i}{\partial x_j} + \frac{\partial u_j}{\partial x_i}\right)\frac{\partial u_i}{\partial x_j}$, P_{kv} and $P_{\varepsilon v}$ are due to the shear force of flow along the vertical: $P_{kv} = {C_f}^{-0.5}\frac{u_*^3}{h}$, $P_{\varepsilon v} = 3.6\frac{C_{2\varepsilon}\sqrt{C_u}}{C_f^{3/4}}$, C_f is the dimensionless friction coefficient and u^* is the shear velocity calculated as $u^* = \sqrt{\frac{C_f}{2}(u^2 + v^2)}$ (Rastogi and Rodi, 1978; Hervouet, 2007).

Large-eddy simulations or direct numerical simulations are ideal in modelling the Karman Vortex Street phenomenon or other flow-structure interaction. It would be ideal to use large-eddy simulation model or direct numerical simulation (Xie et al., 2021), or to embed one of them within the Reynolds Averaged Navier Stokes model (Stoesser, 2014), e.g., TELEMAC, to achieve a more accurate simulation of fluid structure. However, it is currently not practical to simulate a complete TRS and its far-field impacts modelling, particularly in terms of using a large-eddy simulation model due to the computational resources requirement for such a large domain.

The Smagorinsky model is based on the mixing length formulation and includes some aspects of large-eddy simulation modelling (Bartosiewicz and Duponcheel, 2018). The principle of the Smagorinsky model is to add a turbulent viscosity deduced from a mixing length model to represent the small-scale turbulence. From the Smagorinsky model, the eddy viscosity ν_t is calculated using:

$$\nu_t = C_s^2\Delta^2\sqrt{2D_{ij}D_{ij}}, \tag{3.16}$$

where C_s is a dimensionless coefficient to be calibrated and Δ is the mesh size. The D_{ij} is the strain rate tensor of average motion, as

$$D_{ij} = \frac{1}{2}\left(\frac{\partial \overline{U_i}}{\partial x_j} + \frac{\partial \overline{U_j}}{\partial x_i}\right). \tag{3.17}$$

3.1.3 Tracer Transport

It is possible to simulate passive tracers (physical quantities that have no interactions with the flow hydrodynamics in TELEMAC-2D), which is useful for water quality studies.

The non-conservative form of the tracer transport equation is preferred because of difficulties in calculating the tracer value after averaging over the vertical profile, and is written as following:

$$\frac{\partial T}{\partial t} + u\frac{\partial T}{\partial x} + v\frac{\partial T}{\partial y} - \frac{1}{h}\nabla \cdot (hv_T \nabla T) = \frac{(T_{sce} - T)S_h}{h}, \quad (3.18)$$

where T is the value of tracer, v_T is the dispersion coefficient of tracer, T_{sce} is the source value of the racer. Similar to the momentum Equation (3.2), the right side of the above equation is zero when the value of the source tracer is equal to the local tracer value.

3.1.4 Suspended Sediment Transport

The transport process of suspended sediment is considered in this study by solving the two-dimensional advection-diffusion equation, expressed as:

$$\frac{\partial hT_s}{\partial t} + \frac{\partial huT_s}{\partial x} + \frac{\partial hvT_s}{\partial y} = \nabla \cdot (h\varepsilon_S \nabla T_s) + (E - D), \quad (3.19)$$

where T_s is the depth-averaged suspended sediment concentration, ε_S is the turbulent diffusivity of the sediment, E and D represent the deposition and erosion rates of the suspended sediment, respectively. In Equation (3.19), the difference of the erosion and deposition rates (E - D) represents the net sediment flux closely related to the current ability to transport solid matter.

Different treatments of sediment net flux are applied on non-cohesive and cohesive sediment. The net flux E - D for non-cohesive sediment is calculated on the basis of equilibrium concentration:

$$E - D = \omega_s(C_{eq} - C_{Zref}), \quad (3.20)$$

where ω_s is the sediment settling velocity, C_{Zref} is the near-bed concentration, C_{eq} is the equilibrium near-bed concentration which is calculated by the van Rijn equation:

$$C_{eq} = 0.015 d_{50} \frac{(\theta'/\theta_{cr} - 1)^{3/2}}{Z_{ref} D_*^{0.3}}, \tag{3.21}$$

where θ_{cr} is the critical Shields parameter, θ' is the shear stress due to the skin friction. Reference elevation Z_{ref} is determined by $0.5 \times k_s$, with k_s the total roughness, and D_* is a non-dimensional diameter defined as $d[(\frac{\rho_s}{\rho} - 1)g/\nu^2]^{1/3}$.

In 2D model, near-bed sediment concentration C_{Zref} is calculated with a Rouse profile for the vertical concentration distribution, with:

$$C_{Zref} = FC, \tag{3.22}$$

where C is the depth-averaged concentration, F is the reference concentration which has expression of:

$$F^{-1} = \begin{cases} \frac{1}{(1-Z)} B^R \left(1 - B^{(1-R)}\right) & if\ R \neq 1 \\ -B\ logB & if\ R = 1 \end{cases}, \tag{3.23}$$

With B = Z_{ref}/h, $R = \frac{w_s}{\kappa u_*}$, in where κ is the von Karman constant κ = 0.4), u_* is the friction velocity corresponding to the total bed shear stress.

Cohesive sediment is presented as fine particles like silts and clay, with its performance associated with physico-chemical process of the fluid and salinity. The erosion and deposition flux of cohesive sediment is calculated by:

$$E = \begin{cases} M\left[\left(\frac{\tau_b}{\tau_{ce}}\right) - 1\right] & \tau_b > \tau_{ce} \\ 0 & \tau_b \leq \tau_{ce} \end{cases}, \tag{3.24}$$

$$D = \omega_s C \left[1 - \left(\frac{\sqrt{\tau_b/\rho}}{u_{*mud}^{cr}}\right)^2\right], \tag{3.25}$$

where M is the constant in Krone-Partheniades erosion law; τ_b is the bed shear stress; τ_{ce} is the critical bed shear stress for erosion; ω_s is the settling velocity; u_{*mud}^{cr} is the critical shear velocity for mud deposition. The topographic change is computed through conservative law for sediment mass based on the predicted total loads at each computational point.

The settling velocity of suspended sediment is calculated internally with a function of grain diameter:

$$\omega_s = \begin{cases} \dfrac{(s-1)gd_{50}^2}{18\nu}, & if\ d_{50} \le 10^{-4} \\ \dfrac{10\nu}{d_{50}}\left(\sqrt{1+0.01\dfrac{(s-1)g}{\nu^2}}-1\right), & if\ \ 10^{-4} < d_{50} \le 10^{-3} \\ 1.1\sqrt{(s-1)gd_{50}}, & if\ 10^{-3} < d_{50} \end{cases}$$

In where the $s = \rho_s/p_0$ is the relative density of sediment.

The bed evolution is determined by considering the suspended sediment transport:

$$(1-\lambda)\frac{\partial Z_b}{\partial t} = D - E, \tag{3.26}$$

where λ is the bed porosity and Z_b is the bottom bed level.

3.1.5 Solution Algorithm

The TELEMAC model allows combinations of choices for original equations and solution methods; however, it is out of the scope of this thesis to present all the algorithms used to solve the Saint-Venant equations. Thus, the numerical discretization which is mainly based on the finite element method by applying the method of characteristics and adopting a semi-implicit time integration method is briefly explained here. Complete explanation of the Telemac model can be found in Hervouet (2007) and TELEMAC (2020b).

For each point on the mesh, the main hydrodynamics results include the water depth and the two flow velocity components. The initial set of governing Equations (3.1), (3.2), (3.3) are solved by TELEMAC-2D in their non-conservative forms, using a semi-implicit time integration. The governing equations are solved in two computational steps using the fractional steps method, with the method of characteristics to solve the advection step.

In the fractional step method, unknown values are time discretised at the multiples of the given time step Δt, which is $t^n = t^0 + n\Delta t$. The derivative of a function f with respect to time is discretised as:

$$\frac{\partial f}{\partial t} = \frac{f^{n+1}-f^n}{\Delta t}. \tag{3.27}$$

The general principle of fractional steps method is as follows:

$$\frac{\tilde{f}-f^n}{\Delta t} + Advection\ terms = 0, \tag{3.28}$$

$$\frac{f^{n+1}-\tilde{f}}{\Delta t} + other\ terms = 0, \tag{3.29}$$

where *f* represents the variables *h, u, v, k, ε, T*, etc. The f^n is the value of a given variable at time step *n*, starting from the initial solution f^0 at time *t* = 0, then following solution f^{n+1} is achieved by successive iterations. The $\tilde{f}$ is the intermediate values passing through intermediate steps, starting from f^n and end of f^{n+1}, which is computed from the advection step:

$$\frac{\tilde{f}-f^n}{\Delta t} + \vec{u} \cdot \nabla(f) = 0. \tag{3.30}$$

The transport of the physical quantities *u, v, h* (or *k, ε, T* for turbulence and tracer transportation) are computed by solving the advection terms in the momentum equations at the advection step.

Then, the remaining terms, including propagation, diffusion, and source terms, are resolved by the finite element technique; the non-linear terms from the equations are removed by time discretization. Continuous equations are then transformed into a discrete linear system by the variational formulation and discretisation in space and time, with the unknown variables of *h, u, v*. Finally, the discretised equations are solved using an iterative solver based on the conjugate gradient method. It should be noted that the propagation terms here refer to the '$\frac{\partial uh}{\partial x} + \frac{\partial vh}{\partial y}$' in the continuity equation, and '$-g\frac{\partial Z}{\partial x}$' or '$-g\frac{\partial Z}{\partial y}$' in the momentum equation, which are inertia and free-surface gradient.

The typical discretised equations during the propagation and diffusion steps are as follows:

$$\frac{h^{n+1}-\tilde{h}}{\Delta t} + \frac{\partial uh}{\partial x} + \frac{\partial vh}{\partial y} = S_h, \tag{3.31}$$

$$\frac{u^{n+1}-\tilde{u}}{\Delta t} = -g\frac{\partial Z}{\partial x} + \frac{1}{h}\nabla \cdot (hv_e \nabla u) + F_x, \tag{3.32}$$

$$\frac{v^{n+1}-\tilde{v}}{\Delta t} = -g\frac{\partial Z}{\partial y} + \frac{1}{h}\nabla \cdot (hv_e \nabla v) + F_y, \tag{3.33}$$

where $\tilde{h}$, $\tilde{u}$, $\tilde{v}$ are the value achieved from the advection of *h, u, v*.

As to the discretisation in space, Telemac2D provides three types of discretization: linear triangles (3 nodes), quasi-bubble triangles (4 nodes) and quadratic triangles (6 nodes). Linear triangles space discretization has the highest computational efficiency, while discretization in quadratic triangles can result in a more accurate prediction but will increase the computer

memory significantly and processing time. Velocity and depth can be discretised with different space discretisation options according to the requirement of prediction accuracy and computational resources. A space discretisation combination of quasi-bubble velocity and linear depth is recommended when free surface wiggles and strong bathymetry gradients appear in simulation (TELEMAC, 2020b), and can also make a trade-off between model accuracy and efficiency (Hervouet, 2007; Bakar et al., 2017). Therefore the quasi-bubble velocity and linear depth are chosen in this study.

3.1.6 Boundary Conditions

The physical boundaries are discussed in two different types: solid boundary and open boundary.

- Solid Boundary

The solid boundary is an impermeable model boundary that usually refers to a coastal line, riverbank, structure, or island. There are two different velocity settings on the solid boundary: slip boundary condition or no-slip boundary condition. On a slip solid boundary, no friction is applied on the solid boundary. For the no-slip condition, friction is applied and the friction coefficient is entered manually or determined by the turbulence model; the flow velocity and the shear velocity at the wall are then calculated based on the friction law and turbulence region. The friction coefficient α is used to apply stronger conditions than those of the ordinary friction as follows: $\vartheta_t \frac{\partial u}{\partial t} = \alpha u$ and $\vartheta_t \frac{\partial v}{\partial t} = \alpha v$.

- Open Boundary

The input condition for the open boundary requires careful consideration because it has a significant impact on the computational domain. The open boundaries are categorized into four types following the characteristics theory: input with supercritical flow, output with supercritical flow, input with subcritical flow, and output with subcritical flow. The input flow and output flow are differentiated by the sign of the scalar product of the velocity vector and the outward normal vector. An inflow is identified with a negative sign while an outflow stands positive. The supercritical and the subcritical flows are distinguished by their Froude number, which is expresses as $F = \frac{u}{\sqrt{gh}}$. The flow is supercritical if $F > 1$ while subcritical if $F < 1$. The imposed velocity vector at the inflow boundary is normal to the boundary segments.

However, there are restrictive conditions applied on the above boundary theory in two-dimensional modelling. First, the vector attribute of velocity brings about unrealistic boundary conditions during the resolution process when the equations are separated into two fractional steps. Second, the input and output of open boundary conditions can vary with time. Thus, in practice, four different types of boundary are applied in 2D models corresponding to the boundaries mentioned earlier: prescribed velocity and depth (input with supercritical flow), prescribed velocity and free depth (input with subcritical flow), free velocity and free depth (output with supercritical flow), free velocity and prescribed depth (output with subcritical flow).

3.1.7 Momentum Conservation through Tidal Lagoon

The original culvert function in TELEMAC was utilized and reprogramed to represent the turbine and sluice gates, by replacing the original culvert-featured program in subroutine ***buse.f*** with the TRS-featured recompiled code.

To ensure momentum and mass conservation across the structure, a momentum source term was added to the momentum equations, i.e. Equations 3.2 and 3.3, for the cells linked to the turbines or sluice gates. This method has been successfully used in simulating tidal stream turbines (Ahmadian et al., 2012) and is applicable to other hydraulic structures, such as coastal reservoirs (Falconer et al., 2020). The momentum source term in the x-direction was calculated from first principles and is given as:

$$F_x^q = \frac{1}{h}(u_s - u) \cdot S = \frac{1}{h}(u_s - u)\frac{Q}{(\Delta\xi \times \Delta\eta)}, \tag{3.34}$$

where $\Delta\xi \times \Delta\eta$ is the area of the source/sink discharge cell; u is the local velocity at the source point; h is the water depth; and u_s is the source/sink velocity, which was considered as the flow velocity through the hydraulic structure. However, due to the fast-changing velocity in the turbine housing (Ahn et al., 2017b), the choice of u_s value is uncertain. The results with different values of u_s was investigated in this study. In the first scenario, the velocity was taken just beyond the turbine runner, which could be considered as a simplified value since this value ignored the expansion of the flow through the diffusor (Čož et al., 2019). In the second scenario, the value of u_s was considered as the velocity at the end of the turbine diffusor. This was considered to be more realistic, based on Equation (3.34), and included the energy dissipation in the draft tube.

Vertical velocity gradients cannot be accurately accounted for in 2D models for such complex turbine wake structures (Xia et al., 2010a). Furthermore, the velocity of the jet, u_s, can vary significantly across the diffuser. This jet characteristic will differ based on the design of the turbine and its housing and therefore an appropriate velocity profile needs to be used after the turbine characteristics have been finalised. At this early stage of the design process, a typical horizontal velocity profile along the vertical section produced by Wilhelm et al. (2016), as shown in Figure 3.2, was used in this study. The velocity profile is represented in Equation (3.24) by dividing the profile into sub-sections and calculating the accumulated impact of the jet over the area, as shown below:

$$F_{x-3D}^{q} = \frac{1}{h(\Delta\xi \times \Delta\eta)} \int_0^h (u_s - u) Q dZ. \tag{3.35}$$

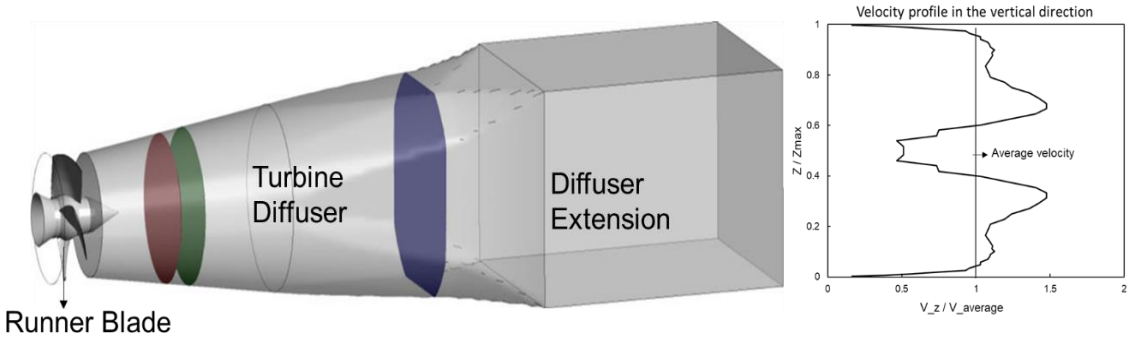

Figure 3.2: Shape of the low head bulb turbine housing and measured velocity distribution in the outer turbine diffuser (Wilhelm et al., 2016)

3.2 Severn Estuary and Bristol Channel Model

3.2.1 Model Setup

Severn Estuary and Bristol Channel (SEBC) model was set up for the computation of the hydrodynamic process in the domain of the entire Seven Estuary and Bristol Channel (Figure 3.3). The open seaward boundary was located at the western extent of the model domain at the mouth of the Bristol Channel, close to Lundy Island, and spanning from Heartland Point in south-west of England to Stackpole Head in south-west Wales. By ensuring that there is enough distance between the open boundary and the region of interest, the effect of the scheme on the open boundary is minimised (Ji, 2017). The model extended upstream to the River Severn, close to the tidal limit at Haw Bridge, near Gloucester, and where there is an Environment

Agency hydrological monitoring station. The entire computational domain covered an area of 5805 km^2.

A tidal time series of water levels was applied using data obtained from the Proudman Oceanographic Laboratory (now National Oceanographic Centre) Irish Sea model (National Oceanographic Centre, 2011) and with the levels being prescribed relative to mean sea level (MSL). The modelling period covers more than a whole neap-spring tidal cycle, based on the date of validation data. Furthermore, the model was allowed to spin up from constant elevation across the domain for 2 days prior to any numerical results being used, in order to achieve a stable model performance, similar to research conducted by Adcock et al. (2013). For the present research, meteorological forcings (wind and waves) and density stratification effects were not considered in this modelling. 7 major rivers have been taken into the model as the input source, based on the location and the mean discharge presented in Appendix A1, Table A.2 (Stapleton et al., 2007; Bakar, 2019).

Bathymetric data in this area were obtained from EDINA Digimap with a grid resolution of 30 m, and were converted relative to mean sea level (MSL). The mesh resolution varied across the domain according to the bathymetric conditions, with the inverse distance interpolation method being used to achieve a higher resolution and better accuracy in shallow waters, with the resolution being based on the following equation:

$$L = -10 \cdot X + 200, \tag{3.36}$$

where L is the mesh resolution and X is the bathymetric elevation at that point. Using this setting, the mesh resolution varies from 800 m at the seaward boundary to around 200 m at the solid boundary except for the interesting area, where it was refined further. The final mesh consisted of 69,404 nodes and 134,64 triangular cells. The geographic coordinate system of this refers to Universal Transverse Mercator (UTM) of Zone 30N. To ensure the model accuracy, the Courant number limitation was set to 1 and a time step of 10 s was set to meet the Courant number limit.

In this numerical model, the method of characteristics was used to solve the advection terms in the governing momentum equations. The finite element method was applied, and the method of characteristics was chosen to solve the advection step. Discretisation in space was carried out by using a quasi-bubble triangle to determine the velocity field and a linear triangle to determine the water elevations, thereby ensuring a balance between model accuracy and

efficiency (Hervouet, 2007; Bakar et al., 2017). Classic k-ε turbulence model was used for turbulence modelling. Since there is an extensive intertidal mudflat in the modelling domain, a special wetting and drying treatment that can correct the gradient of the free surface to semi-wet element is applied, as illustrated in Section 3.1.1.2. This method is more precise to describe half-dry, half-wet elements and has been proven its robust and accurate (Medeiros and Hagen, 2013; Stansby et al., 2016).

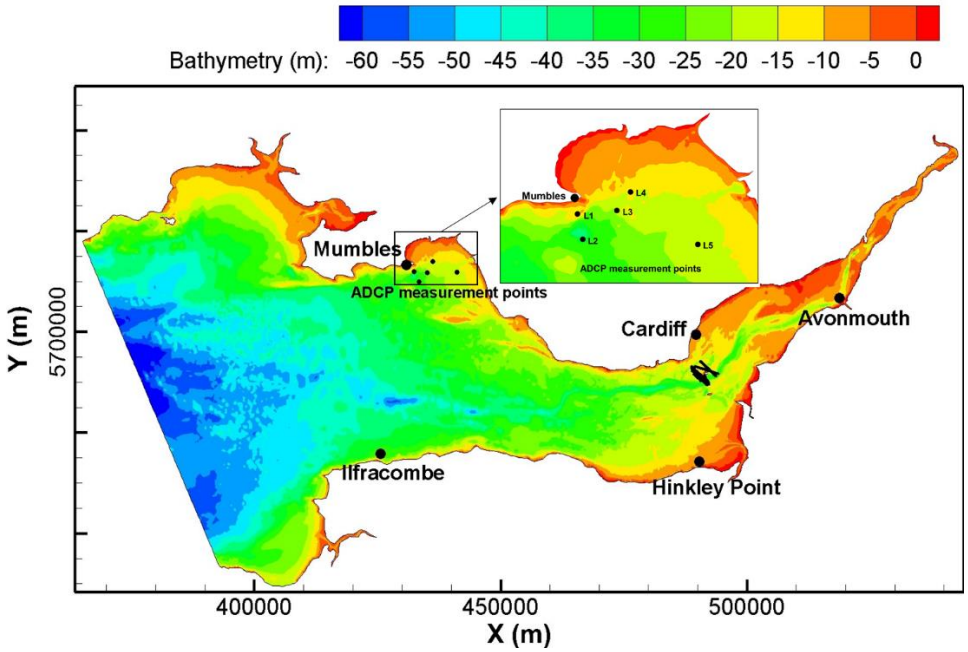

Figure 3.3: SEBC Model domain and the validation data measured points.

3.2.2 Model Validation

The model was first calibrated using water level and velocity data from the Admiralty Charts (Ahmadian et al., 2010a) and 4 tidal gauges covering the Bristol Channel and Severn Estuary. A manning's roughness coefficient of 0.025 was selected during calibration, which was generally found to give the closest agreement between the predicted results and available field data. The model was then validated using further tide level gauges and ADCP measured data.

Sea surface elevation data obtained from four British Oceanographic Data Centre (BODC) tide level gauges were used for model validation. The tidal gauges used were located at Avonmouth, Hinkley Point, Mumbles and Newport, with locations marked in Figure 3.3, were used for model validation. The validation period was from 2 July 2011 to 15 July 2011 due to the availability of current data.

The coefficient of determination (R^2) and the root mean squared error (RMSE) are used to quantify the predictive capability of the model when validated against measured water level data, with the terms being defined as:

$$R^2 = 1 - \frac{\sum_{i=1}^{n}(Y_i - X_i)^2}{\sum_{i=1}^{n}(X - \bar{X})^2}, \tag{3.37}$$

$$RMSE = \sqrt{\frac{1}{n}\sum_{i=1}^{n}(Y_i - X_i)^2}, \tag{3.38}$$

where X_i are the observed values, $\bar{X}_i$ are the mean of the observed values, Y_i are the predicted values, $\bar{Y}_i$ are the mean predicted values. The R^2 and RMSE values are mainly applied to evaluate scalar quantities, not vector quantities. Thus, the mean absolute error (MAE) and relative mean absolute error (RMAE) were also evaluated for quantifying the degree of accuracy of the model in predicting the measured velocities. The MAE contained both errors of magnitude and direction, with the formulation for a vector $\vec{X} = (X_1, X_2)$, being given for MAE and RMAE as follows:

$$MAE = \langle |\vec{Y} - \vec{X}| \rangle = \frac{\sum_{i=1}^{n}\sqrt{(Y_{1n} - X_{1n})^2 + (Y_{2n} - X_{2n})^2}}{n}, \tag{3.39}$$

$$RMAE = \frac{MAE}{\langle |X| \rangle}. \tag{3.40}$$

The preliminary qualification for RMAE ranges suggested by Walstra et al. (2001) that is Excellent (RMAE < 0.2), Good (0.2 < RMAE < 0.4), Reaonable (0.4 < RMAE < 0.7), Poor (0.7 < RMAE < 1.0), Bad (RMAE > 1.0).

Model predictions and measured values at these sites are compared (Figure 3.4 - Figure 3.14), while statistical analysis of the model performance is carried out (Table 3.1). The comparisons between the predicted and measured water levels and velocities show good agreement. All of the R^2 results show a strong correlation between the model predicted and measured free surface elevations, thereby giving confidence in the accuracy achieved using the model for predictions for the preliminary design. The RMSE value is also encouraging considering the high tidal range and currents. However, validation data of the model against the Newport gauges show relatively poor agreement. This is thought to be due to the relatively shallow water depths and the and complex topography in the vicinity of the tidal gauge. The hydrodynamic performance of the model was further validated against data collected using five bed-mounted Acoustic Doppler Current Profilers (ADCPs) deployed in Swansea Bay between September 2012 and

December 2012. The current speeds and velocities were measured throughout the water depth at these sites using seabed mounted ADCPs (Figure 3.3). The corresponding field data were then integrated over depth to acquire the depth averaged values. Typical comparisons between the model predictions and measured data for water levels and current speeds and directions and a summary of the statistical analysis are given (Figure 3.4 - Figure 3.14, Table 3.1). The statistical analysis shows a good correlation between model prediction and ADCPs measurement data. For water level, all R^2 are higher than 0.99 and the MAEs for both current magnitudes and directions were smaller than 0.1, except at site L1.Three of the RMAE indicator values were classified as being 'excellent' and with the others classified as 'good', according to the classifications given in Table 3.1. The validation between the model predicted and the ADCP measurement data therefore shows good correlation, again giving confidence in the accuracy of the model predictions.

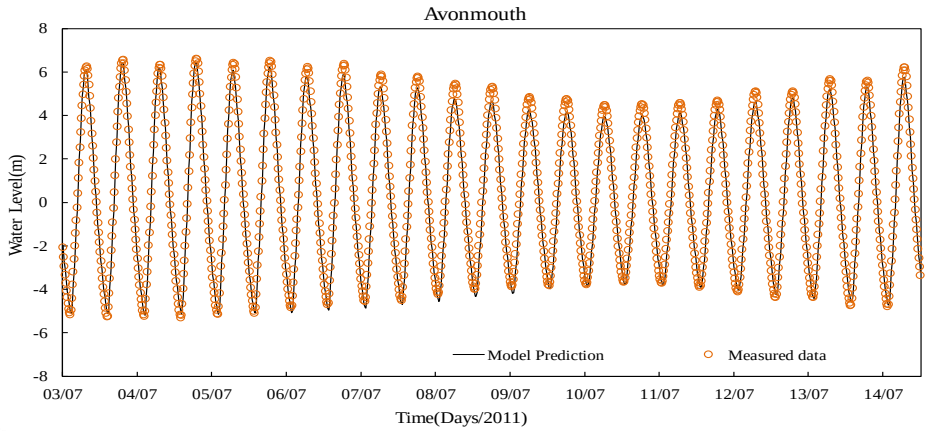

Figure 3.4: Water level comparison of model predictions and BODC measured data at Avonmouth.

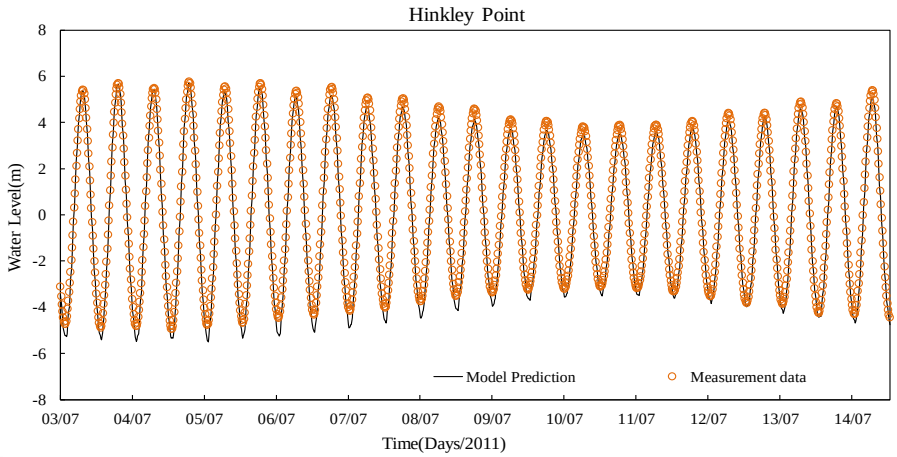

Figure 3.5: Water level comparison of model predictions and BODC measured data at Hinkley Point.

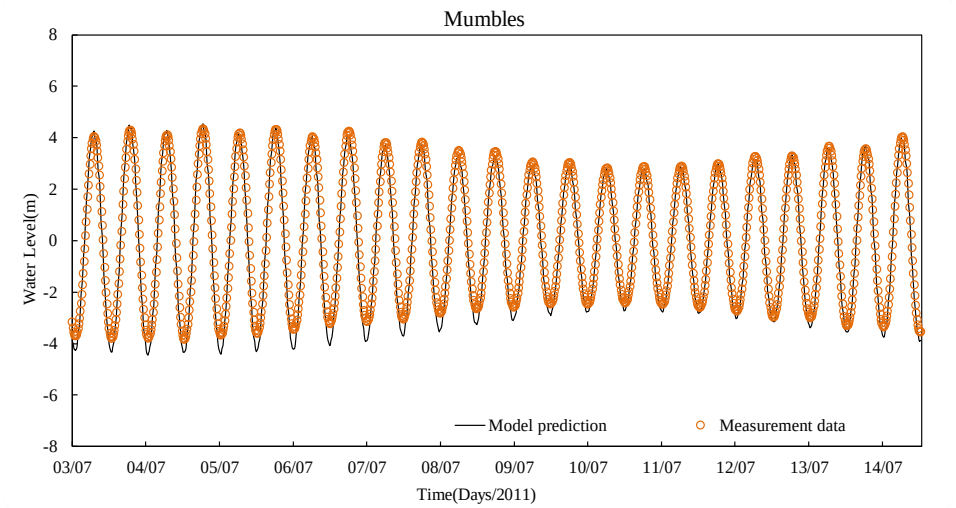

Figure 3.6: Water level comparison of model predictions and BODC measured data at Mumbles.

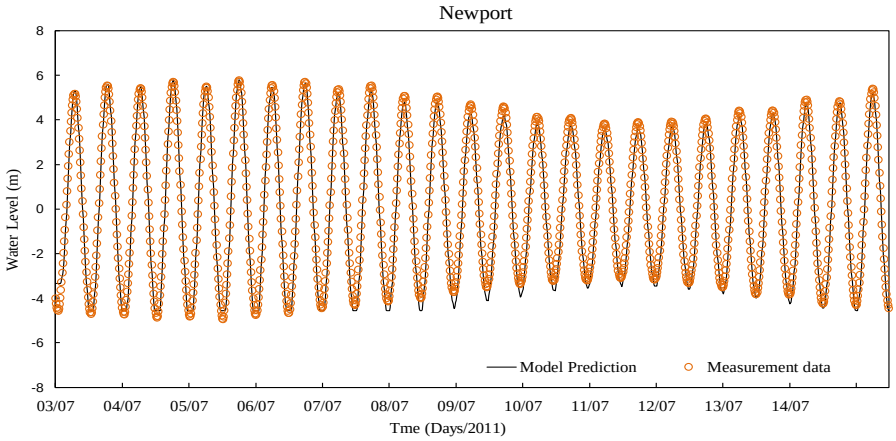

Figure 3.7: Water level comparison of model predictions and BODC measured data at Newport.

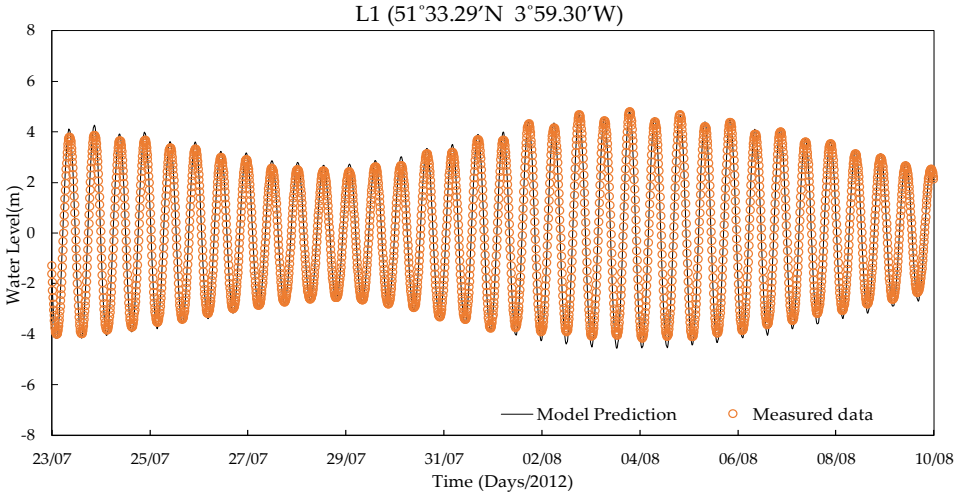

Figure 3.8: Water level comparison of model predictions and L1 ADCP measurement points.

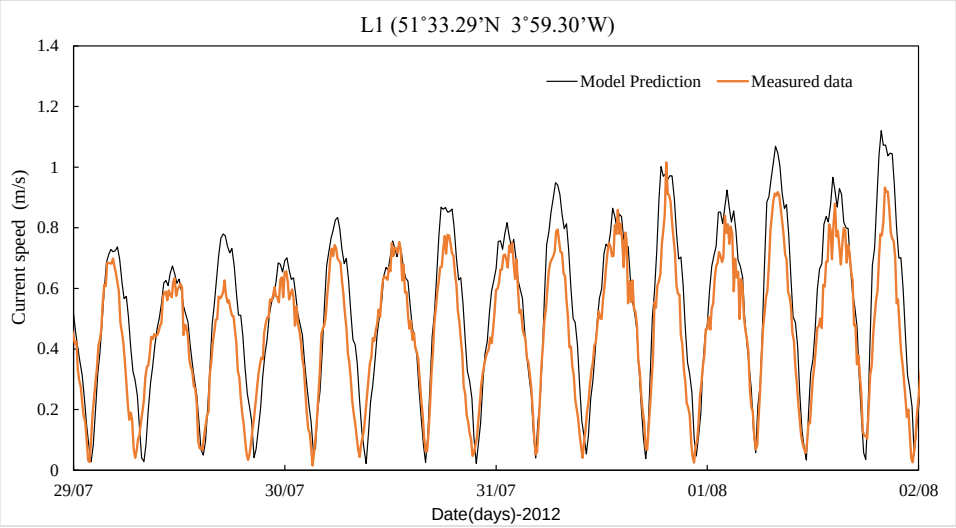

Figure 3.9: Current speed comparison of model predictions and L1 ADCP measurement points.

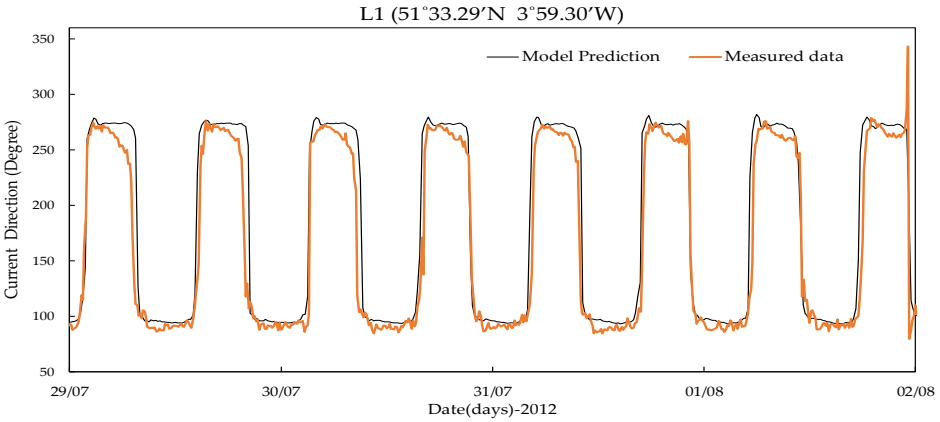

Figure 3.10: Current direction comparison of model predictions and L1 ADCP measurement points.

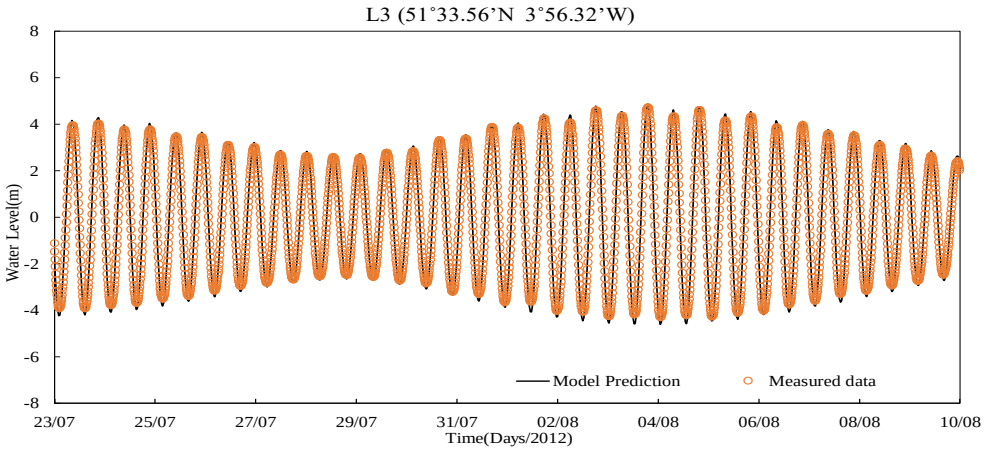

Figure 3.11: Water level comparison of model predictions and L3 ADCP measurement points.

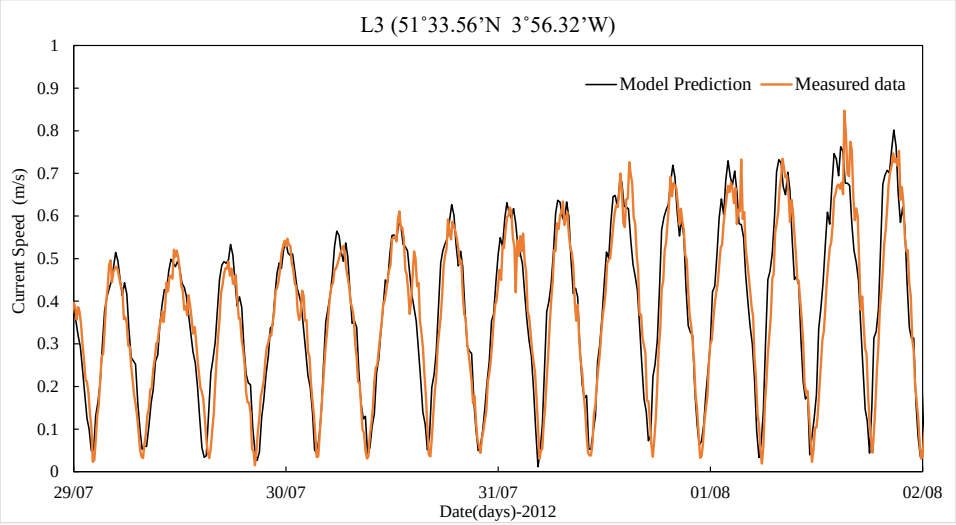

Figure 3.12: Current speed comparison of model predictions and L3 ADCP measurement points.

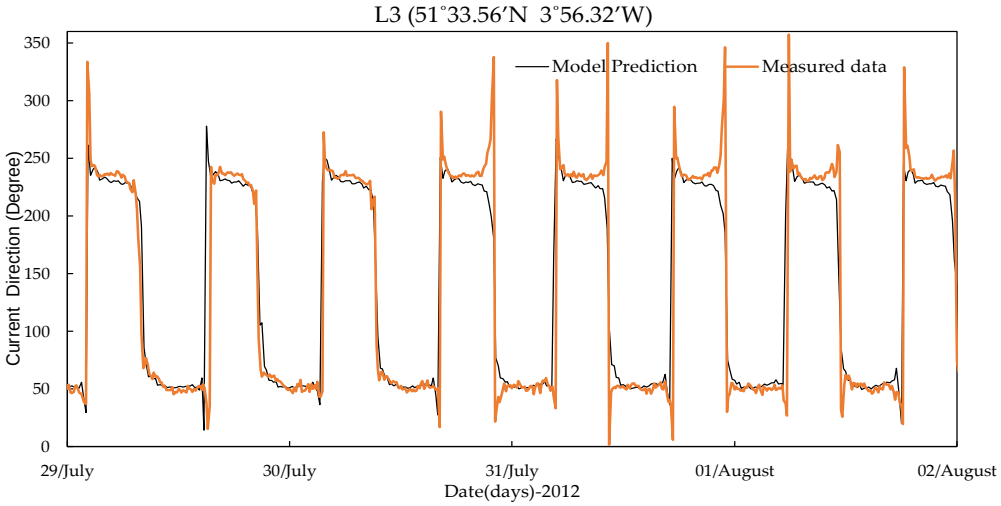

Figure 3.13: Current direction comparison of model predictions and L1 ADCP measurement points.

Table 3.1: Validation statistics of BODC gauge data and Swansea Bay ADCP data.

Water level Statistical Analysis		
Site	R^2	RMSE
Avonmouth	0.992	0.359
Hinkley	0.988	0.351
Mumbles	0.964	0.420
Newport	0.932	0.767
ADCP L1	0.99	0.260
ADCP L2	0.993	0.213
ADCP L3	0.992	0.232
ADCP L4	0.992	0.231
ADCP L5	0.993	0.214

Swansea bay ADCPs measured velocity magnitude

Site	MAE	RMAE
ADCP L1	0.122	0.222
ADCP L2	0.083	0.145
ADCP L3	0.057	0.142
ADCP L4	0.045	0.191
ADCP L5	0.076	0.230

The tidal constituents were then used to validate the model and to explore the tidal resonance characteristics in this area. The model was run for more than 30 days, from 18 January 2012 to 19 February 2012, to achieve an accurate harmonic analysis. Matlab package T-tide (Pawlowicz et al., 2002) was utilized to determine the harmonic constituents, with the top three dominant constituents being the M2, S2 and N2 tides. Tidal BODC measurement data and model predictions were compared at the tidal gauges in the Bristol Channel (Table 3.2).

Results show that the amplitude and phase for the M2, S2 and N2 tidal constituents match very well. However, the M2 phase shows a discrepancy at the Ilfracombe site, where the discrepancy is more than 14°. The Ilfracombe gauge is sited closest to the seaward boundary, which suggests that there might be some impact from the seaward boundary conditions. In comparing with the harmonic analysis results in this area with the findings of other researchers, the results show

that the harmonic components data are close to the published findings, further confirming that the validation agreement is encouraging (Haverson et al., 2017; Robins et al., 2015).

Table 3.2: Amplitude and phase for M2, S2 and N2 tidal constituents at 5 Tidal Gauges.

Tidal gauges		M2 amplitude (m)	M2 phase (deg)	S2 amplitude (m)	S2 phase (deg)	N2 amplitude (m)	N2 phase (deg)
Hinkley	Observation	3.80	185.0	1.42	237.0	0.62	171.75
	Prediction	3.78	187.2	1.52	246.1	0.59	176.1
	Difference	-0.02	2.20	0.10	9.10	-0.03	4.35
Mumbles	Difference	0.02	-7.14	-0.03	-2.30	0.05	-6.61
Ilfracombe	Difference	0.01	-14.32	-0.05	-7.98	-0.03	-3.26
Newport	Difference	0.08	-18.37	-0.03	-12.81	0.01	-5.32
Avonmouth	Difference	-0.02	-11.99	-0.09	-9.56	-0.03	-3.39

3.2.3 Mesh Convergence Test

Further research involves model prediction comparison between different scenarios which with different meshes. Thus, it is necessary to investigate mesh convergence of model prediction. In addition to the mesh applied in the previously validated model, two other meshes were generated to investigate the robustness and response of the model to grid size, as shown in Table 3.3. Furthermore, to achieve a similar Courant-Friedrichs-Lewy number, the time step applied in each scenario were adjusted according to the Courant-Friedrichs-Lewy number by its definition:

$$CFL = \frac{U \cdot \Delta t}{\Delta x} < 1, \tag{3.41}$$

where U is the velocity, Δt is the time step and Δx is the grid size.

Table 3.3: The validation statistics of model results with different meshes.

Mesh	Grid size	Time step	Validation of water level		Validation of velocity	
			R^2	RMSE	MAE	RMAE
1 (Base-line)	200-600	10	0.9818	0.3386	0.0766	0.186
2	400-800	15	0.9774	0.3591	0.0823	0.195
3	600-1000	20	0.9658	0.3642	0.0905	0.213

Table 3.3 shows the averaged validation statistics of water level and ADCP measured velocity for model predictions with three different meshes. It is demonstrated that the model prediction

is slightly related to the mesh grid. The model prediction with coarse mesh, e.g, mesh 2 and mesh 3, have slightly less correlation with the measured data. Figure 3.14 and Figure 3.15 show the typical comparisons of the model prediction between mesh 1, mesh 2 and mesh 3. The differences in modelling prediction are relatively minor between the coarse and finer meshes, demonstrating the independence and robustness of model prediction on the mesh grid.

However, Jones and Davies (2008) reported that the finer mesh model in the TELEMAC system is more suitable for resolving the 'wetting and drying' phenomenon and non-linear effects in the shallow water regions. The prediction of the finer mesh model also presents a higher accuracy. Thus, the finer mesh, i.e., 200-600 m grid-size mesh, is applied in the following study.

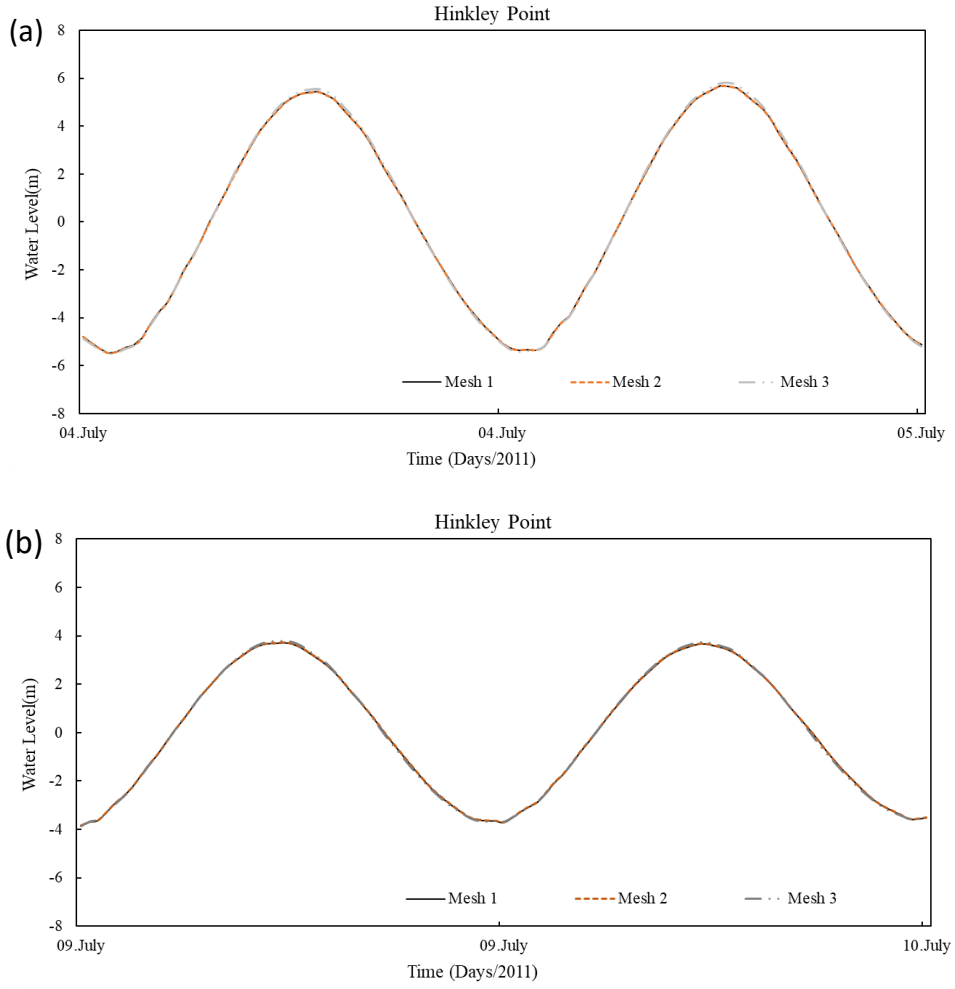

Figure 3.14: Water Level comparison with different meshes at Hinkley points during (a) spring and (b) neap tides.

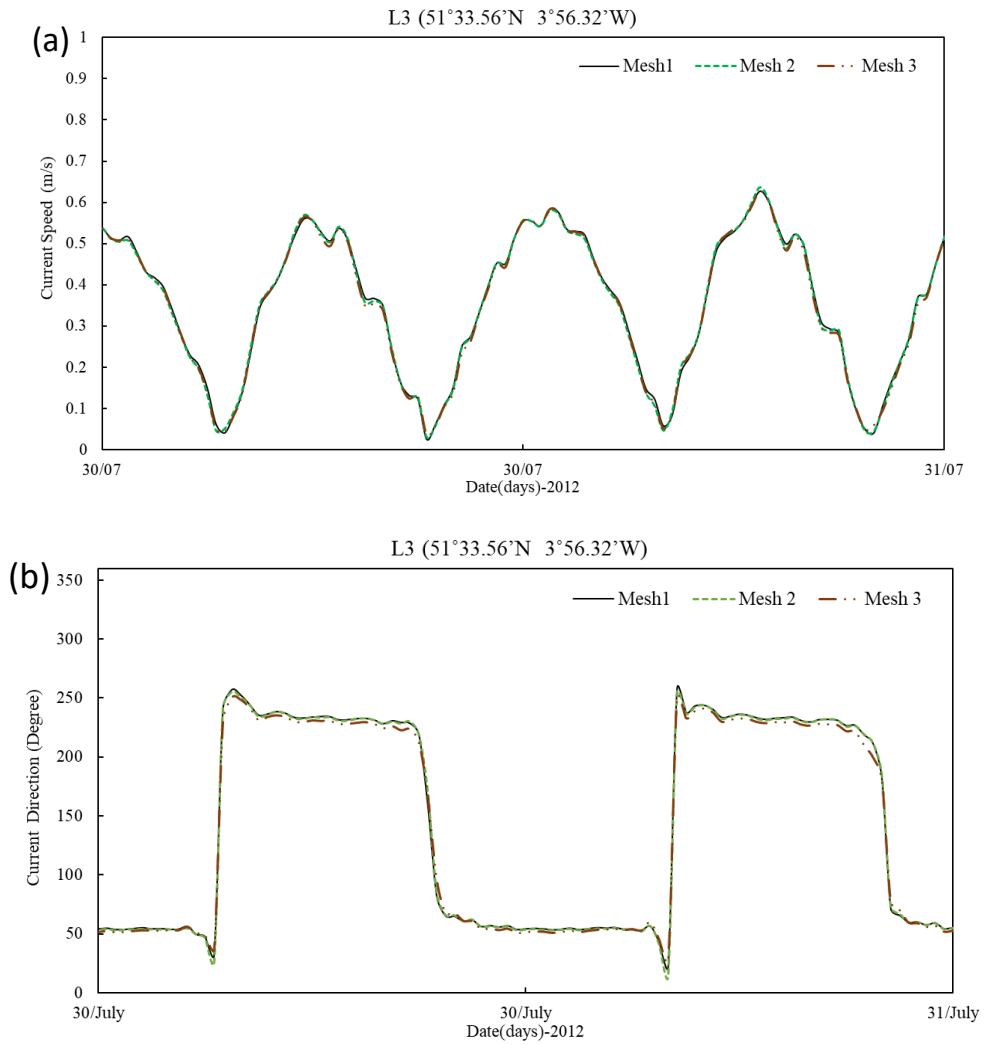

Figure 3.15: Velocity comparison with different meshes at ADCP measurement point L3, (a) velocity magnitude; (b) Velocity direction.

3.3 Continental Shelf Model

The impact of the TRSs on the near-field and far-field hydrodynamics can be equally significant due to the large tidal range in the water impoundment area and the large volume of the enclosed water body (Zhou et al., 2014b). Previous studies indicate that the operation of large TRSs is likely to impact near-field and far-field hydrodynamics, especially for sites with macro-tide conditions (Bray et al., 2016; Adcock et al., 2011). Furthermore, it is reported that an open boundary within the continental shelf may amplify any perturbation associated with the TRS by exciting a resonant mode (Adcock et al., 2015). Thus any model that simply held the same boundary condition for pre- and post-TRS may reduce the model accuracy and cause discrepancies (Zhou et al., 2014b; Rainey, 2009). To solve this issue, either allow the

perturbations to exit the model and re-enter the model as required if the boundary is located on the shelf, or extend the open boundary beyond the continental shelf to capture these resonance changes (Adcock et al., 2015). Meanwhile, it is also interesting to explore the other TRSs located on the west coast of the Irish Sea beyond Severn Estuary and Bristol Channel, such as the North Wales tidal lagoon. Thus, a new hydrodynamic model, the continental shelf (CS) model, was created to address the above considerations.

3.3.1 Model Setup

The CS model covered the whole Irish Sea and a large region of the Celtic Sea, with its open boundary being extended to beyond the Continental Shelf. The open boundary extended from Plymouth in southwest England to the Isle of Mull, on the west coast of Scotland.

Due to the wide modelling domain that spans over two UTM zones, it was necessary to perform a TELEMAC simulation with spherical coordinates to automatically adjust the Coriolis coefficient at each point of the domain. Thus, it is necessary to set the geographic system of this mesh to WGS84 Longitude/Latitude in real degrees. However, to more easily analyse the modelling results and make comparisons with previous research, i.e. WSL and SBL research in the SEBC model and studies from other researchers, the modelling results were converted to Mercator projection coordinate system.

Topography data in this area were taken from two sources with different resolutions and converted to mean sea level (MSL). Most of the domain from the CS model utilised bathymetry data from the EMODnet-Bathymetry portal (https://www.emodnet-bathymetry.eu/), with 1/24 of an arcminute resolution (approx. 75m). Moreover, higher resolution topography data were utilised in the areas of interest. The topography data for the Bristol Channel and Severn Estuary, along with the sea area north of Wales and out of Liverpool Bay, shared the same source of SEBC model, which was obtained from EDINA Digimap (https://digimap.edina.ac.uk/) with a finer resolution of 1 arcsecond (approx. 30m), as shown in the highlighted area in Figure 3.16.

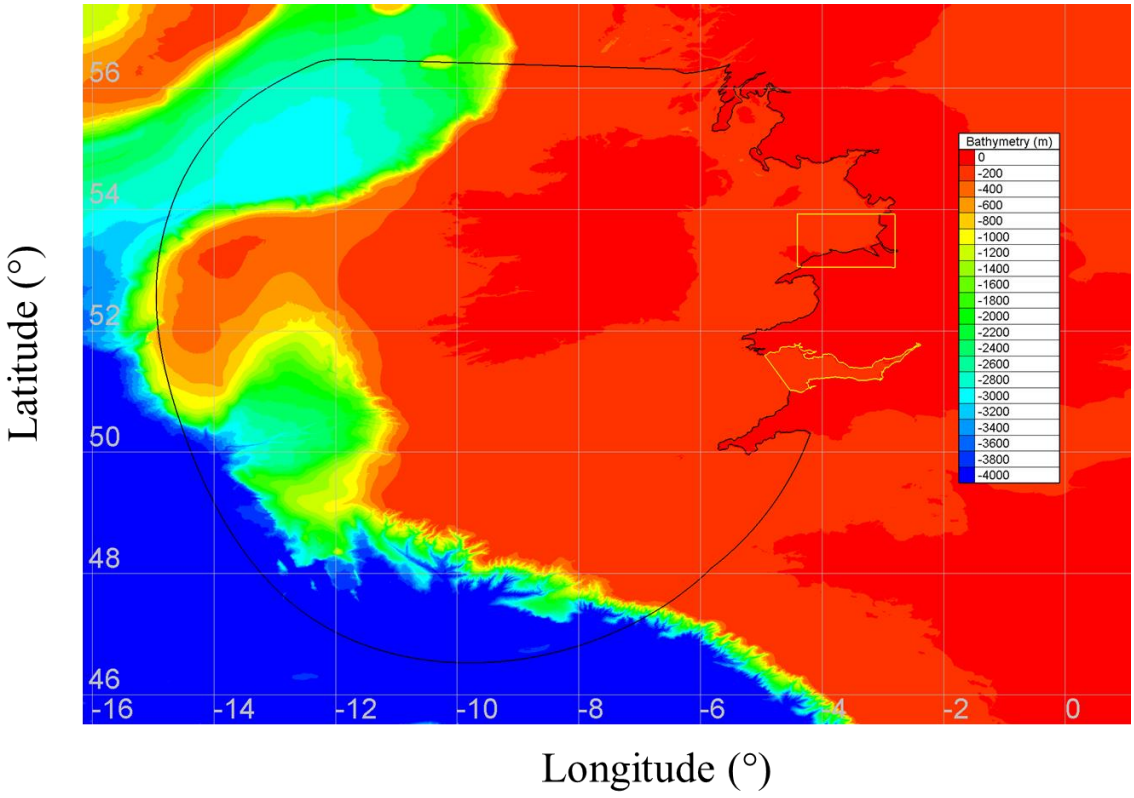

Figure 3.16: Computational domain of the CS model and the bathymetry where the areas of higher resolution data are indicated in the yellow rectangle highlight zone.

The mesh was discretised with 134,291 nodes and 252,382 elements. In the areas of interest such as Bristol Channel and Severn Estuary, the Colwyn Bay and Liverpool Bay, a higher mesh resolution was provided with 50-300 m, as shown in Figure 3.17. The mesh resolution varied from 9km near the open boundary to the maximum value of 35 km in the middle of the model domain; then it reduced to 700 m along the coastline.

The seaward open boundary was driven by spatially varying time histories of tidal elevations and depth-averaged velocity from the TPXO7.2 database (http://volkov.oce.orst.edu/tides) with 13 tide constituents including eight primary, two long-period, and three non-linear constituents, namely M2, S2, N2, K2, K1, O1, P1, Q1, MF, MM, M4, MS4 and MN4, with a resolution of 1/30º. TPXO uses the TOPEX/POSEIDON satellite project mapping tidal levels using both direct observational data and dynamical information (Dushaw et al., 1997), which is one of the most accurate global models of ocean tides (Bourban et al., 2012).

Following the same setup as the SEBC model, the model uses the classic k-ε turbulence model, which has been studied later and proven as the most suitable turbulence model in this research. The Courant number limitation was set to 1, and the time step was set to 10 s to ensure model

accuracy and computational efficiency. After repeated runs, Manning's roughness coefficient of 0.025 was found to produce a satisfactory validation. Moreover, 4 days spin-up time was used in the CS modelling due to the size of the model domain. An investigation about model prediction and the length of spin-up time has been carried out and confirmed the 4 days spin-up time is enough to stabilise the CS model and the model is independent of the spin-up time.

In addition to the river discharges distributed around the Bristol Channel and Severn Estuary in the SEBC model, four river discharges located in the Colwyn Bay and Liverpool Bay were added to the model as water sources. These were River Conwy, River Clwyd, River Dee and River Mersey, with average flows of 19.1 m^3/s, 6.35 m^3/s, 38.1 m^3/s, 14.18 m^3/s, respectively, based on data from the UK National River Flow Archive data (https://nrfa.ceh.ac.uk).

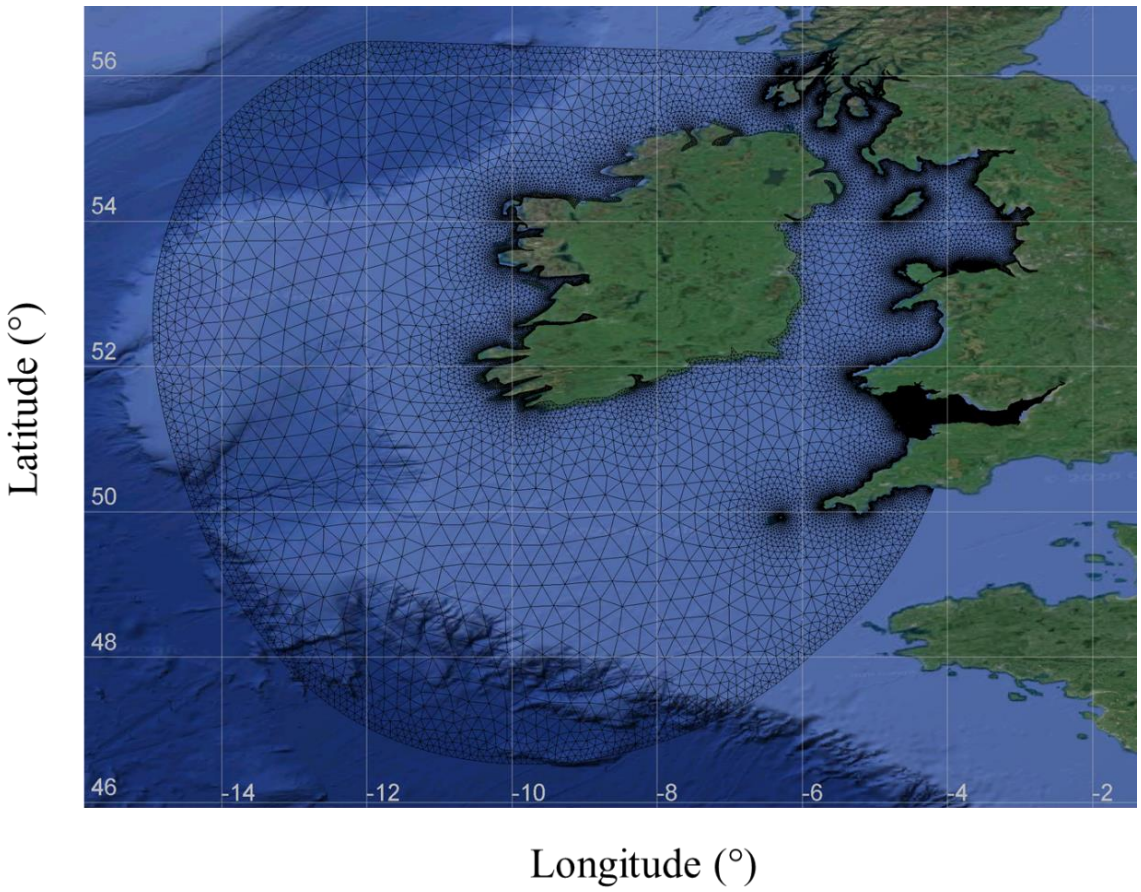

Figure 3.17: Mesh resolution in the CS model, with refined mesh resolution in the Severn Estuary and Bristol Channel, and the Colwyn Bay.

3.3.2 Model Validation

The model performance was validated against BODC water level data at 12 tide gauges in this area, the locations of which are shown in Figure 3.18. The validation period was one month, ranging from 17/05/2012 00:00:00 to 16/06/2012 00:00:00. This period provided sufficient length to meet the requirements for harmonic validation and analysis performed later.

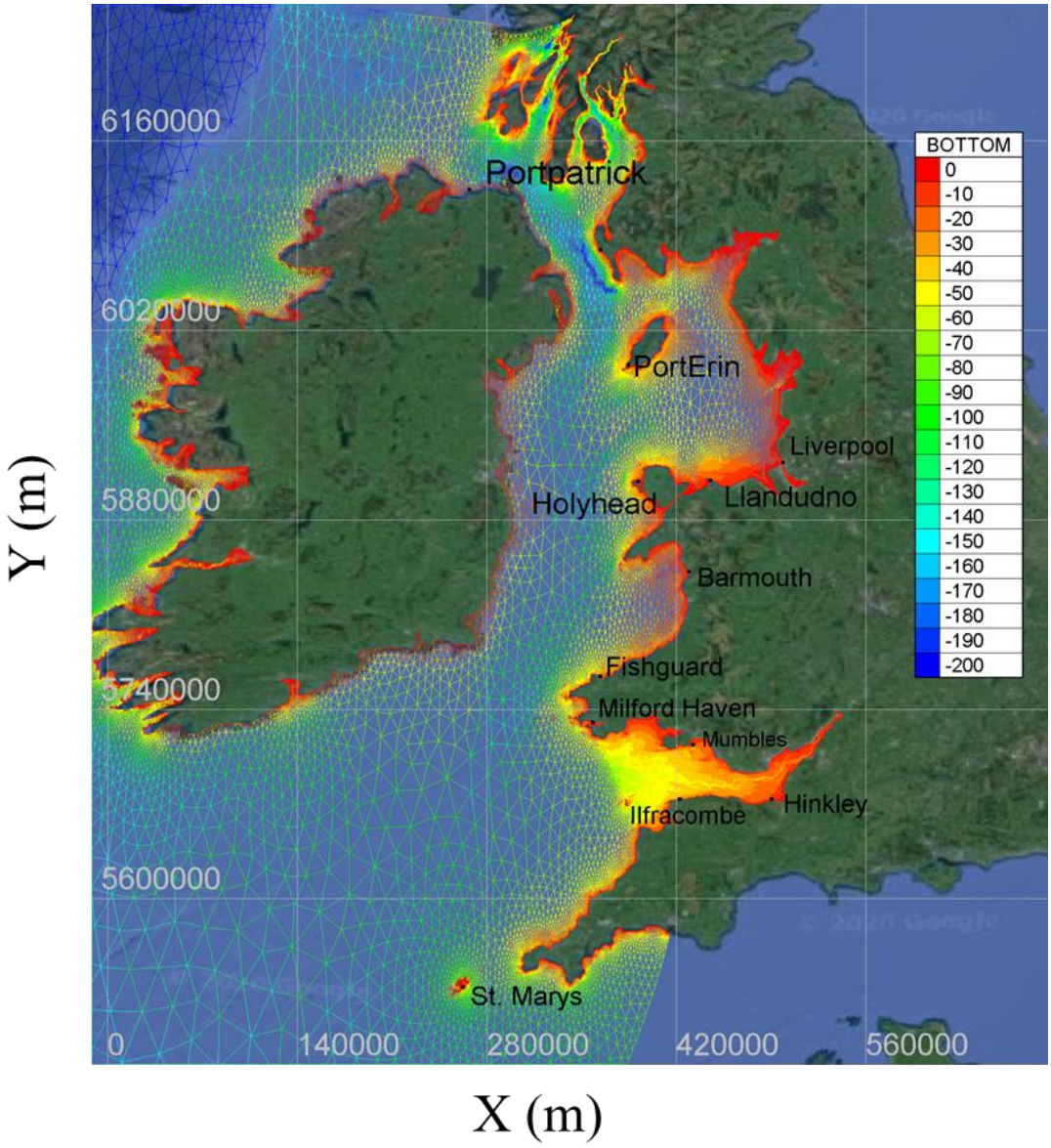

Figure 3.18: The tide gauges used to validate CS model prediction (In UTM 30 coordinate system).

The coefficient of determination (R^2) and the root mean square error (RMSE) for the validation results for the 12 BODC tide gauges are provided in Table 3.4. Additional details of water level comparisons can be found in Appendix B, Figure B1.

Table 3.4: Water level validation statistics of the 12 BODC tide gauges.

Tidal gauge	R^2	RMSE
Portpatrick	0.971151	0.17339
Port Erin	0.967936	0.249349
Liverpool	0.988300	0.280944
Llandudno	0.986939	0.233857
Holyhead	0.987302	0.154665
Barmouth	0.962248	0.221039
Fishguard	0.965417	0.191592
Milford Haven	0.976492	0.258764
Mumbles	0.973969	0.385077
Hinkley	0.964716	0.484798
Ilfracombe	0.977528	0.347919
St Marys	0.983376	0.172226

The model validation showed a good correlation between the model and measured data. The water level in regions of the central Irish Sea, such as Barmouth, Liverpool, Holyhead, Portpatrick and Port Erin, showed close agreement between model results and measured data. However, the high RMSE values for Mumbles, Hinkley and Ilfracombe indicated that comparisons between model results and measurement data for the Bristol Channel and Severn Estuary were not as close, but they were still similar to that of the SEBC model prediction. Besides, the velocity magnitude and direction prediction of CS model was validated with the measured ADCPs data as applied in previous SEBC model validation. Results showed good agreement between ADCPs measurement data and the CS model prediction; a typical comparison is shown in Appendix B, Figure B2.

Furthermore, harmonic constituents validation was carried out in this area. The amplitude and phase of the dominant components, M2 and S2, are shown in Figure 3.19 and Figure 3.21. It is clear that large amplitudes M2 distribute throughout the eastern Irish Sea and in the SEBC area. Two amphidromic points exist in this region. One is located at the east coast of Ireland in the Celtic Sea and another one between the west coast of Scotland and the north coast of Northern Ireland. Compared with the harmonic constituents prediction reported by other researchers, as seen in Figure 3.20 and Figure 3.22, the same distribution of harmonic constituents is found, which validates the model prediction again (Young et al., 2000; Wolf et al., 2009).

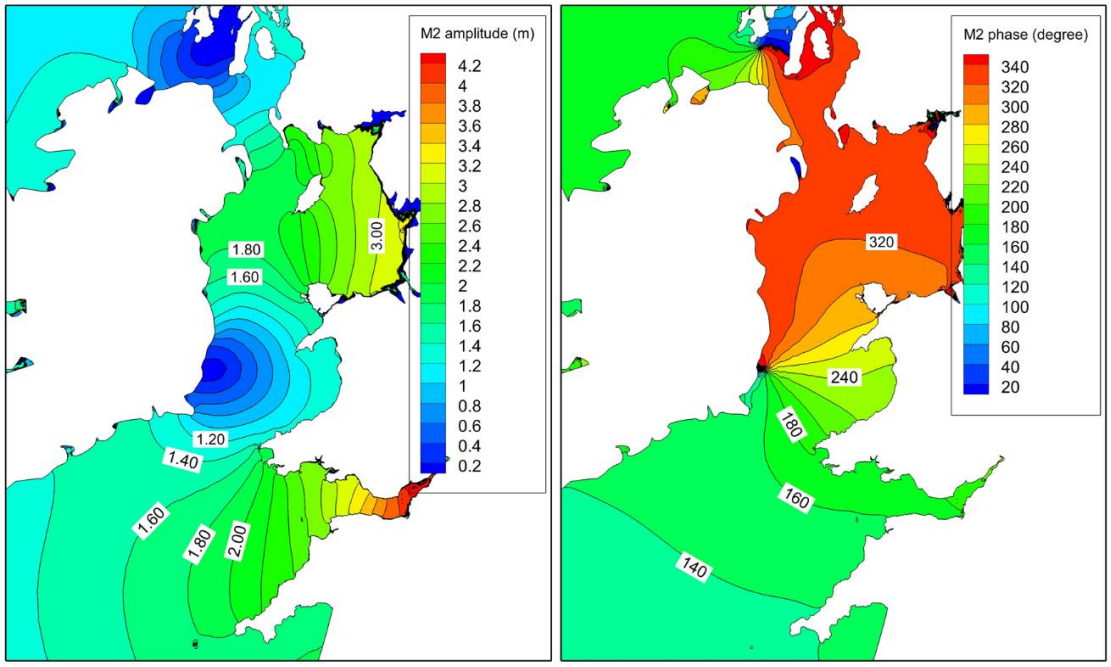

Figure 3.19: Predicted amplitude (left) and the phase (right) of the M2 tidal constituent from the CS model.

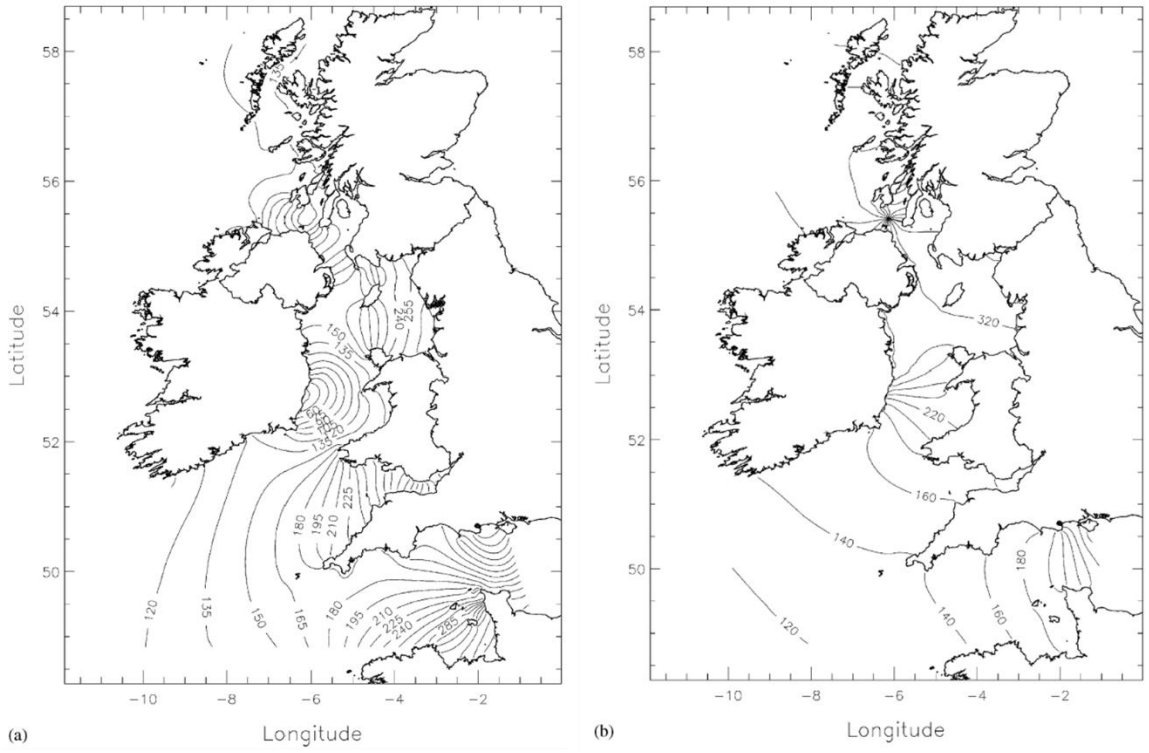

Figure 3.20: Predicted amplitude (left) and the phase (right) of the M2 tidal constituent from Young et al. (2000).

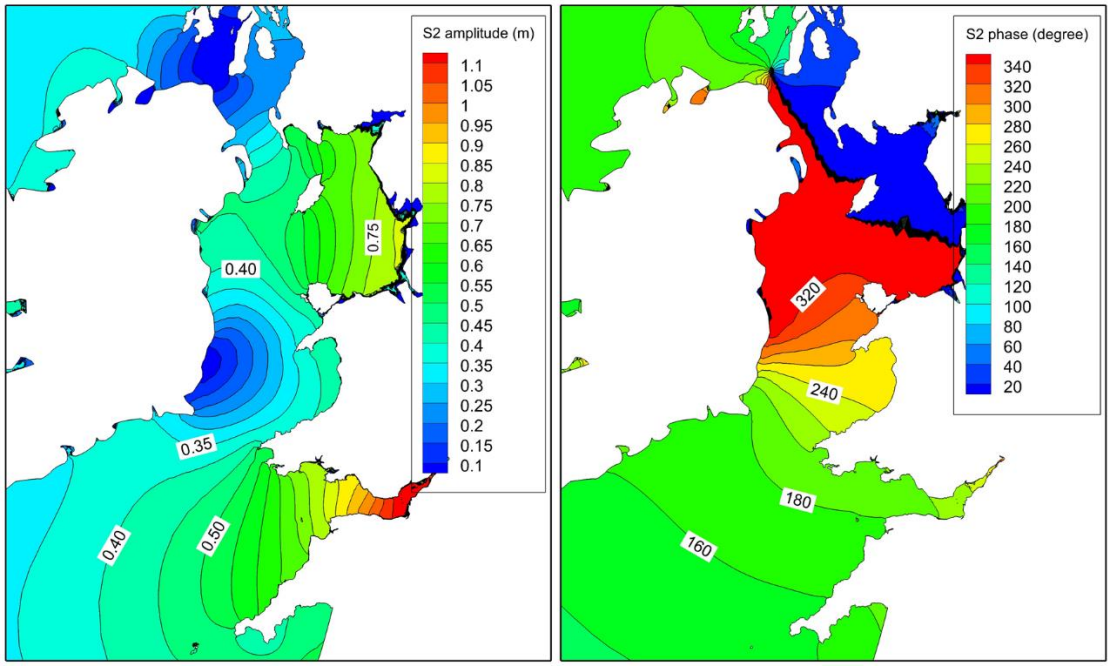

Figure 3.21: Predicted amplitude (left) and the phase (right) of the S2 tidal constituent from the CS model.

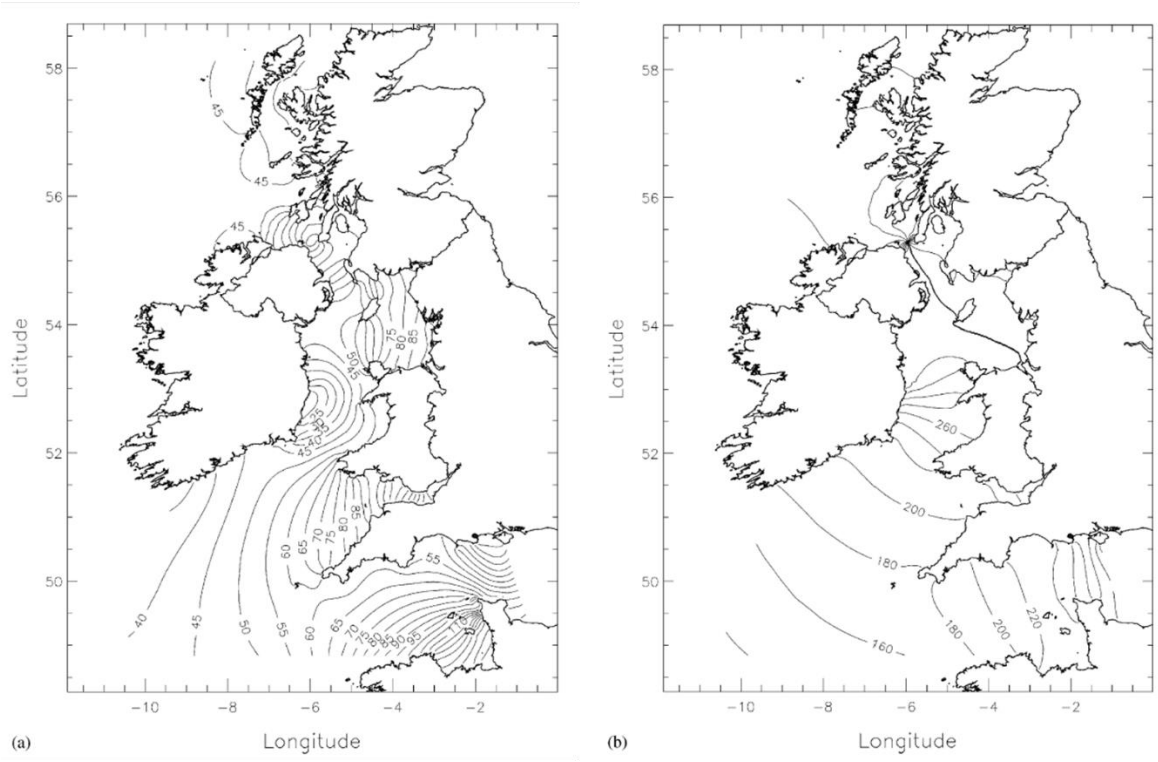

Figure 3.22: Predicted amplitude (left) and the phase (right) of the S2 tidal constituent from Young et al. (2000).

3.4 Summary

TELEMAC-2D was selected as the numerical tool for this research based on its easily accessible code, unstructured mesh, and wide range of marine energy modelling applications. Two numerical models, the SEBC model and CS model, were developed using TELEMAC-2D to simulate the hydrodynamic process in Severn Estuary and Bristol Channel, as well as the Irish Sea and Celtic Sea, respectively. Most of the model parameters were the same between the two models. Manning's roughness coefficient of 0.025 and k-ε turbulence model were applied after calibration. 2 days of spin-up time was allocated to the modelling period before the analysis of the SEBC model prediction, while CS model was given 4 days for its larger domain. However, different boundary conditions were used, that tidal time series of water levels were applied on the boundary of the SEBC model while spatially varying tidal elevations and velocity from the TPXO database were used as the driven force of seaward open boundary for the CS model. Furthermore, different coordinate systems were used in the two models to adapt the Coriolis force setting in the TELEMAC system. The model validations were performed using the sea water level data achieved from BODC tidal gauges and the bed-mounted ADCP-measured tide velocity data. The validation results showed that both models gave satisfactory hydrodynamic prediction. Furthermore, the investigation of mesh convergence demonstrated that model prediction was independent of mesh resolution.

Chapter 4 Island Wake Modelling and Further Model Calibrations

Understanding tidal flow around artificial or natural obstacles, such as tidal lagoon, coastal reservoirs and islands, is an important challenge in coastal, estuarine and river basins research due to the potential impacts of such flows on the environment and ecology in the basin (Evans et al., 2015). The construction of the lagoon itself changes the local coastal line, acting as a cape or peninsula, generating eddies and turbulence in the area. Furthermore, eddies and recirculation zones produced around lagoon structure can significantly impact the sediment transport, water quality processes, and the hydroecology in the region. For example, in the lee of the obstacle like an island, the balance between the inward-directed pressure gradient and the outward-directed centrifugal force will bring a convergence of bedload (Pingree, 1978; Dyer and Huntley, 1999). These impacts will converge the bedload material, forming sandbanks (Neill and Scourse, 2009; Li et al., 2019), which could be a hazard to shipping and the deployment of marine aggregate extraction if no dredging work is regularly undertaken. Furthermore, the strong localised upwelling and downwelling flow in the lee of a natural obstacle (Estrade and Middleton, 2010) will result in the vertical transport of nutrients from deeper waters, thereby enhancing the local biology and ecology.

It is known that model predictions for flows around obstacles are sensitive to the turbulence modelling strategy, advection scheme, mesh refinement et al. (Stansby, 2003). Thus, an accurate representation of the hydrodynamic on the barrage or lagoon location is of crucial importance in terms of the accurate modelling and the hydro-environmental impact study (Neill et al., 2018; Angeloudis et al., 2016b). But it is difficult to validate the prediction of tidal flow around lagoon directly since there is no tidal lagoon has been constructed yet. However, studying the tidal flow in a similar scenario can contribute to the understanding and modelling prediction for such concerns. Flat Holm Island, which is close to a circular island in Bristol Channel, could provide an ideal example to study the flow pattern around an obstacle in a macro-tidal environment. By studying the island wake and flow pattern around Flat Holm Island, a good foundation for modelling the flow structure around tidal lagoon can be achieved.

This chapter aims to investigate the flow pattern around an obstacle in a macro-tidal environment, which can improve the model hydrodynamic prediction and provide a good foundation for modelling the flow structure around the lagoon. The flow velocity in the lee of

Flat Holm Island is measured through vessel-mounted ADCP surveys, as presented in Section 4.1. Then the initial model prediction comparison with ADCP measured data is shown in Section 4.2. Section 4.3 presents the evolution of wake in the lee of the island, to provide a basic understanding of flow structure around an obstacle in macro-tidal environment. Section 4.4 presents the further calibration of model prediction with different turbulence models and corresponding solvers. Last, Section 4.5 summarise this chapter.

4.1 In-Situ Data Collection

Flat Holm Island lies almost at the boundary of the Severn Estuary and Bristol Channel, approximately 8 km south from Cardiff Bay (Figure 4.1). It is roughly circular in shape with a diameter of approximately 700m. Tides in the Severn Estuary are semi-diurnal with the second largest tidal range in the world (Pethick et al., 2009), with typical tidal ranges during peak spring tides ranging from approximately 7 m at the mouth of Bristol Channel to 14 m in the upper reaches of the Seven Estuary. Maximum currents in this region are approaching excess of 2.5 m/s during peak spring tides (Ahmadian et al., 2014a).

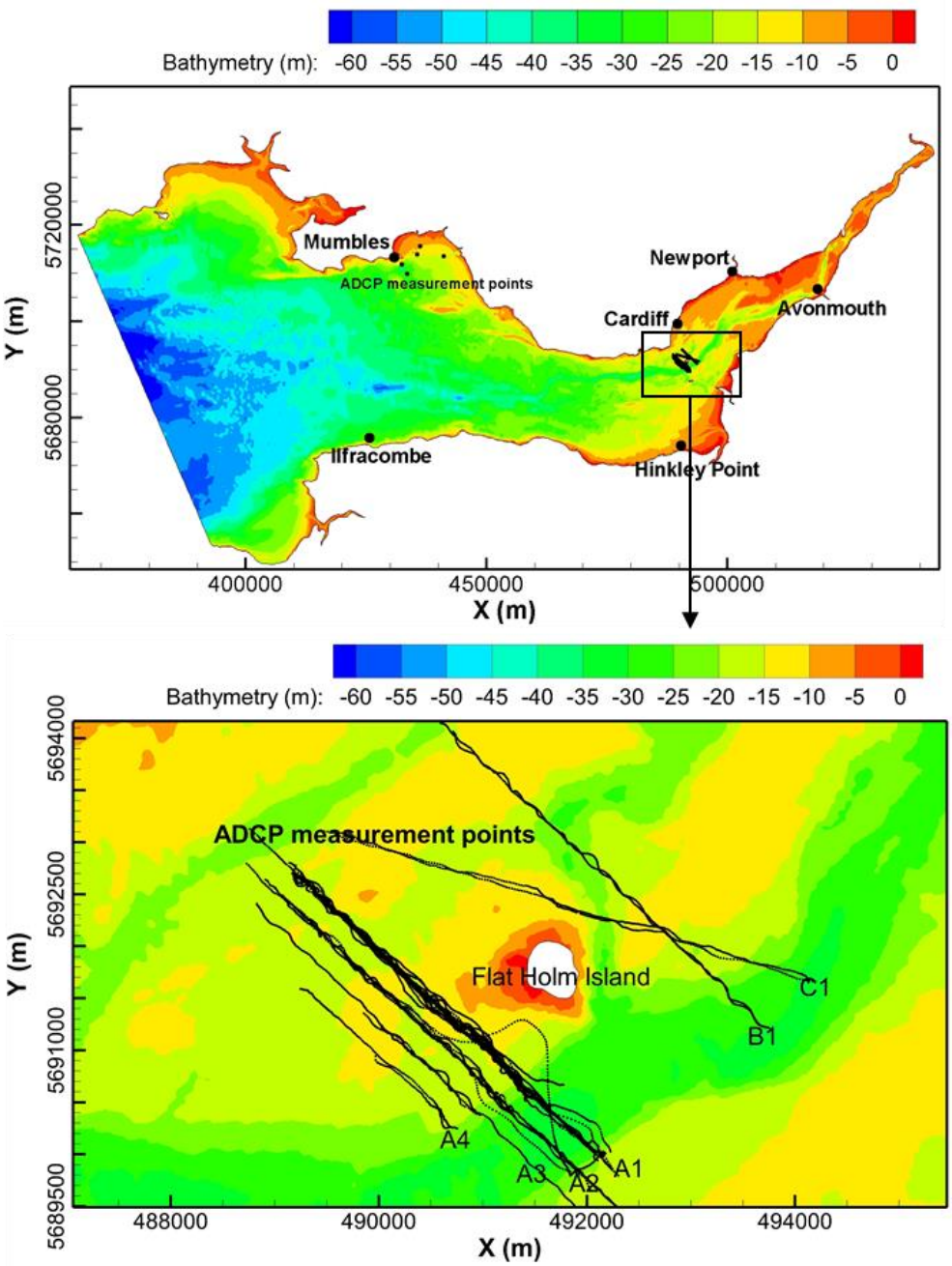

Figure 4.1: Flat Holm Island and the ADCPs measurement transect lines.

In order to get a better understanding of the flow structure and validate the model performance, vessel-mounted ADCP surveys were carried out in the vicinity of the island between 5 July - 30 September 2011 using a Sontek 1000 kHz ADCP. This ADCP unit houses three transducers, measuring the Doppler movement in the east, north and upward directions. An internal compass and a temperature sensor were also housed within this unit. The Sontek 1000 kHz ADCP was mounted on a swing arm placed at one side of a ship, as demonstrated in Figure 4.2. Sontek Current Surveyor software was used to record the survey data, which also recorded the vessel position using an onboard Differential Global Positioning System (DGPS). A single beam echo

sounder was also employed to provide a profile of the seabed. The vessel transected along a series of survey lines downstream of the island, in as straight a line as possible given the strong tidal current conditions (Figure 4.1). The survey transects were planned based on the natural features, tidal current conditions, and the potential location of the wake in the lee of the island (Table 4.1). For example, the survey on 5 July 2011 comprised driving the vessel along a single transect line A1, from the end of the flood tide, throughout the ebb tide and into the beginning of the next flood tide. This ensured that data were acquired to the southwest of Flat Holm, downstream of the ebb tide, and along one transect throughout the ebb tide. The surveying on other days was taken at different tidal phases and locations, with the aim of characterising the flood/ebb tidal currents downstream of Flat Holm Island.

Figure 4.2: Sontek ADCP unit mounted on a swing arm during the survey (Guo et al., 2020).

Table 4.1: Time and transect lines of each ADCPs measurement.

Date	Time (GMT)	Measure route
5 July 2011	09:05	A1
	09:49	A1
	11:00	A1
	11:34	A1
	12:29	A1
	13:00	A1
	13:39	A1
	14:22	A1
	15:00	A1
	16:38	A1
7 July 2011	15:10	A2
	15:47	A2
	16:55	B1
	15:37	B1
	18:50	C1
	19:31	C1

Date	Time (GMT)	Measure route
1 August 2011	09:27	A4
	09:55	A3
	10:08	A2
	10:40	A1
	11:04	A4
	11:20	A3
	11:40	A2
	12:02	A1
30 September 2011	09:37	A2
	10:56	A1
	11:49	A2
	12:33	A1

4.2 Model Comparison with ADCPs Data

Flat Holm Island wake evolution is studied in the SEBC model, following the same model settings as shown in Chapter 3. Furthermore, the mesh resolution around Flat Holm Island has been refined further to less than 50 m to ensure an accurate representation of the bathymetry in this region. The measured and predicted velocity magnitude along these four transects are compared by scatter plots of gene expression (Figure 4.3). The values of the velocities predicted from the model at various points are shown along the Y axis, while the X axis represents the measured velocity values at these same points. This demonstrates the variability in the model performance, which is linked to the location of the measured points. For example, for the ADCP data collected on 5 July 2011 at 10:49, the model behaves well in the low-velocity zone, which corresponds to the recirculation zone in the lee of the island. This indicates that the model simulates the island wake well. On the other hand, the model results show a weaker performance in the high-velocity zones, which are on the two sides of the island to the south east of the island and where the deep trench is located. The results generally show a good correlation between the measured data and the model predictions.

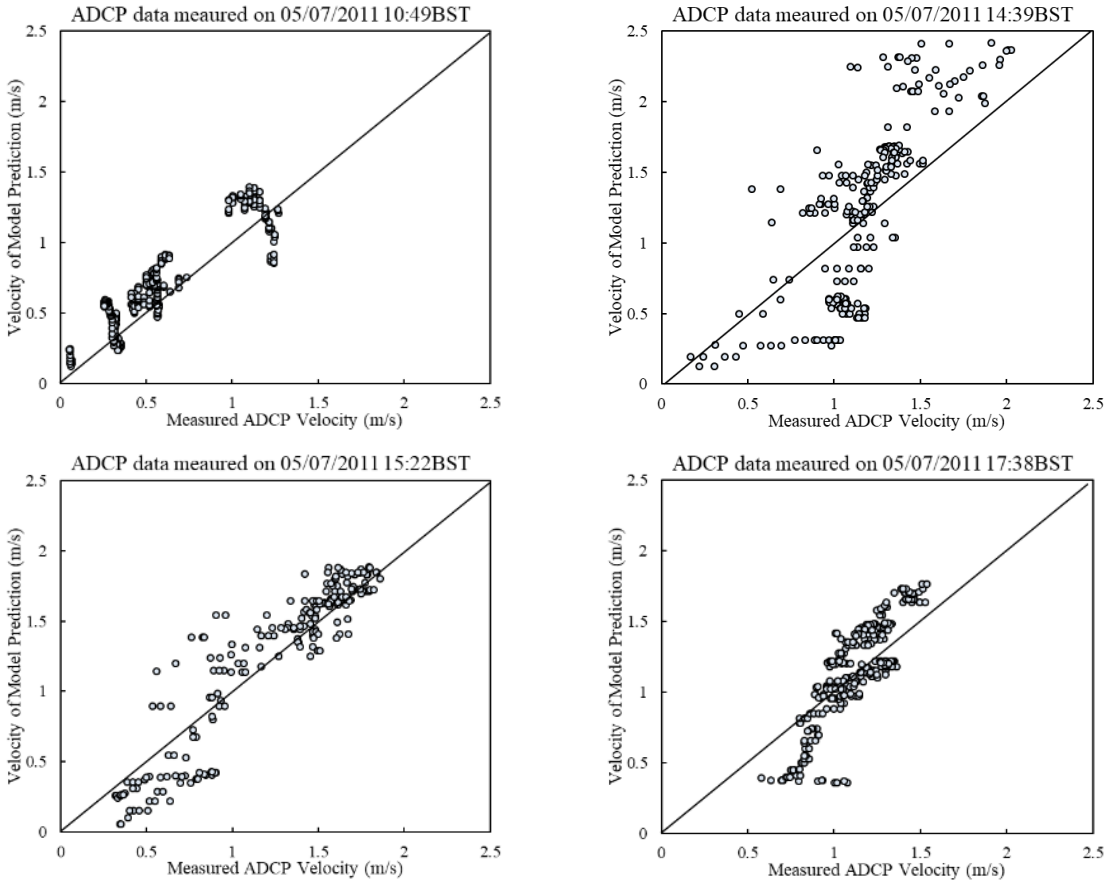

Figure 4.3: Comparison of observed and modelled current speed.

4.3 Evolution of Island Wake

The evolution of wake during the neap tide on 11 July 2011 are shown in Figure 4.4. It can be seen that the evolution of wake has the similar trend during the ebb and flood tide. First, when it is the slack tide condition (high water level or low water level), low velocity tidal currents resulting in steady flow around Flat Holm island, and with no vortex being generated (Figure 4.4 a, d). With the increase of the tide velocity, two vortices were generated at the same time, with relative steady side-by-side position and no eddy shedding occurring (Figure 4.4 b, e). Around the peak velocity of neap tide (Figure 4.4 c, f), typical Karman vortex street appears in the wake. Figure 4.4 shows a similar trend in the developing wake during flood tide and ebb tide, and during neap tides. Thus, model predictions show that the same wake pattern is generated under the same tidal currents despite the different water depths. However, this phenomenon does not directly mean that the wake developing in the lee of Flat Holm is not related to with the water depth. First, the change in the water depth change is relatively slow during neap tides. Second, the bathymetry to the west-south of Flat Holm Island is higher than

that to the north-east side, as shown in Figure 4.1. This difference in the bathymetry results in slightly higher tide speeds upstream of the island (i.e., on the south-west side) during flood tides when compared with the tidal velocity upstream of the island (i.e., on the north-east side) during ebb tides. These reasons combine to account for the same wake evolution being developed during the flood and ebb neap tides.

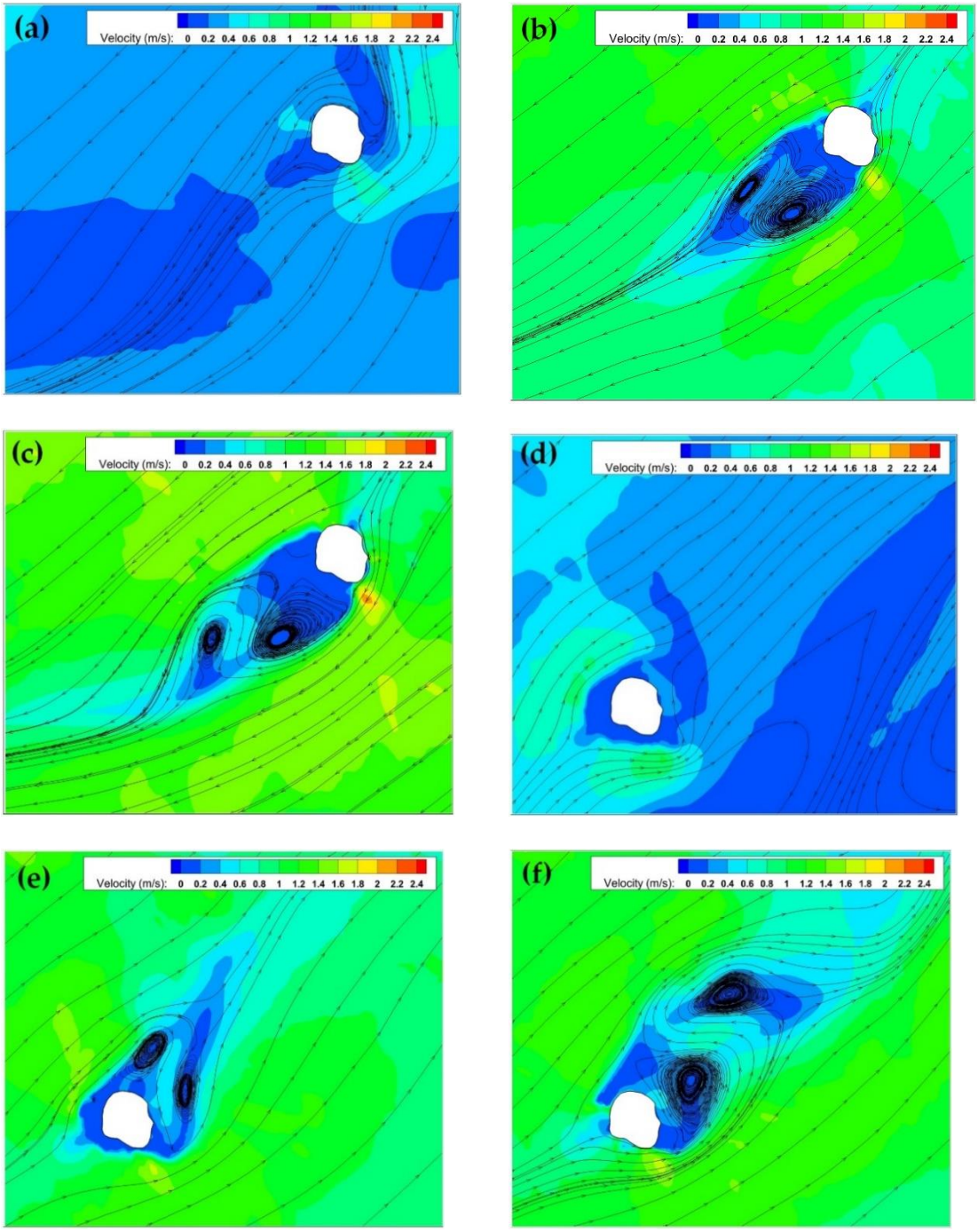

Figure 4.4: Streamlines nearby to Flat Holm Island at date 11/07/2011: (a) High water (slack tide); (b) HW+1.7h (c) HW+3.25h (peak ebb); (d) Low water (slack tide); (e) LW+1.7h; (e) LW+3.25h (peak flood)

To compare the difference in the developing wake between neap and spring tides, an analysis for the wake developing during the spring tide has been undertaken for 5 July 2011 and for a shorter time interval, as shown in Figure 4.5 and Figure 4.6. At the beginning of the ebb spring tide (i.e., Figure 4.5a), no vortex is present in the lee of the island for the relatively low tidal velocities. With an increase in the tidal velocity and a decrease in the water depth, a tidal eddy is generated, which grows in size, as shown in Figure 4.5 b and c and with no eddy shedding occurring. The island wake keeps developing, leading to an unsteady Karman Vortex Street, see Figure 4.5d-f.

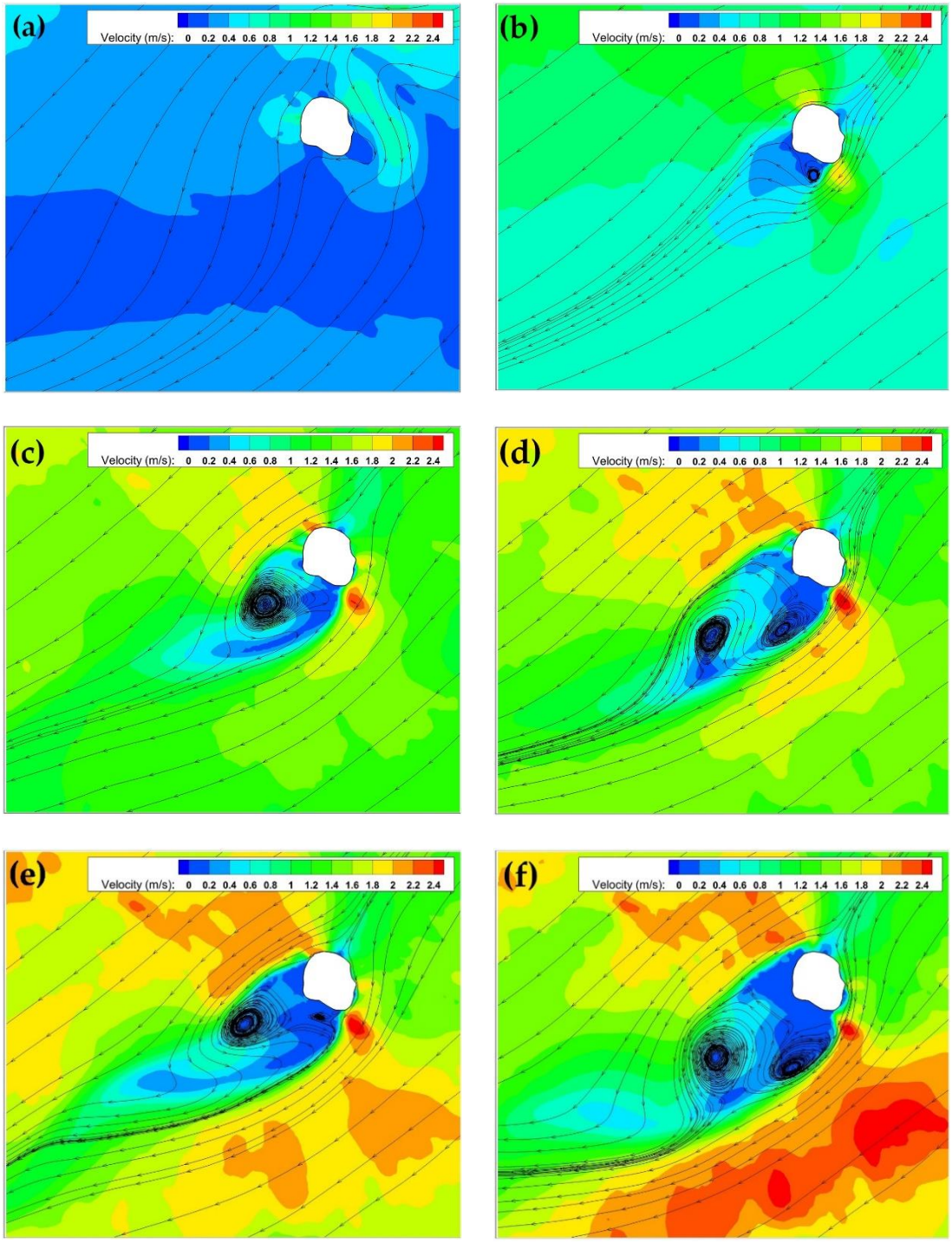

Figure 4.5: Streamlines nearby to Flat Holm Island at date 05/07/2011: (a) High water (slack tide); (b) HW+0.5h (c) HW+1.0h; (d) HW+1.5h (e) HW+2.0h; (e) HW+3.0h (peak ebb).

The wake during the flood phase is somewhat different to the ebb phase, probably due to the higher velocity along with the relatively shallow bathymetry to the south-western side of Flat Holm Island, which can be observed in Figure 4.1. The early stages of wake development during the flood tide is similar to the ebb. One vortex is generated, its size increasing with increasing velocity and water depth (Figure 4.6 b) before a steady wake with two vortices are

generated, no eddy shedding occurring. These two vortices are generally stable with very little migration or increase in size.

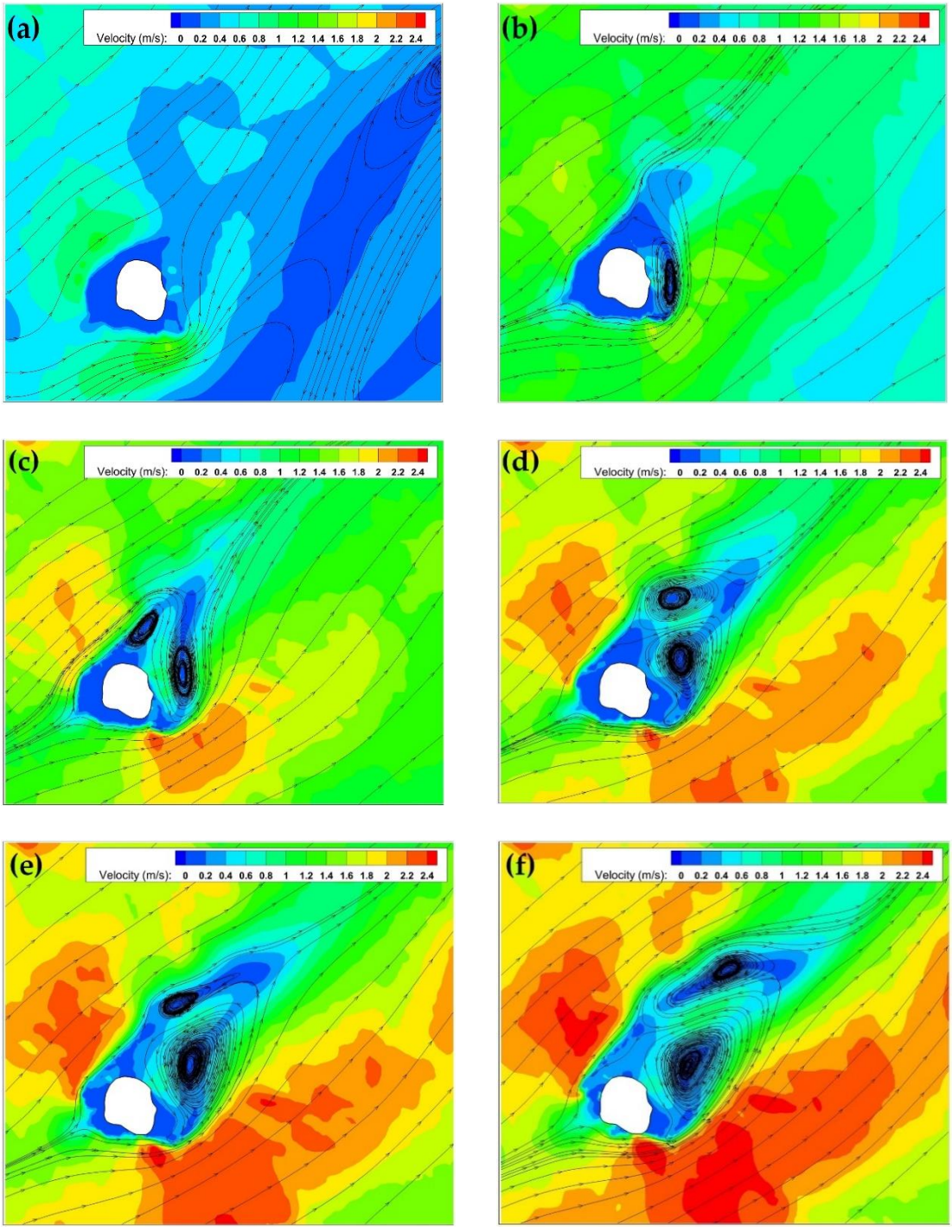

Figure 4.6: Streamlines nearby to Flat Holm Island at date 05/07/2011: (a) Low water (slack tide); (b) LW+0.5h; (c) LW+1.0h; (d) LW+1.5h; (e) LW+2.0h; (e) LW+3.0h (peak flood).

The Reynolds number (*Re*) has been commonly used to describe the characteristics of island wakes, especially in experimental studies, because *Re* is based on the kinematic viscosity of

the fluid and frictional boundary layers, which are generated in the laboratory by friction and boundary layer separation (Tomczak, 1988). However, in real environmental flows, it is the turbulent viscosity which dominates the wake development (Neill and Elliott, 2004), therefore, *Re* is not suitable to quantify the characteristics of wakes since *Re* is based on the kinematic viscosity of the fluid. Subsequently, the wake behind an island in reality is often described by the island wake parameter (Wolanski et al., 1984), namely:

$$P = \frac{U_o h^2}{K_z L}, \tag{4.1}$$

where U_0 is the free stream velocity, h is the water depth, L is the diameter of island, and K_z is the vertical eddy diffusion coefficient. When $P << 1$, friction is dominant and quasi-potential flow results. A relatively stable wake is present when $P \approx 1$. For $P >> 1$, then bottom friction effects are weak, and an unsteady wake is formed, similar to the flow around obstacles at a large Re value in laboratory experiments. For Flat Holm island, the island diameter (L) is about 700 m and kept constant during the rise and fall of tide due to its steep cliff. While the vertical eddy viscosity (K_z) in the Bristol Channel is defined as 0.20 m^2s^{-1} (Neill and Elliott, 2004; Cramp et al., 1991). The free stream velocity U_0 and water depth are taken at 400 m upstream away from Flat Holm Island. The island wake parameter (P) corresponding to different tide condition are calculated, as shown in Table 4.2 and Table 4.3.

Table 4.2: Island wake parameters at a point located northeast of Flat Holm Island during ebb tide.

Figure	Moment	U_o	h	Kz	L	P
Figure 4.5a	HW	0.42	16.2	0.2	700	0.79
Figure 4.5b	HW+0.5	0.51	15.4	0.2	700	0.86
Figure 4.5c	HW+1.0	0.67	14.6	0.2	700	1.02
Figure 4.5d	HW+1.5	0.82	14.1	0.2	700	1.16
Figure 4.5e	HW+2.0	1.05	13.5	0.2	700	1.37
Figure 4.5f	HW+3.0	1.09	13.1	0.2	700	1.34

Table 4.3: Island wake parameters at a point located southwest of Flat Holm Island during flood tide.

Figure	Moment	U_o	h	Kz	L	P
Figure 4.6a	LW	0.62	8.5	0.2	700	0.32
Figure 4.6b	LW+0.5	0.68	9.3	0.2	700	0.42
Figure 4.6c	LW+1.0	0.79	9.9	0.2	700	0.55
Figure 4.6d	LW+1.5	0.95	10.6	0.2	700	0.76
Figure 4.6e	LW+2.0	0.89	11.9	0.2	700	0.90
Figure 4.6f	LW+3.0	1.1	12.4	0.2	700	1.21

The island wake parameter of HW and HW+ 0.5 h are 0.79 and 0.86, respectively, which is between $P << 1$ and $P \approx 1$. This is related to the early stages of wake generation before transforming into a stable wake, which meets the vortex generation process shown in Figure 4.5a-c matches the description of $P \approx 1$, the stable condition. With the increase of P, the wake gradually transforms into an unsteady condition, as illustrated in Figure 4.5e, f.

Figure 4.6 also shows a good correlation to the island wake parameter, with the exception of the early stages of a flood tide (Figure 4.6a) where no wake is generated. Other figures all show a stable wake, with either one vortex or two vortices (Figure 4.6 b-f). The corresponding P varies between 0.42-1.2. Although the P for LW + 0.5h and LW+1h have a relatively low value, the overall revolution of wake meets the prediction of P. These results demonstrate that the island wake parameter was capable of informing on the wake behaviour in the lee of an island located in a macro-tidal environment and could be considered for simulating wakes behind obstacles in similar estuarine and coastal environments.

4.4 Options for Turbulence Model

Modelling turbulence accurately in the region of interest is challenging due to the rapid transform of the tidal flow and the complex turbulence-generating bathymetric features. Various methodologies using different levels of complexity can be used to simulate the turbulence levels and structure observed in the field. Four different turbulence schemes are included in TELEMAC-2D, and they were all assessed to identify the most appropriate scheme to simulate wakes in the lee of islands in a macro-tidal estuary.

In order to compare the behaviour of different turbulence models, four TELEMAC-2D models with different turbulence models have been compared. The MAE and RMAE parameters have been calculated by comparing the measured ADCP data and the prediction data to give the averaged values (Table 4.4). The results highlight the impact of the different turbulence models on the hydrodynamic model performance. Generally, the RMAE are all smaller than 0.4, which in reference to the Qualification of RMAE (In section 3.2.2) this means that all the prediction data with turbulence models have a 'good' correlation with measured data and therefore are suitable for predicting the flow patterns in the wake of an island in a macro-tidal estuary. However, the k-ε model showed the smallest MAE and RMAE, which indicates that is the most accurate turbulence model in this case.

Table 4.4: The statistical data of different turbulence schemes

Scenario	Turbulence model	MAE	RMAE
1	Constant viscosity model	0.3744	0.3672
2	Elder model	0.3950	0.3705
3	k-epsilon model	0.3597	0.3266
4	Smagorinsky model	0.3735	0.3708

Emphasis was then focused on studying the k-ε model for simulating the wake behind Flat Holm Island. The turbulence model equations were solved by the fractional step method, with advection of the turbulence variables: k (turbulent kinetic energy) and ε (turbulent dissipation) being processed at the same time as the hydrodynamic variables, and the other terms relating to the diffusion and production/dissipation of the turbulent parameters being processed in a single step.

The solver used for simulations in the turbulence model has several different options (Table 4.5). The key solvers include the conjugate gradient method and its derivation method and the generalised minimum residual method (GMRES). The conjugate gradient method is the most prominent iterative method for solving sparse systems of linear equations (Shewchuk, 1994). It is an algorithm for finding the nearest local minimum of a function of n variables, which presupposes that the gradient of the function can be computed. The GMRES method is especially useful for poor conditional systems. Furthermore, the Biconjugate Stabilized Gradient method (BICGSTAB) also shows a good performance.

The performances of each solver in predicting the wake behind the island are summarized (Table 4.5 and Figure 4.7). All *k-ε* solvers showed good results, while the conjugate residual showed the smallest MAE and RMAE and subsequently the slightly better performance in simulating the wake flows in the lee of Flat Holm island. Therefore, the conjugate residual solver was used throughout the remainder of this study.

Table 4.5: MAE and RMAE for different k-ε model solvers

Scenario	Solver in TELEMAC-2D model with k-epsilon turbulence model	MAE	RMAE
1	Conjugate Gradient	0.3597	0.3266
2	Conjugate Residual	0.3420	0.3129
3	Conjugate Gradient on Normal Equation	0.3556	0.3254
4	Minimum Error	0.3625	0.3298
5	Squared Conjugate Gradient	0.3607	0.3274
6	BICGSTAB (Biconjugate Stabilized Gradient)	0.3535	0.3231
7	GMRES (Generalised Minimum Residual)	0.3544	0.3251

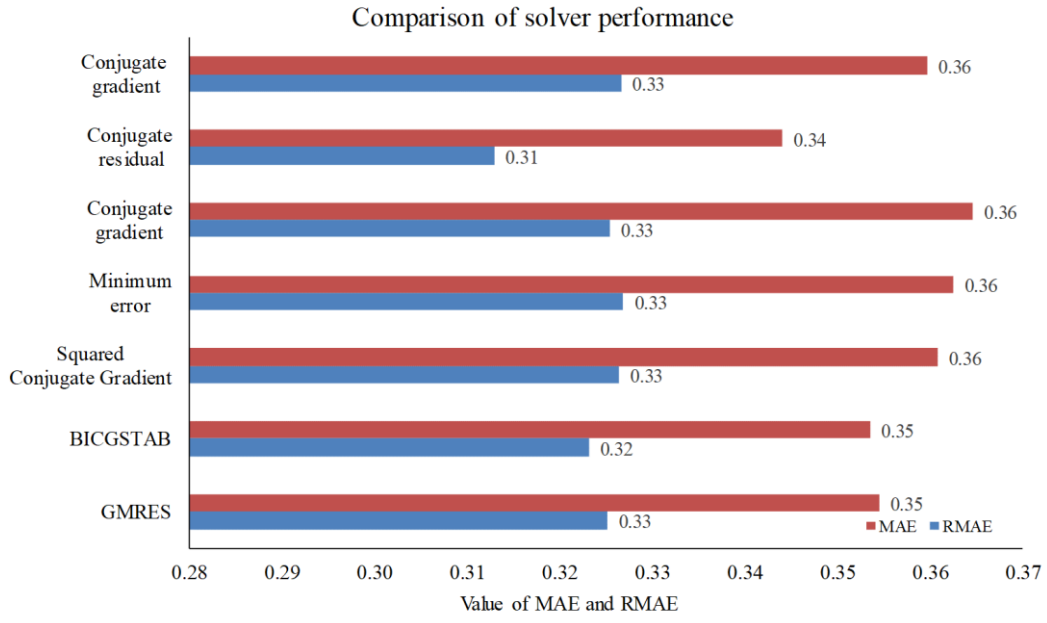

Figure 4.7: The comparison of different solvers in k-epsilon model.

4.5 Summary

This chapter studied the wake developed in the lee of an island in a macro-tidal estuary, namely Flat Holm Island, located in Severn Estuary and Bristol channel. Field surveys were undertaken with vessel-mounted ADCP data being acquired specifically around the island and for different tidal conditions to validate and improve the model predictions.

The simulation results show that the wake development is symmetrical at two sides of the island in the neap tide, that two steady vortices appear in the wake with the increase of the tide velocity, changing into stable Karman vortex street around the peak tide moment. The model results also confirm the applicability of the island wake parameter in predicting wake behaviour behind an island located in a macro-tidal estuarine environment; therefore, similar approaches could be considered for simulating wakes behind obstacles in similar estuarine and coastal environments.

Four different turbulence models were tested and compared to acquire better model predictions, including a constant eddy viscosity model, an Elder model, a *k-ε* model, and a Smagorinsky model. The k-ε model showed the best performance compared with the field measurements and was chosen for this study. Furthermore, six different methods to solve the k-ε model equation were considered and compared. All models showed good predictions compared to the field measurements around the island, while the best results were acquired by using the conjugate residual. The conjugate residual solver was selected and then used in this study. Thus, the classic k- ε model with the solver of conjugate residual will be implanted into further lagoon modelling.

Chapter 5 Lagoon Modelling

This chapter describes the methodology for numerical modelling of tidal lagoon and introduces three application cases. Section 5.1 discusses the parameterisation of lagoon structure components and the operational sequence in numerical models. The modelling methods will be tested and validated through an idealised tidal lagoon model and taken forward for use in the coastal TRS application. Section 5.2, 5.3 and 5.4 introduces the modelling of the three lastest lagoon proposals in the UK, which are West Somerset Lagoon (WSL), Swansea Bay Lagoon (SBL) and North Wales Tidal Lagoon (NWTL). The detailed description of projects, model set up, operation scheme and energy output of each case are presented. This section also discusses the adoption of a full momentum conservation approach in modelling the flow through the turbines in the lagoon and the impact of different velocity profiles at the turbine outlets. Finally, Section 5.5 provides a summary of this chapter.

5.1 Implementations of Lagoons and Operations

5.1.1 Idealised Lagoon Model

The reliability of TRS model is associated with the numerical representation of its hydraulic structures (Bray et al., 2016). To achieve this, a wide range of multi-scale processes is needed either by directly simulation or by approximative modelling methods. However, with present computational capabilities, a formally complete and accurate model (e.g. via direct numerical simulation) of all these hydraulic structures and processes is less realistic (Neill et al., 2018). Thus, approximative modelling methods of TRS are employed to achieve the appropriate levels of accuracy.

To explore the optimal numerical representation of the tidal lagoon components at a relatively low computational cost, an idealised lagoon model (or test model), a simplified representation of a lagoon system, was used to demonstrate the modelling methods of the lagoon components and the operational processes (Schnabl et al., 2019). The idealised model is shown in the form of a simplified channel model in Figure 5.1, with a length of 2400 m and width of 1200 m. The lagoon basin is in a square shape with a length of 380 m, located at the opposite side of the open boundary. Uniform bathymetry is adopted for the whole domain of the idealised channel

model, and a typical semi-diurnal sea water level change was applied as the open boundary condition.

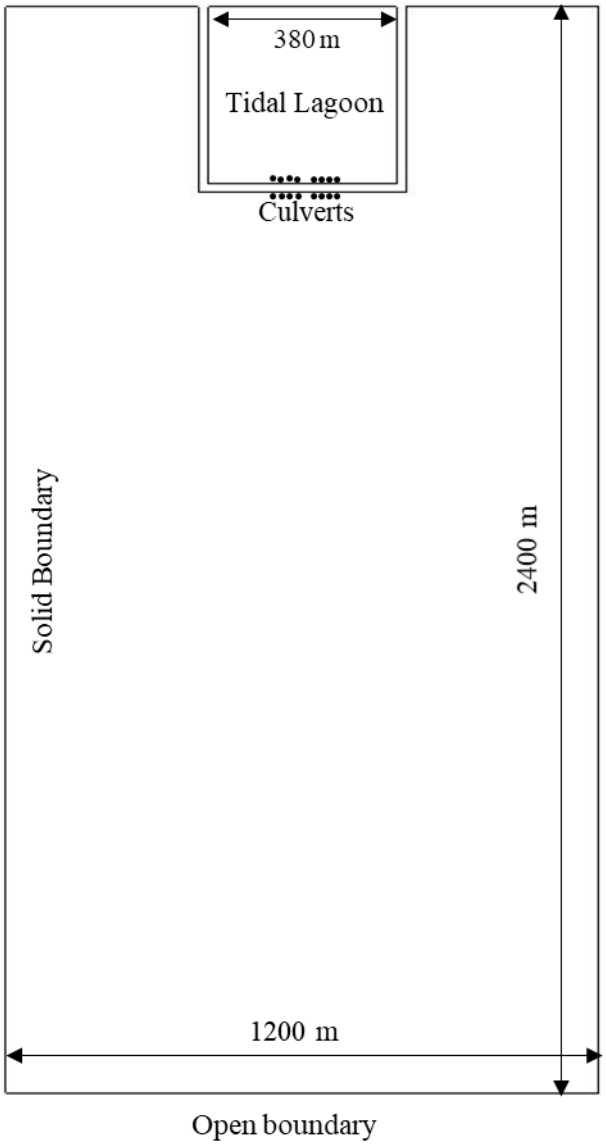

Figure 5.1: The outline and dimension of the idealised lagoon model.

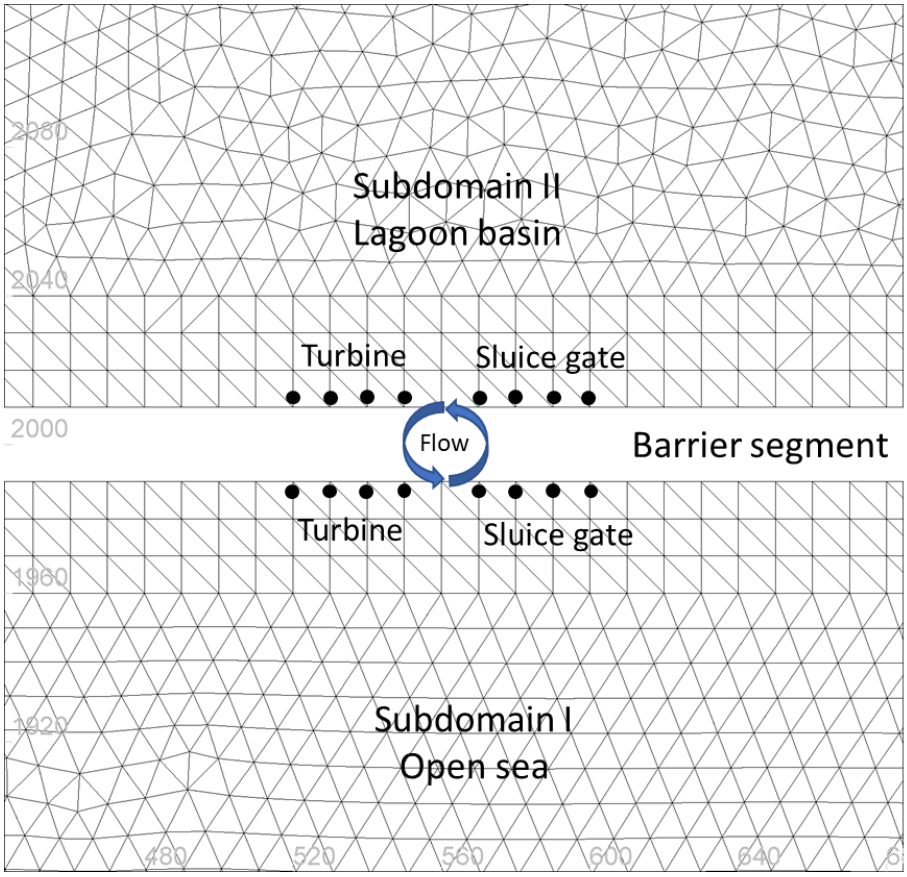

Figure 5.2: Internal barrier and the turbine and sluice gate points.

An internal barrier connects the node pairs between subdomain I and subdomain II, as shown in Figure 5.2. Eight node pairs were selected as culvert points to simulate turbine and sluice gates; the dimension and Hill chart applied on turbine/sluice gates have been adjusted according to the model scale. The numerical representation of lagoon components and operation schemes were investigated in this test model to achieve a suitable numerical method. For example, two different numerical methods for modelling embankments were applied and compared.

A two-way operation scheme with a start-head equal to 2.5 m and an end-head of 1.5 m were implanted into the control system. It can be seen from Figure 5.3(a) and (b) that the idealised lagoon model works well with each stage of two-way generation clearly presented. The water volume change in the lagoon domain is consistent with the sum of the initial water volume and the water volume transferred through turbines and sluice gates, as shown in Figure 5.3(c), confirming the mass conservative of water transferred across the barrier. The typical instantaneous flow structure during the turbine operation is plotted in Figure 5.4, where the strong flow jet through the turbine and the formation of eddies is observed.

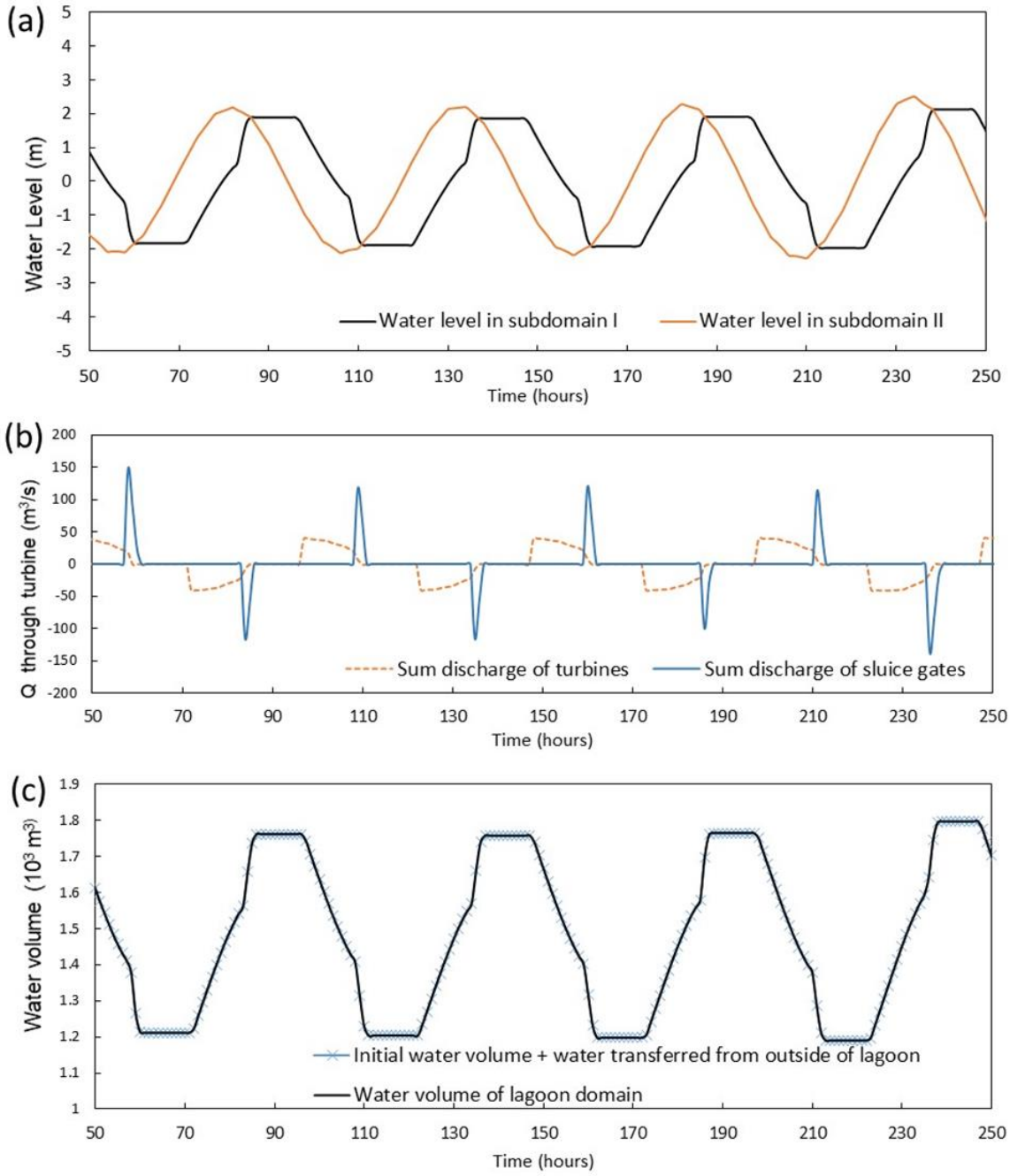

Figure 5.3: (a) the water level change in subdomain I and II; (b) the discharge of turbines and sluice gates; (c) the water volume change inside of lagoon basin.

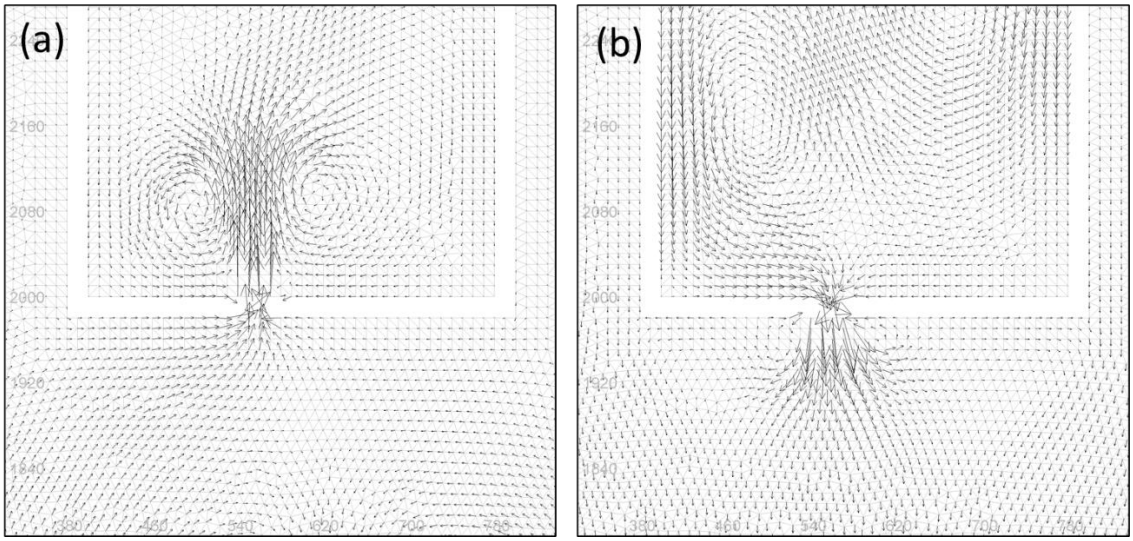

Figure 5.4: The flow structure during the operation of the idealised lagoon during (a) flooding generation; (b) ebb generation.

5.1.2 Operation Schemes

A single-basin structure lagoon can be designed to operate under different modes, considering the regional tidal features, environmental concerns, national grid power absorption abilities and cost controls (Angeloudis and Falconer, 2017). Basic operation schemes include one-way generation and two-way generation; one-way generation could be further divided into ebb generation and flood generation depending on the direction of the turbine inlet. Both one-way and two-way generation could be augmented by a pumping function in which the turbines work to pump water from the low-water-level side to the higher-water-level side. More recently, an optimised operation scheme has been studied by adopting a flexible generation head in each tidal cycle, which potentially could fully utilise the tidal range energy (Neill et al., 2018). Overall, a good operation scheme should make a trade-off between electricity generation and environmental impacts.

5.1.2.1 One-way Generation

One-way generation creates electricity only at either ebb or flood tide, twice a day in a semi-diurnal tidal environment. It has a relatively simple turbine structure and lower cost (Waters and Aggidis, 2016a). One-way generation is currently one of the most commonly used schemes in tidal range energy projects, such as the La Rance barrage in France (Rourke et al., 2010) and the Sihwa tidal barrage in South Korea (Bae et al., 2010).

Ebb generation, for example, generates electricity only when the direction of flow through the working turbine is the same as that of the ebb tide, usually from the tidal lagoon (basin) towards the ocean (Baker, 1991). As illustrated in Figure 5.5, the lagoon impoundment area is filled through sluice gates as the water level rises until the water level is equal between two sides, at which point the sluice gates are then closed. The holding stage starts when the sea level falls on the outside while a high water level remains inside. When a sufficient head difference for power generation is achieved, the generation stage begins with turbines operating until the water head drops to the minimum head needed for generation. Then, another holding stage is implemented to prevent the inside water level from falling. The sluice gates are reopened and the ebb generation process is repeated for the next tidal cycle when the downstream water level begins to rise again with the tide.

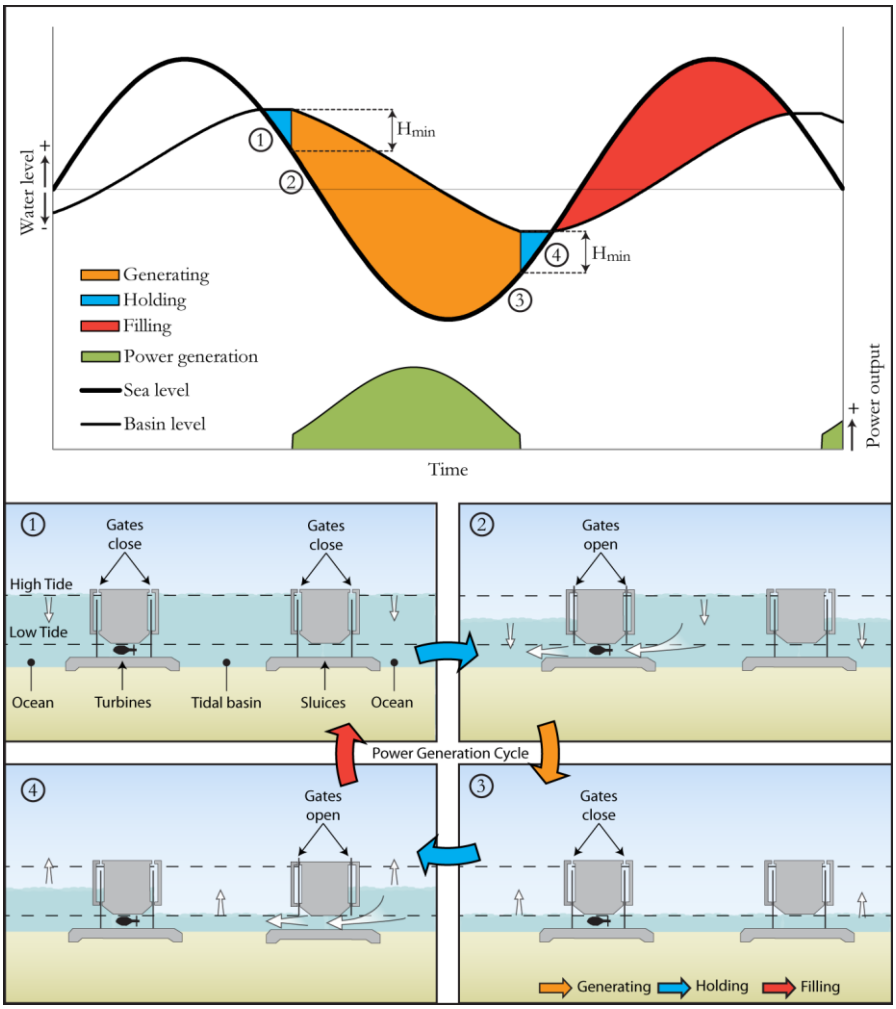

Figure 5.5: Diagram of ebb generation (Cousineau, 2011).

Flood generation is achieved through a process reversed from ebb generation, generating power only during the flood tide. Water is held in the basin during ebb generation, whereas it is

released from the basin during flood generation. However, the different volumes of impounded water in flood and ebb generation result in different decreasing ratios of water level difference and thus result in different power generating efficiencies (Baker, 1991). Compared with ebb or two-way generation, flood generation is regarded as a less efficient method. This is because the lower part of the basin contains less water volume than the higher part due to the bathymetric feature of the lagoon basin, meaning that there is less available water volume for flood generation compared to ebb generation with the same operation head (Waters and Aggidis, 2016a). Moreover, the higher resistance in the impoundment bed also causes a less water flow volume. Furthermore, the environmental impact differs between flood and ebb generation, as flood generation can cause a larger reduction in the maximum water levels inside the water impoundment area than an ebb generation (Xia et al., 2010b).

5.1.2.2 Two-way Generation

A two-way operation scheme generates power at both ebb and flood tides, so the lagoon is able to generate electricity four times in a marine environment with semi-diurnal tides. However, this operation method and the turbine used are more complex and costly than a one-way generation, as they need to be optimised for both directions (Waters and Aggidis, 2016a).

When the tide starts dropping from its highest point, the turbine and sluice gate will remain closed to generate a head difference across the lagoon, as shown in Figure 5.6. This is the holding phase at high tide. The turbines operate and power generation mode starts once the starting head difference is reached. During ebb generation, the water level inside the lagoon drops until the generation head is below the ending head difference. Then, the turbines will stop operating and remain idle. The sluice gates will remain open to empty the water in the lagoon as quickly as possible. When the water levels on both sides are equal, the turbines and sluice gates will be closed. The lagoon is now in another holding phase (low tide), maintaining the minimum water level inside the lagoon. At last, when the generation start head difference is achieved, flood generation will commence. This is similar to the ebb generation but in the opposite direction.

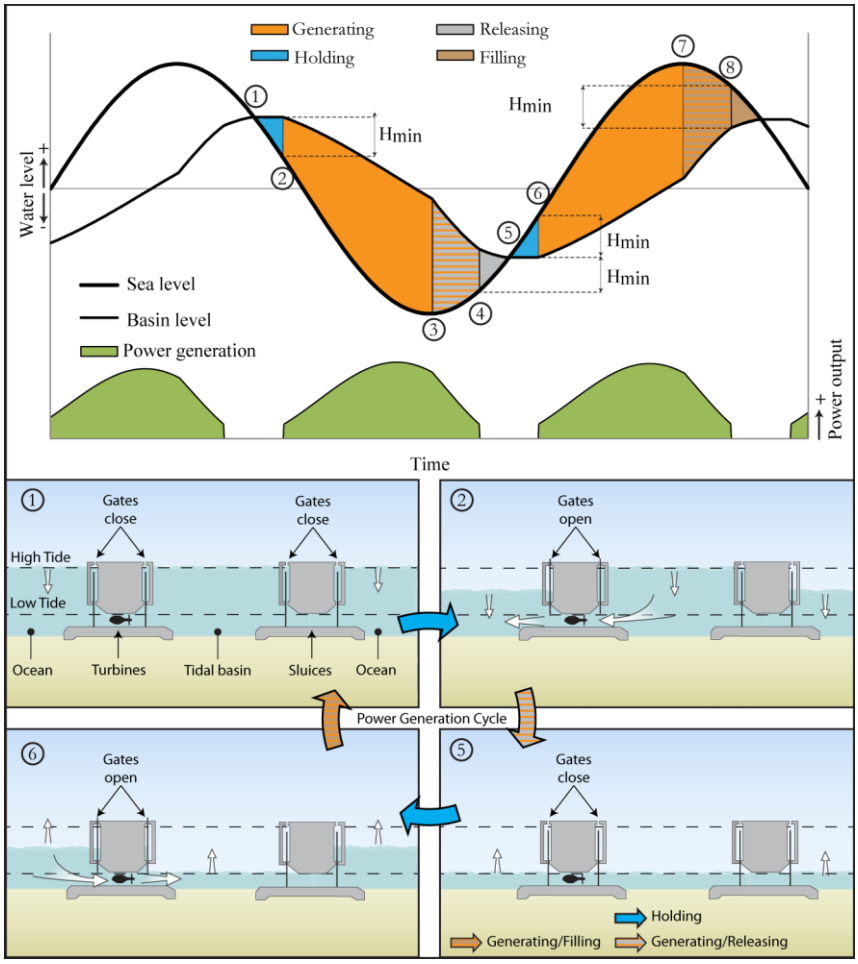

Figure 5.6: Diagram of two-way generation of tidal lagoons (Cousineau et al., 2012).

Although a lagoon with two-way generation may have higher costs due to the complex turbine installation, a two-way generation scheme generates more electricity than one-way generation. Furthermore, the electricity generated by a two-way operation scheme is easier to import into the power grid due to its more evenly distributed electricity generation (Baker, 1991). The tidal range within the water impoundment is much closer to the natural sea level range; therefore, two-way generation is generally regarded as being more acceptable in terms of minimising environmental changes (Xia et al., 2010b).

5.1.2.3 Pumping Function

Bulb turbines can be used to pump water from the lower-water-level side to the higher-water-level side by consuming electricity. A significant increase in energy production is expected with pumping function, although it also costs energy. It is learned from Equation (2.3), the potential energy output from a TRS is based on the square of the vertical water level difference between the lagoon and the sea, so any increase in this figure provides a significant increase in

energy production (Waters and Aggidis, 2016a). Another advantage of pumping is to enable load-following and dispatchable electricity generation for a TRS (Neill et al., 2018). It has the potential capacity to fill or empty the basin storage using excess off-peak grid power and turn to generation when the electricity demand is high. With an optimised operation method, the pumping function can contribute to grid power stability and increase revenue by selling more electricity during periods of peak demand, when electricity prices are highest (Mackie et al., 2020).

5.1.2.4 Flexible Generation and 0D model

The previously discussed operation schemes are based on fixed values of the operational water head, assuming that the turbine starting head and ending head are constant through the neap tide and spring tide cycle. However, because of the difference in tidal ranges through the spring and neap tide cycle, an operation scheme with a fixed head is unable to adapt to the tidal range changes and therefore cannot fully utilise the potential tidal range energy (Yates and Tatlock, 2017). For example, there is low or no power output during neap cycles if the fixed operation head could not reach the prescribed starting or ending operation heads.

Compared with conventional fixed head generation schemes, flexible operation is implemented with variable operational water heads, which can be optimised to take the fluctuating maximum and minimum sea levels for the tidal cycle into consideration, achieving the maximum total energy output. The pumping function could be further added to increase energy generation.

The optimised operation scheme applied in this research was achieved from 0D model and genetic algorithm model developed by Xue et al. (2020). The 0D model used the method of a backward-difference numerical model, developed based on the continuity equation (Neill et al., 2018). Given the water level downstream Z_{dn}^{i} and upstream Z_{up}^{i} time step i^{th}, the upstream water level Z_{up}^{i+1} at time step $(i+1)^{th}$ was calculated as:

$$Z_{up}^{i+1} = Z_{up}^{i} + \frac{Q(H)+Q_{in}}{A(t)}\Delta t, \tag{5.1}$$

where *A(t)* is the wetted surface area of the lagoon for Z_{up}^{i}. Q_{in} is the sum of inflows/outflows through sources/sinks other than the TRS basin, e.g. river discharges or outflows. The water head difference *H* is calculated as $Z_{up}^{i}-Z_{dn}^{i}$, and feeds into *Q(H)*, which is a function to decide the total discharge contributions from turbines and sluice gates. Hill chart (Petley and Aggidis,

2016) is used to determine the discharge from electricity generating turbine; for the flow through a sluice gate, the flow Q is calculated as:

$$Q = C_d A\sqrt{2gh}. \quad (5.2)$$

Then genetic algorithm model was coupled with 0D model to identify an operation scheme that will result in maximum generated electricity (Xue et al., 2019b). An operation scheme including the starting and ending heads for every half-tide was regarded as an individual with different genes in genetic algorithm. A population of solutions/individuals is used in the genetic algorithm method, which update iteratively, with each iteration of solutions was referred to as a generation in the genetic algorithm model. The pseudocode of the genetic algorithm model is shown in Table 5.1.

Table 5.1: Pseudocode of the genetic algorithm (Xue et al., 2020).

The pseudocode of the genetic algorithm	
1:	proc Set_up//Set up algorithms parameters
2:	Generate the initial operation schemes and evaluate their fitness;
3:	While NOT **Termination_criterion** ( ) do
4:	Offspring < - **Copy** (Parents);
5:	Offspring < - **Mutation** (Pm, Offspring);
6:	Offspring < - **Recombination** (Pr, Offspring);
7:	**Evaluate_Fitness** (Offspring);
8:	Survivals < - **Selection** (Ps, Parents, Offspring);
9:	Parents < - Survivals;
10:	End While
11:	End Proc Set_up;

The study of Xue et al. (2020) results showed that the genetic algorithm model generates more than 16% of energy when compared with a fixed-head model. Considering that there is no extra cost for equipment and construction, an optimised flexible operation scheme has a large advantage compared with traditional fixed head generation.

5.1.3 Turbine and Sluice Gate

Prevailing technology and research have suggested that low head bulb turbines might be the most appropriate turbine for TRSs due to their high efficiency over a wide range of flows and water heads (Hendry, 2016; Waters and Aggidis, 2016a). One of the most widely-used bulb turbines was based on the Andritz Hydro model, which has been deployed in TRSs such as the La Rance, Annapolis and Sihwa tidal range plants (Hendry, 2016). It is also the potential

turbine for the proposed Swansea Bay Lagoon and other planned UK TRSs. Following the proposal of Swansea Bay Lagoon, a bi-directional bulb turbine manufactured by Andritz Hydro was used in this study. The structure of a typical bulb turbine is shown in Figure 5.7.

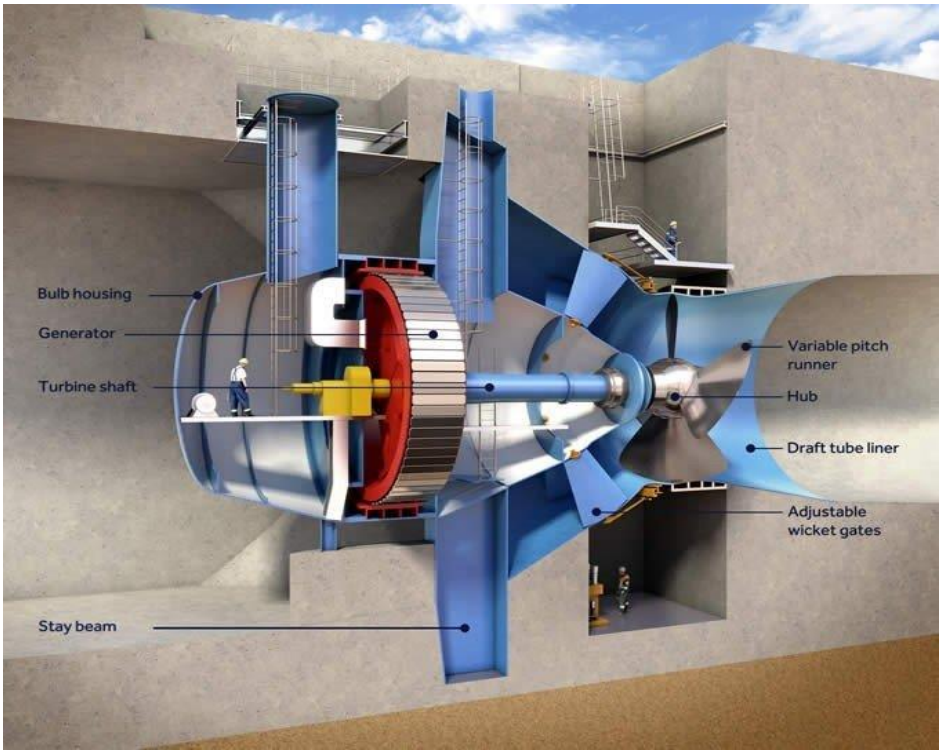

Figure 5.7: The key elements of a conventional hydro double regulated bulb turbine (Tidal Lagoon Plc, 2013).

A Hill chart shows the relationship between power output and water head difference of the bulb turbine, along with the discharge, and is usually provided by the manufacturer. However, it has been difficult to acquire a specific Hill chart, particularly the most recent triple regulated turbines due to commercial confidentiality. Publicly available Hill charts have been used in most studies instead (Xia et al., 2010b; Baker, 1991; Angeloudis and Falconer, 2017). In the current study, a typical Hill chart corresponding to the Andritz Hydro bulb turbine was therefore used, as shown in Figure 5.8 and Figure 5.9 (Aggidis and Feather, 2012; Xue et al., 2020).

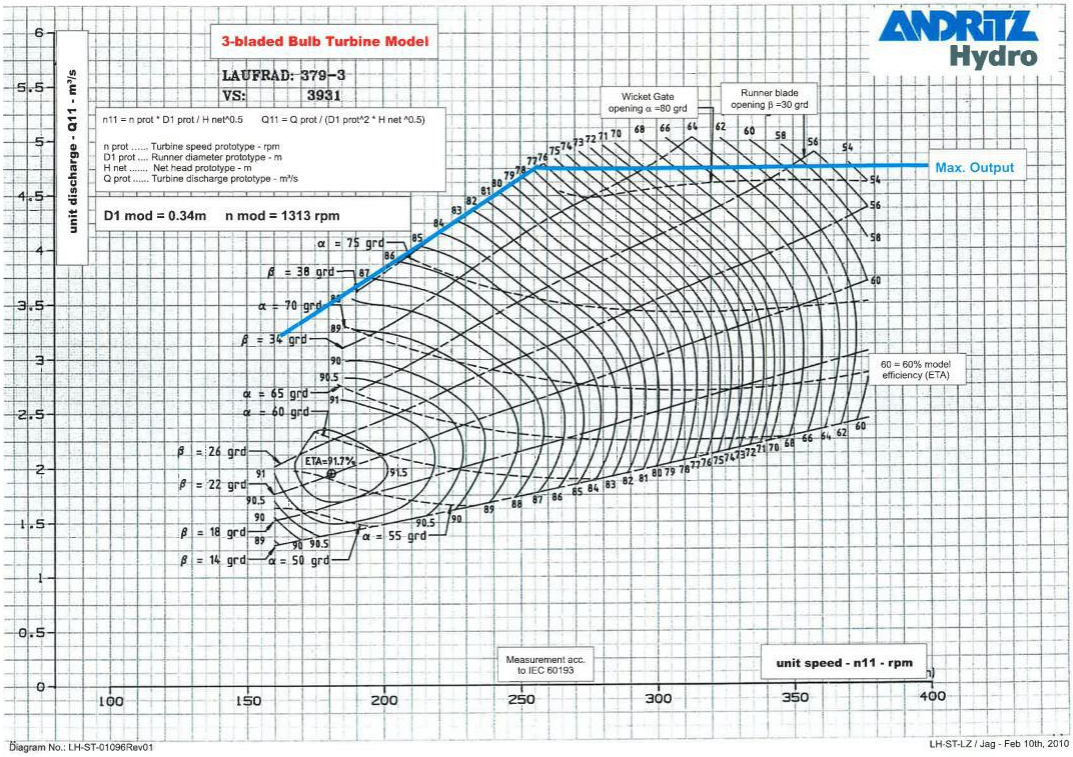

Figure 5.8: Q-H relationships of a typical Andritz Hydro Hill chart for a double-regulated bulb turbine (Aggidis and Feather, 2012).

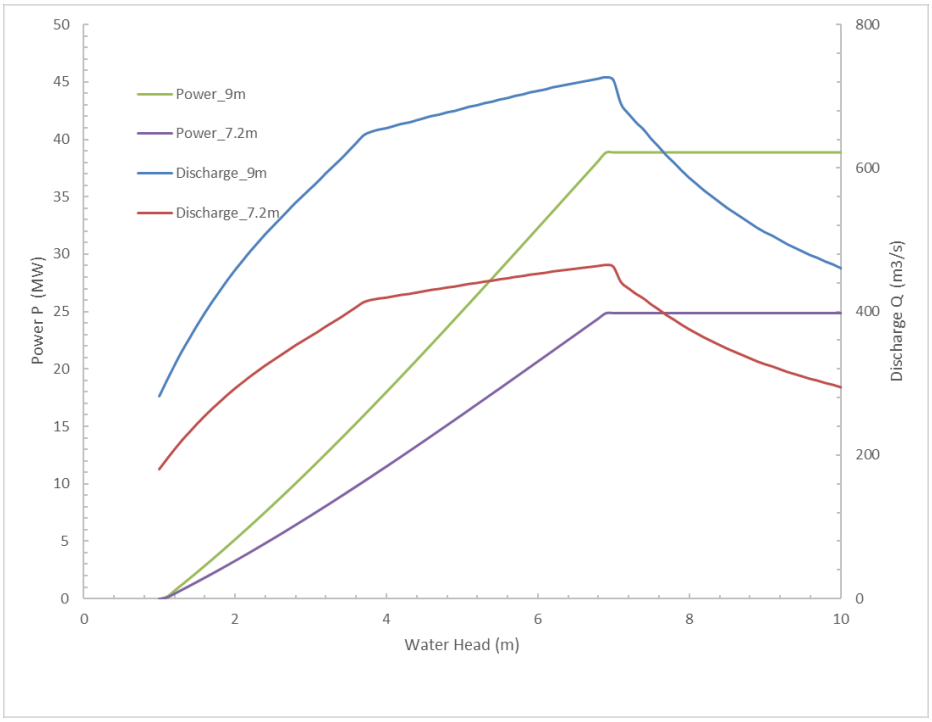

Figure 5.9: Turbine Q-H and P-H comparison for the diameters of 7.2 m and 9 m, respectively (Xue, 2021).

Moreover, a bulb turbine can also be used as a pump to draw water from the lower-water-level side to the higher-water-level side. In this condition, the turbine pump efficiency can be calculated as:

$$\eta_t = \frac{P_{output}}{P_{potential}}, \tag{5.3}$$

$$\eta_\rho = \frac{P_{potential}}{P_{input}}, \tag{5.4}$$

where η_t is the turbine efficiency and η_ρ is the pumping efficiency. The turbine efficiency and pumping efficiency used in this study, following the work of Xue et al. (2019a), is shown in Figure 5.10.

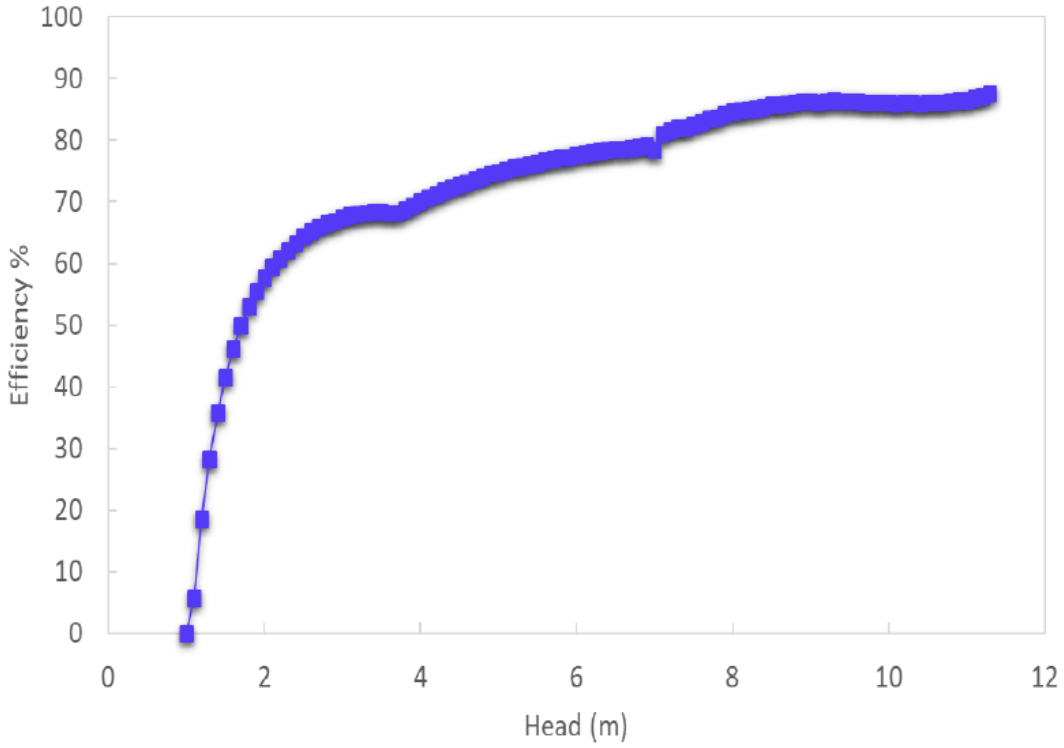

Figure 5.10: Turbine efficiency (Xue et al., 2019a).

The purpose of a sluice gate is to accelerate the filling or emptying phase of a TRS to achieve the highest water head difference between the two sides, thereby increasing the efficiency of tidal power generation (Bray et al., 2016). Meanwhile, a reasonable distribution of sluice gates could contribute to a shorter water retention time in the lagoon basin, benefiting the water quality. A typical design of a sluice gate is shown in Figure 5.11.

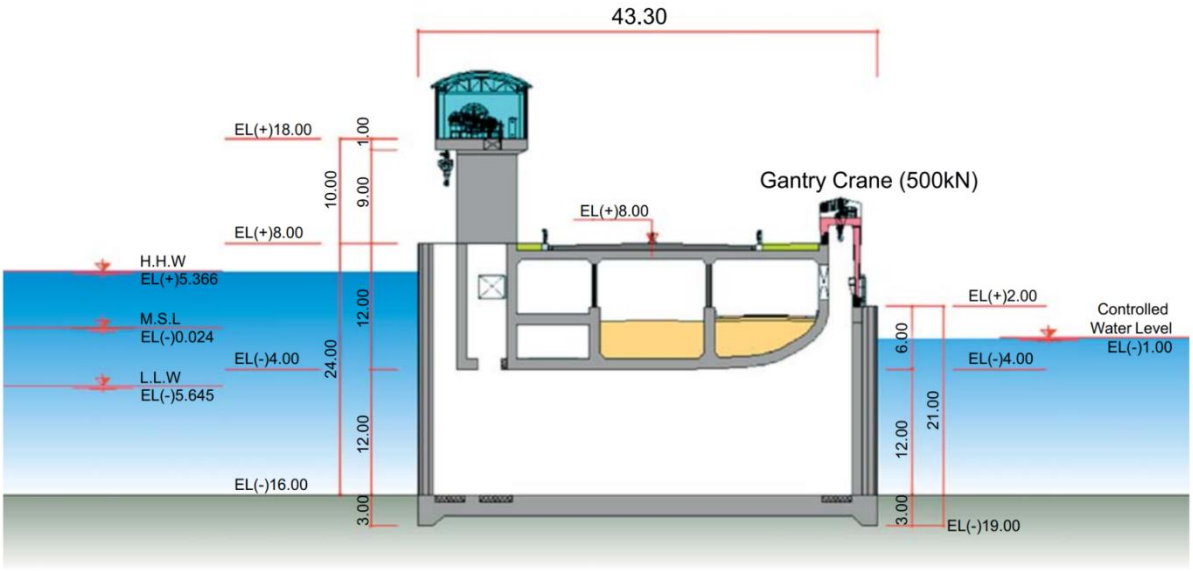

Figure 5.11: Cross-section of a sluice caisson proposed for the Lake Sihwa tidal power plant (Bae et al., 2010)

Two ways to represent sluice gates were used in the past; the first method involved modifying the bed-level of required mesh elements (Carroll et al., 2009). The open condition of the sluice gates was presented as a gap with a pre-set time and gap length. The closed condition of the sluice gates was the same as that of an embankment. The second method utilises a similar method with turbine simulation that flow-controlled culverts represented sluice gates. Although the first method could easily introduce sluice gates into the lagoon, it was more difficult to control the discharge and simulate the progress between opening and closing. Therefore, the latter method was adopted by this study, in which sluice gates were represented as a series of water sources on two sides of the embankment with discharge calculated by an orifice equation (Falconer et al., 2009; Angeloudis et al., 2016a):

$$Q_s = \theta A_s \sqrt{2gH}, \tag{5.5}$$

where Q_S is the flow rate through the sluice gate, θ is the discharge coefficient, A_S is the flow area through the sluice structure, g is the gravitational acceleration and H is the head difference across the structure. The discharge coefficient is a dimensionless factor that is used to reflect the efficiency of the sluice gates. Bray et al. (2016) have tested the sensitivity of the TRS performance to the discharge coefficient and found that the changes in θ have little impact on the performance of TRSs. Thus, the value of θ is taken as 1 in the current study.

5.1.4 Embankments

The highest cost of a TRS is the civil engineering work for the embankment (Hendry, 2016). The embankment of the lagoon consists of cofferdam or caisson structures designed to form the tidal impoundment area (Neill et al., 2018). It should have low permeability (leakage rate) to impound the water from the tide and high structural strength to dissipate wave attack and to protect its structural and functional integrity. Last, it houses the turbines, and sluice gates that are permanently submerged (Bray, 2017).

There are two numerical modelling methods for embankment modelling: the domain decomposition method (Xia et al., 2010a; Čož et al., 2019; Schnabl et al., 2019; Ma and Adcock, 2020) and the bed-level rise method (Carroll et al., 2009). The first method divided the model domain into two subdomains or even more, upstream and downstream of the embankment. The lagoon domain was separated from the main domain and the embankment was represented as an internal barrier, as shown in Figure 5.12(a). In this method, the 'embankments' were impermeable and were treated similarly to other solid boundaries.

The latter method represents the lagoon embankment as a bathymetric feature. In this setting, the bathymetry at the embankment location was raised to the real height of the lagoon embankment with no other special treatment applied. With fine mesh resolution, the slope of the sides of the embankment could be simulated. Dry cells could be introduced at the upper level of the embankment face when the water level drops with the ebb tide, which would become wet again when the water level rises. Although the top of the embankment is designed to avoid submergence, overtopping and embankment failure could be modelled with this setting if needed.

The above two embankment modelling methods were introduced into the idealised lagoon model to determine their advantages and disadvantages. The model mesh in Figure 5.12(a) separate the lagoon domain utilising the domain decomposition method with a barrier width of 10 m, while the bathymetry of the embankment area has increased to 8 m in Figure 5.12(b). Culverts are located at two sides of the embankment and open when a specific water head difference is reached.

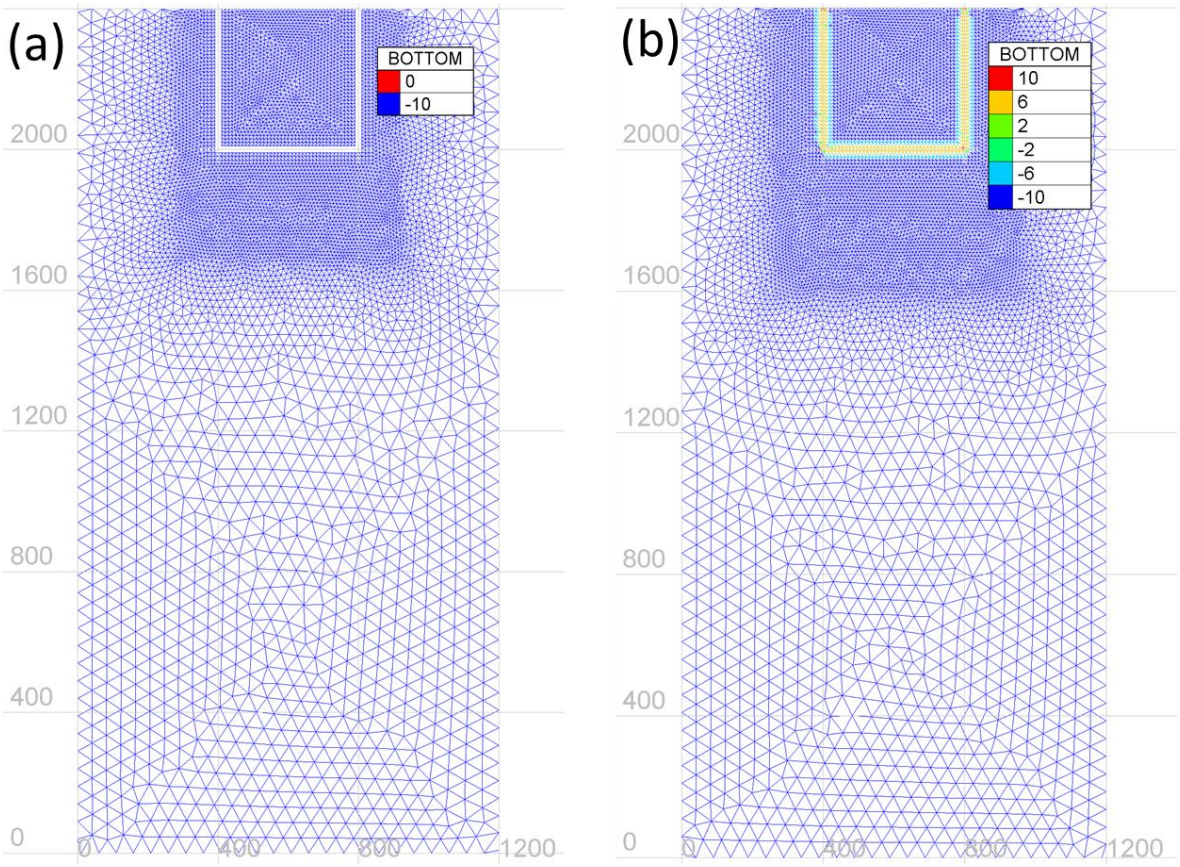

Figure 5.12: The mesh of the lagoon test model with (a) domain decomposition method; (b) bed-level rise method.

Modelling results show that the water levels evolutions are the same between the two models during the culvert operation, indicating the mass conservative of water transfer during the culvert operation. The water jet for the filling phase and the emptying phase of the two lagoon test models are compared in Figure 5.13. It is observed that the velocity of the water jet in Figure 5.13(a) is slightly higher than in Figure 5.13(b), but the size and the direction of the water jet are much the same. Slight differences could be found in the flow patterns around the main water jet in each setting, which has a restricted influence on the lagoon modelling results. Nevertheless, it is concluded that both methods were appropriate for embankment modelling.

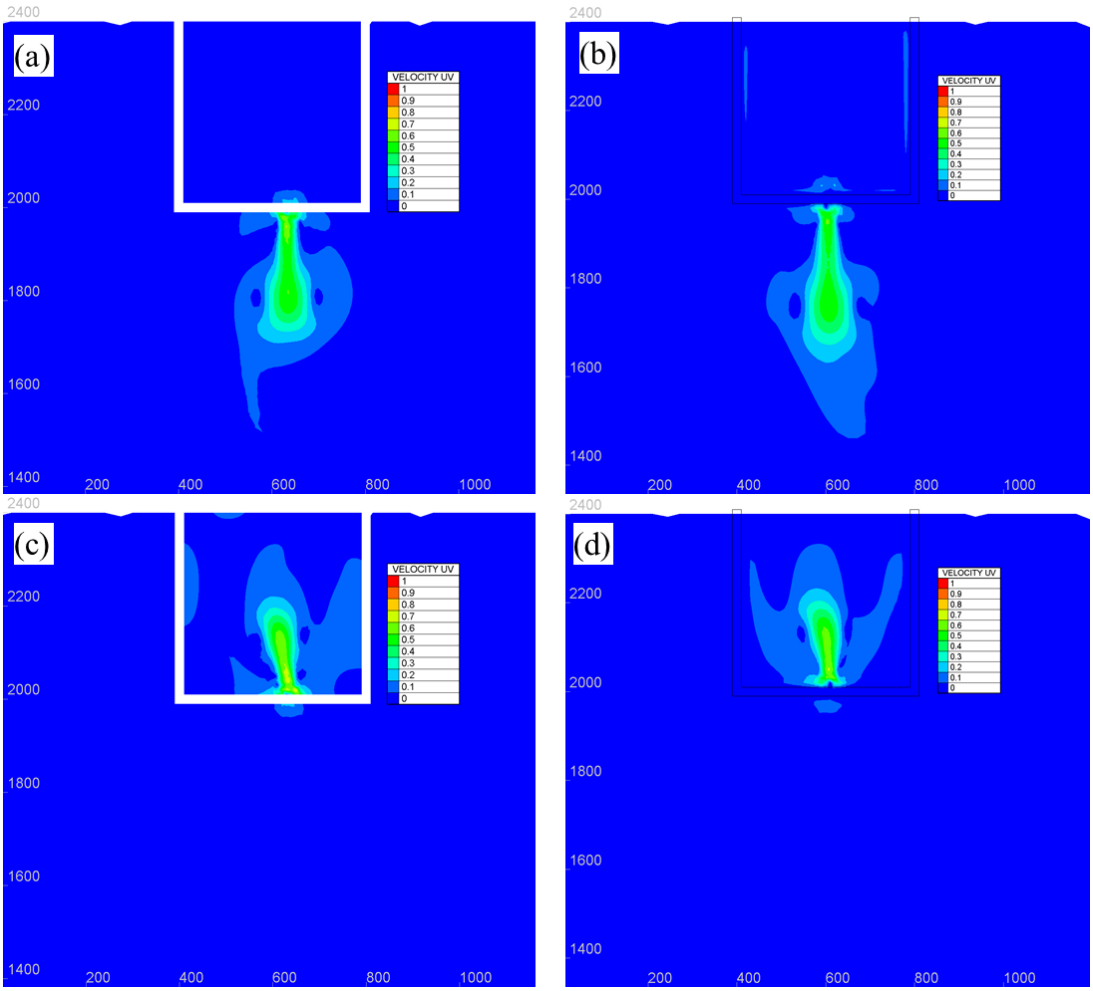

Figure 5.13: The water jets through the turbines in the idealised models with (a) (c) mesh with domain decomposition method; (b) (d) mesh with bed-rise method.

However, it was found that the mesh with the bed-rise embankment might cause some numerical problems during the modelling. For instance, the slope at two sides of the bed-rise embankment could cause issues of unrealistic high velocity and an over-threshold Courant number. Furthermore, insufficient spatial discretisation around the bed-rise embankment might cause parasitic overflows (water present on the crest of the embankment while the surrounding elements are still dry) over some elements with the bed-rise elevation. In this case, a specific treatment algorithm should be implemented to avoid parasitic overflows, increasing the complexity of the model settings. Therefore, the domain decomposition method was applied in the following study to maintain simplicity and computational efficiency while prioritising accuracy.

5.1.5 Other Lagoon Modelling Setups

5.1.5.1 Water Level Representation

The operation of a TRS primarily depends on the head difference between the two sides of the embankment, which is measured at a location near the turbine. However, it was found in the TRS numerical simulation that the vast volume of water and the water jet could cause water level oscillations near the turbines and sluice gates (Xia et al., 2010a), which may affect the operation stage and the discharge calculations. It was found that a relatively stable water level could be achieved by averaging water levels from several points at different distances away from the turbine block. A typical comparison between water levels obtained from a single point and obtained by averaging 3 points are presented in Figure 5.14. By averaging water level on multipoint, water level oscillations can be eliminated, resulting in a smooth water level transition between different stages of TRS operations. Thus, multipoint averaged water level was used in this study to calculate the water head difference and to determine the operation stage.

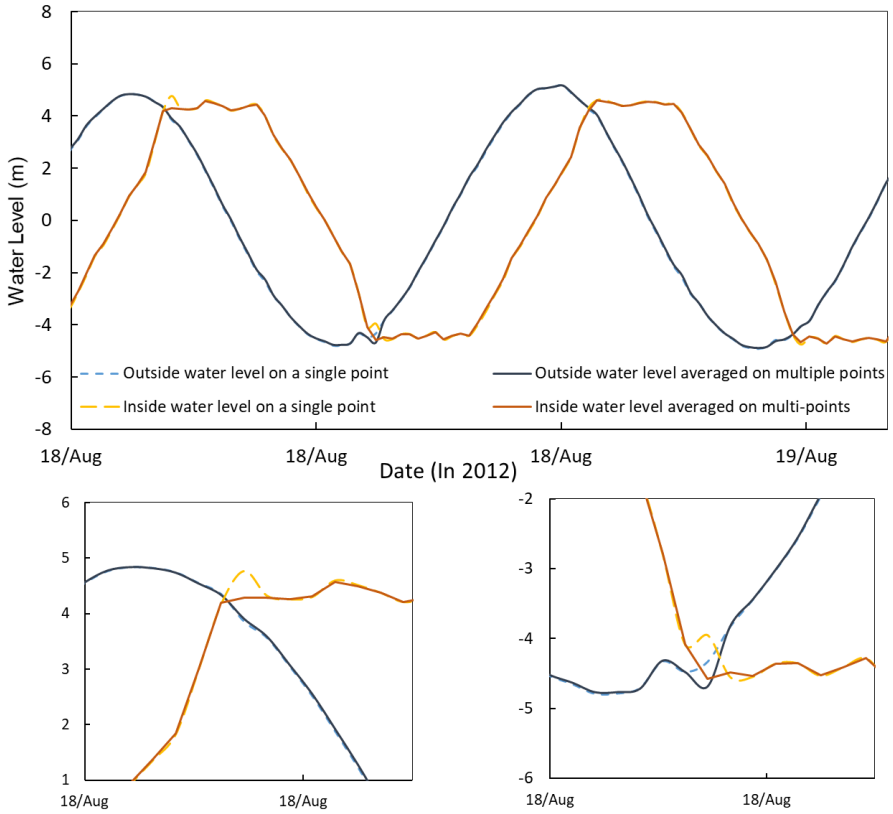

Figure 5.14: Water level oscillations inside and outside of lagoon basin.

5.1.5.2 Ramp Function

In the numerical modelling of the TRSs, it was found that the instant opening and closing of the turbine and the sluice gates easily caused numerical oscillations in water elevations, due to the massive volume of water flows through the turbines or sluice gates during their opening conditions (Zhou et al., 2014a). In reality, the operation of turbine valves and sluice gates usually takes a short period of time to complete the opening/closing process, with a gradual growth/reduction of the discharge during these processes.

To model the operation of TRSs more realistically and to eliminate water level oscillations, a delaying control process on the discharge of the turbine/sluice gates, called a ramp function, was introduced at the initial stage of the opening/closing process (Zhou et al., 2014b). During this period, the discharge of the turbine/sluice gates was multiplied by a variable linked to the time interval. This variable is expressed in the form of a half-sinusoidal function as:

$$f = \sin\left(\frac{\pi}{2T}t\right),\ 0 < t \leq T, \tag{5.6}$$

where *t* is the duration of the operation and *T* is the ramping period, usually 10-20 minutes.

At the beginning of the opening process of the turbine/sluice gates, t = 0 and f = 0; *f* then grows gradually to 1 when *t* reaches the ramping period *T*. The evolution of f represents the change in discharge, growing to the full discharge condition in the ramping period following a half-sinusoidal function. Likewise, when the turbine/sluice gates begin the closing process, the ramp function follows the form of a half-cosine curvilinear function:

$$f = \cos\left(\frac{\pi}{2T}t\right),\ 0 < t \leq T. \tag{5.7}$$

With this equation, the flow volume through the turbines and sluice gates is gradually decreasing following a curvilinear cosine function rather than stopping immediately.

5.2 Case I: West Somerset Lagoon (WSL)

5.2.1 Introduction and Modelling Setup

West Somerset Lagoon was proposed by Tidal Engineering and Environmental Services Ltd (TEES Ltd, 2018). The proposal includes a semi-circular breakwater with a length of 22 km, as shown in Figure 5.15 and Figure 5.16. WSL spans from Culvercliff in Minehead, on the

Western end, to West Quantoxhead, on the Eastern end, and encloses an area of approximately 80 km^2. The location of the turbine housings and sluice gates were distributed uniformly initially, while subsequently they have been adjusted to account for local bathymetric and geological conditions, with further studies being undertaken to investigate the optimal environmental considerations and impacts. Based on optimization studies carried out previously at Cardiff University, using a flexible operation of the turbines and based on the findings obtained from a genetic algorithm model, the optimal layout for the WSL incorporates 125 bulb turbine generators, each of 7.2 m diameter, split equally between 5 housing blocks (Xue, 2021). The capacity of each turbine is 20 MW, with a total installed capacity of 2.5 GW. To enhance the power output and the flushing capacity, 8 sluice gate housing blocks, with 2 different sizes, have been proposed. The sluicing area of each housing block is: 2860 m^2 for S1-S5 and 1900 m^2 for S6-S8. In total, the proposed sluicing area for WSL would be 20,000 m^2. The details of hydraulic structures are shown in Figure 5.16, with T1 to T5 illustrating the location of the 5 turbine housing blocks and S1 to S8 representing the 8 sluice gate blocks.

Figure 5.15: Location of West Somerset Lagoon, and the geography division of Severn Estuary and Bristol Channel.

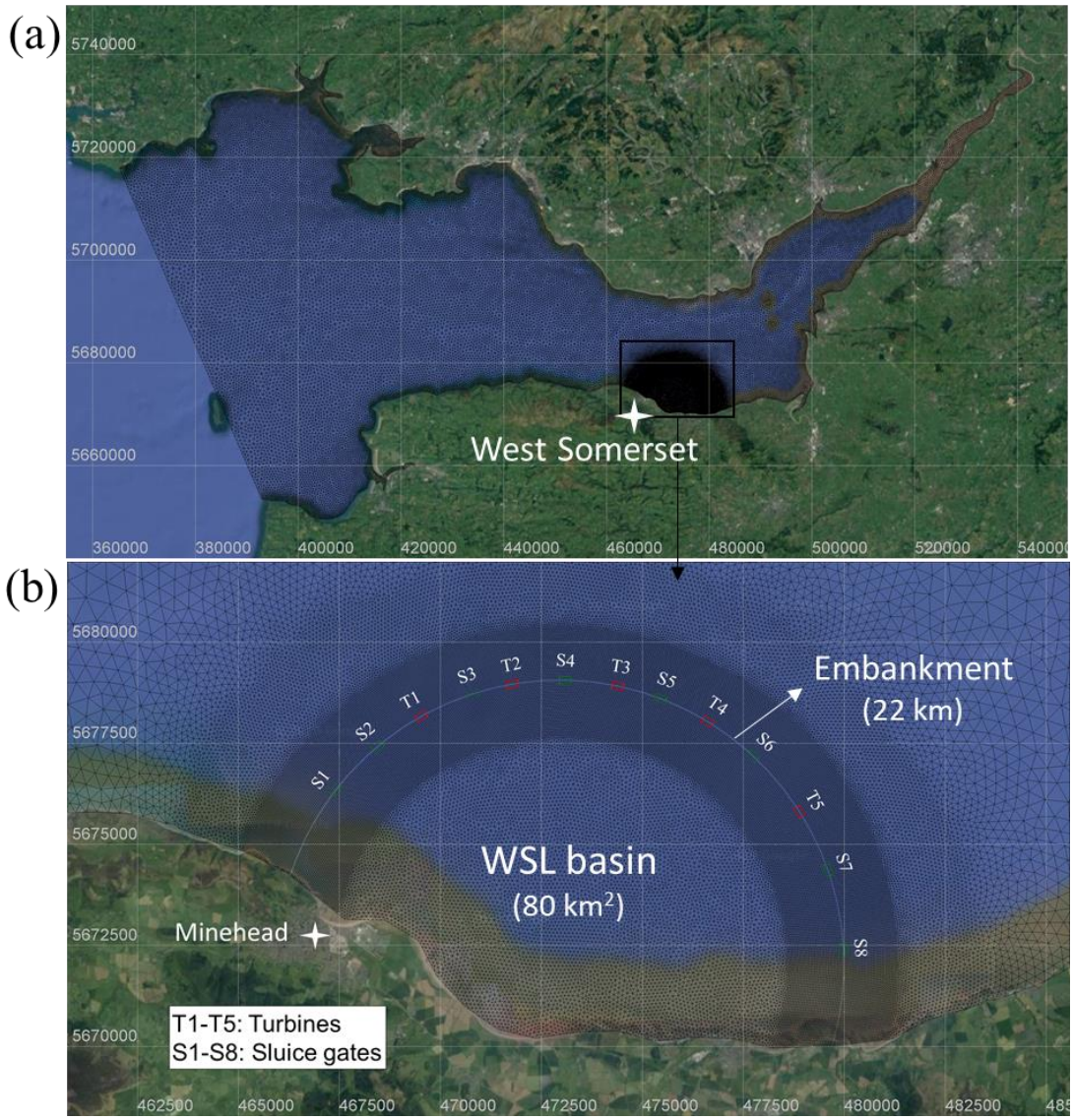

Figure 5.16: (a) The computational domain of the model; (b) layout of the turbine housing and sluice gate blocks around West Somerset Lagoon.

TRSs have different operation modes and operating parameters, which should follow the principle of enhancing high-quality energy generation and mitigating the environmental impact. In this study, two-way generation with two different operation heads, derived from the genetic algorithm model, both with and without pumping function, were adopted and compared for the WSL. The first operation scheme was based on the traditional two-way operation of the turbines, with an optimised fixed generation head, with the energy generation start and end heads being 4.9 m and 2.5 m, respectively. The second scheme considered was based on two-way operation with an optimised flexible generating head (Xue et al., 2019a). The third one is two-way operation with pumping function and fixed head, with the optimised turbine starting head of 5m, ending head of 2.5 m and extra pumping head of 2 m. The fourth scheme is the

two-way operation with pumping function, with both flexible turbine working head and pumping head optimised (Xue et al., 2019a). It should be noted that optimisation for a flexible head is sensitive to the tidal levels and therefore in the current study the tidal levels in the Bristol Channel were predicted using the model setup for this study, i.e. TELEMAC, rather than the DIVAST model (Xue et al., 2019a), which was used in optimised schemes study. The details of 0D optimised model could be achieved from Section 5.1.2.4.

Many TRSs proposed in Bristol Channel and Severn Estuary were modelled in the similar model domain of SEBC model in previously published research (Čož et al., 2019; Angeloudis et al., 2019). It should be pointed that a large-scale TRS such as Severn Barrage would affect the water level at the open boundary if enough distance is not provided between the TRS site and the open boundary (Ma et al., 2019). Some corresponding strategies have been investigated to mitigate this open boundary problem, including theoretically addressing the open boundary problem (Adcock et al., 2011) or extending the open boundary (Zhou et al., 2014b). However, for the tidal lagoons which do not block the whole estuary and directly affect the tidal resonance characteristics, it was estimated that the modelling results should be independent of the far-field open boundary conditions (Angeloudis and Falconer, 2017). For this study, it was deduced that the open boundary of the SEBC model is far enough for WSL to be influenced. Thus, the SEBC model was chosen as the primary hydrodynamic model for WSL hydro-environmental modelling. The method of WSL structure modelling and the basic model setting were following the same setup with the previous idealised lagoon modelling.

However, the tidal conditions near WSL, i.e. time and height of the tides, are different at each of the turbine and sluice gate blocks, as the tide propagates into and out of the Bristol Channel and past WSL. This variation in the tidal conditions is due to the size of the lagoon and the highly variable tidal conditions in the region, resulting in a 10-20 min difference in the time of the high water level along the lagoon wall and over 0.5 m difference between T1 and T5 in the spring tide, as shown in Figure 5.17.

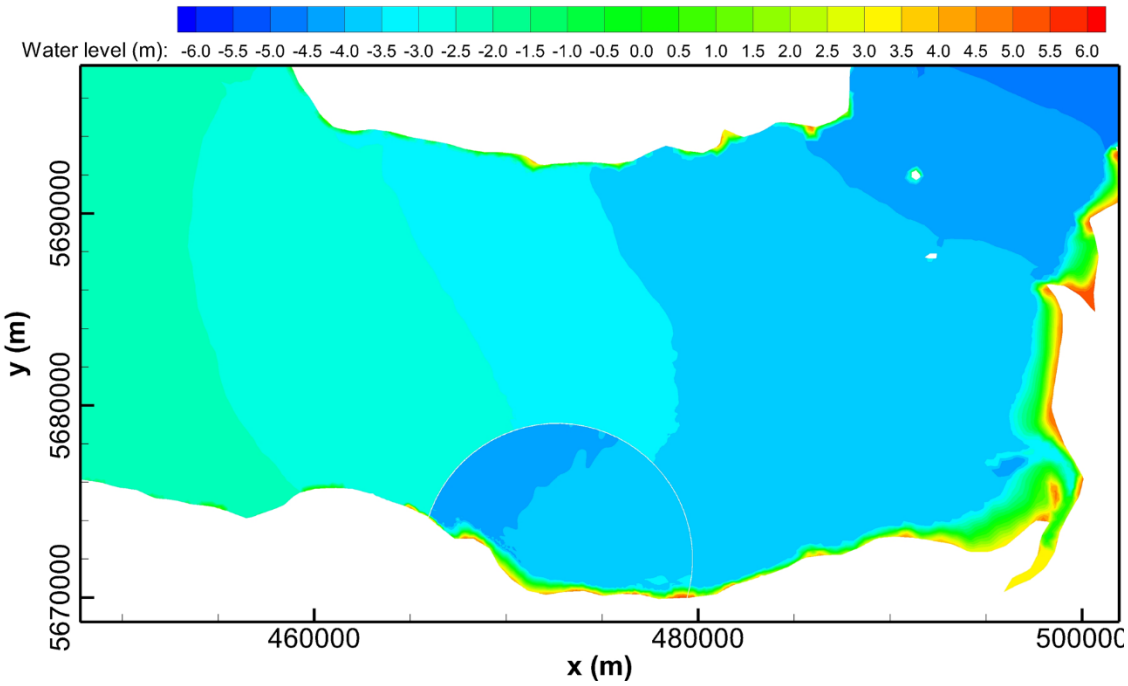

Figure 5.17: A typical tide level distribution in the Bristol Channel during the operation of WSL.

This variation was expected to affect the optimisation and operation of the scheme and it was found that all the turbines and sluice gates, following the same opening and closing rules, as determined by a single water level inside and outside of the basin - as traditionally used, leading to inefficient performance of the scheme (Čož et al., 2019; Xia et al., 2010c). Therefore, the optimisation of the scheme was carried out by separately operating each component, i.e. turbine and/or sluice gate block, using water levels predicted by TELEMAC-2D at the location of each block structure. The model was then revised to operate each structure independently. The operation stage and the discharge of each turbine and sluice gates block are determined by the water level at each block structure, which led to an improved and more efficient operation of the scheme for the 2D and 0D model. The details of the operation scheme are shown in Figure 5.18.

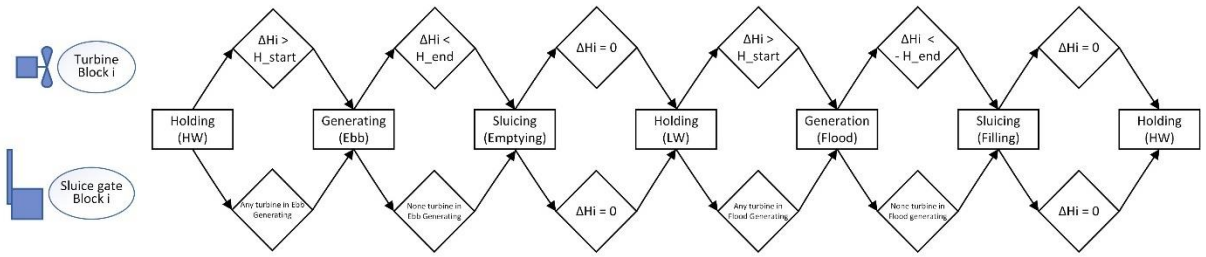

Figure 5.18: Flow chart of the two-way operation scheme in which each block of turbines and sluice gates is operated by its judgement routine (HW/LW = High/Low water level, ΔHi = water level inside lagoon - outside, H_start = Desired head difference for turbine operation (m), H_end = minimum head difference for turbine operation (m)).

It is estimated that the velocity of the turbine jet could easily reach a high magnitude (Angeloudis et al., 2016b); this, in addition to the fine grid resolution around the turbine block, results in a high value of the Courant-Friedrichs-Lewy number by its definition in the Equation (3.41). To achieve a stable and required Courant-Friedrichs-Lewy number, the time step in this model was set as 5 s. A typical spring-neap tidal circle, covering the period from 14:00 on 12 August 2012 to 14:00 on 27 August was used as the baseline for optimising the scheme, plus two more spin-up days at the beginning of simulations to achieve model setup conditions. The model was then run in parallel on HPC Wales (Supercomputing Wales, 2018) or ARCCA (ARCCA, 2018) supercomputing facilities.

5.2.2 Operation Schemes and Energy Output

The electricity generations from 0D and TELEMAC-2D are shown in Table 5.2. The results of TELEMAC-2D are consistent with the 0D model predictions, used to optimise the scheme, leading to differences less than 1% for WSL energy outputs for all four operational scenarios between 0D and TELEMAC-2D. This confirms that the simplified 0D simulated the operation well for the WSL and hence this operation scheme could be used for the 2D modelling (Xue, 2021). The total energy generated during a typical spring-neap cycle for fixed and flexible generation schemes were predicted to be 0.196 TWh and 0.233 TWh, respectively. The energy generated over the typical cycle can then be multiplied by 24.6 to provide the annual generation. This gives 4.82 TWh and 5.73 TWh per annum for fixed-head and flexible head generation, respectively. These results show the advantage of the flexible generation scheme, which can yield up to 19% and 8.9% more energy than fixed two-way operation without and with pumping function.

If adding pumping function, the annual energy output for fixed head and flexible head were 6.076 TWh and 6.617 TWh, respectively, which have increased by 26.0% and 15.5% comparing with the corresponding operation without pumping. Without considering the extra cost and maintenance, the benefit of power output increased by pumping function is significant.

Table 5.2: Summary of the energy output of WSL with different operation schemes.

Turbine operation head (m) (All in two-way generation)	Energy Output (TWh) in one entire tidal cycle	
	TELEMAC-2D	0D modelling
H_start=4.9; H_end=2.5	0.196	0.198
Optimized flexible generation head	0.233	0.232
H_start=5; H_end=2.5; H_Pumping=2	0.247	0.249
Optimized flexible generation head and pumping head	0.269	0.270

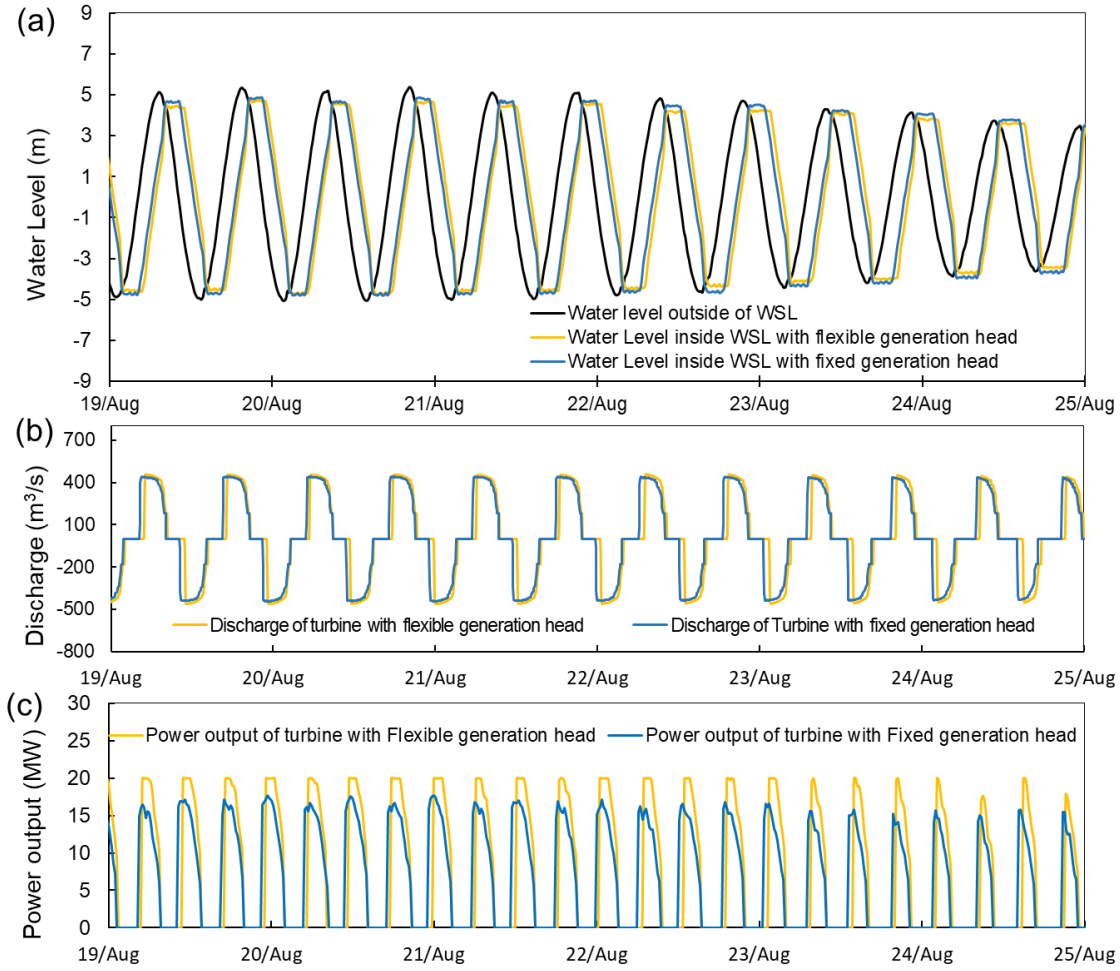

Figure 5.19: (a) Water level variations for WSL operation; (b) discharge through a single turbine; (c) power output for a single turbine.

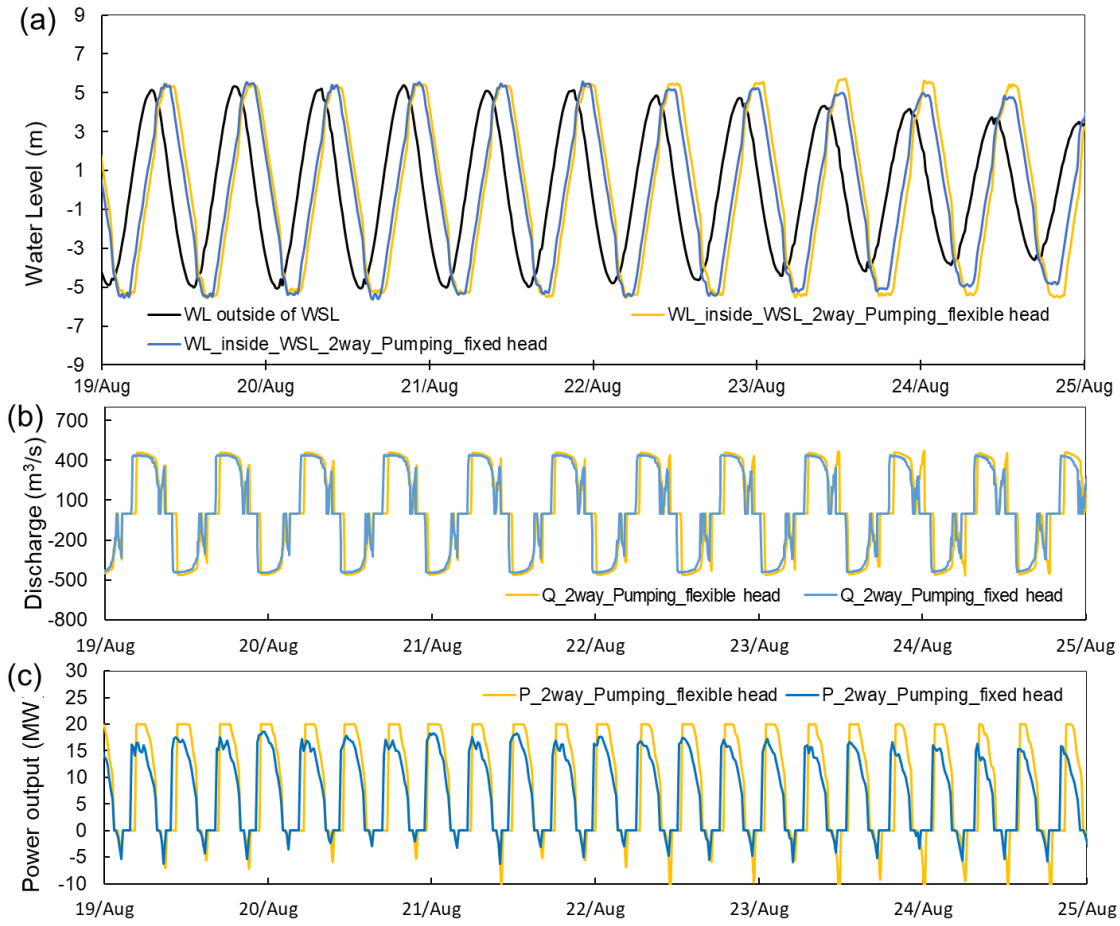

Figure 5.20:(a) Water level variations for WSL operation; (b) discharge through a single turbine; (c) power output of a single turbine in two-way operation with pumping function.

The significant increase in energy generated for optimised flexible head generation compared with traditional fixed head generation shows the benefit of adopting a flexible head generation operational procedure for the turbines and sluice gates. Furthermore, the flexible head generation scheme has the advantage of achieving a better balance between high energy generation and limited environmental impact. For example, water exchange processes may need to be accelerated if eutrophication or a pollution spillage incident occurs within the impounded area.

The model predicted water levels inside and outside of the lagoon, the flow through the turbines and the electricity generation are shown in Figure 5.19 and Figure 5.20. It is noted that the optimised generation scheme delayed the turbine generating time to achieve a higher turbine working head. Although a minor increase in the water level difference and the discharge is gained, the extra energy generated is significant due to the approximate square relationship between power and water head difference in tidal range energy extraction.

Almost all previous hydro-environmental modelling studies undertaken in the past have used a fixed head operation procedure. However, since the flexible generation scheme shows an appreciable increase in the energy generated compared to that generated using a fixed generation head procedure, it is expected that future TRSs use flexible generation schemes. The following analysis will therefore be based on two-way generation with the optimised flexible head.

5.2.3 Momentum Conservation and Velocity Field

The velocity distributions in the vicinity of the WSL, for a peak discharge through the turbines and during high spring tide, are shown in Figure 5.21. The comparisons show the predicted variations for three different representations of momentum conservation across the lagoon wall, in the form of an additional source term, and as outlined in Section 3.1.7.

Figure 5.21 (a, b) shows the model predictions without any momentum source term included and was taken as the baseline model for comparison purposes. From a numerical point of view, this non-momentum model assumed that the water moving through the turbines and the sluice gates flowed at the same velocity as the local current velocity (Hervouet, 2007). In all cases in Figure 5.21 the velocity distribution on the left shows that predicted during a flood tide, with ebb tide predictions being shown on the right. It can be seen that the turbine jet has a length of around 2.2-3.3 km and a core velocity of 1.7-2.9 m/s during flood generation. When the velocity at the end of the turbine diffusor was used to include the momentum source term, it was observed that the turbine jet was slightly increased in comparison with the baseline predicted characteristics, with a length of about 2.5-3.4 km and a core velocity of 2.2-3.2 m/s, as shown in Figure 5.21 (c). The slight difference in the velocity magnitude between Figure 5.21 (a) and (b) and Figure 5.21 (c) and (d) means that the original velocity at the outlet of the turbine diffuser was predicted to be slightly lower than the source velocity taken at the turbine diffusor location. A higher turbine jet velocity is predicted in Figure 5.21(e), reaching up to 3.3 m/s and with the length of the turbine jet reaching 2.7-3.7 km.

The turbine jets for the ebb generation show similar overall results to those predicted for flood generation. Moreover, it is noticeable that the water jet through the turbine block T5, the most easterly block, is clearly more pronounced than the jets effluxing from the other blocks. This is mainly caused by the relatively shallower bathymetry to the east of WSL, and the slightly

larger water head difference of 0.2-0.3 m through this block resulting from the time lag of tidal phase.

The eddy structure also changes with the different momentum source term representations. For example, circulation zones appeared on both sides of each jet in Figure 5.21 (e), which arose as a result of the higher velocity differences. Weaker circulation cells developed in Figure 5.21 (a) and (c), due to the weaker jet velocities. The relatively high tangential velocities in the inner Bristol Channel, meant that outside of WSL the ebb tide jets were strongly deflected by the tidal currents and eddies were mainly generated only on the western side of the lagoon. This ebb flow structure in the main channel could affect the sediment transport processes in the region.

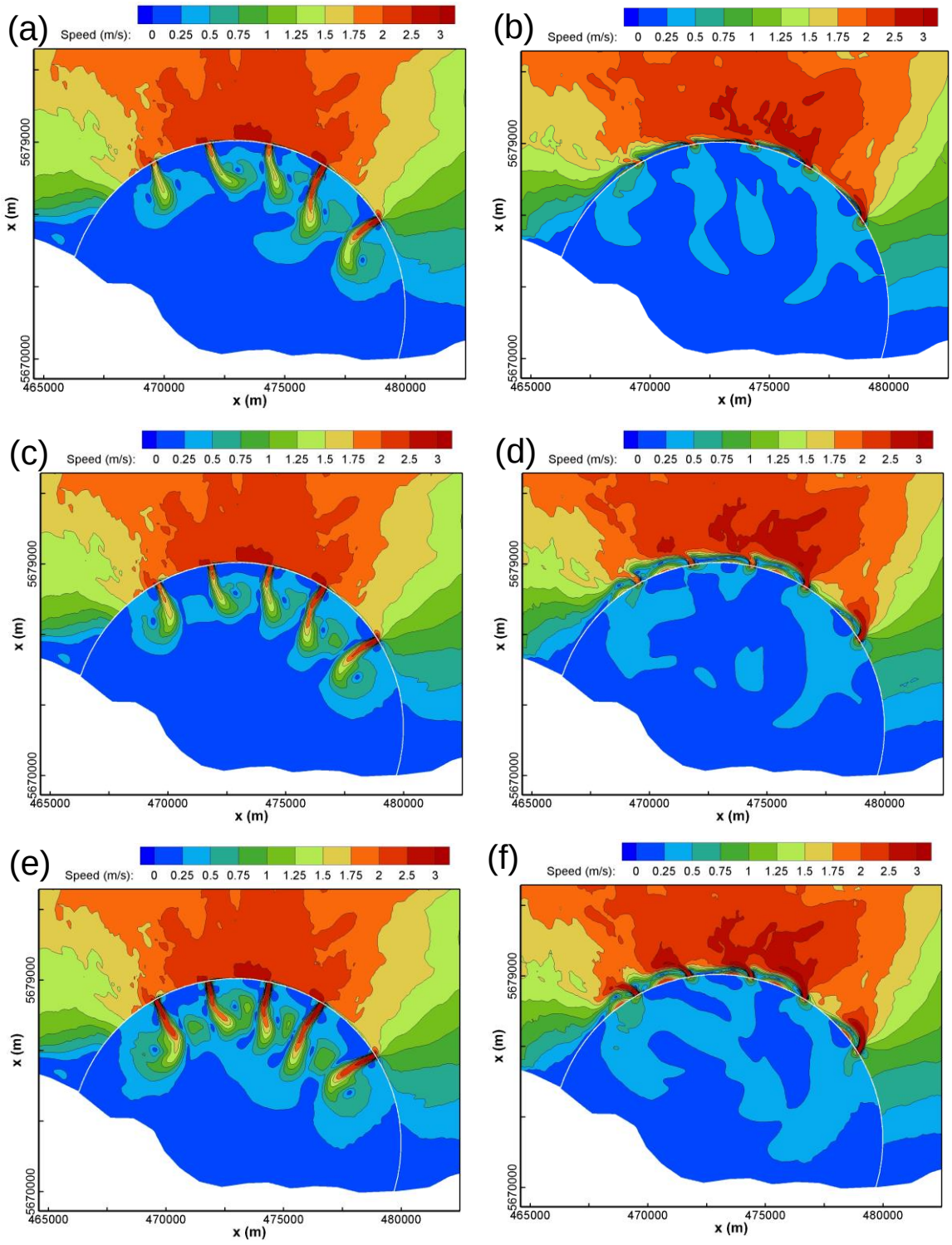

Figure 5.21: Instantaneous velocity fields of WSL for peak discharges during flood and ebb generation, for a typical spring tide and with different momentum source term formulations: (a) and (b) model without momentum source term; (c) and (d) model with momentum source using velocity at the end of the turbine diffusor; and (e) and (f) model with momentum using velocity taken at the turbine blade location.

In comparing with the momentum source velocity taken as the depth-averaged velocity and the model with depth-integrated source velocity, the model shows a limited impact on the turbine jet, as seen in Figure 5.22. This might have some influence on the flow pattern near the turbine, but negligible in the far-field study.

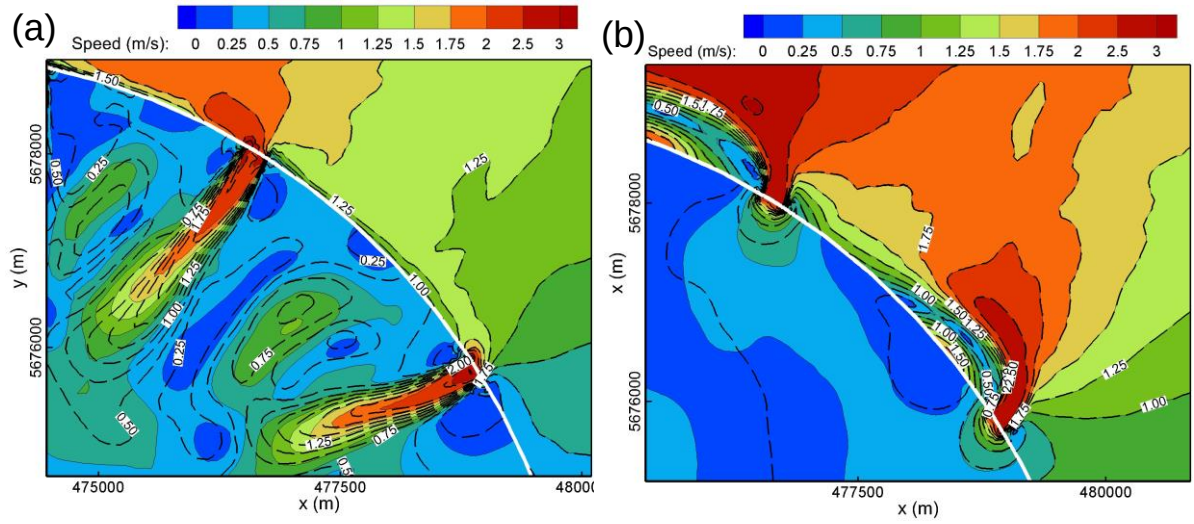

Figure 5.22: Turbine jet comparisons between momentum with depth-averaged source velocity (m/s) (colour contour) and depth-integrated momentum (dotted line) during (a) flooding generation and (b) ebb generation.

5.3 Case II: Swansea Bay Lagoon (SBL)

5.3.1 Introduction

Various tidal lagoon plans have been proposed in Severn Estuary and Bristol Channel in recent decades, and Swansea Bay Lagoon had the greatest commercial viability so far. Swansea Bay is located on the South Wales coastline in the Bristol Channel, with a tidal range exceeding 10 m during spring tide. The lagoon plan in Swansea Bay has been updated by different companies. In 2004, Tidal Electric Inc (TEL) released a proposal to build a 5 km^2 tidal lagoon in Swansea Bay, proposing 24 turbines with a 3.3 m diameter and 2.5 MW capacity for each turbine (Atkins, 2004). After that, proposals for the construction of this lagoon were developed rapidly, most recently by Tidal Lagoon Swansea Bay Plc (TLSB) (Tidal Lagoon Plc, 2016). In the TLSB proposal, the SBL will be located between the River Tawe and the River Neath and include an embankment with a length of 9.5 km, forming an enclosed sea area of 11.5 km^2. Sixteen bulb turbines with a diameter of 7.2 m will be installed. This makes the total capacity

of SBL to be 320 MW and the scheme will generate enough electricity for over 155,000 homes (Hendry, 2016). Sluice gates are located at one side of the turbines with a total sluicing area of 800 m^2. In 2015, the UK government issued a development consent order to the proposal from TLSB. In 2016, the former Energy Minister, Charles Hendry, published an independent review commissioned by the UK government (Hendry, 2016), supporting the development of TRSs in the UK and strongly recommending the Swansea Bay Lagoon proposal. However, the UK government did not support this project in consideration of the high cost of electricity and the potential environmental issues. Regardless of the approval and construction status, the SBL remains one of the most widely studied tidal lagoon, making it suitable for a benchmark study.

Figure 5.23: The horseshoe shape of the SBL proposal and its location in Swansea Bay (Tidal Lagoon Plc, 2016).

Due to the relatively small scale of the SBL and the limited hydrodynamic influence (Angeloudis et al., 2016a; Čož et al., 2019), the negligible influence was expected from the operation of the SBL on the open boundary of the SEBC model. Therefore, the SBL was implanted into the SEBC, following the same model settings as the validated SEBC hydrodynamic model. Based on the idealised lagoon and the WSL modelling results, the SBL was introduced into the SEBC model using the domain decomposition method. The layout and specifications of the SBL model matched the public information acquired from Tidal Lagoon Swansea Bay Ltd (Tidal Lagoon Plc, 2016). The mesh resolution in the whole Swansea Bay area has been refined to an grid size of around 100 m, as seen in Figure 5.24. The mesh around

the turbines and sluice gates were refined to an grid size of 30 m, distributing symmetrically at two sides of the southwest side of the embankment.

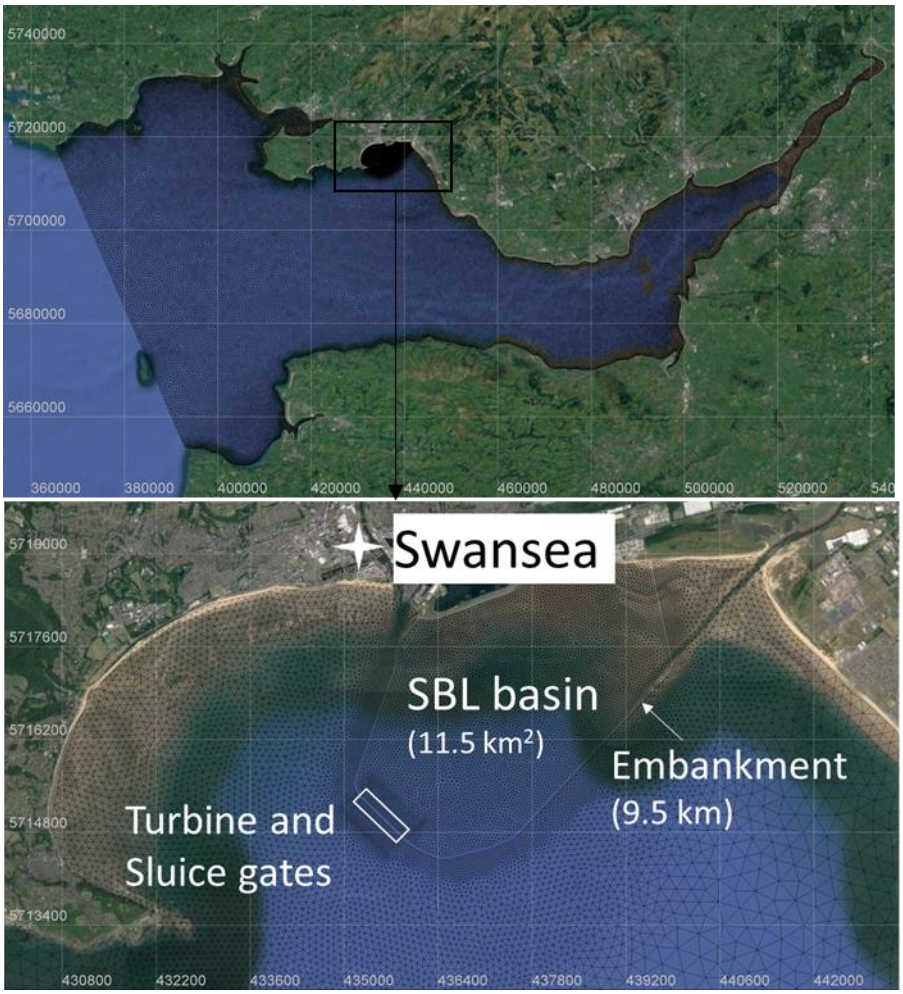

Figure 5.24: Mesh resolution in the whole model domain and around the Swansea Bay Lagoon.

Dredging has been conducted around the turbine and sluice gates to deepen the bottom level, as shown in Figure 5.25. Based on the study of the representative water levels at two sides of TRSs in Section 5.1.5.1, the water levels on each side of the SBL were calculated as averaged values of six evenly spread points with distances from 300 m - 1000 m away from the turbine block. This averaged water level value can avoid the unphysical water level oscillations in the near-sites of turbine and represent the actual water level change in the upstream and downstream of SBL.

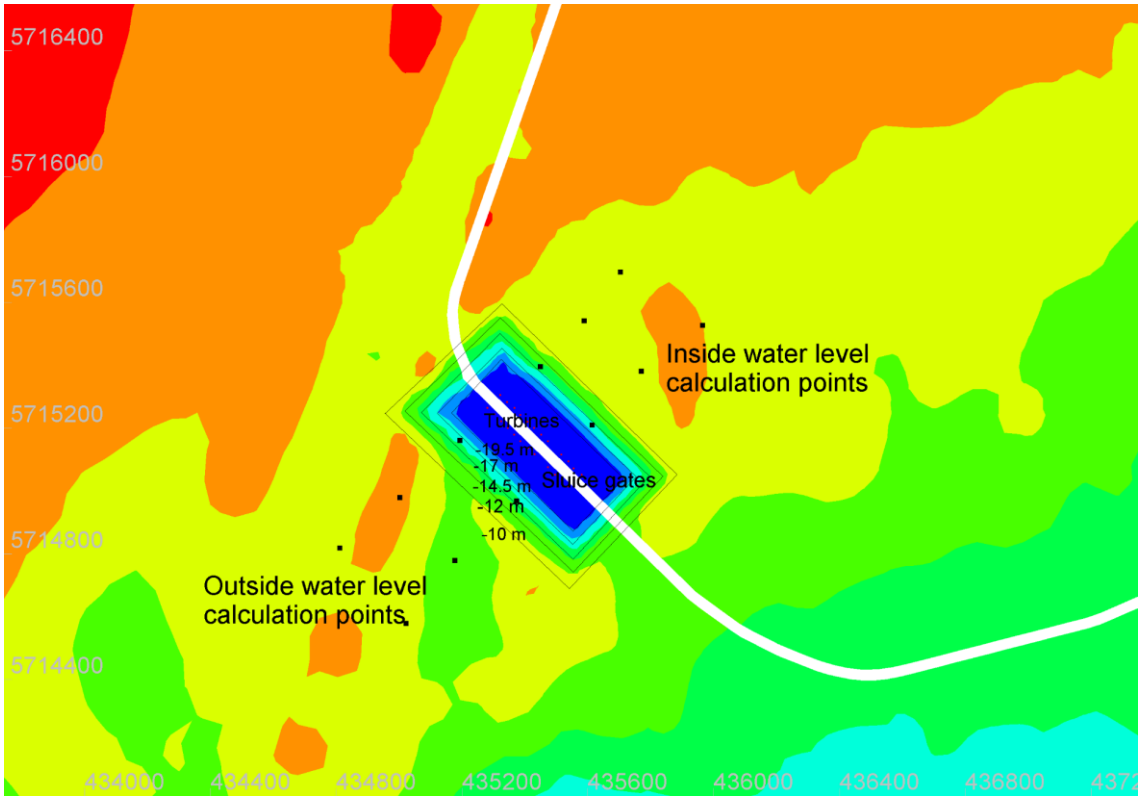

Figure 5.25: Locations of the turbine and the sluice gates of SBL and the dredging area, the points used to calculate the water level change.

5.3.2 Operation Schemes and Energy Output

Although a two-way operation scheme was chosen for the operation scheme of the SBL (Petley and Aggidis, 2016), it is interesting to explore the difference in water level change and power output with different operation schemes. Thus, five different operation schemes were applied to the SBL model and then compared, including ebb generation (Figure 5.26), ebb generation with pumping (Figure 5.27), two-way generation (Figure 5.28), two-way generation with pumping (Figure 5.29) and optimised flexible two-way generation (Figure 5.30) based on the methods of Xue et al. (2019a).

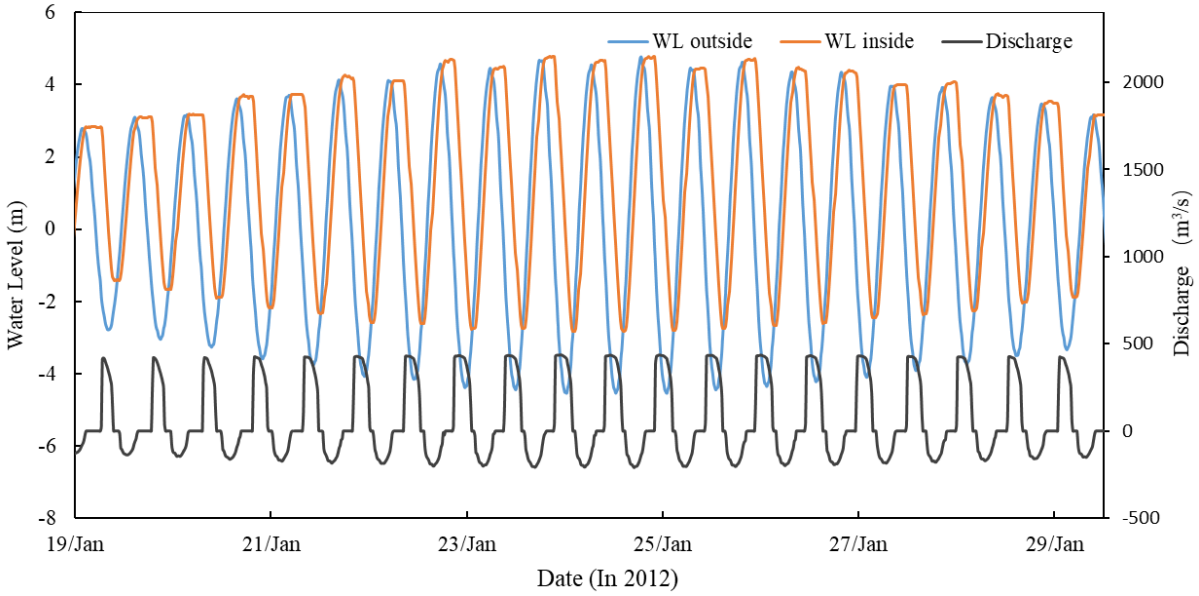

Figure 5.26: Predicted water levels on both sides of the SBL and the corresponding total water discharge of turbines for the ebb generation method.

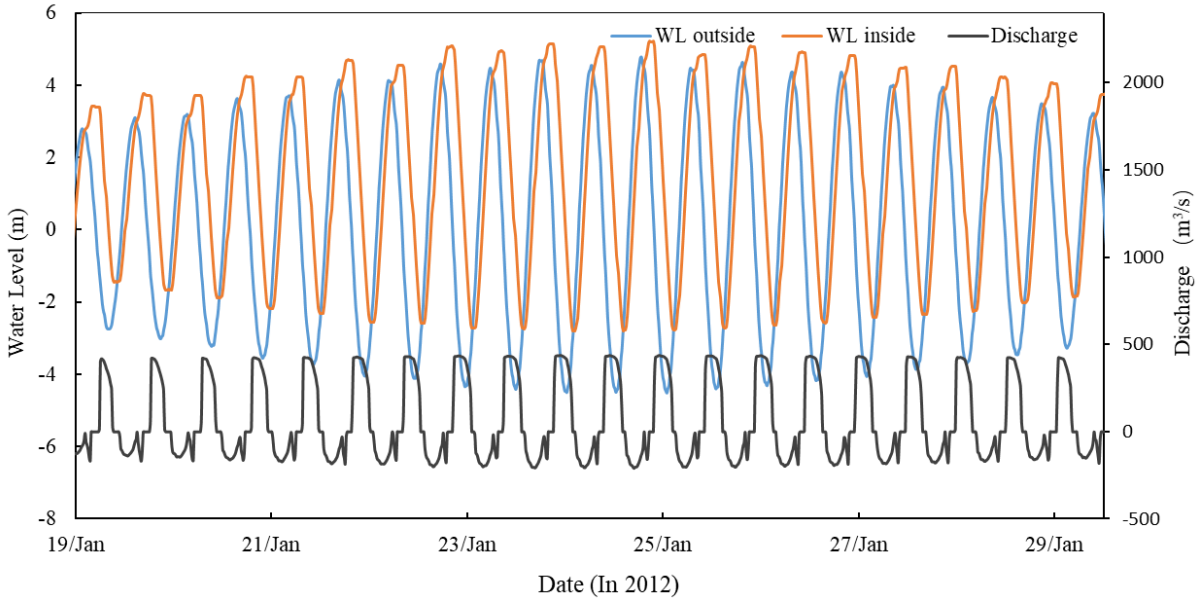

Figure 5.27: Predicted water levels on both sides of the SBL and the corresponding total water discharge of turbines for the ebb/pumping generation method.

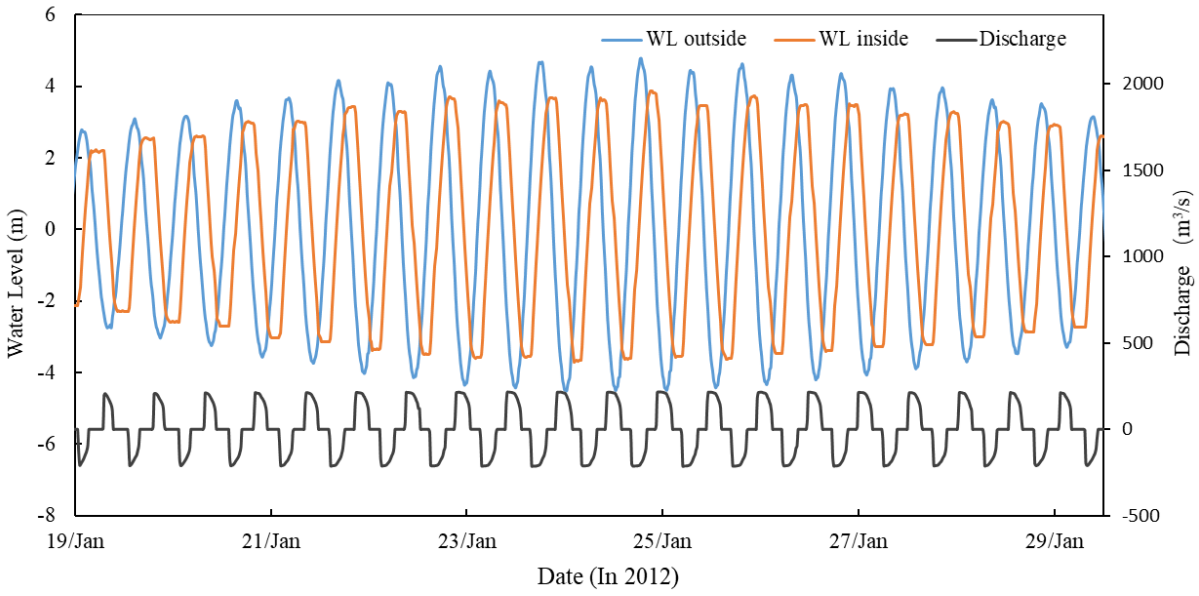

Figure 5.28: Predicted water levels on both sides of the SBL and the corresponding total water discharge of turbines for the two-way generation method.

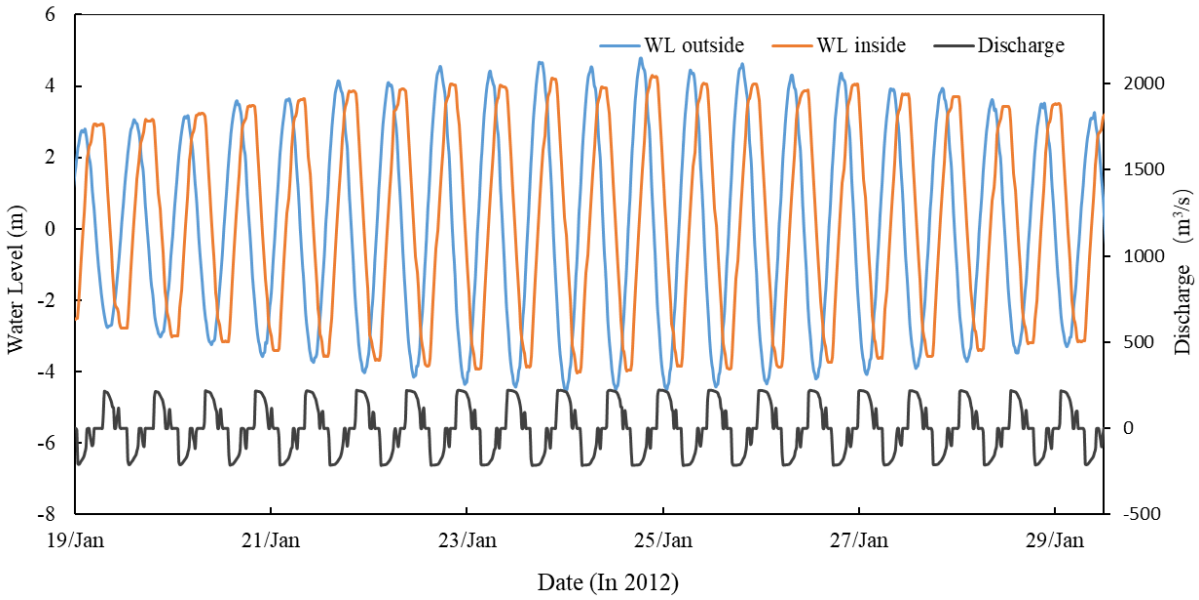

Figure 5.29: Predicted water levels on both sides of the SBL and the corresponding total water discharge of turbines for the two-way/pumping generation method.

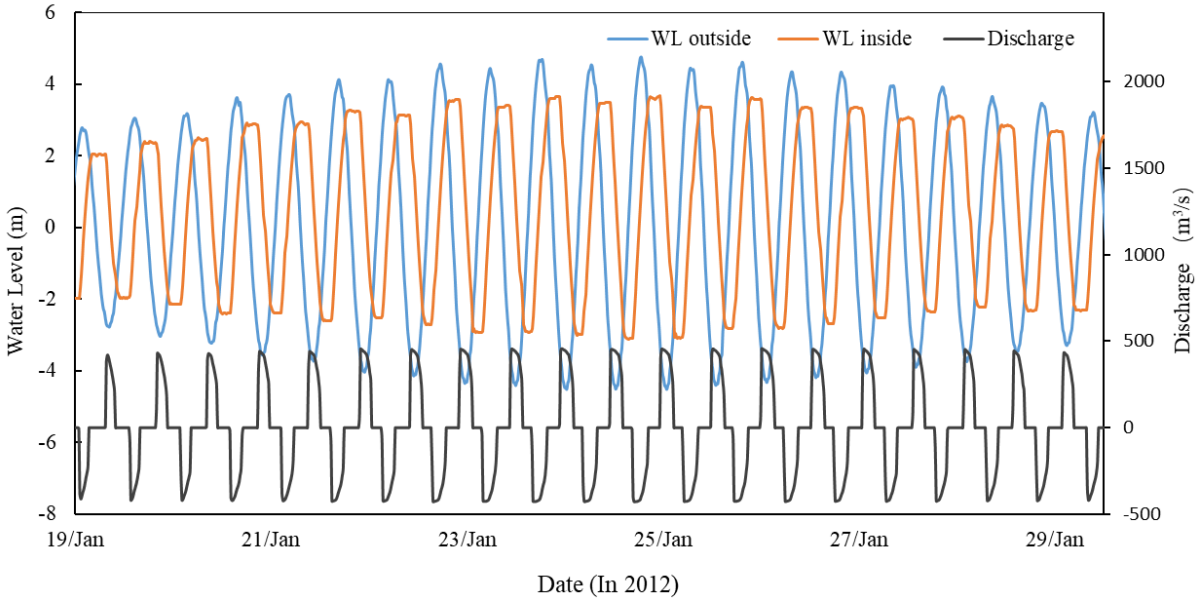

Figure 5.30: Predicted water levels on both sides of the SBL and the corresponding total water discharge of turbines for the flexible two-way generation method.

Table 5.3: The energy output of SBL with different operation schemes.

Operation scheme	Turbine generation start/end head (m)	Energy output over one typical tidal cycle (GWh)
Ebb generation	H_start= 4.0 H_end= 1.5	14.85
Ebb generation with pumping function	H_start= 4.0 H_end= 1.5 H_pump= 1	16.48
Two-way generation	H_start= 4.0 H_end= 1.5	22.34
Two-way generation with pumping function	H_start= 4.0 H_end= 1.5 H_pump= 1	24.12
Optimised flexible two-way generation	See Appendix A, Table A3	23.74

In Figure 5.26 - Figure 5.30, the water levels evolution, the discharge through a single turbine are plotted to demonstrate its working performance. Except for the sluicing stage of the turbine, which takes up only a very small segment at the end of the generation stage, the discharge of the turbine was positively correlated with power output. From the comparison of ebb generation (Figure 5.26) and two-way generation (Figure 5.28), it can be seen that the discharge

of the turbine in the ebb generation scheme was much higher than two-way generation, which indicates a higher unit power output of ebb generation. However, the negative value of discharge in ebb generation, referring to the lagoon filling phase, produces an idle running condition in the turbine without power generation, while both the positive and negative discharge during two-way generation produce electricity. The two-way generation energy output in this entire tidal cycle is 22.34 GWh, as shown in Table 5.3, which is 34% higher than for ebb generation (14.85 GWh). Furthermore, the high electric output in a short interval during the ebb generation will heavily burden the power grid which does not benefit power absorption.

By including the power output for the pumping function with ebb generation or two-way generation, it is concluded that the pumping function could increase the energy output by 8% - 11% in SBL operation, which is in accordance with previous research (Neill et al., 2018). Furthermore, the pumping function could be used to adjust the water level inside of the lagoon basin. For example, the water level in Figure 5.29 is closer to the natural condition, which is more environmentally-friendly.

The advantage of optimised two-way generation with a flexible head can be observed from the discharge line in Figure 5.30, which is much higher than that of two-way generation with a fixed head. This means that the optimised generation scheme has a higher unit power output, and the accumulated power generations in Table 5.3 show that the power generated with flexible two-way generation is 6.3% higher than with a fixed generation head.

The annual electricity production of SBL could be calculated by multiplying a factor of 24.6 to the energy output over the typical tidal cycle, which derives the annual energy output of the two-way operation scheme of 549 GWh/year. Given the difference in turbine operation water head, the SBL energy generation prediction is at the same level with prior SBL 2D modelling research, e.g. 474 - 586 GWh/year (Angeloudis and Falconer, 2017), 515 - 585 GWh/year (Čož et al., 2019), but higher than some research result, e.g. 479.8 GWh/year (Petley and Aggidis, 2016).

5.3.3 Momentum Conservation and Velocity Field

The construction of the SBL structure significantly alters the flow patterns in Swansea Bay. In this aspect, similar to the momentum conservation study of WSL, the effects of different momentum terms on the flow pattern of SBL were studied and shown in Figure 5.31.

The difference between the three momentum terms depends on the selection of the effective velocity used to calculate momentum adjustment in the momentum equation, i.e. u_s in Equation (3.34), which is discussed here. Figure 5.31(a) (b) shows the model predictions without momentum adjustment. Figure 5.31(c) (d) uses the velocity at the end of the turbine diffusor. Figure 5.31(e) (f) uses the average velocity of the water flowing through the turbine blades. The location of turbine blades and diffusor can be observed in Figure 3.2.

It is obvious that Figure 5.31(a) (b) shows the jet through the turbines reach up to 1.5-2 m/s in the centre of the flow wake. Figure 5.31(c) and (d) shows a turbine jet similar in size to that found in Figure 5.31(c). This similarity means that, in this SBL model, the velocity at the end of the turbine diffusor is approximately the same as the local current velocity. It was noticeable that during the ebb generation, the interaction between the flow and the shape of the lagoon formed a large clockwise-rotating vortex in the centre position of the lagoon while vortex appear at east sides of the turbine jet in the flood generation. Similar vortexes were observed in the SBL simulation of Angeloudis et al. (2016b) and Čož et al. (2019). The low-velocity area in the central of large recirculation zones might contribute to the accumulation of scalar quantities, which could have an impact on the water quality and sediment deposition inside the lagoon (Angeloudis et al., 2016b). In comparison, Figure 5.31 (e) (f) demonstrates that including the momentum with the source velocity taken at the turbine blade would increase the turbine jet significantly, with the core velocity in the water jet more than 2 m/s.

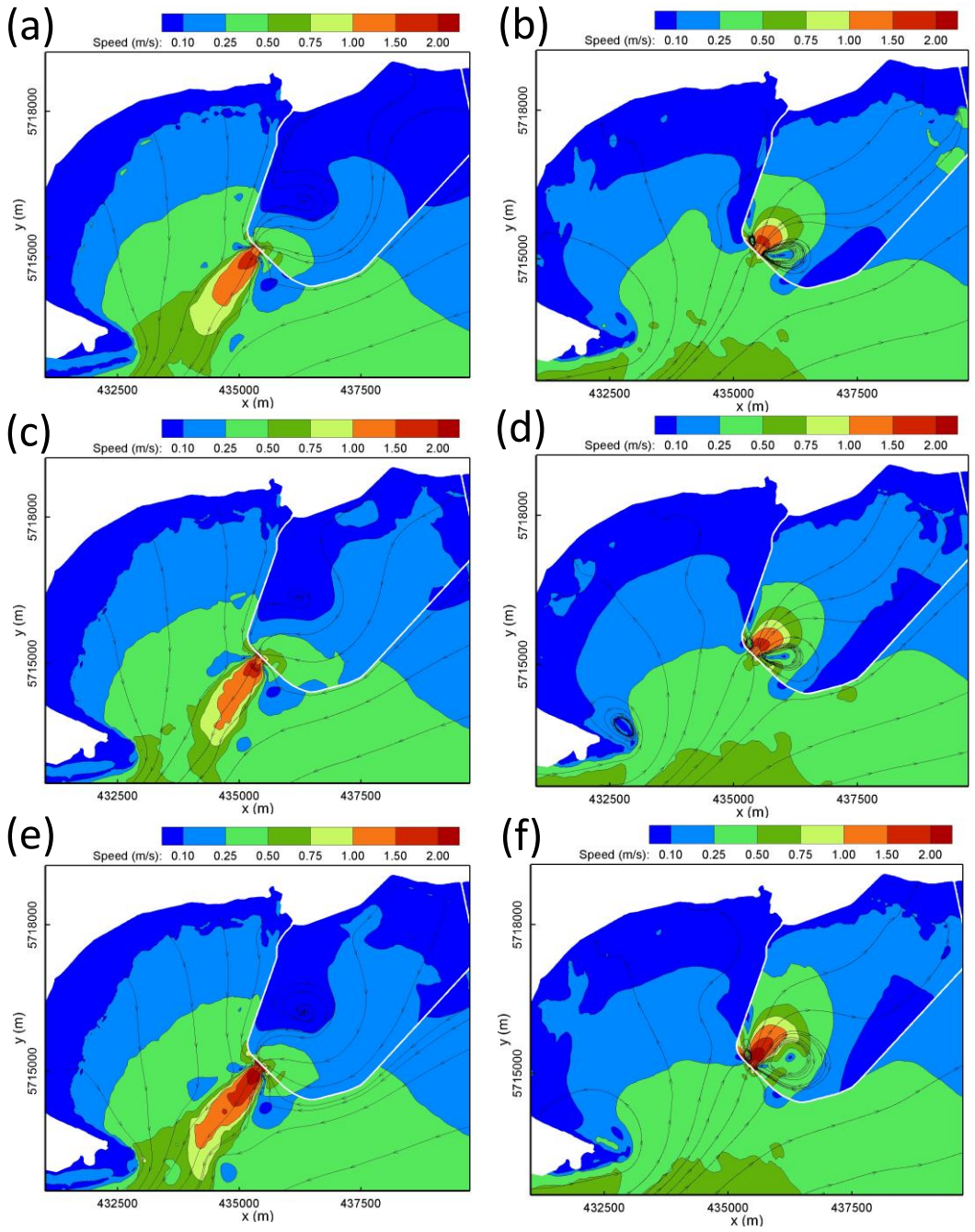

Figure 5.31: Instantaneous velocity fields of SBL for peak discharges during flood and ebb generation, for a typical spring tide and with different momentum source term formulations: (a) and (b) model without momentum source term; (c) and (d) model with momentum source using velocity at the end of the turbine diffusor; and (e) and (f) model with momentum using velocity taken at the turbine blade location.

In addition to the above 2D momentum sources, another momentum term is tested here by integrating horizontal velocity along the vertical axis at the end of the turbine diffusor. The details of this method can be found in Section 3.1.7, with the source velocity taken at the end of the turbine diffusor. As shown in Figure 5.32, comparing with the 2D momentum term, the

semi-3D method shows limited changes to the turbine jet. This might have some influence on the flow pattern to the vicinity of the turbine but is negligible in the far-field study, which is in accordance with the actual 3D and 2D comparison (Čož et al., 2019).

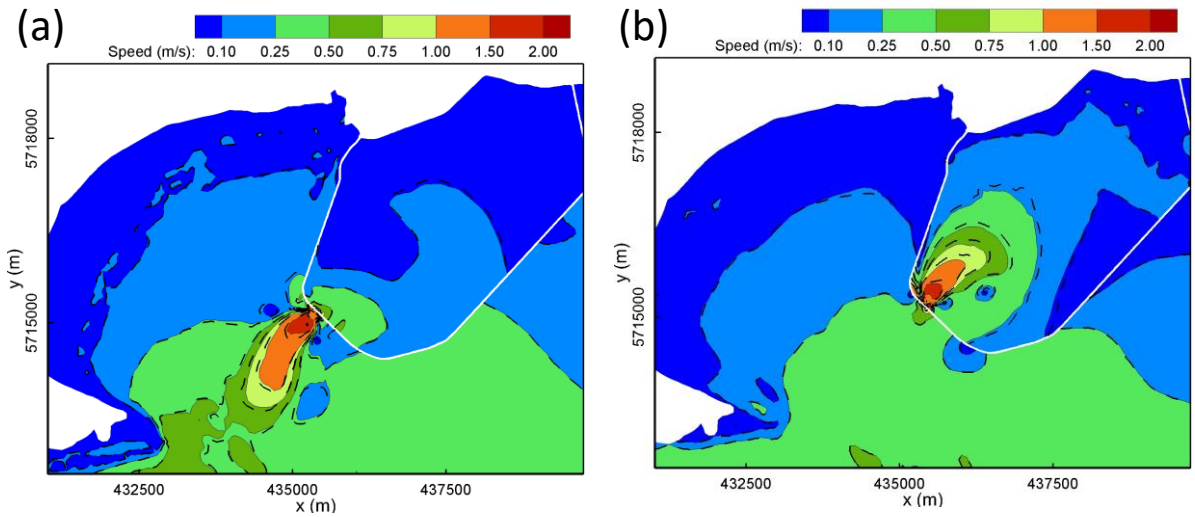

Figure 5.32: Comparison of the turbine jets with depth-averaged source velocity (colour contour) and depth-integrated momentum (dotted line) during (a) ebb generation; (b) flood generation.

It is concluded from the momentum conservation study of WSL and SBL that the introduction of the momentum term has a significant influence on the flow pattern near the lagoon. The momentum term with source velocity included at the end of the turbine diffusor was therefore applied in all subsequent lagoon modelling simulations since it was considered to be more representative of the true hydrodynamics in the near-field of the turbines and sluices. However, in modelling of the turbine wake and momentum conservation, further testing and validation are required. This can be achieved by using field observations or experimental studies with scale physical models of simplified TRSs.

5. 4 Case III: North Wales Tidal Lagoon (NWTL)

5.4.1 Introduction

The tidal range along the North Wales coast is one of the highest in the UK, and the marine topography in this area is featured with shallow waters adjacent to deeper waters which is suitable for the construction of TRS while minimising construction costs, making the North Wales Coast an attractive site for TRS construction. Furthermore, there is a time lag of more than 3 hours between the tidal phase for the North Wales coast and the Bristol Channel

(Ahmadian et al., 2010b). With such tidal phase difference, TRS projects in each region could partially offset the variability of power output from projects in the other region (Neill et al., 2018).

The North Wales seacoast has historically suffered from flooding. For example, the flooding caused by a storm during December 2013-January 2014 caused significant damage to coastal defences (BBC, 2014). The construction of a coastally attached impoundment could mitigate the current flooding risk and the hazards of potential sea-level rise caused by global warming. Thus, the NWTL was proposed as a tidal energy impoundment with the potential benefit of coastal protection.

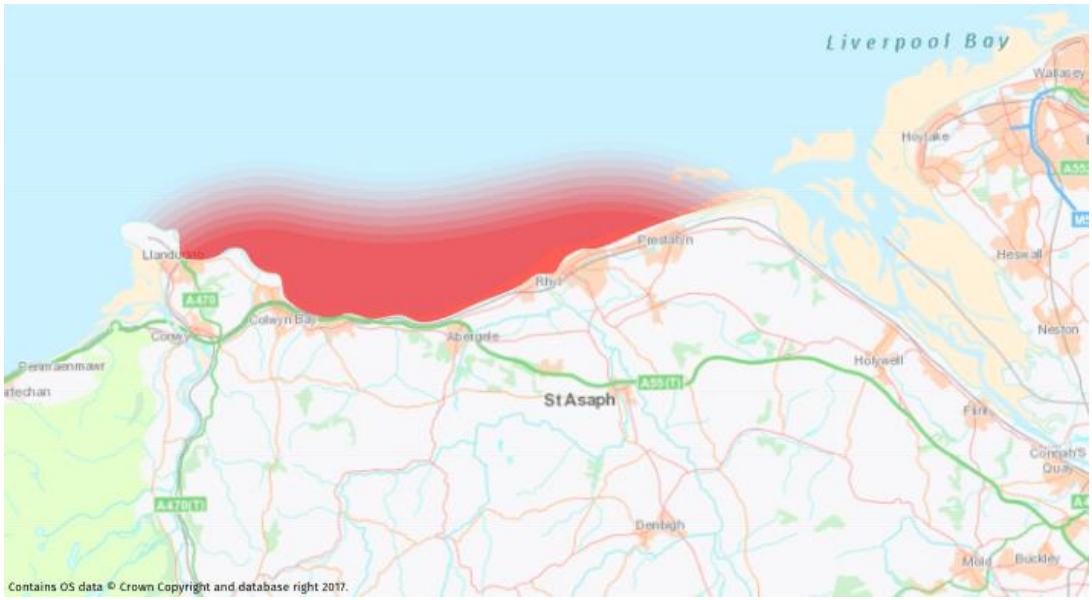

Figure 5.33: The preliminary planned location and scale of the NWTL, as shown in the red area (North Wales Tidal Energy, 2020)

The NWTL is a TRS proposed by North Wales Tidal Energy Ltd (https://www.northwalestidalenergy.com/concept), as illustrated in Figure 5.33. The lagoon was planned to span from Prestatyn to Great Orme, with a breakwater stretching over 30 km in length and a water impoundment area of 150 km^2. The shape of the NWTL along the coastline would be able to secure vulnerable communities such as Abergele, Towyn and Rhyl on the North Wales coast, covering 30 km of coastline and protecting over 100,000 people (Hendry, 2016).

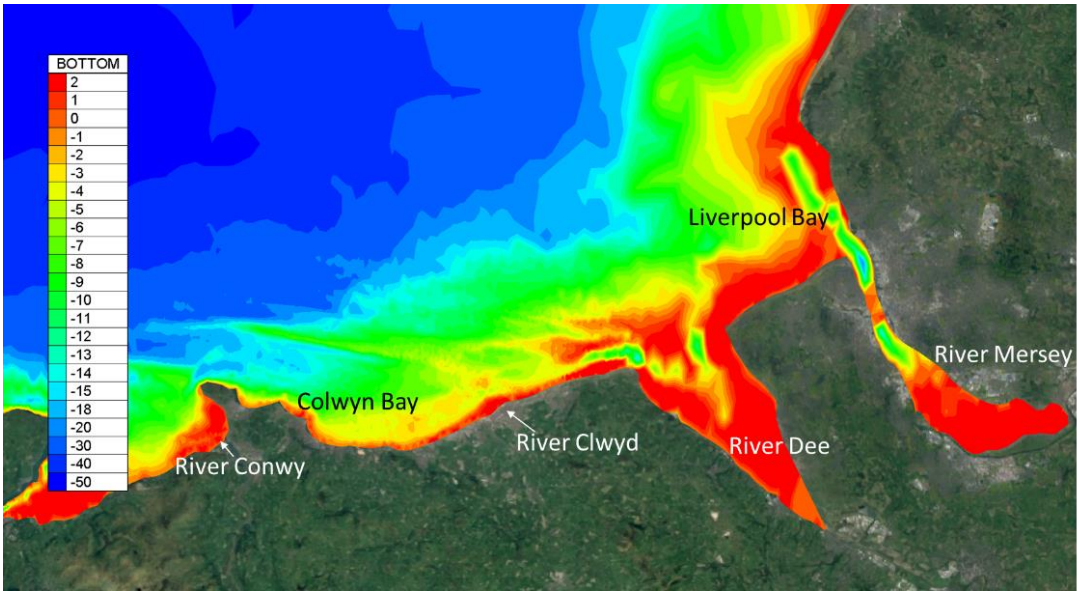

Figure 5.34: Bathymetry of the North Wales coastline and main rivers in this area (bathymetry data refers to MSL).

Figure 5.34 provides an overview of the geography and bathymetry in the proximity of the NWTL. It is noted that the bed elevation in most of the potential impoundment area is above -10 m, especially on the east side of the NWTL plan area. Although the shallow water depth would reduce the embankment cost, moderate dredging work may be needed on the east side of the NWTL to maintain the smooth operation of all sluice gates. Based on the optimised result from 0D research (Xue, 2021), 150 turbines are distributed into 10 blocks, while 9 blocks of sluice gates are designed to contribute to the electricity generation and the water quality, with a total sluicing area of 20000 m^2.

Turbines and sluice gates are distributed primarily based upon the regional bathymetric features, as illustrated in Figure 5.35. However, there are also environmental considerations to the choice of these locations that could provide benefits in water renewal capacity and some operational aspects.

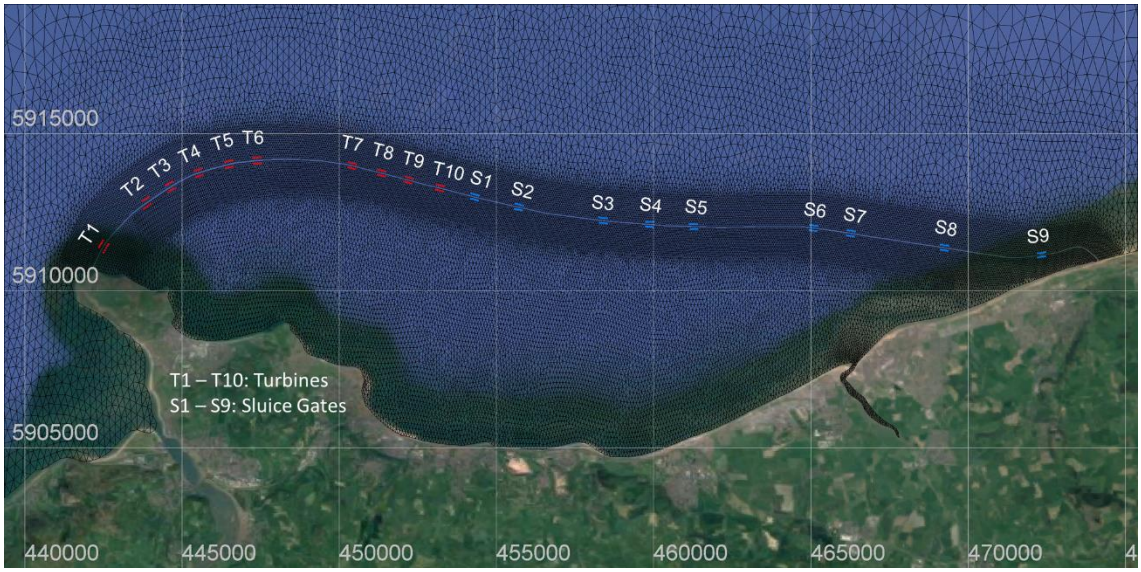

Figure 5.35: The mesh resolution around the NWTL and the distribution of turbine and sluice gate blocks.

Similar approaches to those used for modelling the SBL and WSL were implemented in NWTL simulation. NWTL were implanted into the CS model with the mesh decomposition method. Since the turbine and sluice gate blocks of the NWTL were widely distributed, each turbine or sluice gate block was operated independently in the model, similar to the operation scheme adapted in WSL model. Momentum conservation was achieved with a realistic source velocity applied. Other settings all followed the same rules as the WSL modelling.

As demonstrated by previous findings (Fairley et al., 2014), regional wave conditions have an insignificant impact on a TRS. Hence, although this area experiences strong winds, as evidenced by the presence of the Gwynt y Môr Offshore Wind Farm, regional wave and wind factors were omitted from the numerical model simulations.

5.4.2 Operation Schemes

It was concluded from the SBL and WSL study that the optimised two-way generation scheme with flexible operation heads has noticeable advantages in electricity generation. Thus, the conventional fixed head generation scheme was not considered in the NWTL simulation. Two operational schemes were adopted in NWTL modelling: optimised two-way generation with and without pumping, both with a flexible generation head achieved from the 0D model (Xue et al., 2019a).

Predictions of annual electricity generation from a 0D model (Xue et al., 2019a) and a TELEMAC-2D model are shown in Table 5.4. Power prediction differences of only 1.27% and 2.4% were observed between 0D and 2D model predictions, indicating that the two models agree well with each other. Although the deviations in the power predictions for the NWTL between the 0D and TELEMAC-2D models are higher than for the WSL, it is likely that this is due to the larger size of the NWTL and its complex bathymetric conditions. Annual power output was calculated by multiplying the typical cycle energy output by 24.6, which gave values of 4.80 TWh and 5.48 TWh for optimised two-way generation without and with pumping, respectively.

Table 5.4: The electricity generation from the NWTL for a typical spring-neap tidal cycle.

Operation scheme	0D model (GWh)	TELEMAC-2D (GWh)	Difference (%)
Optimised flexible two-way	197.56	195.04	1.27%
Optimised flexible two-way with pumping function	228.27	222.68	2.4%

Figure 5.36 gives the water level changes and the corresponding discharge and power output of a turbine over a typical neap-spring tidal cycle for the NWTL. It is observed from Figure 5.36 (a) that the maximum water level difference during the spring tide is around 8 m, which is 2-3 m lower than in the WSL area. Furthermore, the comparison of water levels inside the NWTL between the two operation schemes in Figure 5.36 (a) shows that the pumping can mitigate the limitations of natural sea-level variations between spring and neap tide, providing a relatively similar head difference throughout the tidal cycle. Figure 5.36 (c) confirms that the scheme with pumping could have relatively stable electricity output during the entire tidal cycle compared with the generation scheme without pumping.

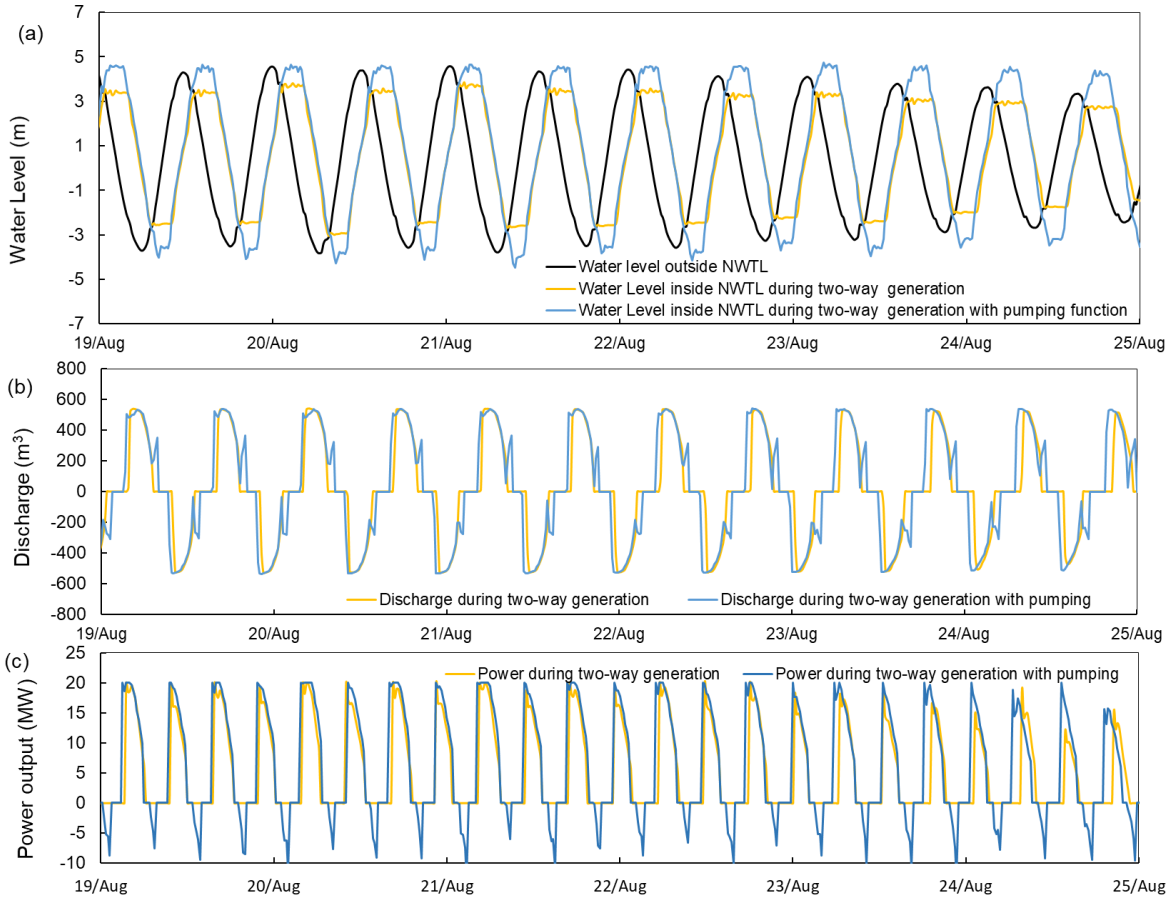

Figure 5.36: (a) Water level variations during the NWTL lagoon operation, (b) discharge through a single turbine and (c) power output for a single turbine. (The yellow line indicates the flexible two-way generation scheme and the blue line indicates the flexible two-way generation scheme with pumping for each panel.)

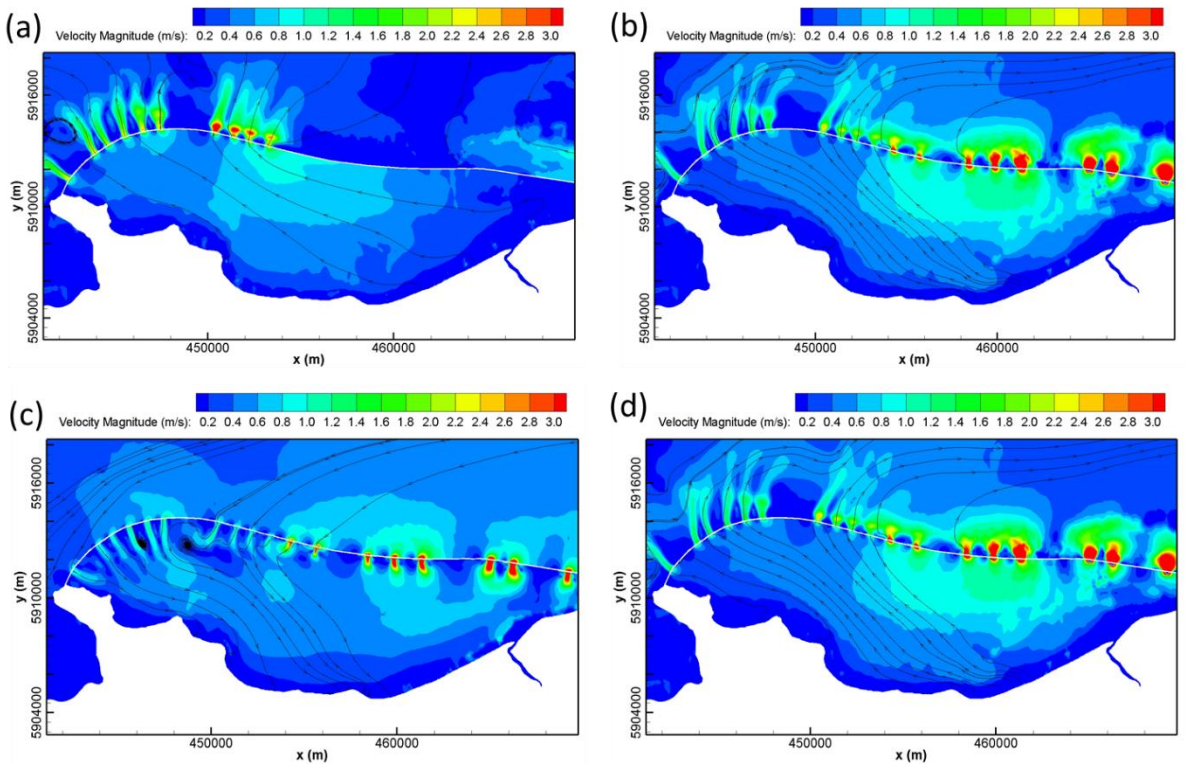

Figure 5.37: Typical instantaneous flow pattern during the two-way operation of the NWTL at (a) ebb generation, (b) emptying phase, (c) flood generation and (d) filling phase.

Figure 5.37 depicts the typical instantaneous velocity magnitude of the NWTL during optimised two-way generation. The velocity close to the turbines is lower than near the sluice gates, due to the great water volume from the sluice gate for its high sluicing area, and also result from the shallower bathymetry on the east side of Colwyn Bay, as seen in Figure 5.34. While several small-scale recirculation zones formed between T1-T2 and T5-T6 during the flood generation and filling phase, no other large recirculation zones appear in the NWTL basin. The existence of recirculation zones beside T1, T6 and T7 during the filling phase indicates the risk of sediment deposition in these low-velocity recirculation zones.

5.5 Summary

The first part of this chapter illustrated the numerical methods for lagoon modelling. An idealised lagoon model was established to test the parameterisation of lagoon structure components. Turbines and sluice gates were modelled as culverts linking two sides of subdomains, with the discharge or power output calculated from the predefined formula. Multipoint averaged water level was used to calculate the water head difference and to

determine the operation stage. A ramp function was implemented to simulate the opening/closing process of the turbine valves and sluice gates.

West Somerset Lagoon (WSL) and Swansea Bay Lagoon (SBL) were simulated in the SEBC model for its relatively small scale, while North Wales were implanted into the CS model. Full momentum conservation between the subdomains was included in all three TRS models by implementing momentum source terms at the turbine locations. Each turbine or sluice gate block was operated independently in WSL and NWTL simulation to accommodate for the time lag of tidal phases, e.g. high water, between different turbine/sluice gate blocks. As a result of these refinements, the WSL and NWTL performed encouraging results, which showed less than 1% and 2.4% differences between TELEMAC-2D and 0D models, respectively.

Different operation schemes were implemented in these TRSs modellings. It was found that although ebb generation has a much higher electricity generation efficiency than the two-way generation scheme in the SBL operation, two-way generation could provide almost 34% more energy than an ebb generation. The additional pumping function can contribute an 8-11%, 15.5%-26%, 15.5% increase in power output for the SBL, WSL and NWTL, respectively. The optimised flexible head generation significantly increases energy output compared with the traditional fixed head generation, e.g., 19% and 6.3% increase for WSL and SBL, respectively. It is noticed that the electricity growth rate from the pumping function or optimised scheme is positively correlated with the scale and installed power of TRS.

It is likely that the flexible generation scheme will be adopted in further TRSs proposed in the future for the appreciable increase in energy generation with no additional investment. Therefore, the following study for all the TRS impact analyses will be based on two-way generation with the optimised flexible head.

To better predict the water jet velocity in the exit of the turbine and sluice gate, momentum conservation was achieved by using a fully conservative momentum formulation which included an additional source term. Different momentum adjustment has been applied compared in WSL and SBL cases, including the adjustments based on the velocity taken from the turbine blade, end of turbine diffusor, and no momentum adjustment. Moreover, a semi-3D momentum term has been implemented by integrating the horizontal velocity along the vertical of the end of the turbine diffusor. The conclusions are the same between WSL and SBL cases that the model without the momentum term is similar to the model with momentum adjustment based on the velocity taken at the end of the turbine diffusor. This indicates that, in this model,

the velocity at the end of the turbine diffusor might be the same as the local current velocity (Hervouet, 2007). If the source velocity is chosen at the turbine blade, the turbine jet will be more significant. The implementation of semi-3D momentum term in the model has a minor impact on the size of turbine jet. It is concluded from WSL and SBL studies that the introduction of momentum term has a noticeable influence on the flow pattern near the lagoon. The momentum term with source velocity included at the end of the turbine diffusor was therefore applied in all subsequent lagoon modelling simulations since it was considered to be more realistic. Further turbine wake measurements and accurate modelling of the wake could improve these predictions in the future.

Chapter 6 Environmental Impact of Tidal Lagoons

Various TRSs have been proposed for sitting within the Bristol Channel and Severn Estuary, but none have yet been developed, due primarily to the potentially significant environmental impacts and the high capital costs (Xia et al., 2010c; Waters and Aggidis, 2016a; Elliott et al., 2018). For example, the proposed Swansea Bay Lagoon has not yet been constructed due to concerns over the electricity costs and concerns about fish kills through the turbines. Other concerns reported have related to the delicate floodplains that are vital to migrating birds (Waters and Aggidis, 2016b). Furthermore, there are areas within the coasts and estuary system that are protected under a number of European and international legislative directives for their unique characteristics and important ecosystem (Ashley, 2014), calling for a thorough investigation of all potential environmental impacts from TRS. Thus, an accurate assessment of the hydrodynamic and hydro-environmental impacts of a TRS, where the performance of the scheme has an impact on the marine environment and ecology, is crucial in optimising the design and development of such schemes.

The main impacts of TRSs, particularly in terms of hydrodynamics, are the changes that arise in the water levels and tidal velocities both within and outside of the impoundment, and the consequential impact on the estuarine environment and ecology. For example, changes in the water levels, and particularly the tidal range, as a result of the operation of a TRS can alter the risk of flooding (Ahmadian et al., 2014b; Ma, 2020). Alterations to the tidal hydrodynamics can also significantly impact the solute and suspended sediment concentrations in the estuary, thereby affecting the geomorphological and benthic environments (Kadiri et al., 2012; Gao et al., 2013; Xia et al., 2010c). Thus, the impacts of any such scheme on the tidal elevation and tidal flow in an estuarine basin are essential to predict in the preliminary analysis of the design and operation of a TRS proposal.

Furthermore, the changes that arise in the water levels both within and outside of the impoundment can cause a significant loss of intertidal mudflats, particularly within the impounded area. Any pronounced loss of intertidal zones can significantly affect the feeding opportunity and habitat area for birds, marine mammals and fish (Kirby, 2010; Adcock et al., 2015). Previous research has shown that the operation of a TRS can have both positive and/or negative impacts on water quality by altering the dispersion and distribution of solutes discharged into the system (Kadiri et al., 2014a; Kim et al., 2017; Evans, 2017), which consequently impact the flushing of dissolved nutrients and turbidity (Nash et al., 2011). These

impacts were being investigated through predicting the water renewal capacity and water renewal time (Matta et al., 2018; Monsen et al., 2002). Moreover, the concentration of dissolved nutrients is closely influenced by the water renewal capacity, and may potentially increase the risk of eutrophication. The eutrophication will then accelerate the growth of algae and other plant life, which may lead to undesirable alteration to the balance of organisms in the water body, e.g. harmful algal blooms, dissolved oxygen depletion and changed PH value (Painting et al., 2007). These alterations would, in turn, result in the deterioration of the ecosystem, loss of biodiversity and increase the mortality of some aquatic organisms, e.g. invertebrates and fish. Thus, it is important to assess how the operation of a TRS would affect the water renewal capacity, suspended sediment transport, the eutrophication potential and the phytoplankton growth of an estuary. However, very little research has been undertaken and reported in terms of the above hydro-environmental influence.

This chapter focuses on studying the hydrodynamic and hydro-environmental impact of the proposed TRSs, i.e., WSL, SBL and NWTL. Section 6.1 - Section 6.4 discussed the basis hydrodynamic impact of TRSs and some of the direct environmental influence, providing the preliminary influence of TRS. Section 6.1 and Section 6.2 investigated the changes of main tidal harmonic constituents and the maximum sea water level, along with the loss of low-level intertidal mudflat resulting from the rise of low water level. Then the Section 6.3 and Section 6.4 presented the maximum velocity magnitude change and the maximum bed shear stress change around the TRSs. The following Sections 6.5 – Sections 6.7 explored the further hydro-environmental influence of TRS, with more research methods developed based on TRS hydrodynamic modelling. The water renewal capacity change with TRS operation was investigated in Section 6.5 by calculating the water residence time, which is estimated by studying the decay characteristics of a passive mass-conservative tracer. Section 6.6 studied the suspended sediment transportation and bed evolution by building a suspended sediment simulation model. Last, with the updated water residence time and the turbidity information achieved from the previous section, Section 6.7 explored the influence of WSL operation on eutrophication potential and phytoplankton growth in the region of Severn Estuary to the inner Bristol Channel.

6.1 Impacts on Tide Constituents

To understand the impact of the lagoon on tidal elevation, the impact of WSL on tidal constituents were studied individually and the results are summarised in Figure 6.1. It can be seen that the operation of the lagoon has generally decreased the amplitude for the M2, N2 and S2 tidal constituents in the inner Bristol Channel and towards the head of the estuary, and particularly after passing WSL in the upstream direction. Furthermore, as for the M2, N2 and S2 phases, these are also noticeably affected by the lagoon, again particularly towards the east of the lagoon and up to the Severn Estuary. In other words, WSL decreases the amplitude of these three tidal constituents in the region and particularly to the east of the lagoon and towards the head of the estuary. In contrast, the phase has decreased slightly to the west of WSL, while it has increased to the East. Thus, the influence of WSL on the tidal harmonic constituents is predicted to be greater towards the head of the estuary, which is thought to be particularly pronounced due to the convergence of the estuary and the natural frequency of the Bristol Channel and Severn Estuary.

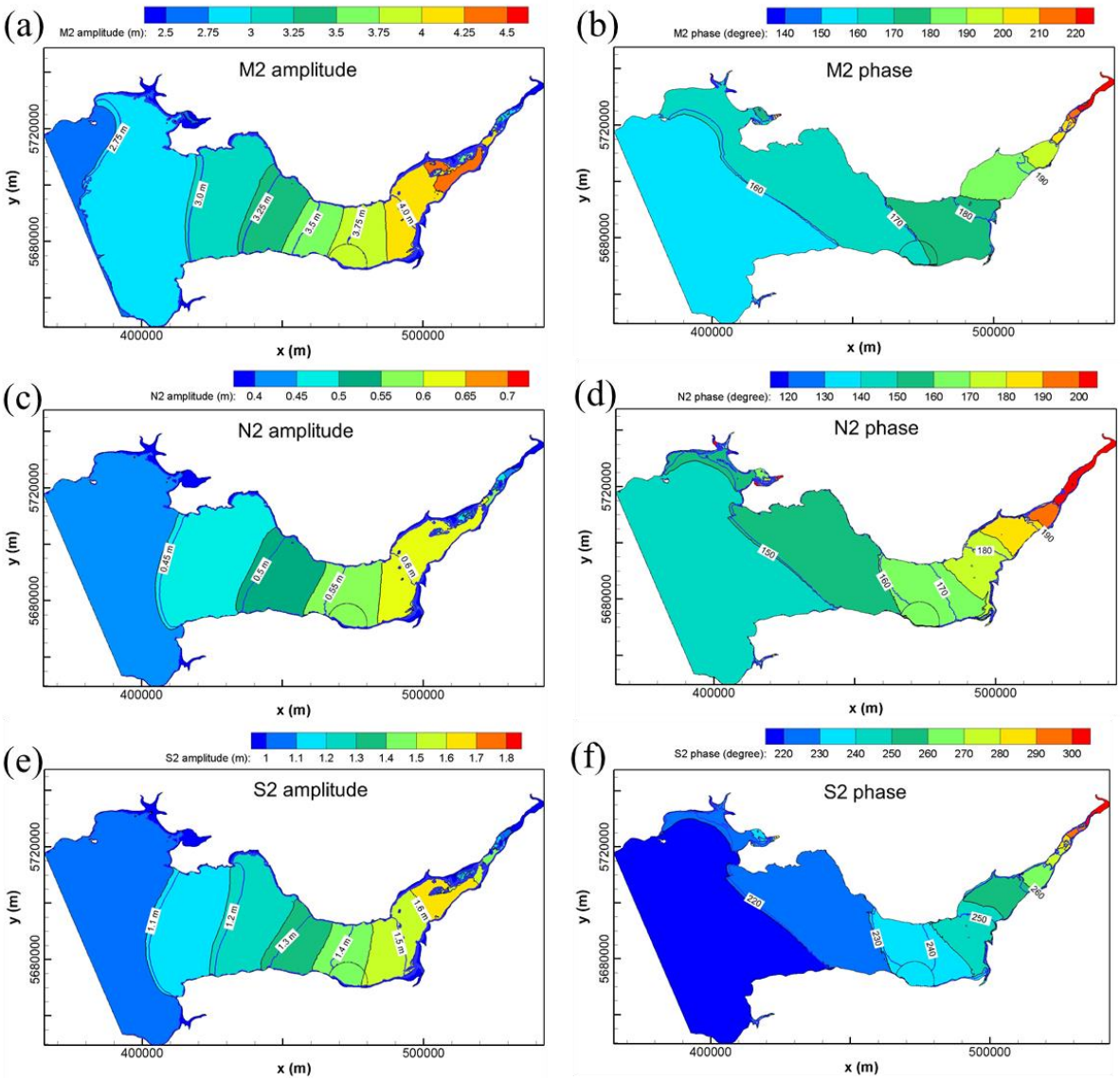

Figure 6.1: Comparison of cotidal charts for M2, N2, S2 before and after the construction of WSL. (a),(c) and (d) the amplitude of M2, N2 and S2; (e), (d) and (f) the phase of M2, N2 and S2. (The colour contour represents the tidal constituents for pre-lagoon construction and the purple line with a label refers to post-lagoon scenario)

The change of the major tidal constituents with the operation of SBL is shown in Figure 6.2. It is observed that SBL causes negligible changes on the harmonic constituents in the Severn Estuary and Bristol Channel region due to its small scale. There is almost no resonance response of the Bristol Channel, while a slight amplitude decrease is observed in the Severn Estuary, which can be explained by the funnelling shape and the resonance effect of the channel (Ma, 2020).

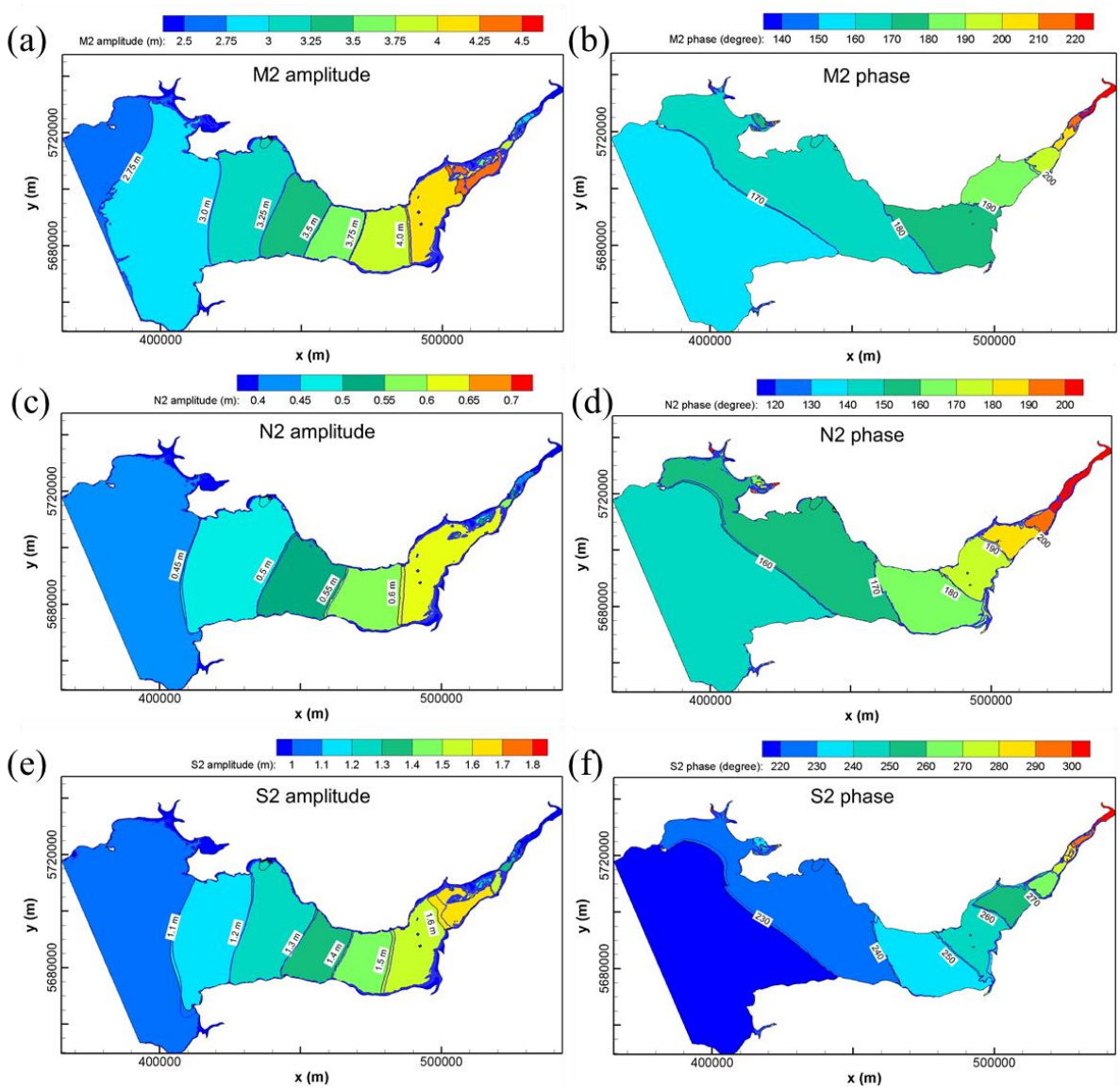

Figure 6.2: Comparison of cotidal charts for M2, N2, S2 before and after the construction of SBL. (a),(c) and (d) the amplitude of M2, N2 and S2; (e), (d) and (f) the phase of M2, N2 and S2.

Figure 6.3 and Figure 6.4 show the resonance response of the Irish Sea and the part of Celtic Sea to the presence of NWTL. The amplitude and phase of M2 shift slightly in the near-field of NWTL while the influence on N2 is more noticeable and extend farther. A minor decrease of both M2 amplitude and phase is observed in the north of NWTL, and no obvious far-field oscillation is presented. The change of N2 extends farther, with both the amplitude and phase increase in the middle Irish Sea and north of Celtic Sea, especially around the amphidromic point off the east coast of Ireland.

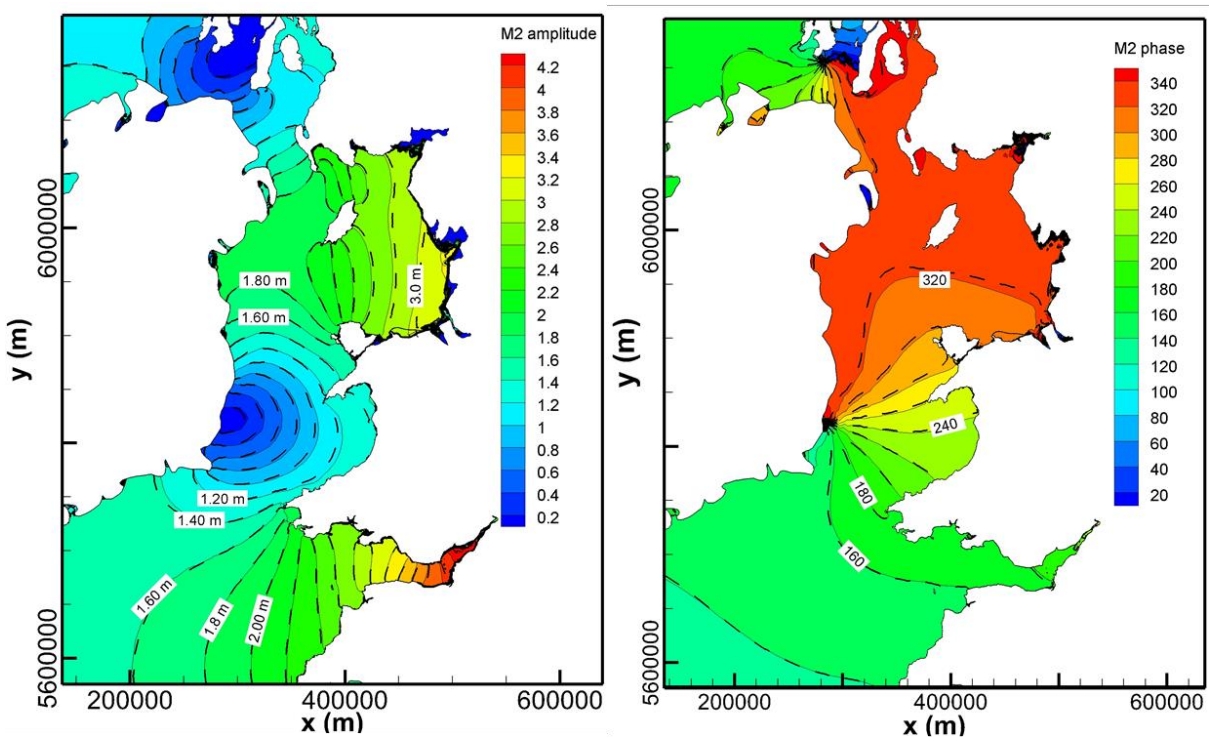

Figure 6.3: Comparison of cotidal charts for M2 before and after the construction of NWTL. (The colour contour represents the tidal constituents for pre-lagoon construction and the dot line with a label refers to post-lagoon).

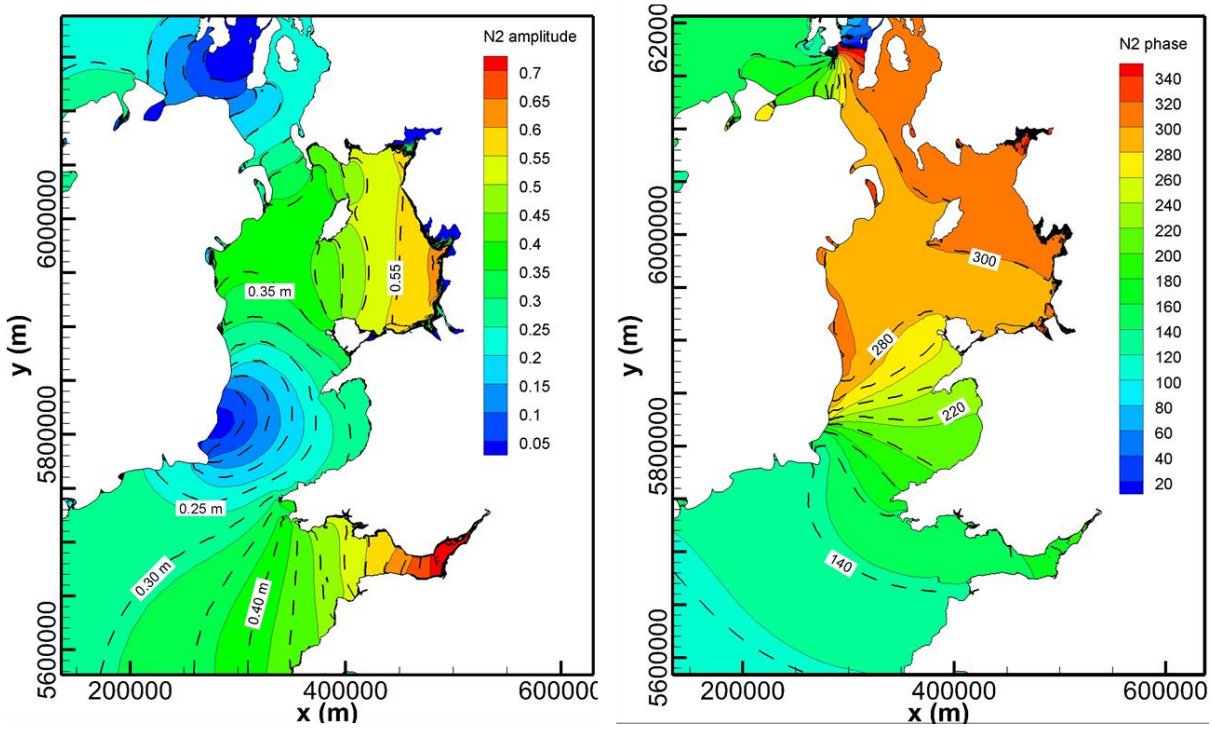

Figure 6.4:Comparison of cotidal charts for N2 before and after the construction of NWTL.

6.2 Impacts on Water Level and the Intertidal Flat

6.2.1 Case I: WSL

The model predictions showed that the highest water levels inside the lagoon dropped up to 1.2 m as a result of the operation of WSL, as illustrated in Figure 5.19 (a). Figure 6.5 shows that in the middle and inner Bristol Channel, the water level has dropped by 0.05 - 0.2 m. The changes in the peak water levels across the domain were more remarkable within the Severn Estuary and were predicted to be 0.2 - 0.3 m. The envelope curves of high water levels along the estuary in Figure 6.6 confirm this phenomenon, in that the high water level upstream of Rhossili decreased for the post-lagoon condition, while the high water level near the open boundary increased slightly. These results suggested that the reduction in flow area across the Bristol Channel at the WSL site had an effect on the resonance characteristics of the tide as it propagated up the Bristol Channel and Severn Estuary.

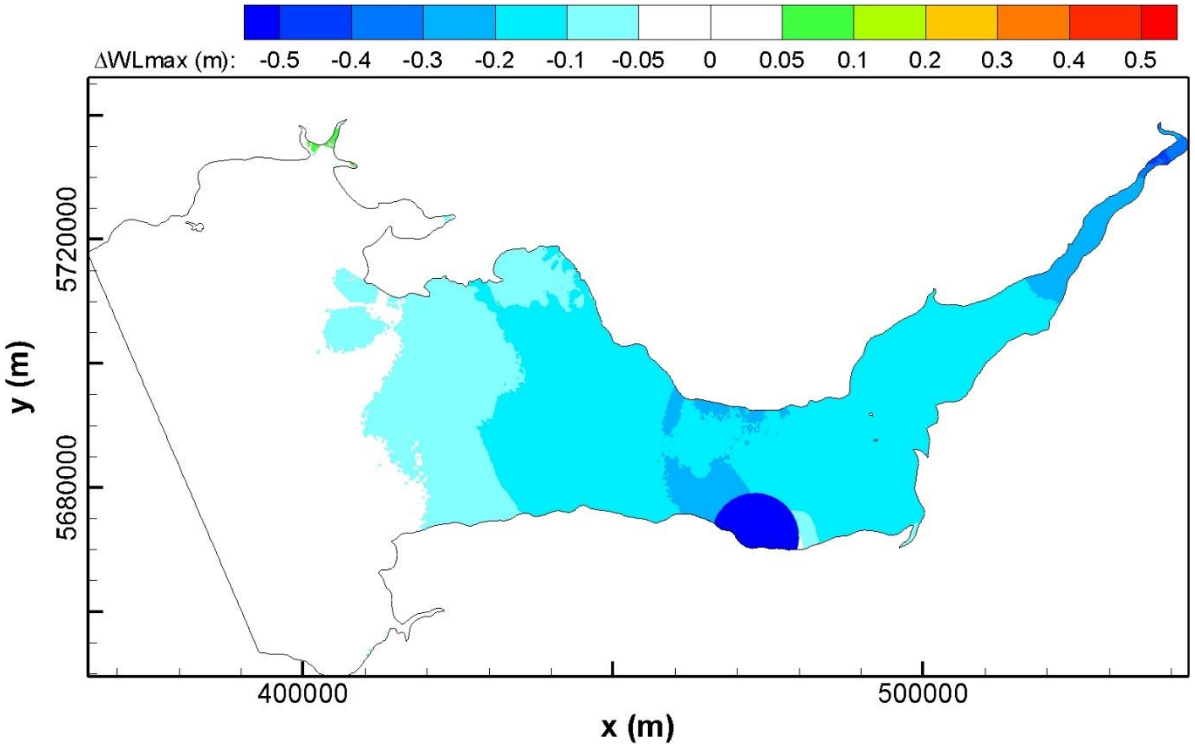

Figure 6.5: The cumulative effect of WSL on maximum water level during a spring-neap tidal cycle.

Table 6.1: High and low water level differences with WSL at selected sites in the Bristol Channel and Severn Estuary. (DHWS: Difference in water level at high spring tide; DLWS: Difference in water level at low spring tide; DHWN: Difference in water level at high neap tide; DLWN: Difference in water level at low neap tide)

Site	DHWS(m)	DLWS(m)	DHWN(m)	DLWN(m)
Proposed Lagoon Scheme				
Cardiff Lagoon	-0.165	0.266	-0.070	0.121
Swansea Bay lagoon	-0.094	0.031	-0.019	0.036
Severn barrage	-0.155	0.271	-0.052	0.088
Newport Lagoon	-0.151	0.253	-0.077	0.162
Bridgewater bay Lagoon	-0.141	0.300	-0.054	0.085
The Docks				
Avonmouth dock	-0.156	0.187	-0.086	0.132
Cardiff dock	-0.155	0.198	-0.056	0.072
Swansea dock	-0.091	0.072	-0.008	0.022
Porlock dock	-0.164	0.18	-0.088	0.045
Birds feeding area				
Bridgwater Bay	-0.091	0.256	0.042	0.135
Welsh grounds	-0.154	0.110	-0.103	0.161
Important Sea defences				
Hinkley nuclear power station	-0.094	0.322	-0.015	0.068
Somerest	-0.156	0.040	0.008	0.010
Peterstone flats	-0.157	0.264	-0.071	0.088
Slimbridge	-0.368	0.012	-0.276	0.011

There are a number of cities and towns and key infrastructure (such as the Port of Bristol) located along the Severn Estuary and Bristol Channel. These predicted changes in the peak water levels are generally insignificant and will only have a modest impact at the various coastal sites and facilities, such as the Port of Bristol. Table 6.1 lists the high and low water level changes in spring tide (DHWS and DLWS) and neap tide (DHWN and DLWN) at various locations along the basin after the introduction of WSL. For the potential tidal range energy plants, the positive value of DLWS/DLWN and negative value of DHWS/ DHWN means that

the tidal range will decrease slightly at several of these sites, which will lead to a limited reduction in the estimated energy output at some sites after the construction of WSL.

The critical indicator for shipping is the minimum water level that determines the available time for manoeuvering into docks, etc. While a positive value of DLWN for docks refers to an increase in the minimum water level, this means that the shipping industry and leisure yachting, etc. could benefit marginally from WSL. Furthermore, the positive DLWN and negative DHWS at the key bird feeding sites would also mean a slight increase in the minimum feeding area and a corresponding decrease in the maximum feeding area. Furthermore, the positive DHWS stands for a drop in the peak water level at some important sites, thereby reducing the relative risk of flooding at these sites.

In considering the predicted changes in the water levels after including WSL, these changes are all relatively small and within the error of measurement at the reported observation gauge sites, as shown in Figure 6.6. Moreover, for more accurate predictions of the impact of WSL then the open seaward boundary should be extended beyond the existing location and seawards to the Continental Shelf; this would remove any potential impact of the lagoon on the open boundary.

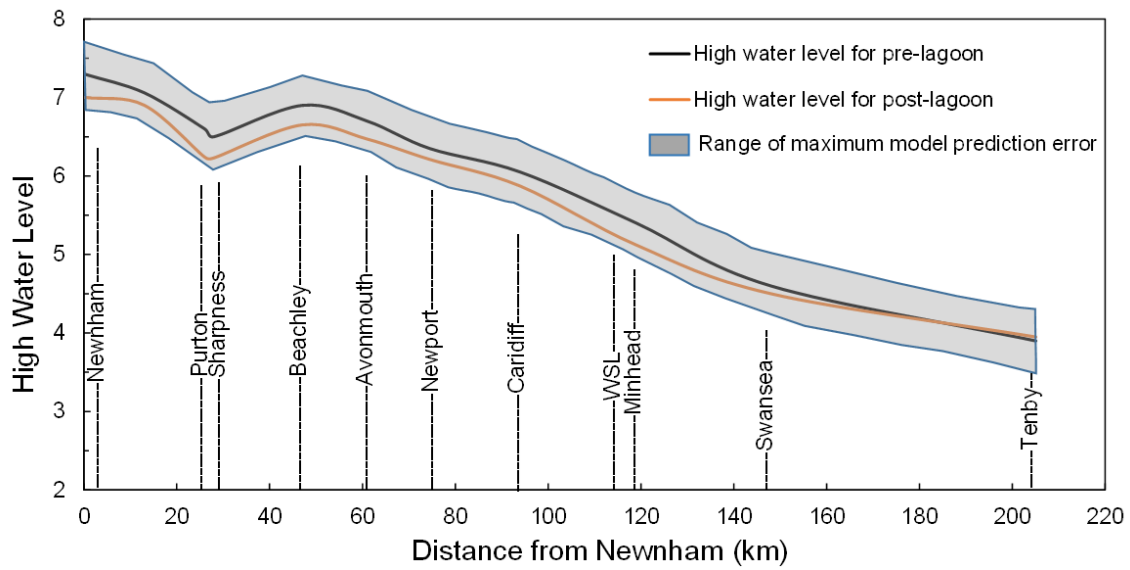

Figure 6.6: Envelope curves of high water levels for pre- and post-WSL and maximum predicted model deviation.

Changes to the intertidal mudflats zones are considered as one of the key ecological concerns of tidal range schemes. Intertidal zones are important feeding habitats for birds, mussels and insects, which are crucial for the biodiversity of the estuary (Burton et al., 2010; Clark, 2006). Figure 6.7 (a) shows that the construction and operation of WSL would slightly reduce the maximum intertidal area during low water levels for both spring and neap tides, while the minimum area generally would remain unchanged at the same level. The area change in Figure 6.7 (b) confirms that WSL could decrease the mudflat area during most of the tide cycle by up to 20 km^2, mainly in the upper Severn Estuary. The loss of the intertidal mudflats is mainly caused by an increase in the predicted low water level, with a slight increase in the water level causing a noticeable decrease in the intertidal area in some parts of the estuary. The instantaneous changes in the intertidal areas are shown in

Figure 6.8. It can be seen that with the operation of WSL, the intertidal mudflat region around Welsh Grounds, the Severn Beach and the outer Severn Estuary have all decreased slightly. It should be noted that the changes in these areas are mainly due to the shallow bathymetry and the gentle slope, which makes them very sensitive to modest changes in the lowest water levels. There are some other factors that need to be included for an accurate qualitative prediction of the changes, including: the qualitative change occurring for specific wetland conservation areas, whether the lagoon can be operated specifically to minimise its impact on intertidal mudflats, the period that intertidal area is submerged within a day and the relationship with bird feeding times. Therefore, further studies are required to identify more accurately the impact of the lagoon, and its operation, on the intertidal mudflats and particularly in the Severn Estuary.

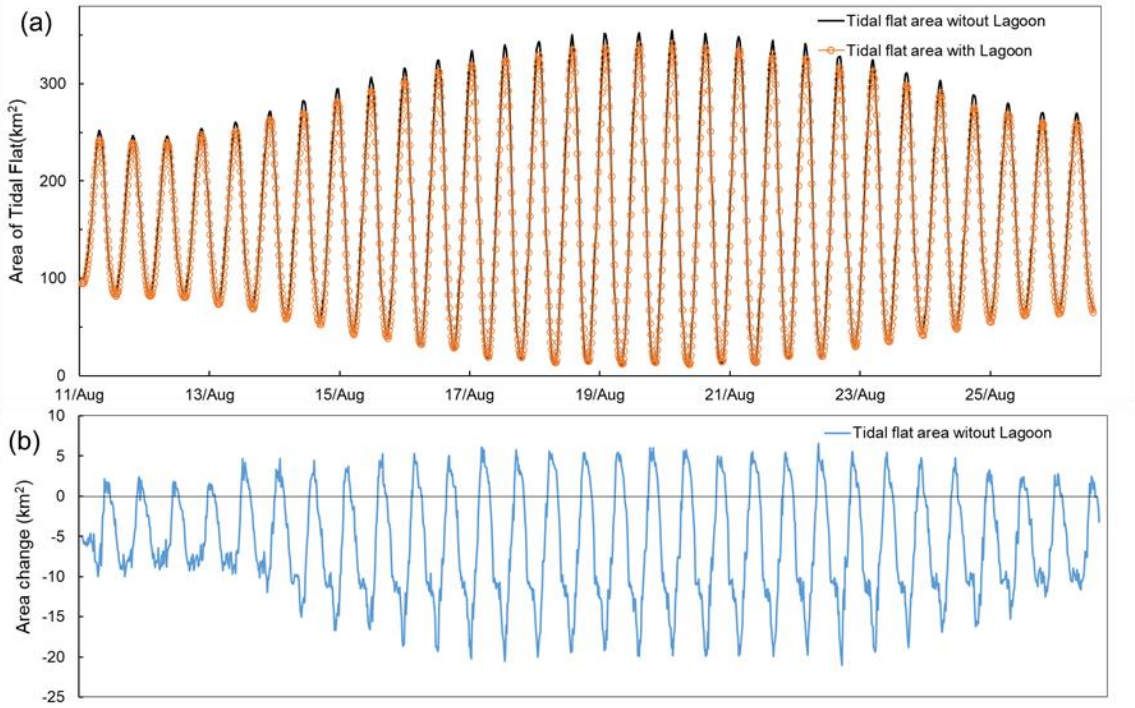

Figure 6.7: Change in intertidal mudflat areas before and after the construction of WSL, (a) the area of tidal flat area for pre- and post-WSL; (b) the change in tidal flat area with WSL.

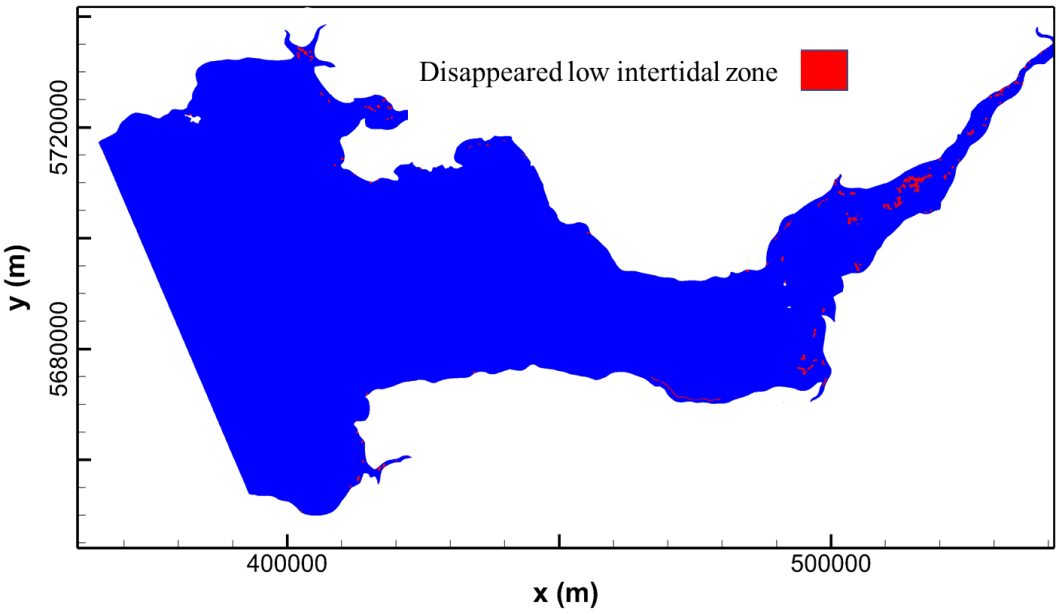

Figure 6.8: The loss of low intertidal zone after the operation of WSL.

6.2.2 Case II: SBL

There is approximately 1.45 m reduction in the maximum water levels in the SBL basin, as indicated in Figure 5.30, and about the same value in the rise of the minimum water level.

Figure 6.9 shows the presence of SBL on the maximum water level change in the region of Swansea Bay. Trivial water level oscillation is found outside the SBL basin area due to the small impoundment area and low water storage volume, with a minor high water level decrease (less than 5 cm) at the west side of SBL. The research result agrees with previously reported research, compared with Figure 2.12 and Figure 6.10. However, different water level changes occur in the SBL basin mainly due to the different operation schemes. For example, Angeloudis and Falconer (2017) adopted a two-way generation on SBL with 4.10 m generation start head and 1.00 m minimum generation head, obtaining a prediction of a 0.65 m reduction in maximum water levels and an increase of 0.35 m in minimum water levels. Čož et al. (2019) predicted an approximate 1.4 m reduction in maximum water levels and 1.33 m increase of minimum water levels, with the start and end generation heads of 2.5 m and 1.5 m, respectively.

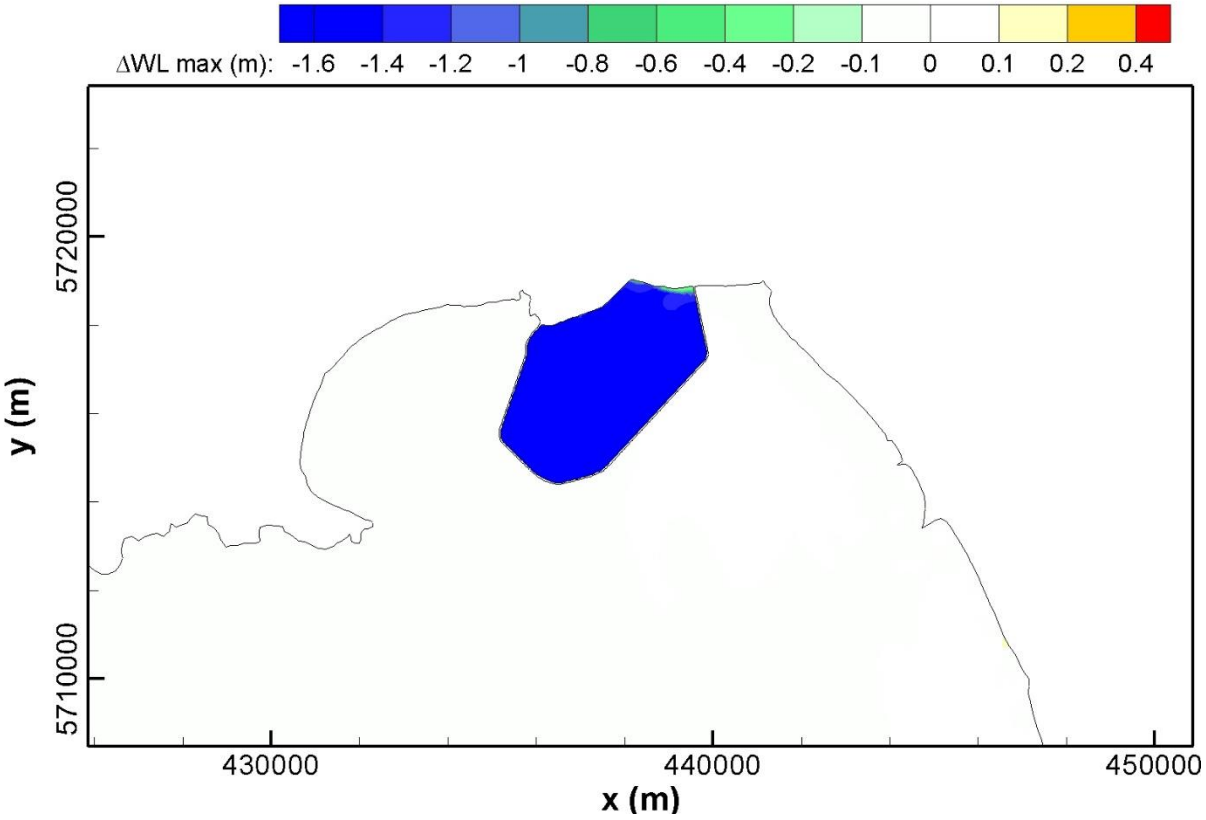

Figure 6.9: The cumulative effect of SBL on maximum water level during a spring tidal cycle.

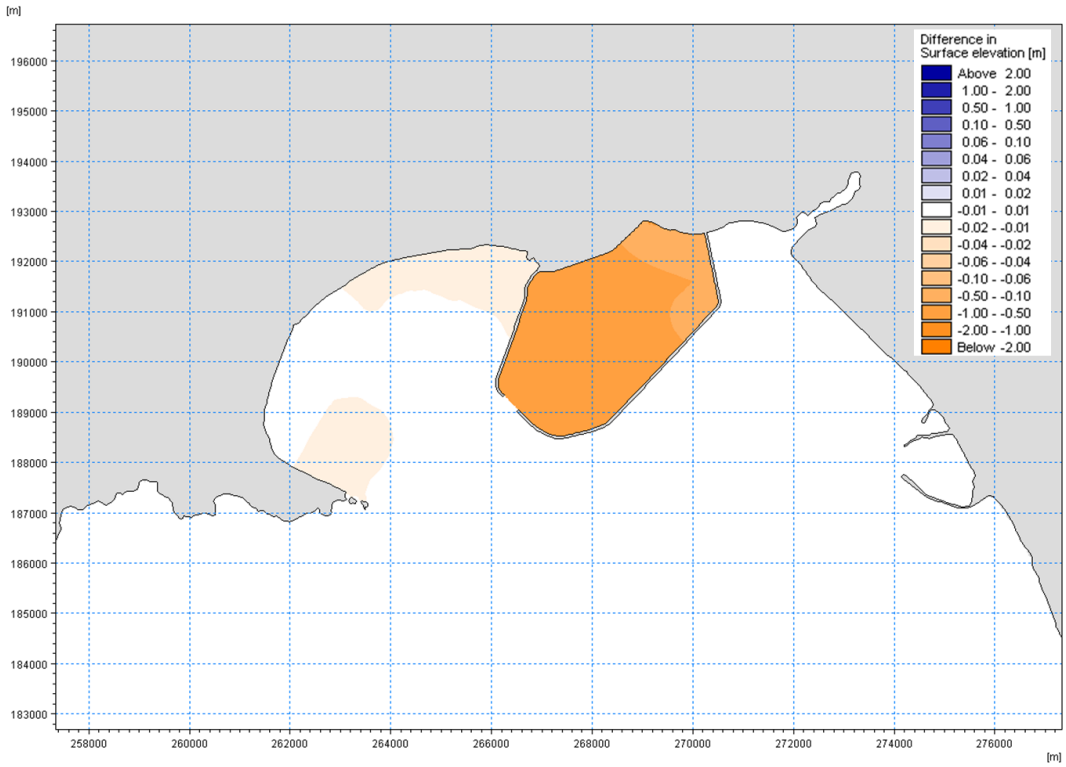

Figure 6.10: Predicted changes to mean high water level of spring tide (MHWS) (Tidal Lagoon Plc, 2013).

Although the water level variation by the presence of SBL is confined within the impoundment area, the knock-on effect, such as intertidal area change, is still regarded as one of the resistance to the SBL construction (Messenger, 2016). The alteration of the low-level intertidal mudflats zones triggered by the operation of SBL is shown in Figure 6.11. The loss of the low-level intertidal mudflats zones is mainly confined on the low-slope beach inside the SBL impoundment area, which is up to 1.027 km^2, while no loss of intertidal zone occurs outside of SBL. It is doubtful that this small intertidal mudflat variation within SBL would seriously negatively impact the bird population, as they are likely to adapt to the changes by finding food in adjacent areas. However, the specific effects could only be achieved by extensive bird surveys, including specific species, bird behaviour, etc.

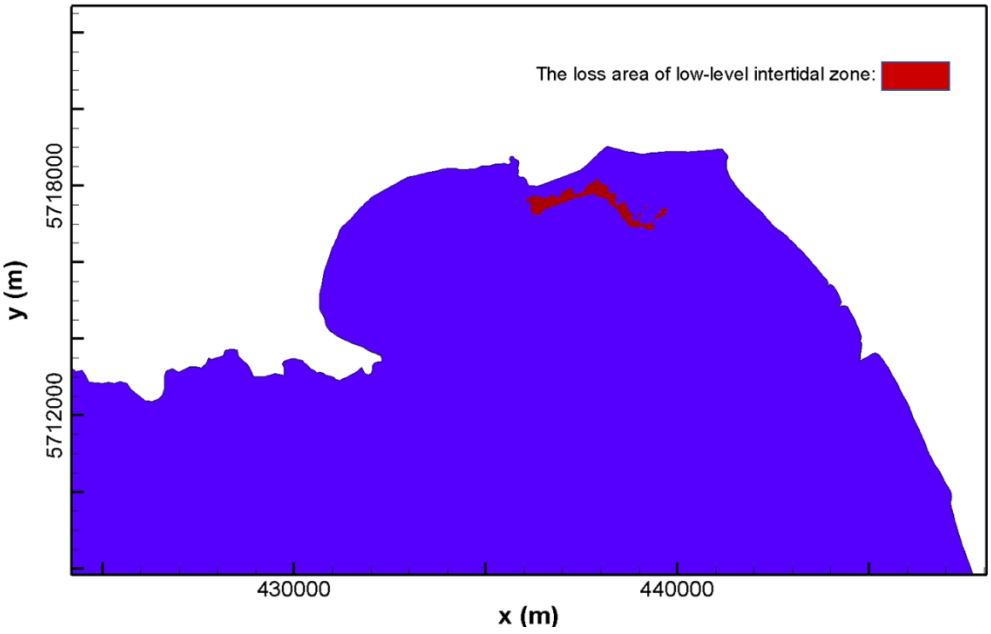

Figure 6.11: The loss of low-level intertidal mudflats after the construction of SBL.

6.2.3 Case III: NWTL

As shown in Figure 6.12, the significant reduction of the high water level inside the NWTL effectively reduced the flooding risk of North Wales from the storm and long term sea-level rise (Ahmadian et al., 2014b). Furthermore, the presence of NWTL would slightly reduce the high water level in Liverpool Bay while increasing it in Cardigan Bay, with both variations ranging from 5 - 10 cm. However, it is difficult to distinguish if the slight influence on far-field like Cardigan Bay results from the deviation of the numerical model prediction.

Figure 6.13 shows how the NWTL influence the low-level intertidal mudflats zones. There is a noticeable loss of low-level mud flat inside the NWTL basin, up to 20 km^2, due to the relative high bathymetry and the gentle slope in this area, as shown in Figure 5.34. It should also be noticed that the above estimation of the intertidal mudflat change is a preliminary study. Only essential dredging work was carried out near the turbine and sluice gates block in this modelling study, due to the lack of information for the preliminary design stage of NWTL. In the later design or the construction process, deep dredging work is expected to be carried out over a large area, which will mitigate the change of the low-level mudflat area.

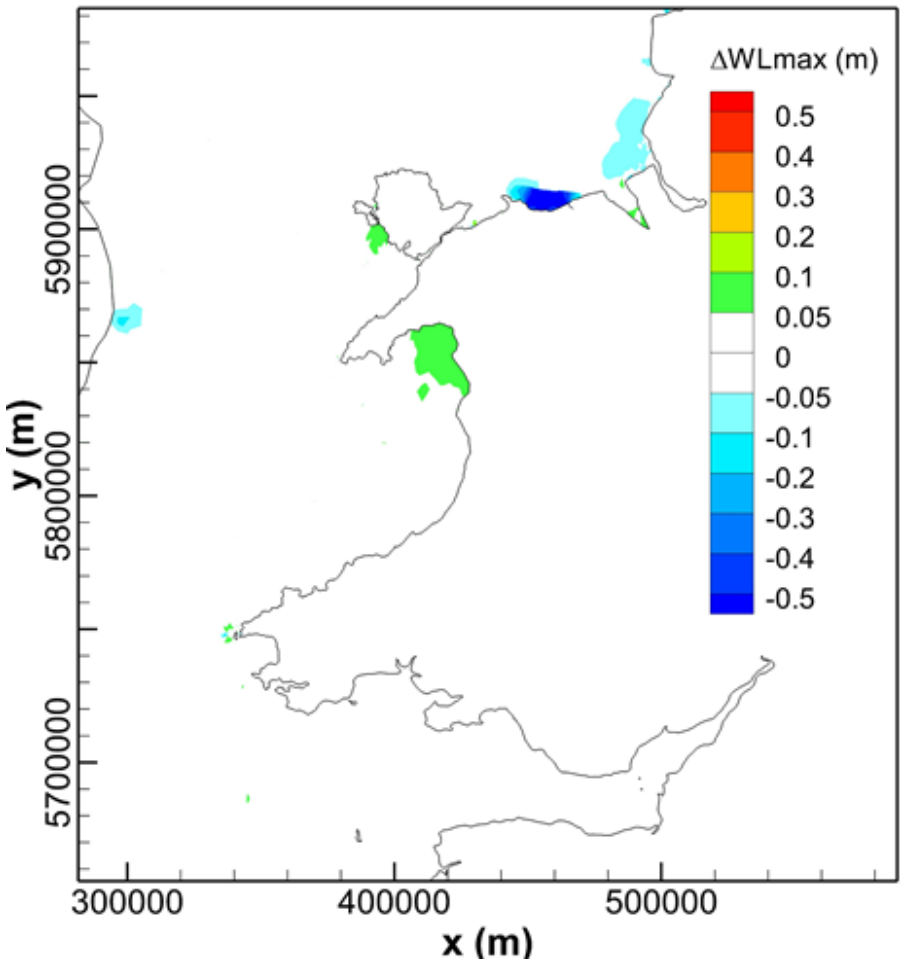

Figure 6.12: Cumulative effect of NWTL on maximum water level during a spring-neap tidal cycle.

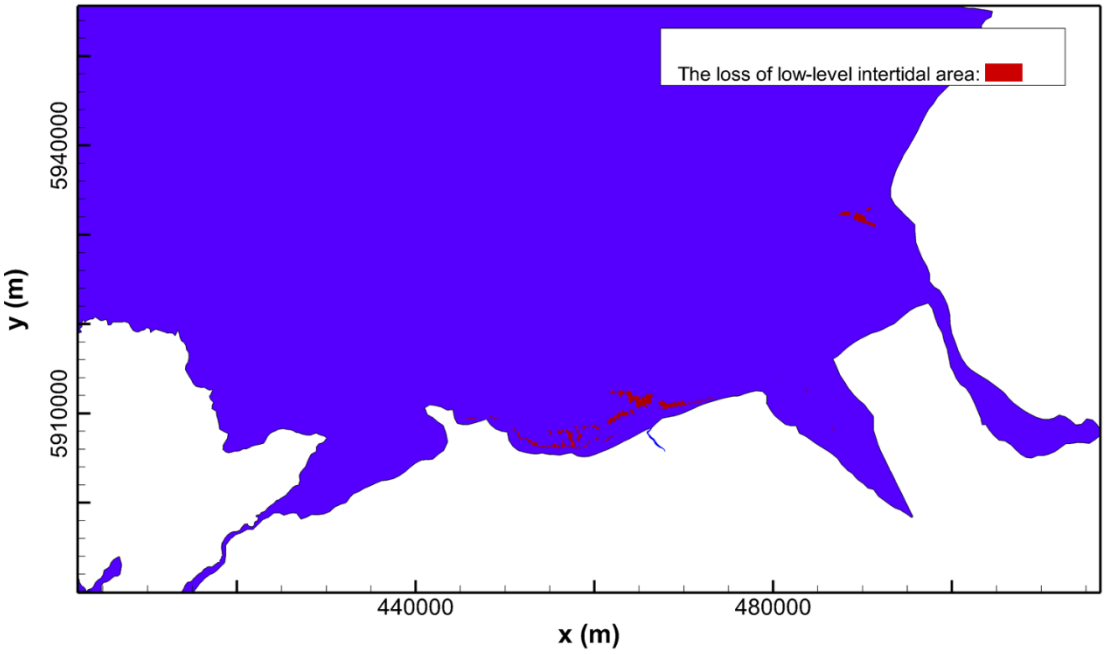

Figure 6.13: The loss of low level intertidal mudflats after the construction of NWTL.

6.3 Impacts on Maximum Velocity Magnitude

6.3.1 Case I: WSL

The introduction of WSL structure and the operation of the turbines and sluice gates changed the tidal currents, to varying degrees, across the model domain. Figure 6.14 shows the accumulated impact of WSL on the current speed during a maximum spring tidal cycle. As expected, the existence of a jet in the exit of turbines and from the sluice gates results in a significant increase in the maximum velocity magnitude of up to 1.5 m/s, in the vicinity of the turbines and sluices. The corresponding current speed in the inner Bristol Channel, further away from the structure, show a typical increase of 0.25 to 0.75 m/s. These changes in the velocities are more noticeable closer to WSL. This is to be expected due to the blockage effect of the scheme which reduced the effective cross-sectional area of flow across the Bristol Channel at the lagoon site, thereby resulting in slightly higher velocity magnitude in the region. However, the velocity magnitude inside the impoundment was markedly reduced except in the vicinity of the turbine and sluice gate wakes. This is consistent with the pattern observed at other TRSs (Bray et al., 2016; Čož et al., 2019; Angeloudis et al., 2016b) and is primarily due to the limited interaction between the water volume within the basin and the natural flow in the estuary and outside of the lagoon. There is a relatively large area to the west of the WSL where the velocity magnitude is predicted to be reduced, which contributes to the blockage effect of the lagoon on the freestream flow as observed around headlands and natural obstructions (Guo et al., 2020; Neill and Scourse, 2009). Moreover, the lower natural velocities on the shallower bathymetric region to the eastern side of WSL causes a greater increase in the maximum velocity magnitude in the vicinity of the turbines and sluice gates in comparison with conditions on the western side of the scheme.

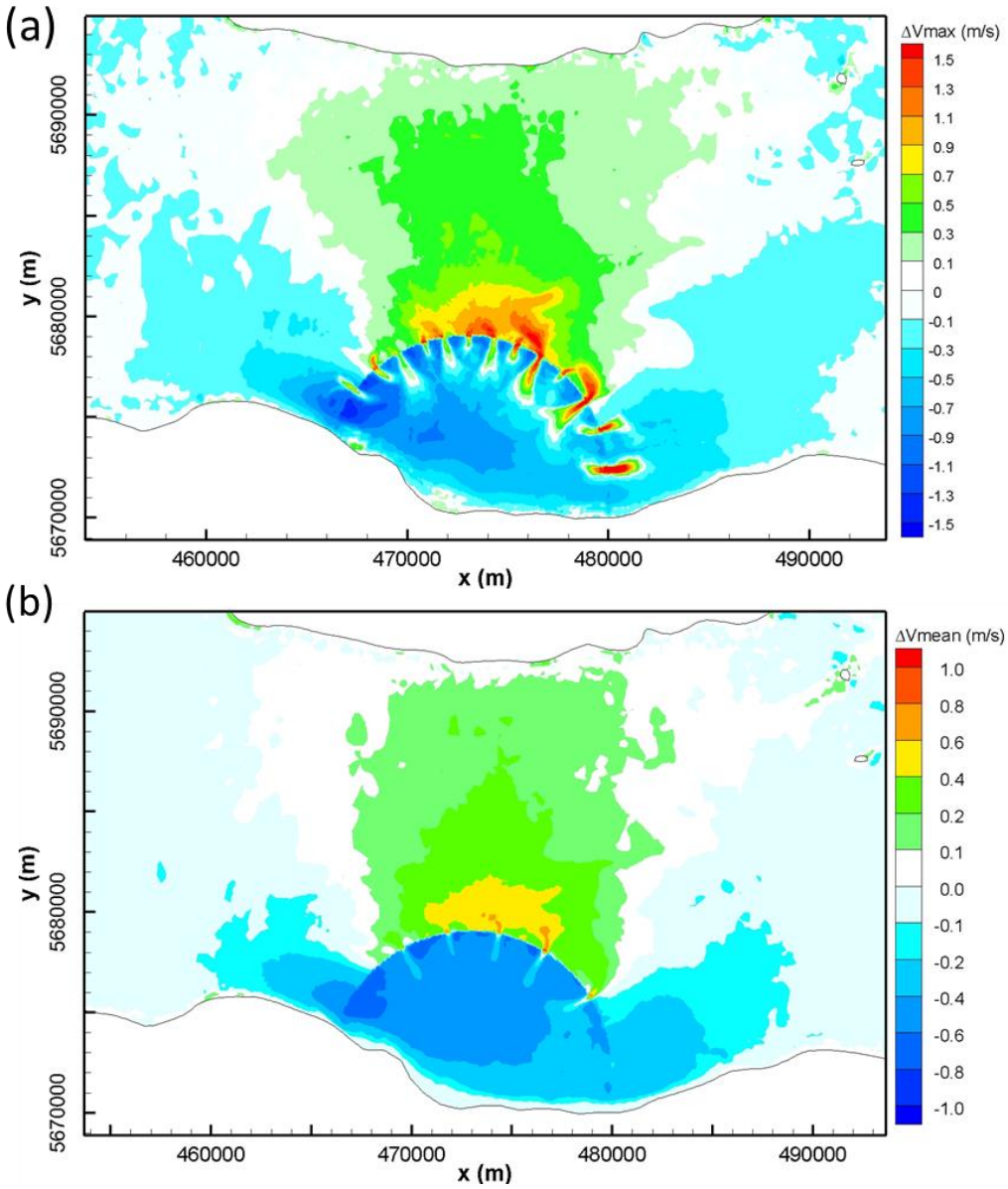

Figure 6.14: The cumulative effect of WSL on (a) maximum current speed and (b) averaged current speed for a spring-neap tidal cycle. ΔVmax is the difference in the maximum current speed and ΔVmean refers to the average current speed difference during the spring-neap tidal cycle.

6.3.2 Case II: SBL

The influence of SBL operation on maximum and averaged current speed is shown in Figure 6.15 and Figure 6.16, respectively. It should be noted that the mean current speed is averaged over spring tide to compare with the previous study (Tidal Lagoon Plc, 2013).

Similar to the maximum water level change, the influence of SBL on current speed is also limited within Swansea bay. The water jet through turbine and sluice gates results in a

noticeable direct increase of maximum velocity magnitude in the influence region, which exceeds 1.5m/s. A visible current speed reduction zone presents at the south of the SBL impoundment, leading to potential sedimentation risk. The average velocity magnitude increased up to 0.75 m/s in the turbine wake. While in the west side of Swansea Bay and the SBL impound area away from the turbine wake, slightly reduced averaged velocity magnitude is observed.

The alterations to current speeds in this study are at the same level as previous research, as shown in Figure 2.12 and Figure 6.17, and the influence is mainly restricted near the SBL structure, especially around the turbine and sluice gates. However, a difference could be observed in the core velocity of the turbine jet among different research, which might be associated with the momentum conservation, or the difference of the Hill chart that applied.

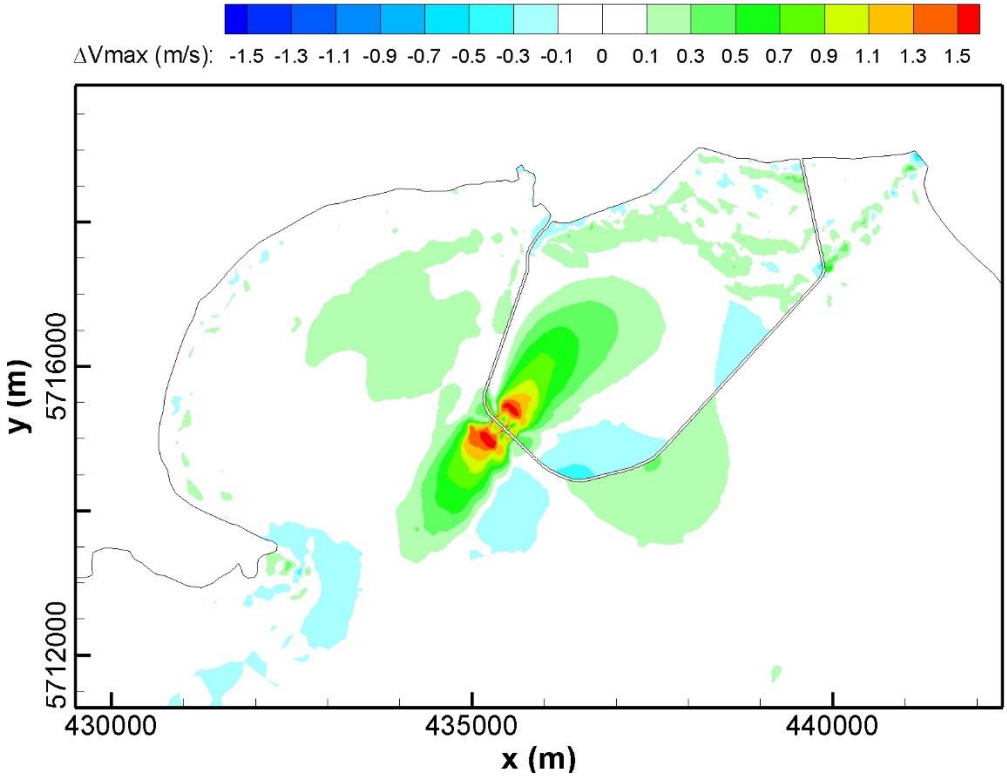

Figure 6.15: The cumulative effect of SBL on maximum velocities magnitude during a spring-neap tidal cycle.

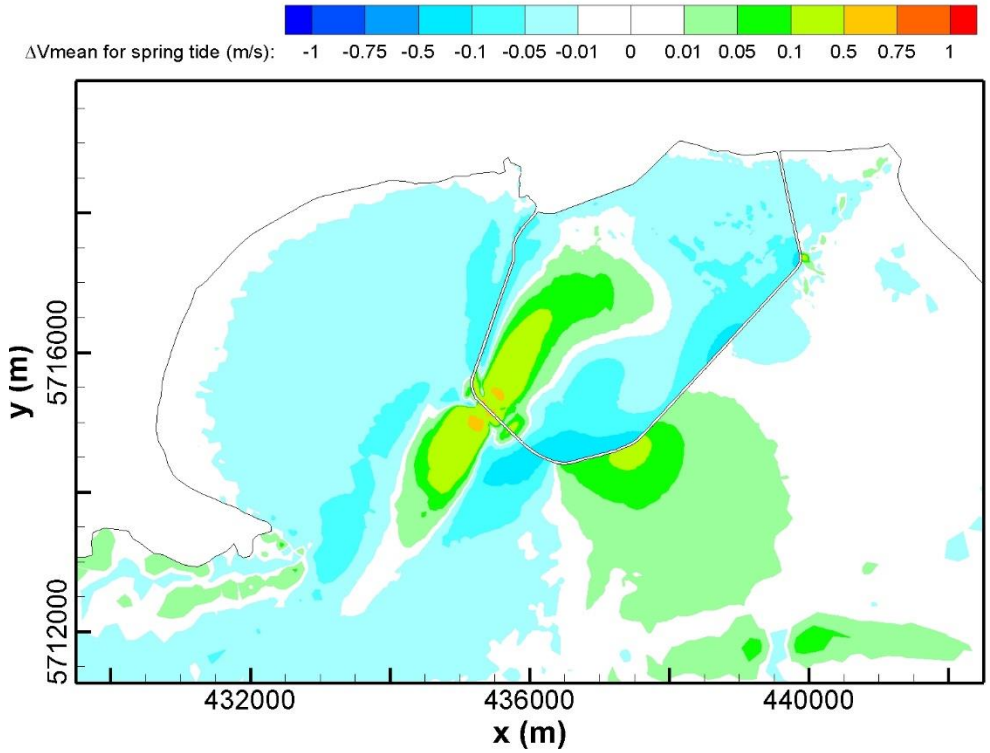

Figure 6.16: The cumulative effect of SBL on maximum velocities magnitude and averaged velocities during a spring-neap tidal cycle.

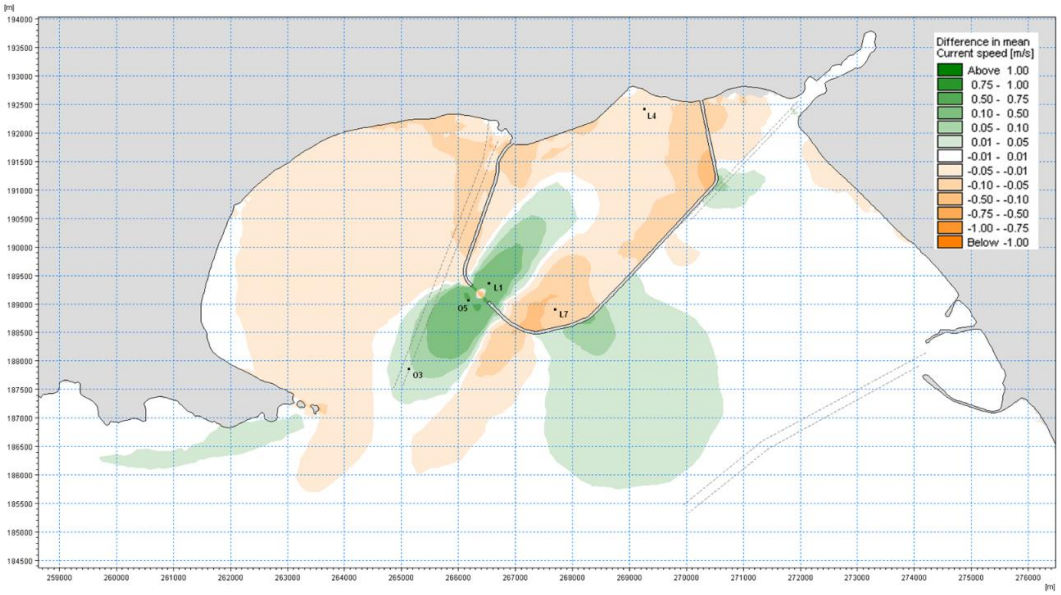

Figure 6.17: Predicted difference in mean spring tidal flow (Tidal Lagoon Plc, 2013).

6.3.3 Case III: NWTL

The predicted maximum current speed variation for the presence of NWTL is shown in Figure 6.18. The impact of the NWTL operation on tide speed is mainly concentrated in the near-field and within the impoundment basin. Noticeable current speed acceleration occurred at the exits of the turbines and the sluice gates due to the released water jets. However, the accelerated flow is more noticeable around sluice gates due to the shallower bathymetry in this region and the relatively large sluicing area. Given the dredging workload would be needed near the turbine and sluice gates, which might have a different impact on velocity change in the actual project.

Besides the significantly increased velocity magnitude near the turbines, 0.1-0.6 m/s increase of velocity also occurs in most areas inside the NWTL. This phenomenon is inconsistent with previous research results from many other TRSs, that current speed usually decreases in most TRS impoundment regions. The increased current speed inside the NWTL occurred should be contributed by the split layout of the turbines and sluice gates, which caused a convergence of a water stream along the east-west direction inside the lagoon basin, as shown in Figure 6.18. Furthermore, the operation of NWTL also introduced a 0.1-0.3 m/s velocity magnitude variation in the River Dee estuary, which is probably caused by irregular shallow bathymetry in the River Dee estuary, as seen in Figure 5.34.

The high tidal velocity to the west of Anglesey has long attracted research on the deployment of tidal stream turbines (Haverson et al., 2017; Lewis et al., 2015; Serhadlıoğlu et al., 2013). However, Figure 6.18 shows that the operation of the NWTL would introduce velocities fluctuations at the northwest side of Anglesey. The detailed development scheme of tidal stream energy schemes in this area remains unclear. However, even trivial alteration of the tidal current speed would have a noticeable cumulative impact on tidal stream energy generation over a long period. Thus, an integrated tidal energy development strategy that includes all promising projects is needed to avoid potentially negative interactions.

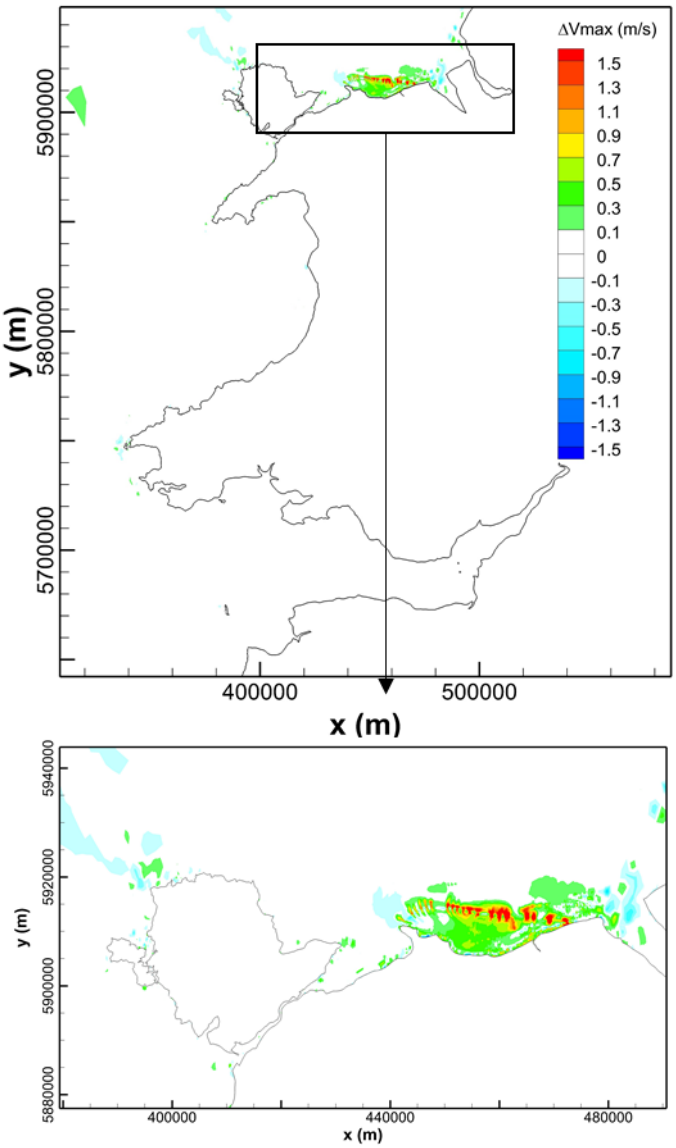

Figure 6.18: Top, regional maximum velocity deviation between pre- and post-NWTL simulations; bottom, close-up of inset rectangle from the top panel.

6.4 Bed Shear Stress Study

The impact of the lagoon on bedload transport, including potential erosion and deposition changes, and particularly long-term geomorphological changes, was another key concern for such schemes. The bed shear stress is a major controller of potential sediment transport and the investigation of its distribution and variations can contribute to the understanding of mobility and settling (Martin-Short et al., 2015). Hence, the bed shear stress was predicted and compared in the region for pre- and post- lagoon construction, by using a conventional quadratic formulation:

$$\tau = \rho C_d |u| u, \tag{6.1}$$

where ρ is the seawater density, assumed to be 1025 kg/m^3, C_d is the bottom drag coefficient, assumed to be 0.0025 in this study (Easton, 2013; Haverson et al., 2018; Martin-Short et al., 2015), and u is the velocity and $|u|$ is the magnitude of the velocity. The variations in both the maximum and averaged bed shear stress for the scenario of WSL, SBL and NWTL are shown in Figure 6.19, Figure 6.21 and Figure 6.22, respectively. It is observed that the changes of bed shear stress is qualitatively similar to the maximum velocity magnitude changes but has a distinguishing quantitative effect, due to their square relationship with the tide speed.

In the WSL scenario, the peak increase in the maximum bed shear stress occurs in the lee of the turbine and sluice gate wakes, with the peak increase reaching 10-20 N/m^2, while there is a large area outside WSL identified where there is a slight increase in the bed shear stress. According to the distribution of surficial sediment deposits in the Bristol Channel (Figure 6.20) and the corresponding critical bed shear stress for determining the approximate condition for bedload mobility (Table 6.2), gravel dominates most area of WSL impoundment while mud is distributed near the coastline. The peak increase of bed shear stress near the turbine and sluice gate (10-20 N/m^2) exceeds the critical value for medium gravel (5.7 - 12.2 N/m^2), which indicates the mobilising of gravel and sand, and the potential scours and erosion in the influence area of turbine wakes. Given that most of the inner Bristol Channel area has extensive bedrock outcrops at seabed, covered by a thin discontinuous sediment veneer, the potential bed level evolution should be limited.

Both the maximum and averaged bed shear stress show a slight decrease by 1-6 N/m^2 across most of the lagoon of WSL. The slight reduction of the bed shear stress may have less influence on gravel but slightly increase the settling of the sand or mud, which indicates potential sedimentation and siltation in the landward area of the WSL basin. This is a common problem for most TRSs and needs to be carefully considered in any future design studies (Carroll et al., 2009; Wolf et al., 2009; Xia et al., 2010c). Furthermore, the reduction in bed shear stress inside the WSL basin indicates less turbidity of the water column and higher light penetration, consequently permitting greater biodiversity in the benthic habitat (Kirby and Retière, 2009).

Unlike the West somerset coast area, the dominant components on the seabed of Swansea bay are sand and muddy sand, as shown in Figure 6.20, which are more sensitive to bed shear stress change. The Figure 6.21 shows the spatial extent of the bed shear stress change is more

localised than velocity change, mainly concentrated at the turbine wakes. During a typical tide cycle, the mean increase of bed shear stress in the turbine wake ranges from 0.1 - 1.3 N/m^2, and the maximum increase range from 1 - 10 N/m^2. The increments of bed shear stress generally exceed the critical bed shear stress value of sands, suggesting that scour would occur in the wake of turbine, especially near the exit of turbines and sluice gates.

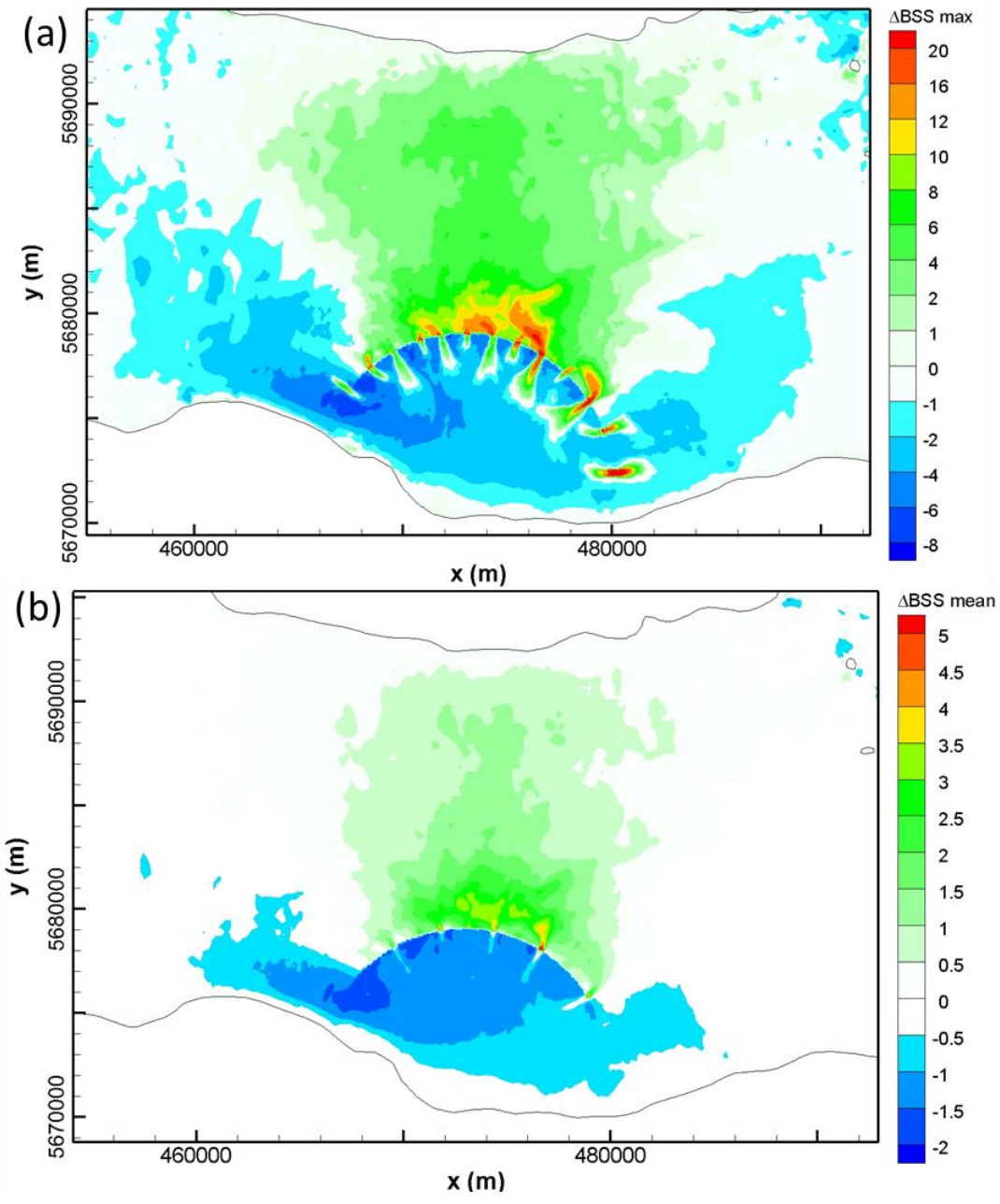

Figure 6.19: Variation in (a) maximum and (b) averaged bed shear stress with the operation of WSL.

Figure 6.20: Distribution of sand and rock outcrops (toned zone) at the sea bed in the Bristol Channel and Severn Estuary (Kirby, 2010; British Geological Survey, 1986).

Table 6.2: Critical bed shear stress (τ_c) conditions and the critical flow velocity for the entrainment by particle-size classification (Haverson et al., 2018; Berenbrock and Tranmer, 2008).

Sediment classifications	Diameter (mm)	Critical velocity (m/s)	Critical bed shear stress (τ_c) (N/m^2)
Coarse Gravel	16 - 64	2.16 - 3.19	12.2 - 53.8
Medium gravel	8-16	1.49 - 2.16	5.7 - 12.2
Fine gravel	2-8	0.70 - 1.49	1.3 - 5.7
Coarse sand	0.5-2	0.325 - 0.7	0.27 - 1.3
Medium sand	0.25-0.5	0.275 - 0.375	0.194 - 0.27
Fine sand	0.0625-0.25	-	0.110 - 0.194
Coarse silt	0.0310 – 0.0625	-	0.0826 - 0.110
Medium silt	0.0156 – 0.0310	-	0.0630 - 0.0826
Fine silt	0.0078 – 0.0156	-	0.0378 - 0.0630

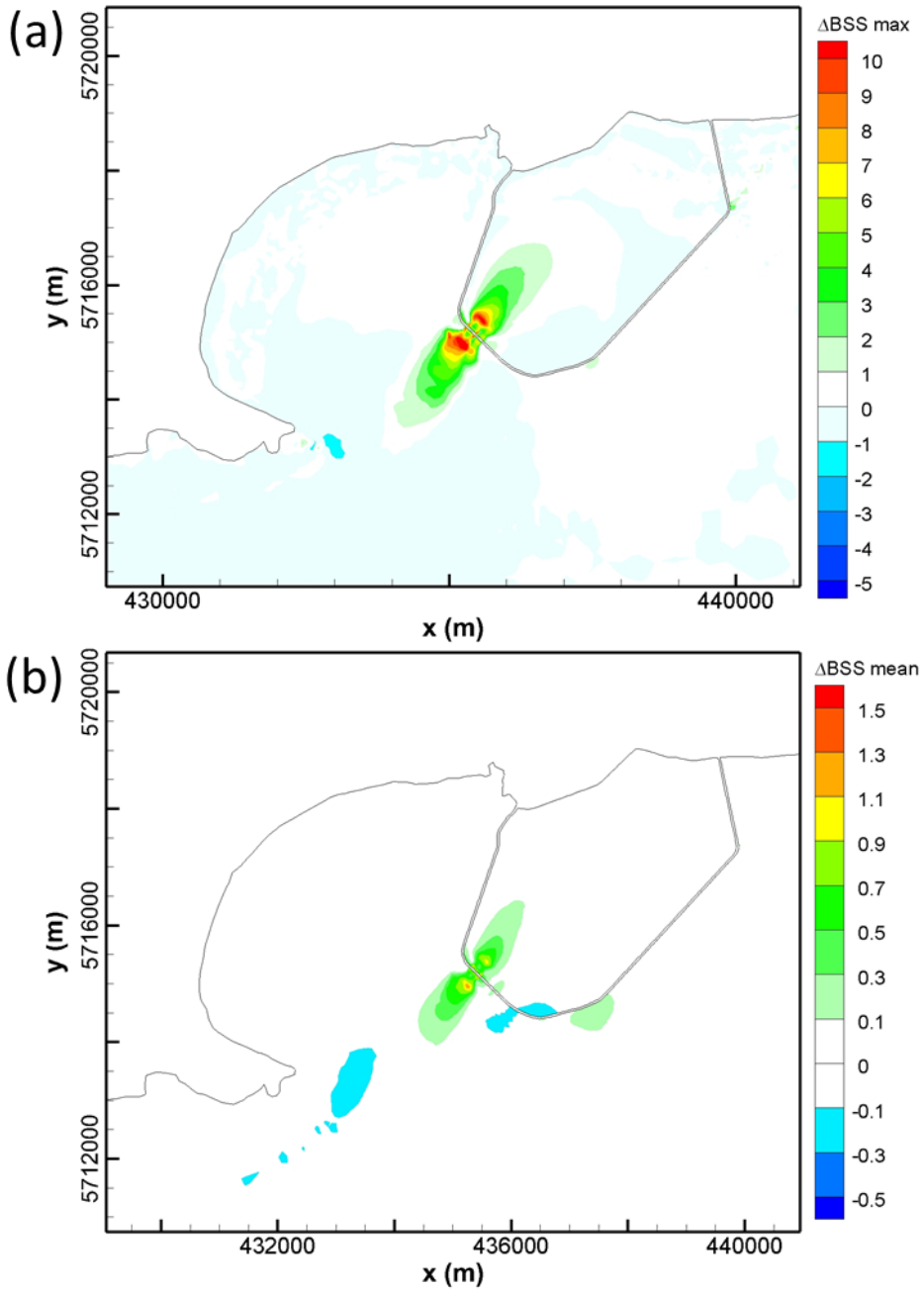

Figure 6.21: Variation in maximum (a) and averaged (b) bed shear stress with the operation of SBL.

In the NWTL scenario, noticeably increased bed shear stress is observed in the wake of sluice gates, resulting from the shallow bathymetry and the high discharge, as shown in Figure 6.22. While slight increase of bed shear stress, 1-4 N/m^2, is observed in the most middle area of NWTL impoundment, which is different from the decreased or unchanged bed shear stress in the landward area of lagoon impoundment for WSL and SBL. However, it is interesting to find that the mean bed shear stress change in the sluice gate wake is close to zero. This is because of the brief opening of sluice gates, as shown in Figure 6.34, resulting in a low time-averaged value. According to Figure 6.23, the diameter of most sediment in this area is less than 0.25

mm, classified as fine sand, with critical bed shear stress of 0.194 N/m^2. The increased maximum bed shear stress in the most middle region of NWTL markedly exceeds the critical value, indicating a larger amount of sediment will be resuspended and mobilised, and scour occurs in these areas.

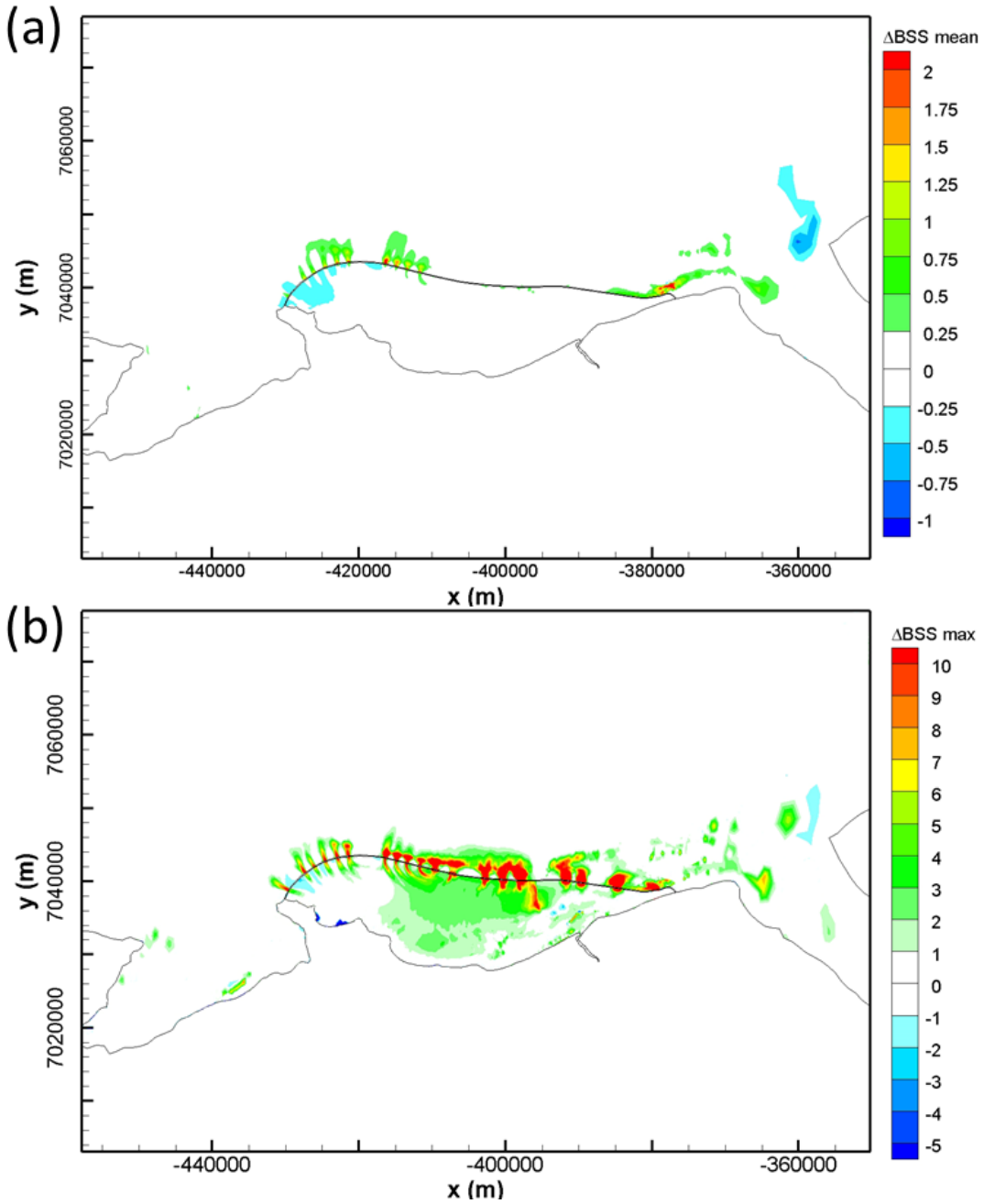

Figure 6.22: Variation in maximum (a) and averaged (b) bed shear stress with the operation of NWTL.

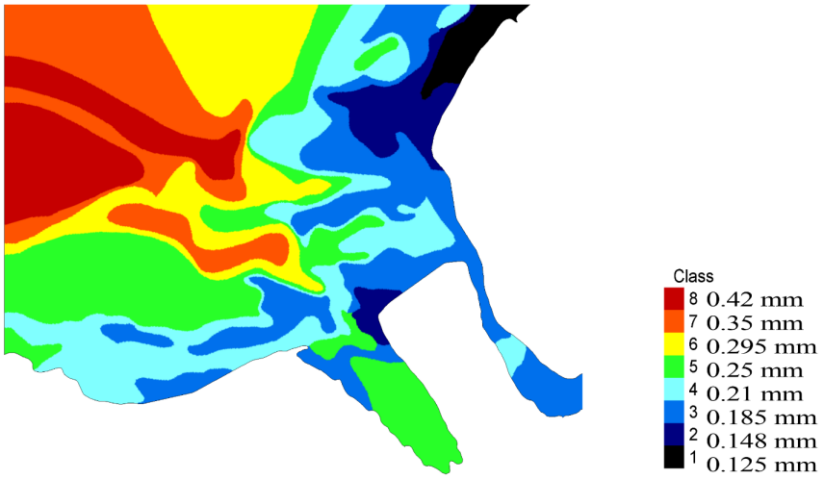

Figure 6.23: Median grain size (d50) distribution map of Liverpool Bay (Christie, 2014).

The changes in the tidal velocities and the bed shear stress may have a noticeable effect on the morphological characteristics and the benthic environment with subtle changes in a long-term. For example, the decrease in the velocity field and bed shear stress distribution within WSL is likely to lead to an accumulation of suspended sediments through deposition, which could, in turn, increase the risk of sedimentation and reduce the water storage over the longer term. Moreover, both sediment accumulation and erosion could have an impact upon the species prevalence and species due to lack of habitat availability (Rogers, 1990; Short and Wyllie-Echeverria, 1996). However, it should be noted that the investigations of such ecological impact are site and species specific, and general conclusions should not be drawn (Baker et al., 2020).

6.5 Impacts on Water Renewal Time

In order to study the water renewal capacity change with the operation of TRS, the renewal time was estimated by studying the characteristics of a passive mass-conservative tracer, which was introduced inside the studied area. This tracer was then monitored to give the concentration changes with time. It is also known that the renewal time depends on the tracer release time during a tidal cycle and different calculation methods of renewal time were applied (Guillou et al., 2019; Matta et al., 2018; Dabrowski et al., 2012; Monsen et al., 2002). For the current study, the tracer was introduced at low-water for a typical spring tide, with the tracer being released instantaneously within the studied area and dispersed uniformly. A tracer remnant function was adopted to represent the remaining tracer in the studied domain (Gao et al., 2020), as follows:

$$r(t) = \frac{\int_{\Omega} h(x,y,t) \cdot T(x,y,t) d\Omega}{\int_{\Omega} h(x,y,t_0) \cdot T(x,y,t_0) d\Omega}, \quad (6.2)$$

where *x*, *y* are the spatial coordinates; t_0 is the initial time of tracer releasing; *h* is the water depth and *T* is the tracer concentration.

The residence time was calculated based on a commonly used method that was defined statistically equal to the e-folding times when the tracer concentration reduced to 1/e, which is 37% of its initial concentration (Ranjbar et al., 2020; Monsen et al., 2002; Guillou et al., 2019). These times were recorded on each mesh point to generate a residence time map, which quantified spatial heterogeneity of the water renewal ability. One of the most attractive study areas is the lagoon impoundment area, where the dispersion and distribution of tracer/pollutions were directly confined with the lagoon and affected by the water jet (Evans, 2017; Ahmadian et al., 2010b). Thus, the tracer was introduced inside the lagoon domain, then monitored to give the temporal concentration changes. However, the tracer concentration decreases rapidly at the early stage after release, making the conventional threshold (1/e) fails to accurately describe the water renewal capacity in the lagoon basin. Thus, a new threshold of 10% that was used by Matta et al. (2018) and Guillou et al. (2019), was adopted to determine the residence time in the lagoon basin.

6.5.1 Case I: WSL

The flow pattern within the lagoon and in the region will have an impact on the water retention and renewal capacity, particularly inside the basin, as indicated by the flow patterns in Figure 6.14. To detect the water renewal capacity of the WSL impoundment area, the tracer was first released in the lagoon location at high water level for a typical spring tide. The SEBC model is estimated eligible for carrying tracer transportation modelling due to the relatively low-level tracer releasing volume.

In the first instance the tracer movement was modelled without the lagoon in place, and was flushed freely with the tides and without any restrictions. The tracer concentration distribution after 2 tidal cycles is illustrated in Figure 6.24(a). This result shows a significant change in the average tracer concentration in the lagoon impoundment after the release, as seen in Figure 6.25. This oscillation continues for some time, with the tracer being diluted mostly by the process of dispersion. The renewal time for this natural condition is about 22.4 days. This high renewal time for the pre-WSL impoundment plan region is considered to be due to the

magnitude of the ebb and flood tides and the low residual currents in the area (Neill et al., 2009).

In the subsequent simulations WSL was included in the model, with the flushing processes inside the lagoon being much more confined due to the marked changes in the local velocity patterns arising from the lagoon operation. A comparison of the concentration distributions shown in Figure 6.24 (b), (c) and (d) illustrate the impact of the mixing processes on the tracer and the impact of the vortex trapping associated with the jet induced vortices inside the lagoon and induced by the turbine and sluice gate wakes. The larger wakes induce larger and stronger vortices and extend further into the impoundment area, resulting in more mixing. While smaller jets cause less interference with high concentration areas and encourage more of the concentration towards the shoreline. Figure 6.25 shows that tracer concentrations oscillate to a lesser degree after the inclusion of the lagoon in the model. The momentum conservation through adjusting the momentum source terms tends to have a higher impact on the renewal times. The model renewal time predictions without the momentum source terms, and with realistic source velocity and simplified source velocity momentum adjustments, were 9.75, 8.10 and 6.29 days, respectively. This highlights the importance of accurate representation of hydraulic structures and the preference for 3D modelling in future studies. In particular, the results show that the operation of WSL, with momentum conservation, could improve the water renewal capacity in the water impoundment area by 64%. The concentration of tracer for the model without momentum adjustment also depicted high oscillations, which indicated that the tracer had limited mixing due to the smaller jets. This led to the accumulation of the channel water into the proximity of the openings and flushing the tracers towards the shoreline with limited mixing. Figure 6.26 illustrates the tracer distribution at the end of renewal time for each scenario. Higher concentrations were observed inside the WSL near the coastline and particularly at the junction of the embankment with the coastline. This was due to the significant reduction in the velocity in these regions as a result of the structure, as observed in Figure 6.14. The concentration outside and to the east of WSL had also increased due to reductions in the local velocity as a result of the lagoon, i.e. Figure 6.14, and the sheltering effect of the lagoon.

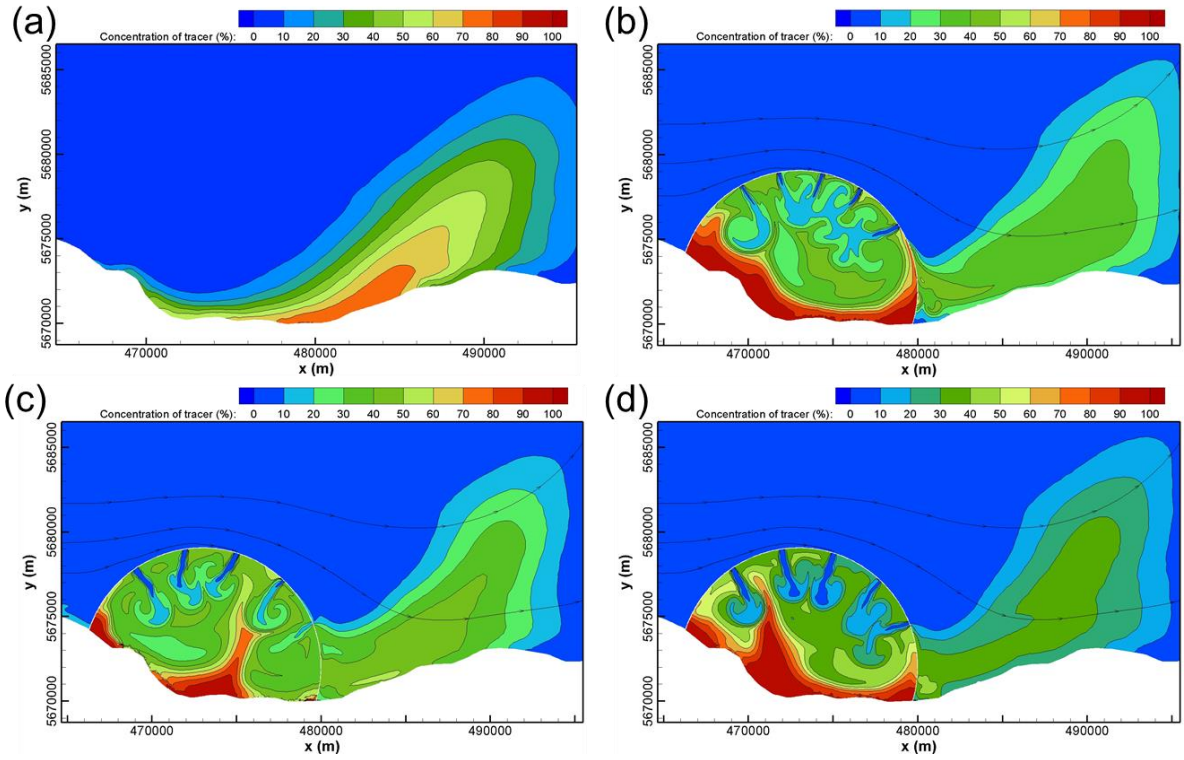

Figure 6.24: Instantaneous tracer flushing distribution after 21.7 hours of release: (a) without lagoon; (b) with lagoon and mass balance only; (c) with lagoon and momentum using realistic source; (d) with lagoon and momentum using simplified source.

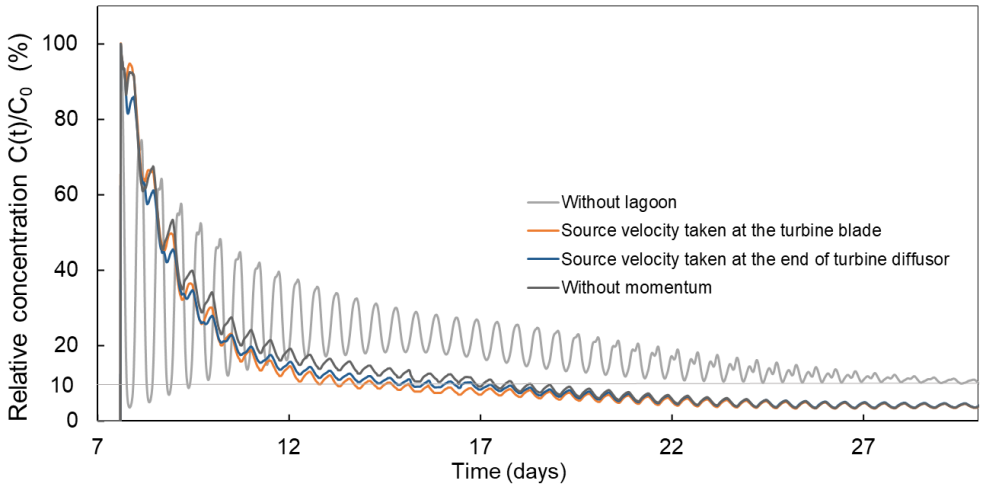

Figure 6.25: Concentration variations of tracer in the initial release area for pre-WSL, and post-WSL with different momentum term settings.

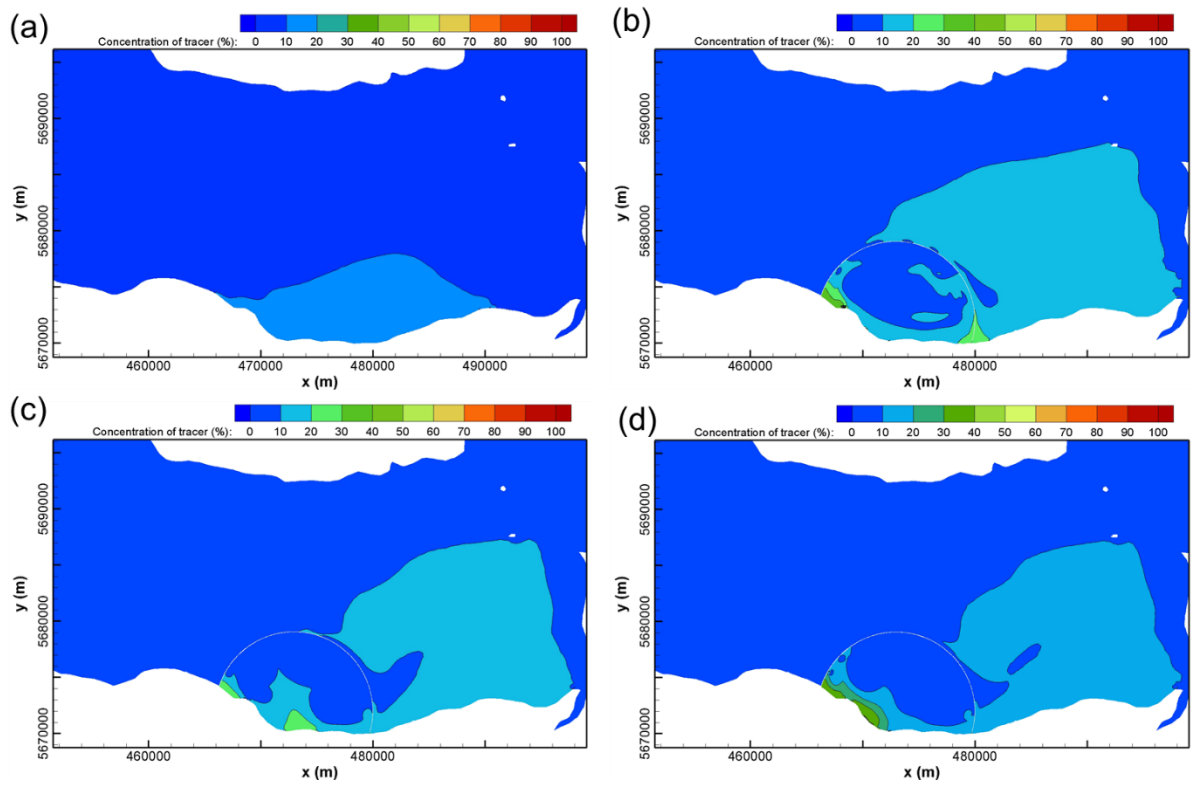

Figure 6.26: Instantaneous tracer flushing distribution at the end of renewal time: (a) without lagoon; (b) with lagoon and mass balance only; (c) with lagoon and momentum using realistic source; (d) with lagoon and momentum using simplified source.

It was reported that the Severn Estuary was among the top 5 estuaries with the highest annual nutrient load out of the 93 UK estuaries (Nedwell et al., 2002). Thus, it is important to investigate the influence of WSL operation on the water renewal capacity in Severn Estuary and Bristol Channel. However, the transport of tracer released in Bristol Channel or Severn Estuary cannot be accurately predicted in the SEBC model, for the SEBC model domain is not sufficiently large enough for the propagation and diffusion of tracer. Thus, the Continental Shelf (CS) model was used to study the tracer transport in Bristol Channel and Severn Estuary for pre- and post-WSL cases. Furthermore, it is also necessary to take into account the spatial variability of residence times to better understand the impact of WSL on the water renewal capacity of different regions (Dabrowski et al., 2012). Therefore, tracers were released in three selected regions which were distinct with regards to the geography division, which are Severn Estuary to outer Bristol Channel (Figure 6.27(a)), Severn Estuary to Inner Bristol Channel (Figure 6.27(b)), and Severn Estuary (Figure 6.27(c)). For these wide domains study, the residence times (with e-folding times threshold) for each computational point were calculated

and plotted as contour plots, showing the spatially heterogeneous water renewal capacity and the clearly marked flushing pathways.

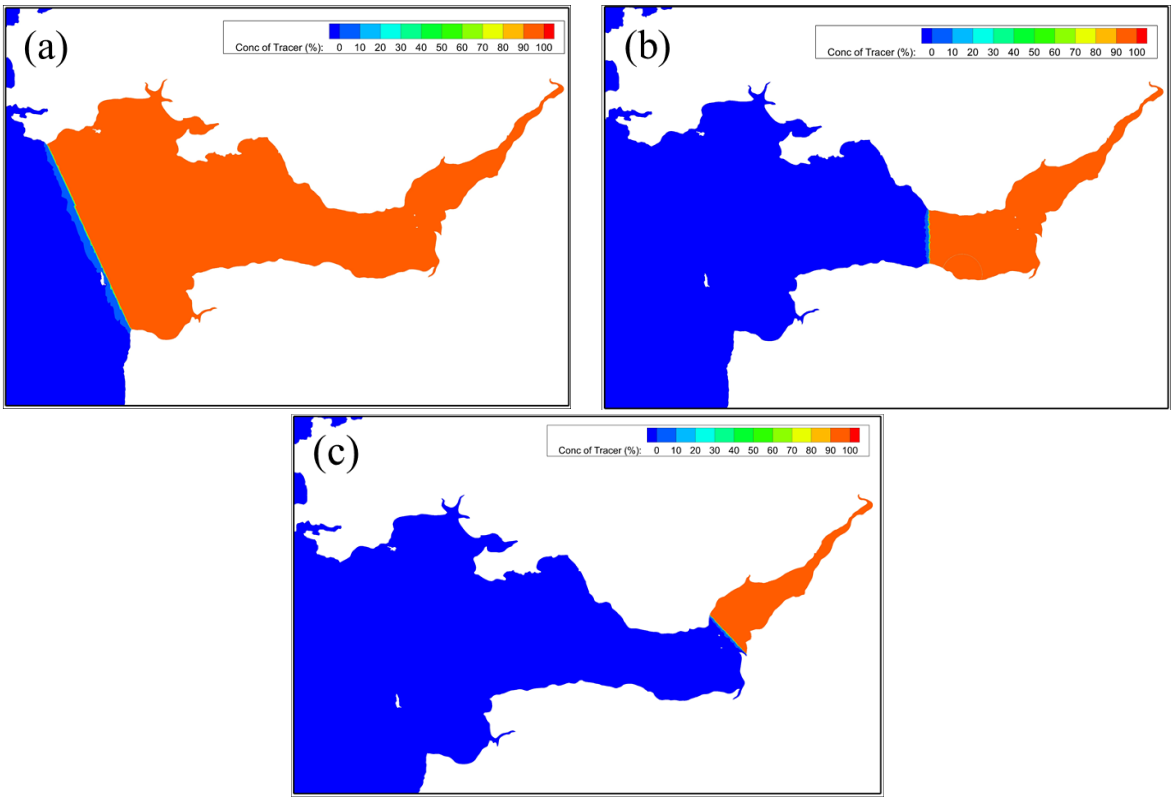

Figure 6.27: The release area of tracer, in (a) Severn Estuary and Bristol Channel; (b) Severn Estuary and inner Bristol Channel; (c) Severn Estuary.

The spatial distribution maps of residence time with tracer for pre- and post-WSL scenarios are shown in Figure 6.28. It is observed that for all three tracer releasing regions, the operation of WSL reduces the residence time in most of the study areas, which indicates that WSL could accelerate water exchange in both Severn Estuary and Bristol Channel. This is because of the increased tide speed in the inner Bristol Channel, as presented in Figure 6.14, along with the disturbance introduced by the WSL operation. It is noted from Figure 6.28 (a) and (b) that the waters adjacent to the mouth of the Bristol Channel are renewed considerably quicker due to the relatively high mixing process with the sea water. However, the waters adjacent to the releasing boundary in Figure 6.28 (c) - (f) show a lower renewal rate, which should be attributed to the tidal asymmetry in this area. It is learned that the inner Bristol Channel and Severn Estuary is featured with tidal asymmetry with flood tide dominating over the ebb tide (Cannard, 2016; Uncles, 2010), moving the tracer up to the estuary, as shown by the flushing pathways shown in Figure 6.28 (c) - (f).

Furthermore, it can be seen from Figure 6.28 (a) and (c) that the relative higher residence time shows in Bridgewater Bay, indicating the relative lower water exchange rate, which is probably the result of the low tide speed and the half-enclosed shape of the bay. However, this situation has improved considerably in the post-WSL scenario due to more disturbance introduced in this area. It should be noted that the river discharges also contribute to the water renewal capacity near their estuary, although these effects are mainly confined near the river mouth due to their low discharge, as shown in Figure 6.28.

Table 6.3 summarises the spatially averaged residence time, which is the period when the averaged tracer concentration in the study domain dropped to 1/e of its original concentration. With the operation of WSL, the spatially averaged residence time in the whole Bristol Channel and Severn Estuary decreased by 43%, while it decreased 20% in the inner Bristol Channel and 13% in Severn Estuary, respectively. These results indicate that the WSL significantly improves the water renewal capacity in the Bristol Channel while less effect on water in Severn Estuary.

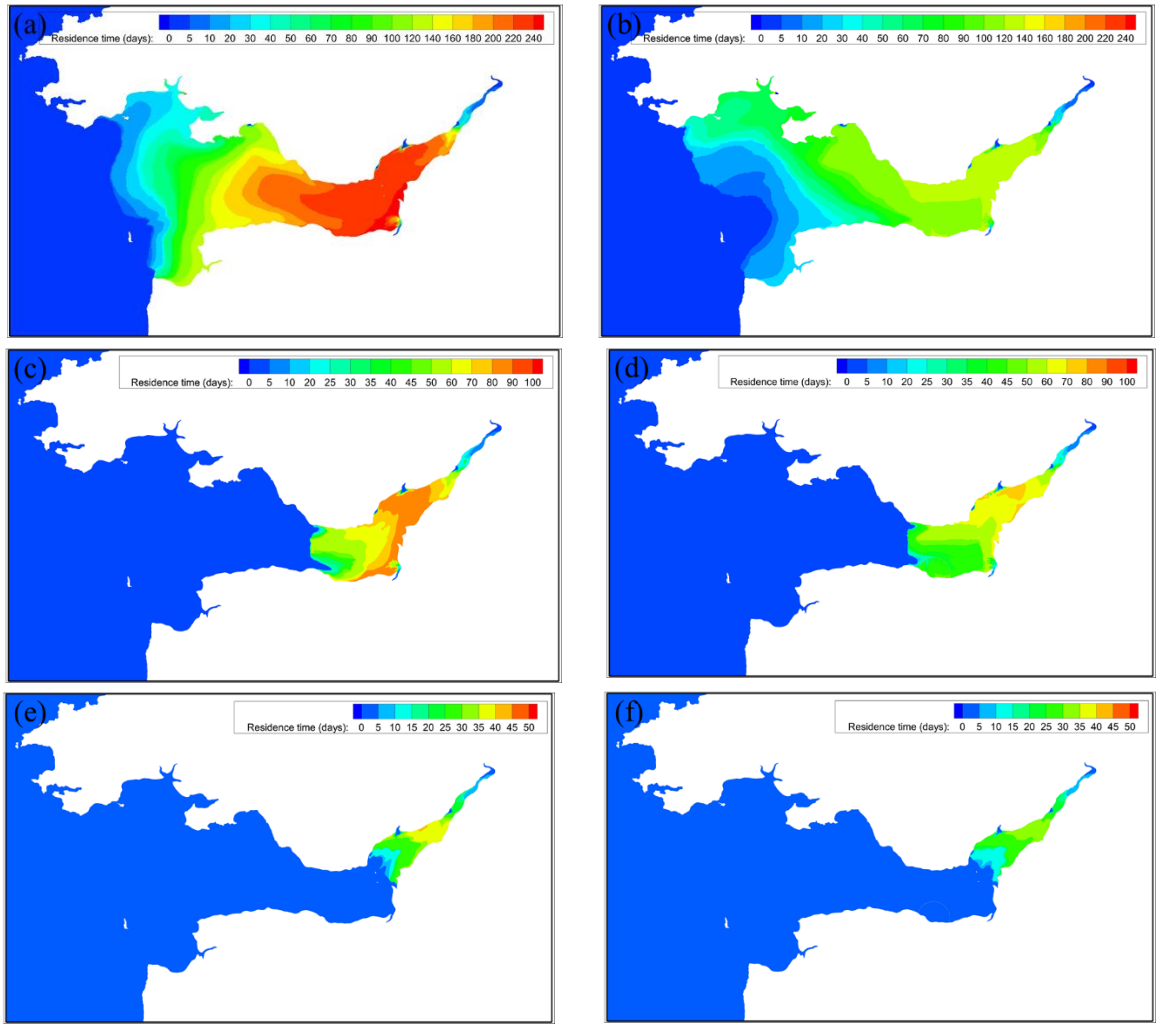

Figure 6.28: Residence time distribution for tracer release in (a) Severn Estuary and Bristol Channel without WSL; (b) Severn Estuary and Bristol Channel with WSL; (c) Severn Estuary and inner Bristol Channel without WSL; (d) Severn Estuary and inner Bristol Channel with WSL; (e) Severn Estuary without lagoon; (f)Severn Estuary with WSL.

Table 6.3: The spatially averaged residence time in the study area.

Tracer release and tracking region	Post-WSL (days)	Pre-WSL (days)
Severn Estuary to outer Bristol Channel	65.45	113.96
Severn Estuary to inner Bristol Channel	49.46	62.04
Severn Estuary	20.64	23.70

6.5.2 CaseII: SBL

The water renewal capacity of Swansea Bay was investigated for the pre- and post- SBL construction scenarios. Swansea Bay has gone through severe pollution for the last two decades of the 20th century (Kadiri et al., 2021). Part of the reason is the inappropriate locations of sewerage and the low water exchange rate in this area (Smith and Shackley, 2006). Thus, besides the SBL impoundment, the water renewal capacity in the whole Swansea Bay was also studied. According to the marine character areas of the Wales government (LUC, 2015), Swansea Bay and Porthcawl, shown in Appendix A, Figure A1, is selected for releasing and tracking tracer for water renewal time study. Thus, the tracer initial release areas for SBL scenarios are shown in Figure 6.30(a) and Figure 6.31(a).

The evolution of the spatially averaged tracer concentrations in the study area is shown in Figure 6.29. The operation of the SBL could increase the water exchange rate in Swansea Bay and Porthcawl. The reason for this increase might be the existence of more disturbance in the area of study as a result of the operation of SBL. However, when releasing tracer in the impoundment of the SBL area, the operation of SBL would slow down the water exchange rate of SBL at the early stage of flushing. However, the negative effect of SBL on tracer transport will be reversed at later stages of flushing, as presented in Figure 6.29.

The residence times for Swansea Bay and Porthcawl for pre-SBL and post-SBL construction, are 35.4 days and 31.7 days, respectively, when the tracer concentration of 10% was taken as the threshold; these values were 11.7 and 12.2 days for the tracer released in the impoundment of the SBL without and with lagoon structure, respectively. Generally, differences between residence time evolution with and without SBL vanished in the latter stage of tracer flushing progress. It took an approximate same duration for the tracer concentration to drop below 10% of the tracer concentration initially released in the control domain.

The remaining tracer distributions at the end of the simulation, i.e. when the average concentration dropped to 10%, are presented in Figure 6.30 and Figure 6.31. These figures confirmed that the coastal area of Swansea Bay or the landward part of SBL could be water retention area. Comparison between Figure 6.30 (b) and (c) shows that the presence of SBL would lead to a lower water renewal capacity in the landward part of SBL impoundment. Comparison between Figure 6.31(b) and (c) demonstrate that SBL would accelerate the water exchange rate in the region to its west while reducing it to its east side.

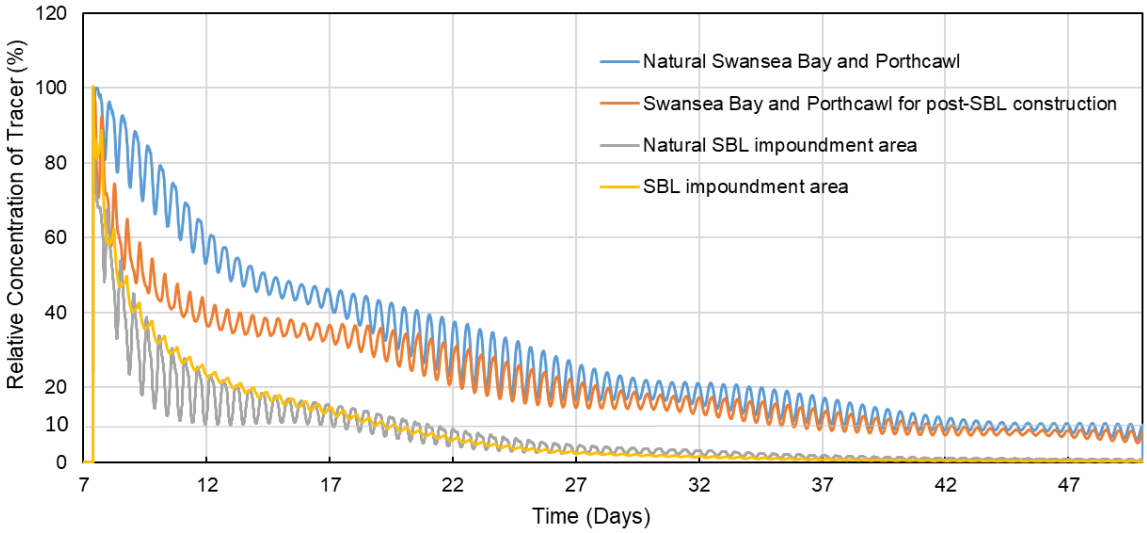

Figure 6.29: Concentration variations of tracer in the initial release area for pre-SBL, and post-SBL with different momentum term settings.

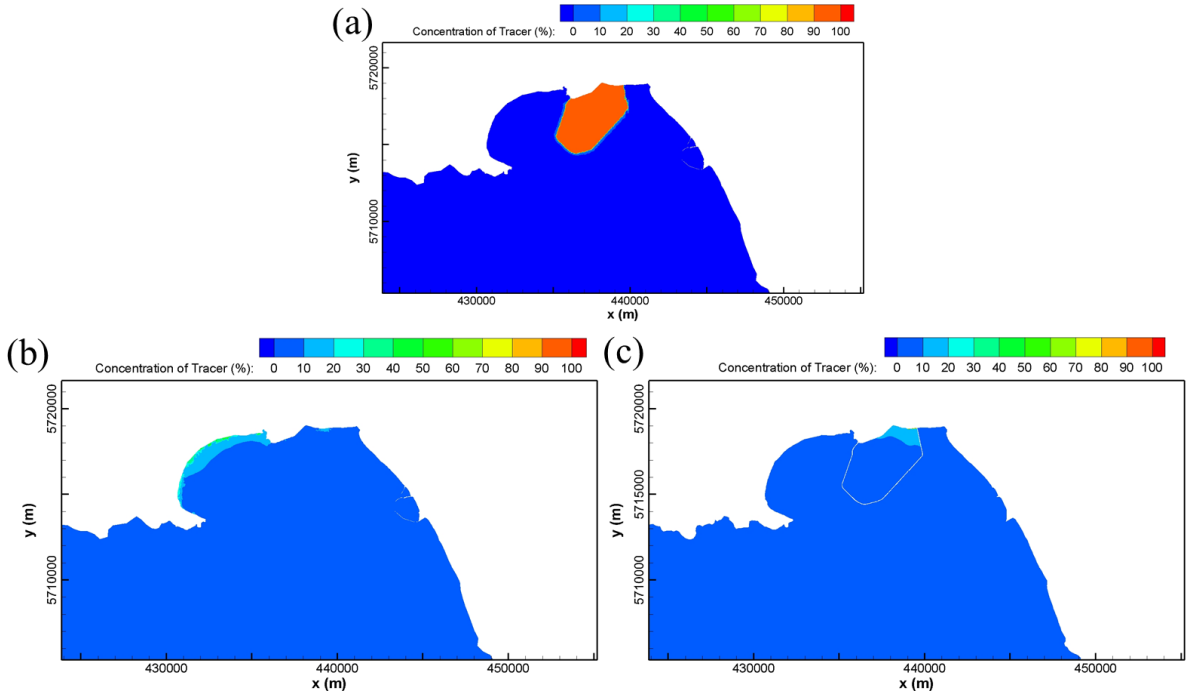

Figure 6.30: Instantaneous tracer concentration distribution at (a) initial releasing moment with release area of SBL impoundment; (b) end of renewal time in natural condition; (c) end of renewal time in post-SBL condition.

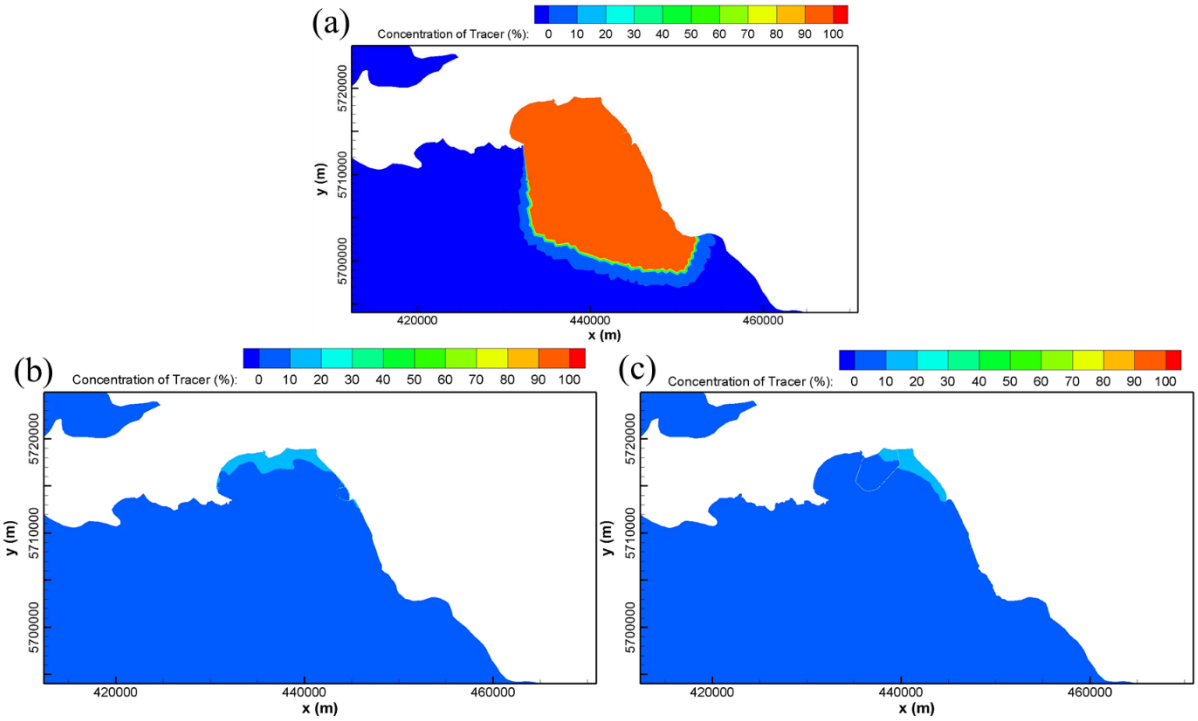

Figure 6.31: Instantaneous tracer concentration distribution at (a) initial releasing moment with release area of Swansea Bay and Porthcawl; (b) end of renewal time in natural condition; (c) end of renewal time in post-SBL condition.

6.5.3 Case III: NWTL

The water renewal capacity in the water impoundment area for pre- and post-NWTL was also studied. It should be noted that the tracer was released at high water for a typical spring tide, which is 8.6 days after the start of the model. Figure 6.32 shows the changes in the tracer concentration averaged over the NWTL area. The operation of NWTL reduces the water exchange in the potential impoundment area, and it took 11.36 and 16.55 days, respectively, for tracer concentration to decrease to 10% of its release concentration are for pre- and post-lagoon. Comparing with the tracer decay period for WSL study, which takes 22.4 days for the tracer concentration to decrease to 10%, the NWTL proposal area presents a better natural water renewal capacity than the WSL area, even with a larger area. This should be attributed to the tide asymmetric and the higher residual currents in the NWTL plan area, which is supported by the lower oscillation range of tracer concentration evolution in the NWTL scenario, as shown in Figure 6.32. However, different to the improved water renewal capacity for the post-WSL scenario, the operation of NWTL reduces the averaged water residence time by 45.7% in the lagoon impoundment basin.

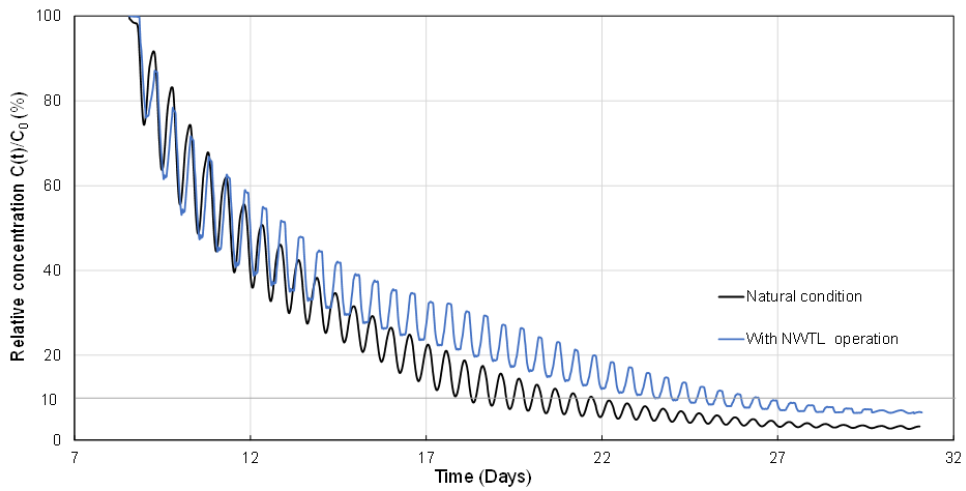

Figure 6.32: Concentration variations of tracer in the tracer release area, i.e, The NWTL impoundment area, for pre- and post-NWTL scenarios.

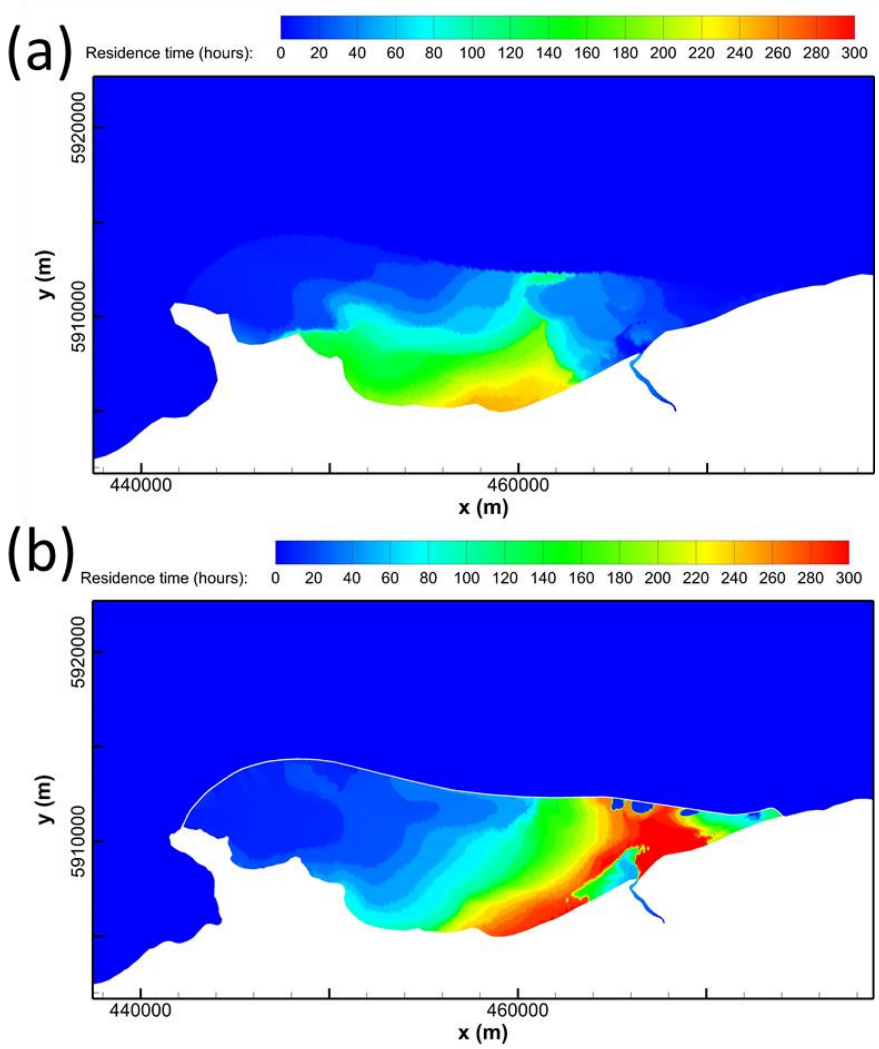

Figure 6.33: The residence time distribution with the threshold taken as 1/e, (a) the natural condition, (b) the scenario for the post-NWTL.

Figure 6.33 presents the spatial distribution of residence time. It should be noted that the threshold of residence time is the classic value: 1/e, in order to be consistent with studies in Section 6.5.1. High water exchange rate is observed in the west side of the NWTL area, which is the direct result of a strong water jet from turbine block T1 - T9. The water jets from turbines push the tracer to the west side of the lagoon, where there is a lower water exchange rate between the impoundment and the sea.

The typical discharges of turbines and sluice gates are presented in Figure 6.34, noting that the value is for a whole block of turbines and sluice gates for a better demonstration. It shows that although the sluice gates also have a high discharge in unit time, the working period is brief compared with the turbine. Consequently, the short opening of the sluice gate results in a lower volume of discharge and a small scale of water jet from sluice gates, which should be responsible for the low water exchange rate in the east of NWTL impoundment. However, given the primary purpose of a sluice gate is to accelerate the filling or emptying phase of a TRS to increase the electricity generation (Bray et al., 2016), the performance of sluice gates in Figure 6.34 meet the expectation of a power generation scheme. Furthermore, the tracer discharged out of NWTL during the ebb generation is flushed to the east side of NWTL during the flooding phase, which is then partly absorbed into NWTL again through the filling phase of sluice gates, partly responsible for the high residence time at the east of NWTL.

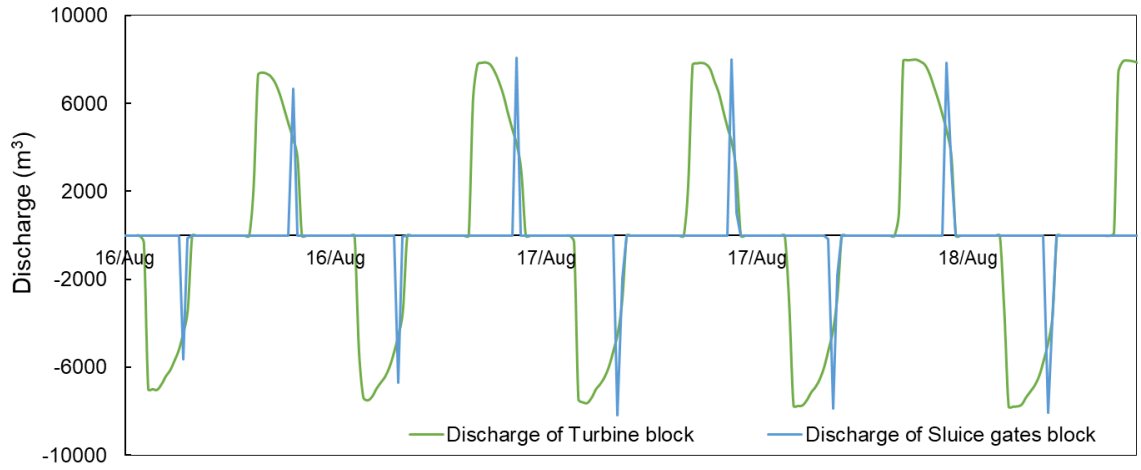

Figure 6.34: The typical discharges of a turbine block and sluice gates block in NWTL.

6.6 Suspended Sediment Transport Study

The alteration on tidal flow structure by a TRS would consequently influence the tide current ability to transport solid matter, which will have a profound impact on the environment and ecology, including the benthic ecology, biogeochemistry, and marine geology. In order to identify the potential impacts of a tidal lagoon on suspended sediment (SS) pathways, the SS concentration change and the bed level evolution needs to be investigated for pre- and post-TRS construction scenarios. Research into the impact of TRSs on sediment processes requires significant resources including a large amount of field data for setting up, calibrating and validating the models which were available in this study. This section aims to highlight the importance of such study, particularly including enhancements made to the model as a part of this study such as momentum conservation across the structure. Furthermore, sensitivity analysis carried out in this study could help with planning more targeted field surveys for future studies. This section is not carried out to provide an accurate prediction of the impact of TRSs on sediment transport processes and the results should be considered with the main aims of the study as stated here.

Figure 6.35: Distribution of suspended sediments in Bristol Channel and Severn Estuary observed from a satellite image (Parsons Brinckerhoff Ltd, 2010).

The Severn Estuary and Bristol Channel is characterised by high turbidity (Manning et al., 2010a), as can be seen from satellite photos of the region in Figure 6.35. The powerful but variable strength tidal currents in this area continuously mobilise and redistribute a large amount of sediment. The general pathway of suspended sediment is parallel with the strong

tidal current, which is basically parallel to the main axis of the estuary in the Severn Estuary as shown in Figure 6.36. An eastward-directed sediment transport pathway distributes at the northern channel, mobilising sand into Severn Estuary, while a westward sand transport pathway dominates the central zone (Otto, 1998). The sand pathway and tidal current result in sandy, gravelly, or rocky areas in the axial region, with fine sand occupying the margin areas (Manning et al., 2010b; Parker and Kirby, 1982).

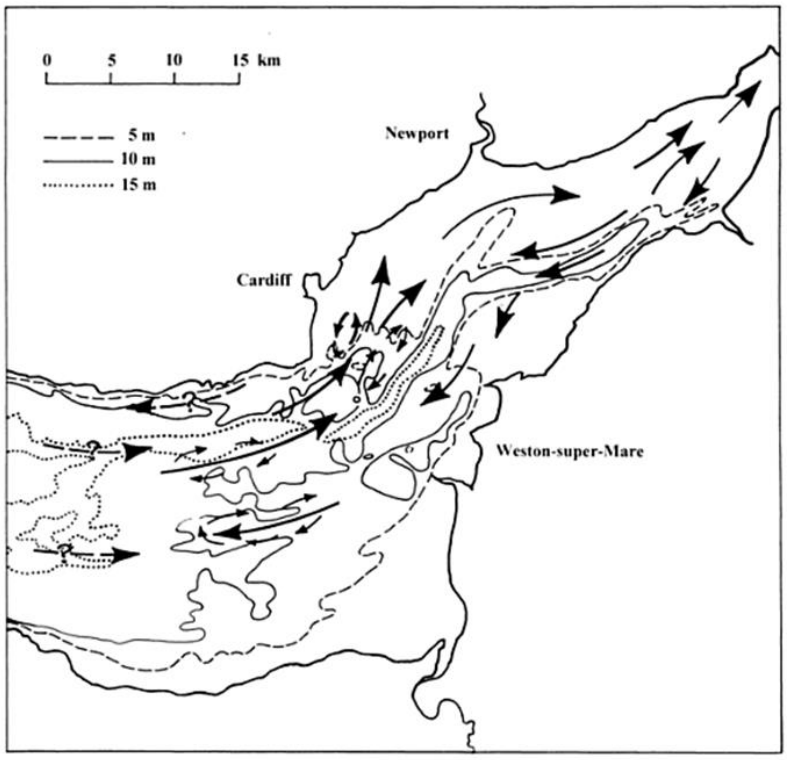

Figure 6.36: Sand transport pathways for the inner Bristol Channel and outer Severn Estuary (Otto, 1998)

A sediment module, GAIA within TELEMAC-suite, is used to simulate sediment transport and bed evolution, which is coupled with the TRS hydrodynamic model for studying such impacts. With the given sediment parameters (sediment diameter, sand/mud density, settling velocity, etc.) and the flow variables calculated in the hydrodynamic module (flow velocity, water depth, wave, etc.), GAIA is capable of simultaneously modelling a combination of sediments with multiple size classes for both non-cohesive (diameter larger than 60 μm) and cohesive (diameter less than 60 μm). The active layer model and cohesive sediment consolidation process are allowed in GAIA to simulate the complex morphodynamic process (TELEMAC, 2020a).

6.6.1 GAIA Settings and model validation

Four classes of the sediments with different sizes were considered in modelling the suspended sediment transport in the Severn Estuary and Bristol Channel, including both the cohesive and non-cohesive sediment. The sediment with diameters of 0.013 mm, 0.029 mm, 0.064 mm and 0.25 mm were applied with a corresponding proportion of 16%, 34%, 34%, 16%, respectively (Stapleton et al., 2007). However, given that the Bristol Channel and Severn Estuary is a complex mixed sediment system with regional differences in sediments distribution, future work will use spatially varying median grain diameter values, including mud, sand, and gravel.

Besides the sediment source that eroded and/or mobilised from the subtidal and intertidal area, rivers discharges are one of the main new sediment supplies (McLaren et al., 1993). Four main river sources of suspended sediment were included, as shown in Table 6.4.

Table 6.4: A summary of the main sediment inputs from the tributaries in the Bristol Channel and Severn Estuary (Cannard, 2016).

River	Sediment input (Tonnes/year)
River Severn	262,883
River Wye	347,227
River Avon	53,060
River Usk	41,733

The equations used to solve the suspended sediment transport, the net erosion flux (E) and net deposition flux (D) are presented in Section 3.1.4. Different equations for calculating sediment net flux (E - D) were applied to non-cohesive and cohesive sediment. Since minimal fine sediment enters the Bristol Channel from the Celtic Sea (Allen, 1991; Cannard, 2016) and considering the distance of the area of interest from the mouth of seaward open boundary, the seaward open boundary of Telemac-2D was also treated as the outflow boundary of sediment transport in GAIA. So the suspended sediment can mobilise freely in the water column throughout the modelling domain and through the open boundary (Bi and Toorman, 2015). The 3D flow pattern near the turbine increases the difficulty to simulate the SS transportation in the water jet through the turbines and sluice gates. Moreover, this study is more focused on SS transportation in the large domain rather than the vicinity of the lagoon structure which requires further field data. Thus, the SS transiting through the turbines and sluice gates are not considered in the simulation. Such study is very important and needs to be conductuted in a highly calibrated and validated 3D model of sediment processes.

The SS concentration computed from GAIA was compared with the field data measured at Minehead and Porthcawl in July 2001 (Stapleton et al., 2007). Typical comparisons are shown in Figure 6.37. It can be seen that the SS prediction of GAIA is generally consistent of the measured data. Discrepancies exist during the flood and ebb tides, which might be caused by the sensitivity of fine sediment on settling velocity or the temporal lags between SS and flow. Although the SS concentration evolution process was not completely predicted, the range and the trend of SS concentration change predicted by the model are consistent with the measured data. Based on the above results, and comparing with the SS concentration validation from other studies (Dong et al., 2020; Bi and Toorman, 2015), it was concluded that this SS prediction is within an acceptable range.

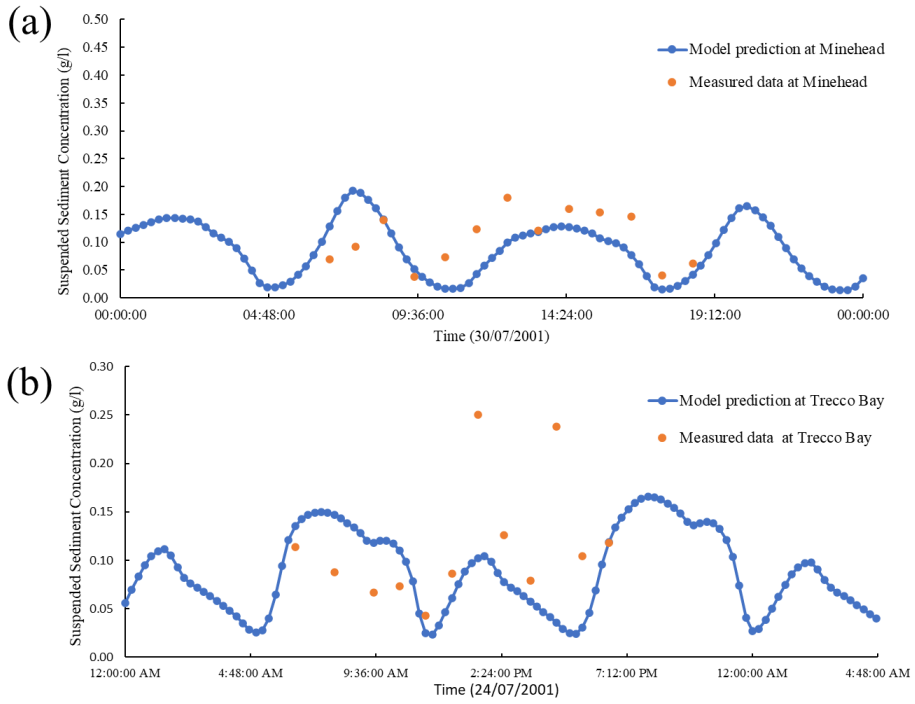

Figure 6.37: The comparison of predicted and measured suspended sediment concentration at (a) Minehead and (b)Trecco Bay.

6.6.2 Impact on Maximum Suspended Sediment Concentration

The primary source of sand in the Bristol Channel originates from the depositions in the Celtic Sea that were generated from glacial rivers during the last ice age (Severn Estuary Partnership, 2011; Allen, 1991). Then the sand was mobilised up to the estuary with the strong flood tide currents (Otto, 1998; Parsons Brinckerhoff Ltd, 2010). It is observed in Figure 6.38 that the inner Bristol Chanel and Severn Estuary is a region of high turbidity, with the high SS

concentration exceeding 1000 mg/l. As for Swansea Bay, the average SS concentration in Swansea Bay is generally less than 50 mg/l (Pye and Blott, 2014), which is much lower than it in the inner Bristol Channel.

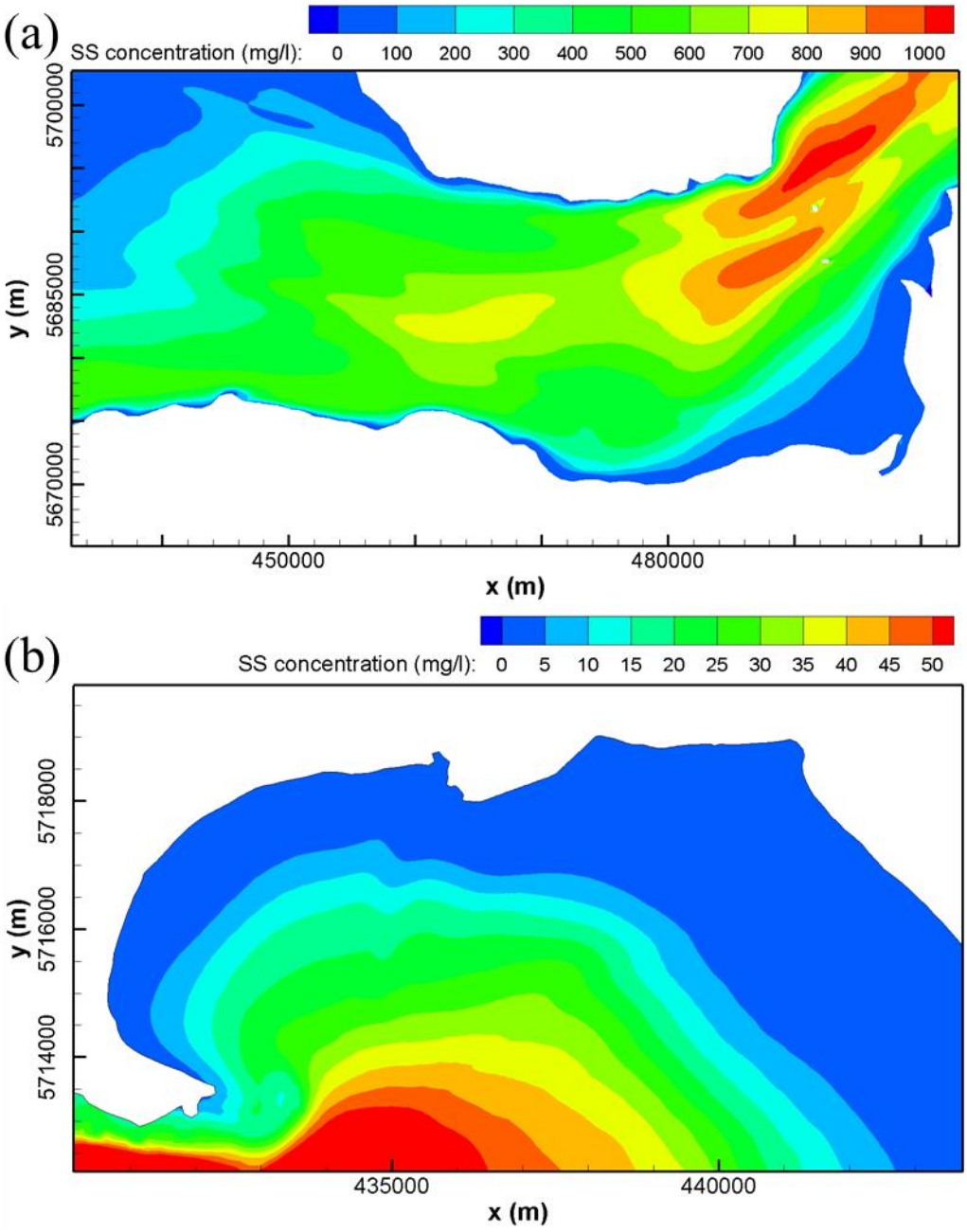

Figure 6.38: The predicted suspended sediment concentration at spring flood tide across the (a) inner Bristol Channel and (b) Swansea Bay.

The tidal current energy is crucial in studying the sediment dynamics within a marine system (Hooper and Austen, 2013). The hydrodynamic impact study of WSL indicated the maximum velocity magnitude would have a noticeable increase at the turbine exit and the inner Bristol Channel, while current speed decreased noticeably across most of the interior of the lagoon.

Correspondingly, the maximum SS carrying capacity of tidal flows should correlate with the current speed change.

Figure 6.39 presents the SS concentration distribution in the inner Bristol Channel and outer Severn Estuary at the flood spring tide for post-lagoon scenarios. Comparisons between Figure 6.38(a) and Figure 6.39(a) show that the maximum SS concentrations in the inner Bristol Channel would be increased significantly after the construction of WSL, rising from 500 - 900 mg/l to more than 1000 mg/l. The SS concentration increase region extends to the outer Severn Estuary and the Bridgwater Bay. Meanwhile, a markedly lower maximum SS concentration inside WSL impoundment is observed, indicating a lower SS carrying capacity in the impounded water.

The influence of SBL on the tidal current speed is mainly restricted in Swansea Bay. Consequently, the SBL has little impact on SS concentration outside Swansea Bay, as shown in Figure 6.39(b). A high SS concentration region appears in the turbine wake near the SBL due to the resuspension of fine sand from the seabed, while it drops significantly in the SBL impounded area due to the reduced current speed. The SS carrying capacity distribution inside of SBL indicates that the accelerated water flow may mobilise sand from the immediate region of the turbine block downstream into the landward SBL impoundment.

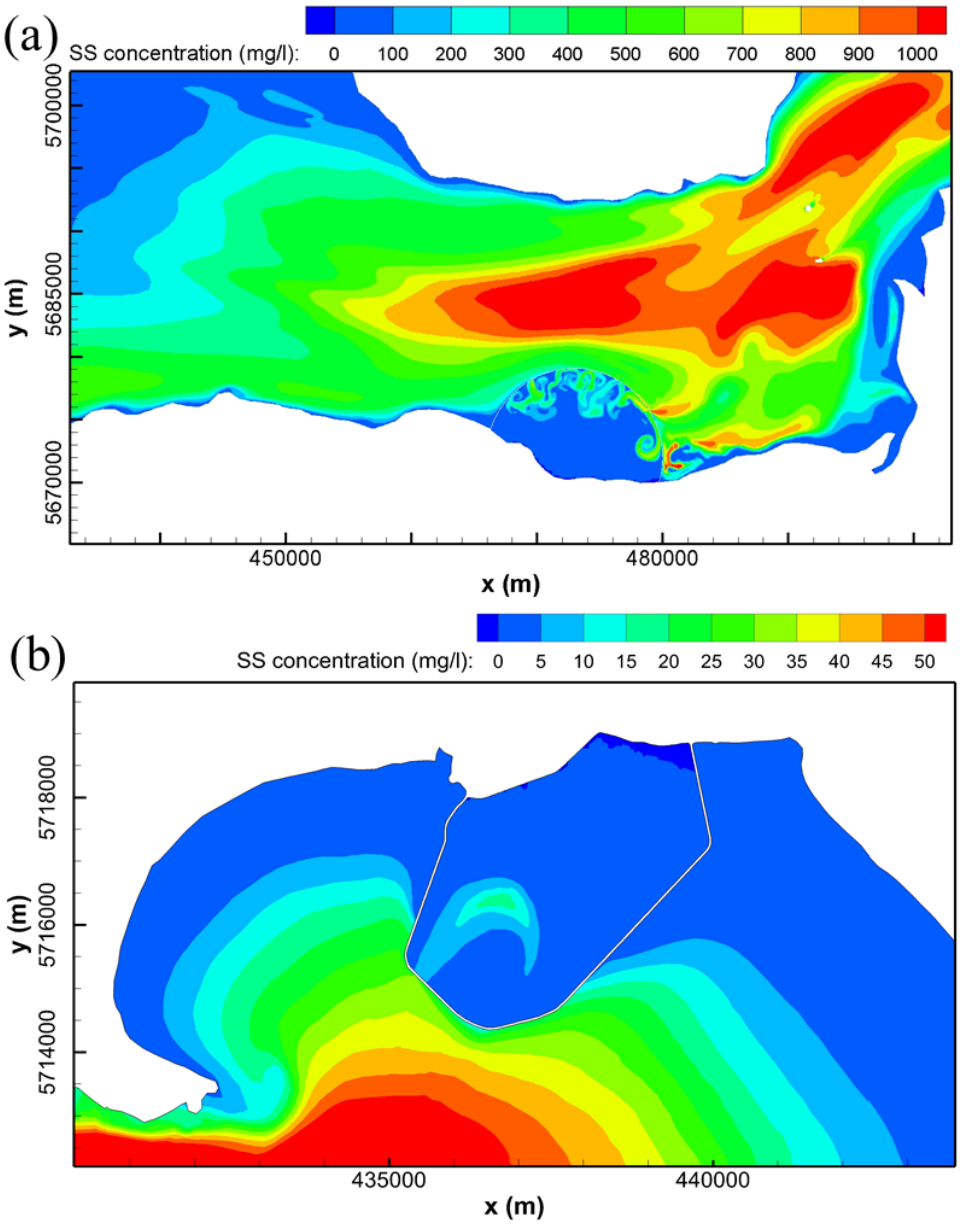

Figure 6.39: The predicted suspended sediment concentration at spring flood tide for (a) post-WSL and (b) post-SBL scenarios.

6.6.3 Morphological Changes

The difference of the erosion and deposition rates (*E* - *D*) in Equation (3.19) represents the net sediment flux which is closely related to the current ability to transport solid matter. This term is usually estimated based on the equilibrium concentration concept, that when the bed shear stress exceeds the threshold of erosion, erosion occurs on the bed and sediment is resuspended. In contrast, deposition of suspended sediment occurs when the bed shear stress is smaller than a critical value. The formulations for calculating erosion and deposition rates use semi-empirical formulas, as illustrated in Section 3.1.4, which are subject to great uncertainties (Thiébot et al., 2015). Therefore, proper calibration and validation with in-situ measurement data are necessary for the application of such an approach. Accuracy and reliability in sediment modelling can only be defined as the model prediction matching the measured data within an acceptable band of uncertainty (Simons et al., 2000; Bi and Toorman, 2015). However, the lack of sediment fluxes measurements in the Bristol Channel and Severn Estuary makes it difficult to calibrate the sediment erosion and deposition rate predictions and therefore, it is challenging to analyse morphological evolution in this area quantitatively without enough data. Therefore, with the existing uncertainties, the morphological evolution study was conducted by investigating the sensitivity of the model prediction to some key parameters.

Two key parameters that are crucial for accurate simulation of morphological modelling are the critical shear stress for erosion (τ_{ce}) and critical shear stress for deposition (τ_{cd}), which are associated with the resuspension and deposition of sediment (Stapleton et al., 2007; Bi and Toorman, 2015). According to the physical definition of τ_{ce} and τ_{cd}, the erosion occurs when the bed shear stress at the bed exceeds the τ_{ce}, because the shear-induced hydrodynamic lift is higher than the sediment buoyant weight, and deposition is in the opposite order. There is a distinct discrepancy among the values of τ_{ce} and τ_{cd} used for different numerical simulations (Park et al., 2008; Dong et al., 2020) and in-field measurement (Sanford and Halka, 1993), for τ_{ce} and τ_{cd} depend upon the seabed material characteristics (such as sediment composition, particle size, density, et.al.) and bed structure. Thiébot et al. (2015) carried sensitivity test of morphological modelling in Alderney Race with τ_{ce} varies from 1 - 10 N/m^2, and found the distribution of the sediment deposit differs strongly depending on the τ_{ce} value. In previous studies, different values of τ_{cd} were assigned to SS modelling with typical values of 0.05 - 0.1 N/m^2 (Shi et al., 2015; Winterwerp and Van Kesteren, 2004). Values of 2 and 0.1 N/m^2 has

been used for τ_{ce} and τ_{cd} in simulating the SS in Bristol Channel and Severn Estuary (Ahmadian et al., 2010a; Gao et al., 2013; Stapleton et al., 2007).

Thus, given the lack of field measurement data to validate the value of τ_{ce} and τ_{cd}, the sensitivity analysis of morphological evolution modelling was performed with different values of τ_{ce} and τ_{cd} to investigate the potential impact of these parameters on simulating morphological evolution. Based on the prior public research (Thiébot et al., 2015; Stapleton et al., 2007; Gao et al., 2011), the values of τ_{ce} tested in this study are 2, 2.5, 3, 3.5 N/m^2, with the values of τ_{cd} equal to 0.05, 0.1 and 0.15 N/m^2, respectively.

Figure 6.40 presents the model predicted cumulative bed level evolution in the inner Bristol Channel with τ_{ce} values to 2, 2.5, 3, 3.5 N/m^2 and τ_{cd} equal to 0.1 N/m^2. The morphological changes in this area were highly sensitive to the value of τ_{ce}. It was found that the seabed erosion increased significantly with a lower critical erosion shear stress. The model with τ_{ce} of 2 N/m^2 shows a large erosion area in the natural condition which is unrealistic, while τ_{ce} of 3 N/m^2 and 3.5 N/m^2 result in an insignificant bottom evolution. This phenomenon continues with the presence of WSL. According to Equation (3.24), erosion began when the bed shear stress τ_b exceeded the τ_{ce}. It is learned from Section 6.4 that bed shear stress rises noticeably with the presence of WSL in the inner Bristol Channel, with the peak value rising increasing by 10-20 N/m^2 near the WSL structure, and the average value increasing by 1.5-3.5 N/m^2, as shown in Figure 6.19. Thus, the value τ_{ce} in the range of 2 - 3 N/m^2 can be easily exceeded by τ_b, leading to erosion on the seabed and resuspension of sediment.

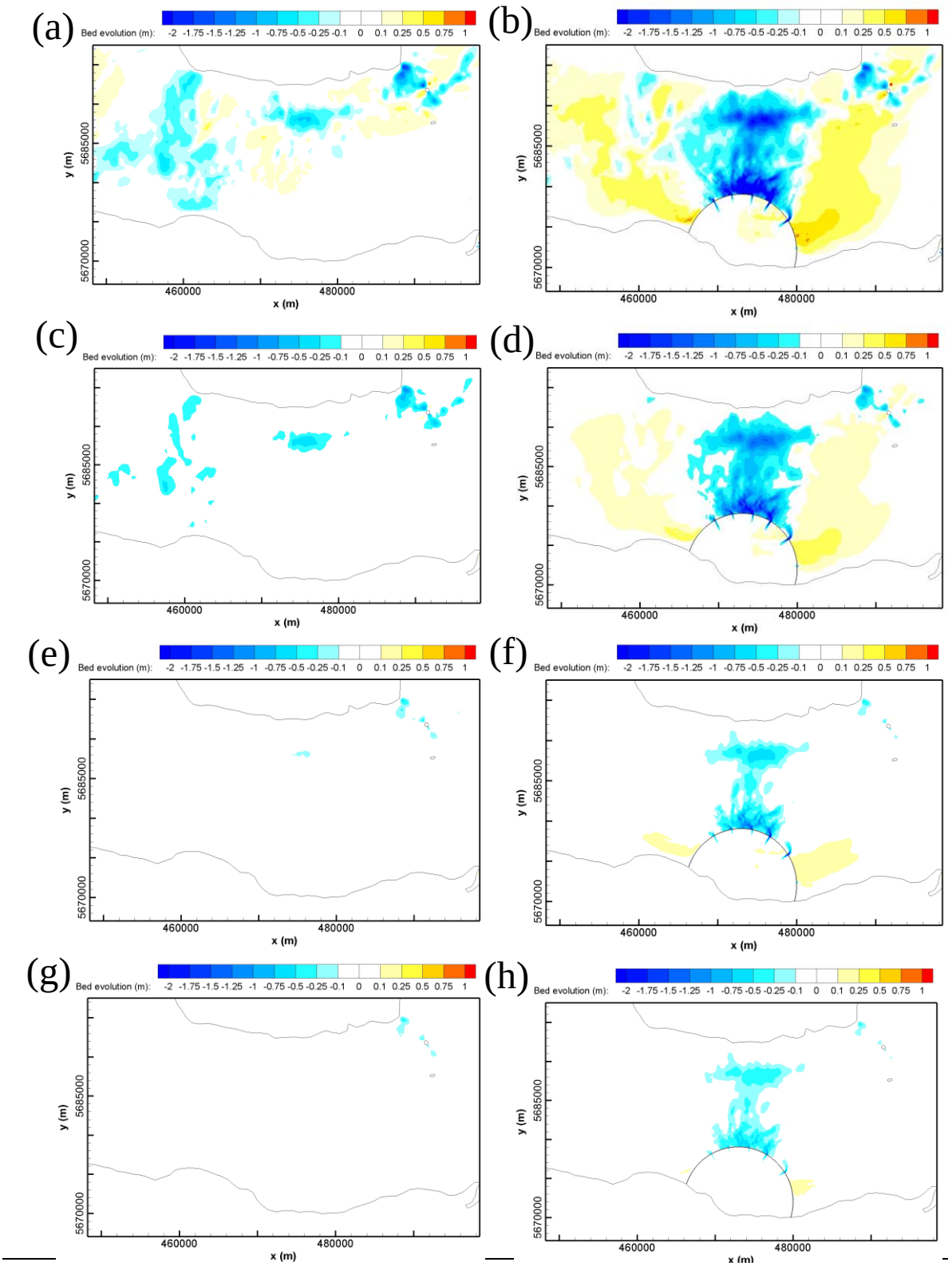

Figure 6.40: Seabed evolution in the inner Bristol channel for the pre- and post-WSL scenarios after a spring-neap cycle, with the critical deposition shear stress (τ_{cd}) equal to 0.1 N/m^2 and the critical erosion shear stress (τ_{ce}) equal to (a) (b) 2 N/m^2; (c) (d) 2.5 N/m^2; (e) (f) 3 N/m^2; (g) (h) 3.5 N/m^2.

The sensitivity tests of morphological evolution regarding the change of τ_{cd} showed that the model predictions were not sensitive to the change of τ_{cd} values. Little differences in morphological evolution were found with different τ_{cd} values and hence the results were presented in Appendix D, Figure D1- Figure D2, for brevity. According to the feature of the equilibrium transport equation of sediment, as demonstrated by Equation (3.25), sand deposition occurs when the bed shear stress is lower than the τ_{cd}, that is also when the tide speed is lower than a certain small value (approximately 0.15 – 0.25m/s). However, due to typically high tide speeds in this macro-tidal environment, the time period for sand deposition is too short, which is probably the reason why the morphological evolution prediction was insensitive to τ_{cd} changes.

Figure 6.40 (a) shows the erosion at the north side of the inner Bristol Channel and outer Severn Estuary in the natural condition, and sand deposition can be seen in the central part of the estuary. The flood tide dominates the north side of the inner Bristol Channel and outer Severn Estuary, transporting the sand up the estuary (Morris, 2006; Otto, 1998). While the ebb tide is higher in the central of inner Bristol Channel, where the sand moved downstream and deposited (Harris and Collins, 1991), as shown in Figure 6.36. Thus, the bottom evolution trend in this simulation matched the previously reported sand transport pathways in this area.

Results show that the erosion in the inner Bristol Channel was increased after the construction of WSL, especially the near-field area outside of WSL. Meanwhile, the siltation zone appeared on two sides of WSL, especially the west side. This is thought to be because the WSL blocked suspended sediment transport pathways at the south side of the inner Bristol Channel. Furthermore, it is learned in Section 6.4 that the bed shear stress was reduced on both sides of WSL where higher SS deposition rates appeared. In the WSL impoundment, noticeable scouring was found at the exit of the turbine, which was the direct impact of the accelerated flows in the immediate region around the turbines. Moreover, there was a slight siltation region observed inside WSL, which might be because of the distribution of resuspended sediment in a relatively large area beyond the water jet influence zone, resulting in the rise of bed level.

The morphological evolution of Swansea Bay for the pre- and post-SBL construction were also studied, with different τ_{ce} values. Model predictions were consistent with WSL modelling results, that morphological evolution was sensitive to τ_{ce} values and seabed erosion was more noticeable with a lower value of τ_{ce}. Unlike the strong current in the inner Bristol Channel, the tidal current speeds throughout most Swansea Bay are generally too low to transport sediment

particles larger than fine sand (Pye and Blott, 2014). Thus insignificant morphological evolution in Swansea Bay was observed in Figure 6.41. The hydrodynamic impact study of SBL in Section 6.3.2 shows that the operation of SBL only influences the current speed near the turbine and sluice gate. Figure 6.41 shows that the high-speed water jet flow through the turbine causes scour near the turbines, especially outside the dredging area. The accelerated flow erodes seabed in the near-field of the turbine and moves the sediment downstream, resulting in slight siltation just beyond the scouring zone, where the velocity magnitude of the water jet is lower.

However, given the uncertainty in estimating the net sediment flux and the lack of calibration process, and only the suspended sediment transport was simulated here, the morphological evolution in the presence of tidal lagoons should be considered cautiously. Furthermore, the inner Bristol Channel is mainly covered by the areas with extensive outcrops of bedrock, often covered by thin and discontinuous sediment veneer, as shown in Figure 6.20. Seabed erosion in the inner Bristol Channel was likely to be overpredicted since this feature was not presented accurately in the model. Therefore, further substantiation and improvement are needed. For example, a three-dimensional model would predict the near-bed flow more accurately. Furthermore, the spatially heterogeneous distribution of sand/bedrock constituents and the critical erosion shear stress should also be considered.

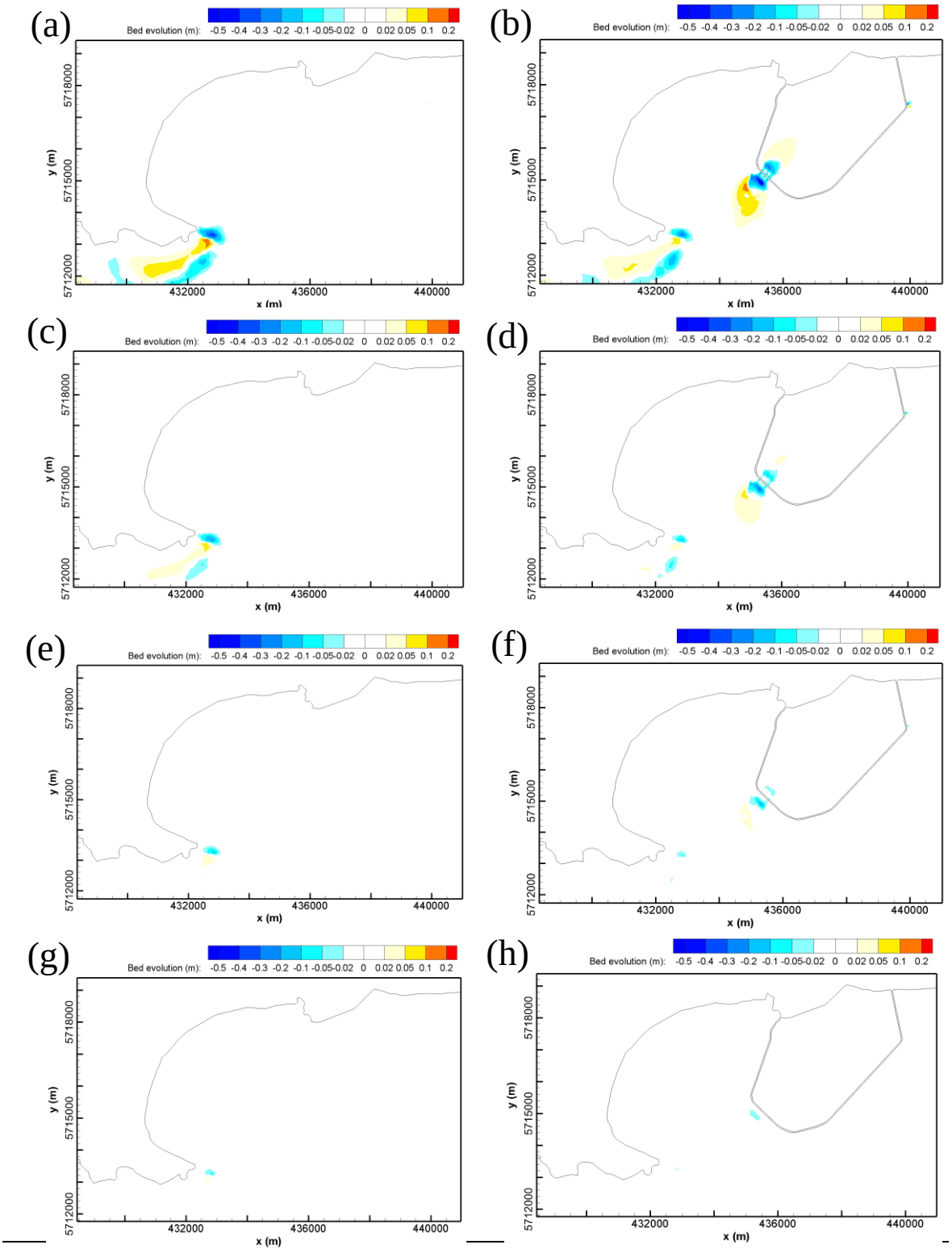

Figure 6.41: Seabed evolution in the Swansea Bay for the pre- and post-SBL scenarios after a spring-neap cycle, with the critical deposition shear stress (τ_{cd}) equal to 0.1 N/m^2 and with the critical erosion shear stress (τ_{ce}) equal to (a) (b) 2 N/m^2; (c) (d) 2.5 N/m^2; (e) (f) 3 N/m^2; (g) (h) 3.5 N/m^2, respectively.

6.7 Impacts on Phytoplankton Biomass - WSL

6.7.1 Phytoplankton Biomass

To investigate the effects of the nutrient enrichment on the UK estuaries and coastal waters, a simple single box, also called screening model, which was initially developed by the Comprehensive Studies Task Team (CSTT, 1997), was applied to investigate the eutrophication potential and phytoplankton growth in the region of Severn Estuary to inner Bristol Channel. This model aims to assess water quality in response to the EU Urban Waste Water Treatment Directive (UWWTD), by predicting the easily observed variables and then comparing with the defined thresholds, e.g. phytoplankton biomass chlorophyll (CSTT, 1997).

This model treats the sensitive area of the estuary ecosystem as a well-mixed box of volume, with nutrient exchange happening between the land, rivers, atmosphere and adjacent sea. With the UWWTD's definition, the 'Sensitive Area' is a water-body that is found to have the potential to be eutrophic if protective action is not taken (UWWTD, 1991). The mixing process in the sensitive area is described by the daily water exchanged rate (E), which expresses the instantaneous probability of the exchange of nutrients and phytoplankton in the replaced water from the adjacent sea or river discharge at a daily rate. The water exchange rate is equal to the reciprocal value of relative water residence times based on data presented by Tett et al. (2003a).

To begin with, equilibrium nutrient concentrations, including dissolved available inorganic nitrogen (DAIN) and dissolved available inorganic phosphate (DAIP), were calculated with the input nutrient from sources like river discharges, the nutrient concentration of the adjacent seawater, and the water exchanged rate between the study area and the adjacent sea region. Next, with a simplified assumption that there was a fixed yield efficiency of phytoplankton chlorophyll from dissolved available nutrient inputs, the maximum potential phytoplankton biomass is calculated. Based on potential maximum phytoplankton biomass values, then the potential maximum primary production was predicted using the light-controlled growth rate. In the end, the model prediction will compare with the defined CSTT thresholds, that the water body was judged as potentially eutrophic if the DAIN concentration exceeds 12 μM and DAIP exceeds 0.2 μM, along with the predicted potential maximum phytoplankton biomass chlorophyll concentrations of 10 mg Chl m^{-3} (CSTT, 1997). In this study, the region defined in this model was Severn Estuary and Inner Bristol Channel, which is from the tidal limit near Gloucester to Minehead.

Equilibrium nutrient concentrations (S_{eq}) for DAIN and DAIP are calculated as:

$$S_{eq} = S_0 + (S_i / (E \cdot V)), \quad (6.3)$$

where S_0 is the nutrient concentration (including DAIN and DAIP) from the surrounding seawater, S_i is the total of local nutrient inputs from sources of river, land etc. Other than seawater, E is the water exchange rate which refers to the daily rate at which water is exchanged, V is the volume of water in the studied estuary.

Total nitrogen and phosphorus loads were obtained from Jonas and Millward (2010). However, the mean daily water flow and mean annual concentration of nutrient monitoring data might underestimate peak nutrient loads during periods of extreme river flows. Thus, a magnification factor of 1.4 should be multiplied to mean annual concentration to correct the potential underestimation (Nedwell et al., 2002; Kadiri et al., 2014a). Furthermore, denitrification loss is included, as:

$$\% \text{ N\_denitrified} = 20.8 \cdot \log RT + 22.4, \quad (6.4)$$

where the RT is the residence time input as months (Nixon et al., 1996).

The potential maximum phytoplankton biomass yield from dissolved nutrient enrichment is predicted with the worst outcome, in which all of the dissolved nutrient is converted to phytoplankton:

$$X_{max} = X_0 + S_{eq} \cdot q, \quad (6.5)$$

where X_0 is the nutrient concentration of the surrounding seawater, q is the yield of chlorophyll from available nutrient inputs. According to the study of Underwood (2010), the concentrations of nitrogen, phosphate and chlorophyll at the Bristol Channel South were 80, 2.5 and 6 μM, which were used in this study as the nutrient input concentration from the adjacent seawater. The yield q of chlorophyll from DAIN and DAIP were taken as 0.25 mg Chl (mmol DAIN)$^{-1}$ and 4 mg Chl (mmol P)$^{-1}$ separately, which have been used as for the study in the Severn Estuary (Kadiri et al., 2014b).

Light controlled growth rates of phytoplankton are calculated as (Tett et al., 2003b):

$$\mu(I) = \alpha^B \cdot (I - I_c), \quad (6.6)$$

where α^B is the effective photosynthetic efficiency at low illumination which is taken value of 0.006 as the recommendation of CSTT, *I* is the upper mixed layer photosynthetically available radiation (PAR) averaged over 24 hours for a typical summer day, I_c is compensation photosynthetically available radiation (PAR).

24-h averaged photosynthetically available radiation (PAR) is calculated as follows (Tett et al., 2003b):

$$I = (1 - m_0) \cdot m_1 \cdot m_2 \cdot I_0 \cdot (1 - e^{-k_d \cdot h})/(k_d \cdot h), \tag{6.7}$$

where I_0 is the mean annual 24-h solar radiation at the sea-surface, m_0 is sea-surface albedo, m_1 converts solar radiation to photosynthetically available radiation photons and m_2 represents losses additional to those of Beer–Lambert decay, k_d is the diffuse attenuation for photosynthetically available radiation. The diffuse attenuation for photosynthetically available radiation in k_d includes components due to seawater itself, coloured dissolved organic matter (CDOM) which is also referred to as yellow substance, phytoplankton pigments, other organic particulates, and inorganic particulates. *h* is the depth of the upper mixed layer.

A linear regression model was applied to calculate the diffuse light attenuation K_d (Devlin et al., 2008), as followed:

$$K_d = 0.08596 + 0.06729 \cdot SPM, \tag{6.8}$$

The *SPM* is the suspended particulate matter in marine waters, which is taken as the value of suspended sediment concentration (mg/l).

Potential maximum primary production is calculated in conjunction with Light Controlled Growth Rates and the predicted phytoplankton biomass (Painting et al., 2007)

$$\mathrm{P_{max}} = (X_{max} \cdot \mu(\mathrm{I}) \cdot C{:}Chl \cdot 365 \cdot h)/1000, \tag{6.9}$$

where X_{max} is maximum potential phytoplankton biomass, $C{:}Chl$ is the annual carbon to chlorophyll ratio.

In summary, the parameters used in this model are summarised in Table 6.5.

Table 6.5: input variable and parameters for the screening model.

Symbol	Meaning of symbol	Value	Units
Model predicts variables			
Seq	Equilibrium nutrient concentration		μM
Xmax	Potential maximum phytoplankton biomass		$mg\ m^{-3}$
$\mu(I)$	Microplankton relative growth rate		d^{-1}
P_{max}	Potential maximum primary Production		$gCm^{-2}yr^{-1}$
Site-determined Parametrers			
E	Water exchange rate		d^{-1}
L	Loss rate of microplankton due to mesozooplankton and benthic grazing, sinking	0.0	d^{-1}
S_i	Total nutrient inputs to enclosed basin from all sources except sea		$Kmol\ d^{-1}$
	N load (Jonas and Millward, 2010)	170.3	$10^3\ kg\ d^{-1}$
	P load (Jonas and Millward, 2010)	12.2	$10^3\ kg\ d^{-1}$
S_0	Seawater nutrient concentration		μM
	Seawater nitrogen (Underwood, 2010)	80	μM
	Seawater phosphate (Underwood, 2010)	2.5	μM
	Seawater chlorophyll (Underwood, 2010)	6	μM
V	Volume of enclosed basin		$10^6\ m^3$
	Pre-WSL	52507	$10^6\ m^3$
	Post-WSL	51182	$10^6\ m^3$
X_0	Seawater chlorophyll concentration		$mg\ m^{-3}$
Standard parameters			
q	Chlorophyll yield (DAIN)	0.25	$mg\ Chl\ (mmol\ N)^{-1}$
q	Chlorophyll yield (DAIP)	4	$mg\ Chl\ (mmol\ P)^{-1}$
α^B	Effective photosynthetic efficiency	0.006	$d^{-1}\ (\mu Em^{-2}S^{-1})^{-1}$
C:Chl	Carbon to chlorophyll ratio (annual)	40	
I_c	compensation irradiance	5	$\mu Em^{-2}S^{-1}$
Used to calculate standard parameters			
α_m	Algal (chlorophyll related), nutrient replete, photosynthetic efficiency	0.042	$mmol\ C\ (mg\ Chl)^{-1}\ d^{-1}(\mu Em^{-2}S^{-1})^{-1}$
b	Rate of increase of (microplankton) respiration with growth = $b_a(1 + b_h\eta) + b_h$	1.4	---
b_a	Rate of increase of (autotroph) respiration with growth	0.5	---
b_h	Rate of increase of (heterotroph) respiration with growth	1.5	---
η	'Heterotroph' fraction = microheterotroph carbon	0.4	---
Biomass/total microplankton biomass			---

Continued Table 6.5

Q_{maxa}	Maximum autotroph nitrogen content	0.2	$mmol\ N\ (mmol\ C)^{-1}$
${}^{x}q_a^N$	Autotroph chlorophyll nitrogen ratio	3	$mgChl(mmol\ N)^{-1}$
r_{0a}	Autotroph basal respiration (at zero growth)	0.05	d^{-1}
r_{0h}	Heterotroph basal respiration (at zero growth)	0.07	d^{-1}
Submarine optics			
I	24-h mean photosynthetically available radiation (PAR)		$\mu E m^{-2} S^{-1}$
I_0	Mean annual sea-surface 24-h solar radiation	150	$W\ m^{-2}$
m_0	Sea albedo	0.06	---
m_1	Conversion from total solar energy to PAR photons	1.909	---
m_2	Fraction of the surface PAR that is penetrating light	0.4	---
h	Depth in the photic zone	0.2	m
k_d	Diffuse attenuation for PAR (Kadiri et al., 2014a)	80.8	m^{-1}

6.7.2 Eutrophication Potential

The water exchange rate and suspended particulate matter values are the main unknown factors in evaluating nutrient concentration and phytoplankton growth. It was shown in Section 6.5.1 that the averaged residence times in the Severn Estuary and inner Bristol Channel are 62.04 and 49.46 days for the natural condition and post-WSL scenario, respectively. These correspond to the water exchange rate of 0.016 and 0.020 for each scenario, correspondingly. After processing the data achieved from Section 6.6, the time and spatial averaged suspended sediment concentrations are achieved, as 0.8599 g/l and 0.920 g/l in the Severn Estuary and inner Bristol Channel for pre- and post-WSL, respectively. It was then estimated that the diffuse light attenuation K_d values are 57.955 m^{-1} and 61.99 m^{-1}, respectively, according to Equation (6.8).

The predictions of the equilibrium nutrient concentrations, potential maximum phytoplankton biomass chlorophyll and phytoplankton primary production for pre- and post-WSL scenarios were calculated and shown in Table 6.6. Previous measurement or modelled data from other researchers and the thresholds set by the UK's Comprehensive Studies Task Team (CSTT) are also shown in Table 6.6. The predicted nutrient concentrations and chlorophyll concentrations for the natural conditions are all within the range of measured nutrient concentration (Owens, 1984; Underwood, 2010), demonstrating the reliability of this model.

Table 6.6: Range of dissolved nutrients and chlorophyll concentrations in the research area and the model predictions for pre- and post- WSL.

	Equilibrium nutrient concentrations (μM)		Potential maximum phytoplankton biomass chlorophyll (mg m^{-3})		Phytoplankton primary production (g C m^{-2} yr^{-1})	
	S_{DAIN}	S_{DAIP}	X_{max} (N)	X_{max} (P)	P_{max} (N)	P_{max} (P)
CSTT thresholds	12	0.2	10		--	--
Owens (1984)	40.7-351.4	0.6-5.3	5.0-80.0		--	--
Underwood (2010)	70.0- 550.0	3.0-15.0	0.5-36.0		--	--
Radford (1994)	--	--	--		0.73	
Kadiri et al. (2014a)	236.7	6.4	65.2	31.7	1.9	0.9
Pre-lagoon prediction in this study	89.33	2.71	28.33	16.84	2.14	1.27
Post-lagoon prediction in this study	87.56	2.67	27.89	16.68	1.80	1.08

For the no-lagoon scenario, it is noticeable that both the nutrient concentrations significantly exceeded the defined CSTT thresholds, which indicated the hypernutrified (i.e. nutrient enriched) seawater in Severn Estuary. This conclusion is in accordance with the previous investigation and research (Nedwell et al., 2002; Kadiri et al., 2014b), that the Seven Estuaries to inner Bristol Channel received high drain nutrient load from the tributary rivers, agriculture drain and other anthropogenic activities, resulting in high nutrient concentrations in this area. The potential maximum phytoplankton biomass chlorophyll concentrations are 28.33 mg m^{-3} for X_{max}(N) and 16.84 mg m^{-3} for X_{max}(P), respectively. These values are also much higher than the CSTT thresholds indicating the eutrophic feature of this region. However, this value might be over-predicted because the maximum phytoplankton growth ratio used in this study is considered an ideal situation and may rarely be reached over an extended period realistically. This could be the reason why no eutrophication was reported in the Severn Estuary (Langston et al., 2010).

The phytoplankton primary productivity for the natural condition is 2.14 g C m^{-2} yr^{-1} and 1.80 g C m^{-2} yr^{-1} for N and P, respectively, which is at the same level as the previous study (Radford, 1994; Kadiri et al., 2014a). The phytoplankton primary productivity is strongly associated with light availability. Higher turbidity indicates a higher diffuse attenuation for photosynthetically available radiation (k_d), resulting in a lower available light radiation for phytoplankton production. It is derived from Section 6.6 that the operation of WSL increased the SS concentration by 7% in this study domain, therefore WSL operation would reduce the phytoplankton growth rate and phytoplankton primary production to 2.14 g C m^{-2} yr^{-1} and 1.80 g C m^{-2} yr^{-1} for N and P, respectively.

With the operation of WSL, the predicted value of equilibrium nutrient concentrations, the chlorophyll concentration decreased by 1% - 2%, and phytoplankton primary production decreased by 15%. These slightly decreased values of equilibrium nutrient concentrations and the chlorophyll concentration are mainly the consequence of improved tidal flushing characteristics, which benefit nutrient dispersion and reduce the retention time of nutrients. However, phytoplankton primary production is noticeably affected by the increased SS concentration, which result in a lower available light radiation and slow the phytoplankton growth and photosynthesis. These results indicate that the operation of WSL would slightly reduce the hypernutrified and eutrophic risk.

6.8 Summary

This chapter provides a comprehensive study on different aspects of the environmental impact of the proposed TRSs. The impact of TRS on basic physical indicators of tide change, i.e. water level and velocity magnitude, are investigated. Then the following influence of hydro-environment is studied, including the change of intertidal mudflat area, water quality characteristics, suspended sediment transport, as well as nutrient concentration, phytoplankton biomass in the TRS influence region.

The tidal harmonic constituents changes were explored to achieve a better understanding about the water level and the tidal phase change. The operation of WSL will decrease the amplitude of the M2, N2, S2 tidal constituents while decreasing the phase on the western side of the lagoon and increasing it to the east. Correspondingly, the operation of WSL would generally increase the low-water levels and decrease the high water levels in the Bristol Channel and Severn Estuary. The reduction in the high water levels would decrease coastal flood risk, and the increase in the low water levels would slightly benefit port access to shipping and recreational yachting in the shallow waters of the Severn Estuary. SBL has a similar effect with WSL on the tidal constituents and water level change in Bristol Channel. However, the impacts are relatively minor and localised compared with the WSL for its small scale. The tidal amplitudes decreased in the Severn Estuary while tidal phases barely changed. The high water level decrease is mainly confined in SBL impoundment, which is approximately 1.45 m. For the operation of NWTL, a slight decrease of both M2 amplitude and phase is observed in the north of NWTL, while N2 constituent increased in the east coast of Ireland and the Celtic Sea. Results show that NWTL could influence sea water levels in both near-fields (i.e. Colwyd Bay

and Liverpool Bay) and far-fields (i.e. Cardigan Bay). The noticeable lowering of water levels inside the NWTL was the result of the two-way operation, which could provide extra protection for defences against flooding. Furthermore, the operation of the NWTL could also decrease the water level in Liverpool Bay by 5-10 cm while causing increases of the same value in Cardigan Bay.

One of the most direct results of water level change is the evolution of intertidal mudflat, which was investigated in this research as an indicator of the ecological impact. WSL decreased low intertidal mudflat up to 20 km^2 due to increased minimum water level. Besides the coastwise area within the WSL basin where gone through a noticeable increase of minimum water level, the lost low intertidal mudflats mainly concentrate on Welsh Ground and the Severn Beach due to its shallow bathymetry and the gentle slope. For the SBL, the loss of low-level mudflat inside the SBL is about 1.027 km^2, while the mudflat area beyond the SBL basin remains unaffected. The NWTL operation results in a noticeable loss of low-level mudflats inside the NWTL basin, up to 20 km^2, due to the relatively high bathymetry and the gentle slope in this area. The change of intertidal zones might affect the biodiversity and feeding grounds for birds, mussels, and insects. These findings need further investigation in the future to enable the impacts to be determined more precisely, and particularly identifying the key sites of any changes within the estuary.

Significant maximum velocity increases are observed in the wake from turbine and sluice gate for all TRSs, which could exceed 1.5 m/s. Furthermore, the maximum velocity in the inner Bristol Channel was predicted to increase by 0.25-0.75 m/s with the operation of WSL, while the corresponding maximum velocity decreased inside the WSL basin, and across most of the plan-surface area away from the turbine and sluice gate wakes. For SBL case, the influence on current speed is also limited within Swansea Bay. The velocity reduction zone is found south of SBL basin. The averaged velocity magnitude increased up to 0.75 m/s in the turbine wake, with a large velocity reduction area appear beyond the turbine wake influence zone. The impacts of the NWTL on tidal currents were mainly concentrated in the near-field. Besides the significant increase in the velocity at the turbine and sluice gate exits, the tidal velocity magnitude inside the impoundment area increase by 0.1-0.5 m/s. Zones of both increased and decreased velocity appeared to the east of the island of Anglesey, which might influence the deployment of potential tidal stream devices.

The bed shear stress is related to the square of the velocity and therefore showed similar but more distinct patterns of change as the velocity distribution. For the post-WSL scenario, the maximum bed shear stress was predicted to increase by up to 20 N/m^2 in the wake of the turbines and to decrease by 1-4.0 N/m^2 for most of the lagoon inside the area. The slight decrease in the bed shear stress slightly increases the settling of the sand or mud, which indicates potential sedimentation in the landward area of the WSL basin. The noticeable change of bed shear stress in Swansea bay is the increase in the turbine wake, which suggests scouring near the turbine and sluice gate block, especially because the sand and muddy dominate the seabed of Swansea bay. In the NWTL scenario, besides the noticeably increased bed shear stress observed in the wake of sluice gates, a slight increase of bed shear stress, 1-4 N/m^2, is observed in the most middle area of NWTL impoundment. This indicates that scouring will occur at both turbine wakes and the area inside of NWTL impoundment.

To achieve more details about how the tidal lagoon operation influence the suspended sediment (SS) concentration distribution and potential topography evolution, a sediment transport and morphodynamic simulation module, GAIA, is coupled with Telemac-2D to simulate the transportation of SS. Results found that the operation of WSL increases the SS carrying capacity markedly in the inner Bristol Channel, especially north of the WSL structure. In contrast, the impounded water inside of WSL shows immediate notable low SS concentration, away from the water jet influence area.

A series of critical erosion shear stress (τ_{ce}) and critical deposition shear stress (τ_{cd}) are applied in morphological simulation to test the model sensitivity and to explore the seabed level change. Results show that morphological evolution is highly sensitive to τ_{ce} values, and seabed erosion is more noticeable with a greater value of τ_{ce}. While the value of τ_{cd} in the range of 0.05 – 0.15 N/m^2 has an insignificant influence on morphological evolution in this simulation. Overall, the presence of WSL would lead to seabed erosion in the inner Bristol Channel, especially the area just out of WSL. The high-speed water jet caused scouring near the turbine, both inside and outside of WSL. Furthermore, the sedimentation zone appears at two sides out of WSL and water impoundment area, resulting from the blocking of sand pathway and the reduced SS carrying capacity. As for SBL, due to its small scale and limited hydrodynamic impact, the consequent influence on SS transport is also mainly limited near the turbine block. The water jet through turbines mobilise sand downstream, causing souring near the turbine, and the resuspended sand settled at the reduced water jet speed.

Moreover, in the hydrodynamic impact study, the well-studied SBL hydrodynamic impact has been compared with the previously reported research as a benchmarking study. The consistency of the SBL modelling results gives the confidence of the TRS modelling for this research (Tidal Lagoon Plc, 2013; Čož et al., 2019; Angeloudis and Falconer, 2017)

The residence time was predicted to assess the general water renewal capacity in the interesting area with the operation of TRS. When releasing tracer inside of WSL, the results indicated that the operation of the lagoon would decrease the renewal time from 22.4 days to 8.1 days for the pre-lagoon and post-lagoon cases, respectively. This demonstrates that WSL could improve the renewal time and flushing characteristics in the water impoundment area by 63.8%. The conservative momentum formulation modelling result indicated an increase in the renewal time of 24% compared with the renewal time for a mass balance-only model. This suggests that the operation of WSL would accelerate the pollution decay inside of the lagoon, which would be meaningful in the future design of such TRS where there are potential pollution risks.

Furthermore, the water renewal capacity of Bristol Channel and Severn Estuary for the pre- and post-WSL were studied. Results show that the residence time in Bristol Channel, inner Bristol Channel and Severn Estuary has decreased by 43%, 20%, and 13% respectively after the inclusion of WSL. This is brought about by could be due to the increased tide velocity in the inner Bristol Channel, which contributes to an improved water exchange rate in the Bristol Channel. Consequently, the decreased residence time results in a 1.2% - 2% decrease of the equilibrium nutrient concentrations, potential maximum phytoplankton biomass chlorophyll, and a 15% decrease of phytoplankton primary production. Although the nutrient concentrations and chlorophyll concentration still exceed the defined CSTT thresholds for both pre- and post-lagoon conditions, the decreased values indicated that the operation of WSL would slightly reduce the hypernutrified and eutrophic risk.

The residence time study in SBL scenario shows that SBL could decrease the water residence time by 10.45% in the Swansea Bay and Porthcawl, while increasing it by 4% in the SBL basin. The impact of SBL on the water exchange rate is more noticeable at the initial stage after releasing the tracer, but turn to mitigate in a longer time scale. The remaining tracer concentration suggests the low water renewal capacity at the landward part of the SBL basin and the improved water exchange rate on the west side of SBL. The residence time study in the NWTL impoundment basin indicated that the water renewal capacity was reduced by 45.7% with the operation of NWTL. This is deduced to be due to the high natural water exchange rate

in the proposed impoundment basin and the limited discharge volume of the sluice gates on the East side of the lagoon.

Chapter 7 Interactions of Lagoons

Accumulated hydrodynamic impacts and interactions were expected from the conjunctive operation of multiple TRSs (Wilson et al., 2012; Wolf et al., 2009; Cornett and Cousineau, 2011). Although it was learned from Chapter 6 that the hydrodynamic impacts of each lagoon are mainly distributed in the near-field, it is still important to evaluate the potential interactions between TRSs on electricity generation and the environment. Furthermore, the interactions and accumulated impact of tidal lagoons cannot be simply added together to estimate cumulative impacts because both lagoons are in operation condition, and any hydrodynamic changes, especially the water level change, will induce the consequent alteration of the impact of another lagoon and vice versa. For this purpose, the power output and the environmental impact of both the individual operation of each lagoon and the conjunctive operation should be predicted and compared. It is thus required to simulate the tidal lagoons in the same model domain. Considering the influence area of each TRS and potential combined interaction of the TRS system, two conjunctive TRSs operation cases were considered in this study; WSL and NWTL in the CS model, and WSL and SBL in the SEBC model. Meanwhile, it is important to explore and compare the performance of the WSL individual operation in the CS and SEBC models, to ensure a stable TRS simulation with different boundary locations and assess the potential impacts of WSL on the SEBC model boundary.

The structure of this chapter is organised as follows: The WSL modelling results using the CS and SEBC models are compared in Section 7.1, to explore the effects of the open boundary location on the near-field and far-field hydrodynamics of WSL, and to confirm the consistent lagoon modelling between the two models. Section 7.2 and Section 7.3 present the conjunctive operation of SBL&WSL and WSL&NWTL, respectively. The potential interaction between TRSs, including impact on hydrodynamic and energy output, were investigated. Furthermore, the continuous energy output from the conjunctive operation of WSL and NWTL were discussed in Section 7.3, which indicates a potential continuous power generation provided by the TRSs system.

7.1 Effect of Open Boundary Location

It is learned from previous research that the influence of WSL on high water level variation is limited within the Bristol Channel (Guo et al., 2021). However, given that a pre-defined water

level input is applied on the open boundary of the hydrodynamic model, it is deduced that the tide level near the open boundary condition is free from the influence of TRS operation (Rainey, 2009; Garrett and Greenberg, 1977). Evidence shows that discrepancies may exist if the computational domain is not sufficiently large when simulating a large scale TRS, such as Severn Barrage (Bondi, 1981; Zhou et al., 2014b). In this situation, a certain method should be applied to reduce the influence of TRS on the open boundary, either addressing the open boundary problem theoretically (Adcock et al., 2011), or extending the open boundary to the seaward to capture the change to the tidal resonance (Zhou et al., 2014b). However, with a relatively smaller scale and not blocking the whole estuary comparing with the Severn Barrage, it is unknown whether the open boundary of the WSL model should be extended seaward. Thus, before investigating the potential far-field impact of WSL, it is important to evaluate the WSL performance in the CS and SEBC models, which is also studying the effect of open boundary location on the impact of WSL lagoon operation.

To detect the far-field impact of WSL and to identify the effect of open boundary location on WSL lagoon operation, WSL was simulated in the CS model to study its hydrodynamic impact, which was then compared with the predictions from the SEBC model. The WSL simulated in both CS and SEBC models have the same configuration, operation scheme and turbines and sluice gates settings. Moreover, to eliminate the potential prediction deviation as a result of differences in the mesh, the mesh resolution in the overlap area between the CS and SEBC model was identical. It was estimated that the predicted influence of the WSL should be similar between the SEBC and CS models if there were less influence of WSL operation on the SEBC open boundary.

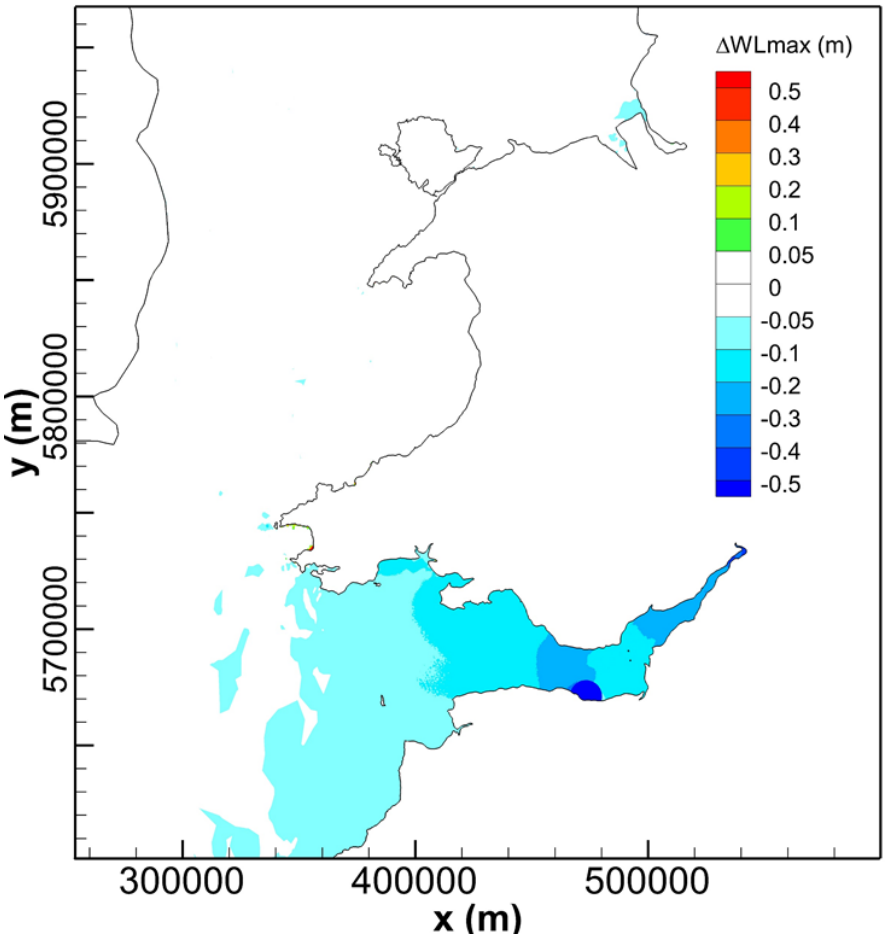

Figure 7.1: The impact of the WSL on maximum water level during a spring-neap tidal cycle in the CS model.

Figure 7.1 shows that the impact of WSL operation on the high water level extends to the mouth of Bristol Channel, with the maximum water level in the outer Bristol Channel decreasing by 5-10 cm. The decrease in maximum water level becomes more noticeable in the landward direction, with a 10-20 cm reduction in the central Bristol Channel and a 20-30 cm drop distributed in the inner Bristol Channel and the Severn Estuary. However, no significant water level changes are found outside Bristol Channel, in the Irish Sea and the Celtic Sea.

Comparing the impact of the WSL on the high water level in the CS model (Figure 7.1) and in the SEBC model (Figure 6.5), it was found that higher decreases of maximum water level appeared in the CS model. For example, a 20-30 cm high water level decrease is shown in the inner Bristol Channel and the Severn Estuary in the CS model, while only a small area in the SEBC model shows this perturbation. The high water level variation extends to the outer Bristol Channel in the CS model while it only reaches the central Bristol Channel in the SEBC model. This observation is consistent with previous research studying the effect of an open boundary

location on modelling a Severn Barrage, that the area where water levels were affected varied when an inappropriate boundary was selected (Zhou et al., 2014b).

The impact of WSL on maximum velocity magnitude in the CS model is shown in Figure 7.2. Most of the maximum velocity magnitude changes were observed in the proximity of the WSL in the CS model, that an increase in velocity of 0.1-1.3 m/s appeared in the inner Bristol Channel, while a slight decrease of 0.1-0.7 m/s occurred on two sides of the WSL, which is similar to the prediction by the SEBC model (Figure 6.14). Negligible maximum velocity change was observed in the far-field, except in some shallow areas like shallow parts of Liverpool Bay. However, it is doubtful that the slight velocity change in Liverpool Bay is caused by the WSL, and more specific research is needed to determine this phenomenon.

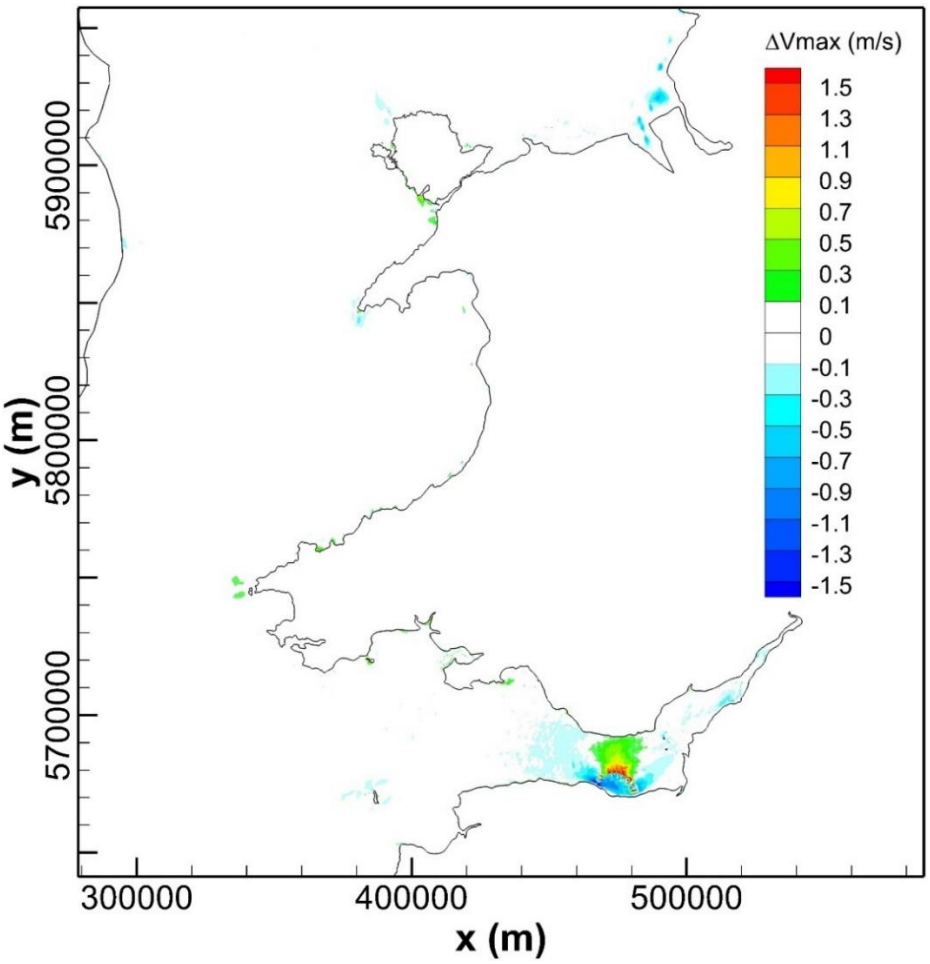

Figure 7.2: The impact of the WSL on maximum tide speed in the CS model during a spring-neap tidal cycle.

The main differences between the results of CS and SEBC models when simulating the impacts of the WSL on the hydrodynamics of the region are the range and extent of the maximum water level. This indicates that the operation of the WSL would influence the open boundary

condition of the SEBC model. Figure 7.3 indicates that the WSL will increase the low water level and decrease the high water level by a few centimetres at the SEBC open boundary. Thus, a certain solution may be needed to mitigate the influence of WSL on SEBC open boundary, either extending the model domain or addressing the open boundary problem theoretically. However, the comparison between Figure 6.5 and Figure 7.1 shows that although there is an obvious difference of maximum water level at the outer Bristol Channel between the two models, the range and extent of maximum water level changes are similar in the Severn Estuary and the inner Bristol Channel. Moreover, this research focused on the hydro-environmental impact assessment, e.g., water renewal capacity and suspended sediment transport, which is more related to the tidal flow pattern changes. Meanwhile, the maximum current speed changes were consistent between the two models. Thus the SEBC model is adequate in this research for the energy output and hydro-environmental impact study of WSL.

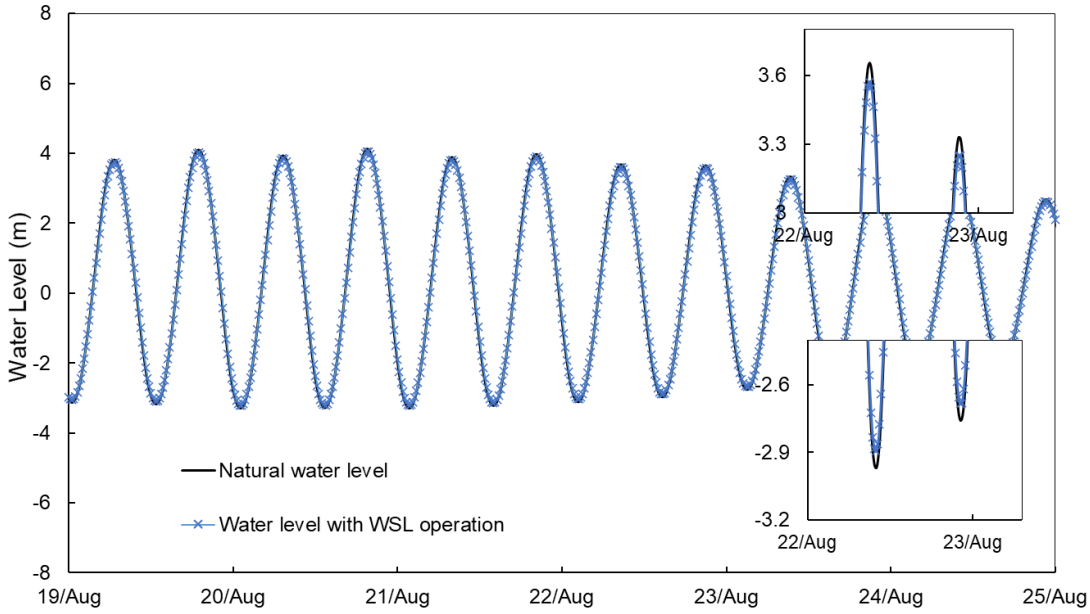

Figure 7.3: The water level comparison on the location of Bristol Channel mouth in CS model, for pre- and post-WSL.

The electricity generation of WSL in the CS model for the typical tidal cycle is 0.219 TWh and 0.254 TWh for the optimised flexible generation without and with pumping, respectively. Compared with the prediction from the SEBC model, the WSL energy outputs with the two operation schemes in the CS model were 6.0% and 5.6% lower, respectively. This power outputs difference is a result of the different tidal range predictions between SEBC and CS models.

7.2 Interaction between WSL and SBL

The WSL and SBL were operated in the same model to investigate their interaction and the cumulative impact on the surrounding waters. It was expected that their cumulative impacts are not noticeably magnified because of the small scale of SBL. Furthermore, the internal comparison results of individual operation and conjunctive operation of tidal lagoons should not be noticeably affected by the open boundary issue. Therefore, SEBC model was expected to be eligible for this study purpose. The lagoons conjunctive operation model settings follow the previous individual TRS simulation settings. The time lag of tidal phases between WSL and SBL is less than half an hour, thus the operation of SBL and WSL generally follows similar operation phases. To accurately assess the hydrodynamic impacts of two lagoons, the mesh for the pre-lagoons and post-lagoon scenarios modelling have adopted the same spatial distribution away from the lagoons (as seen in Appendix C). As expected, the mesh was refined in the location of the lagoon when the lagoon was simulated.

Figure 7.4 and Figure 7.5 show the high water level and the maximum velocity change in the Bristol Channel with the joint operation of WSL and SBL. By comparing the individual operation of WSL (Figure 6.5) and SBL (Figure 6.9), and the conjunctive operation (Figure 7.4), it was concluded that the maximum water level change is similar between the scenario of conjunctive operation and the WSL individual operation. However, there are slight differences in the high water level decrease region, e.g. the 0.2 - 0.3 m high water level decrease zone in the Severn Estuary extends toward seaward with the conjunctive operation. The impact of individual operation and conjunctive operation of SBL and WSL on the maximum velocity could be observed from Figure 6.14, Figure 6.15 and Figure 7.5. Regarding the maximum velocity magnitude change, there are negligible interactions between WSL and SBL. It is clear that each lagoon itself dominates the flow structure around the lagoon structure.

The energy outputs from WSL snd SBL were summarised in Table 7.1 for different scenarios. It is noted that the operation of SBL has negligible influence on WSL power generation, while the existence of WSL has reduced the SBL energy output by 3.7%. The variations of power output from WSL and SBL agree with the hydrodynamic impacts, that the WSL reduces the tidal range in Swansea Bay by a few centimetres, as shown in Figure 7.6. Furthermore, this power output change could be to slight changes in water levels comparing to the water levels used for optimisation. By contrast, SBL has barely any influence on the water level change in far-field such as the West Somerset coast. The interaction between WSL and SBL on power

generation is limited but should not be overlooked, for any loss of electricity generation would bring a lower investment return.

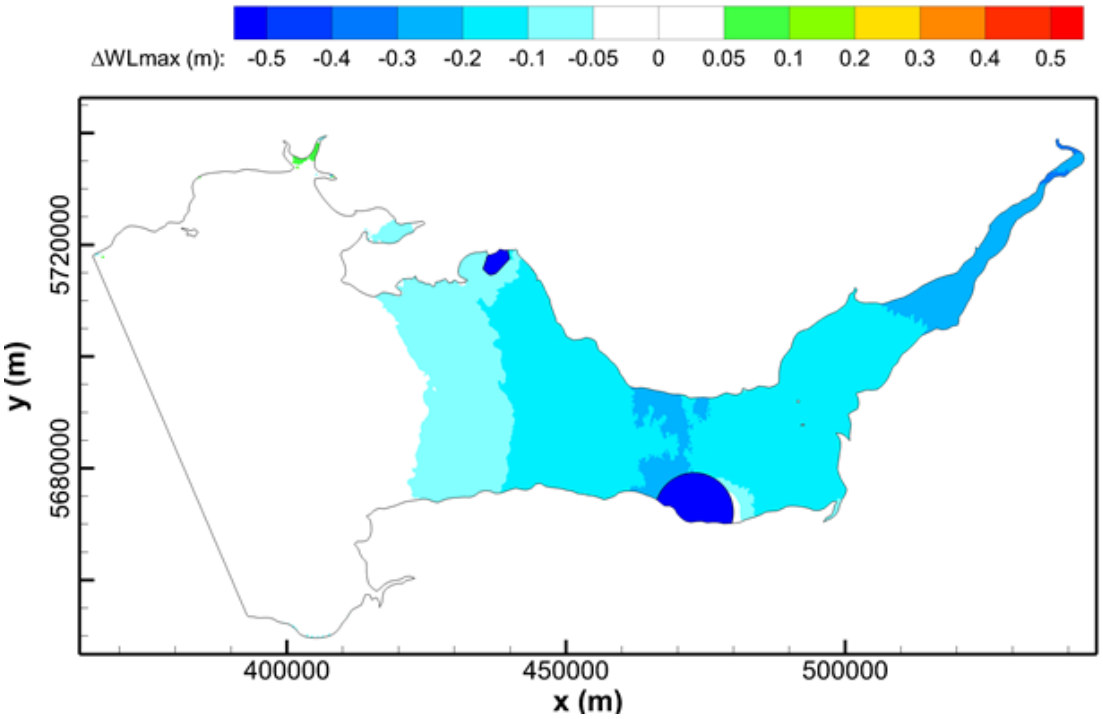

Figure 7.4: The accumulative impact of SBL and WSL on maximum water level.

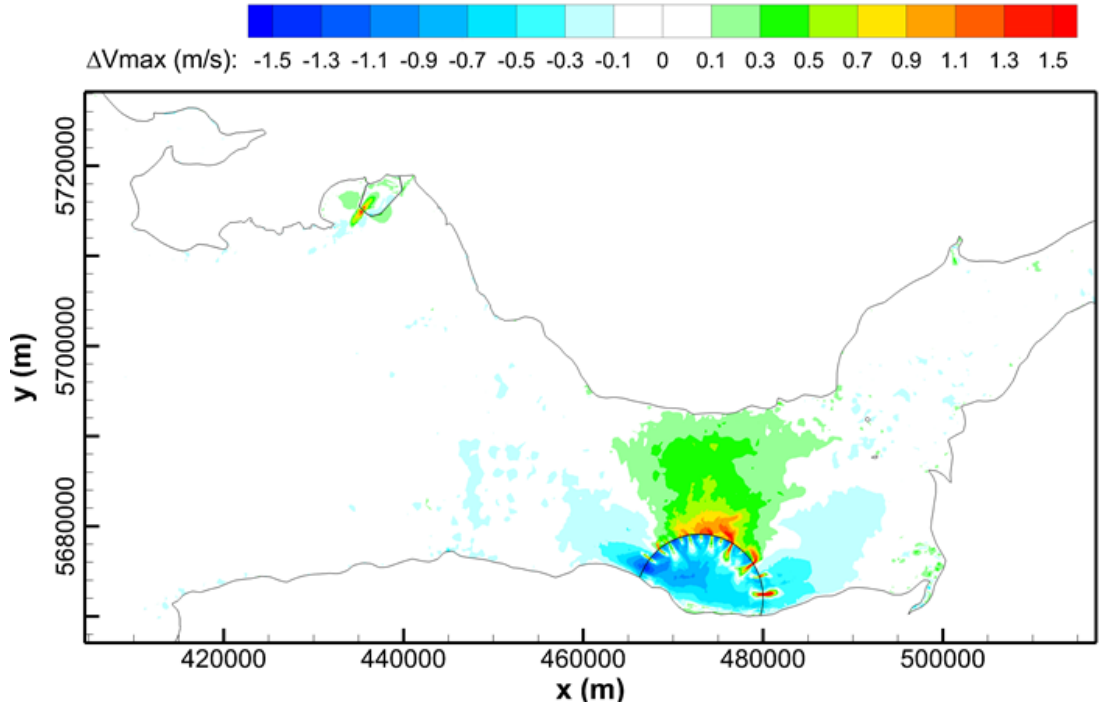

Figure 7.5: The accumulative impact of SBL and WSL on maximum velocities.

Table 7.1: Typical energy outputs for the WSL and SBL with and without interaction between the two.

TRS	Condition	Flexible two-way (GWh)
WSL	Without SBL	233.48
	With SBL	231.84
	Difference	-0.76%
SBL	Without WSL	23.74
	With WSL	22.87
	Difference	-3.7%

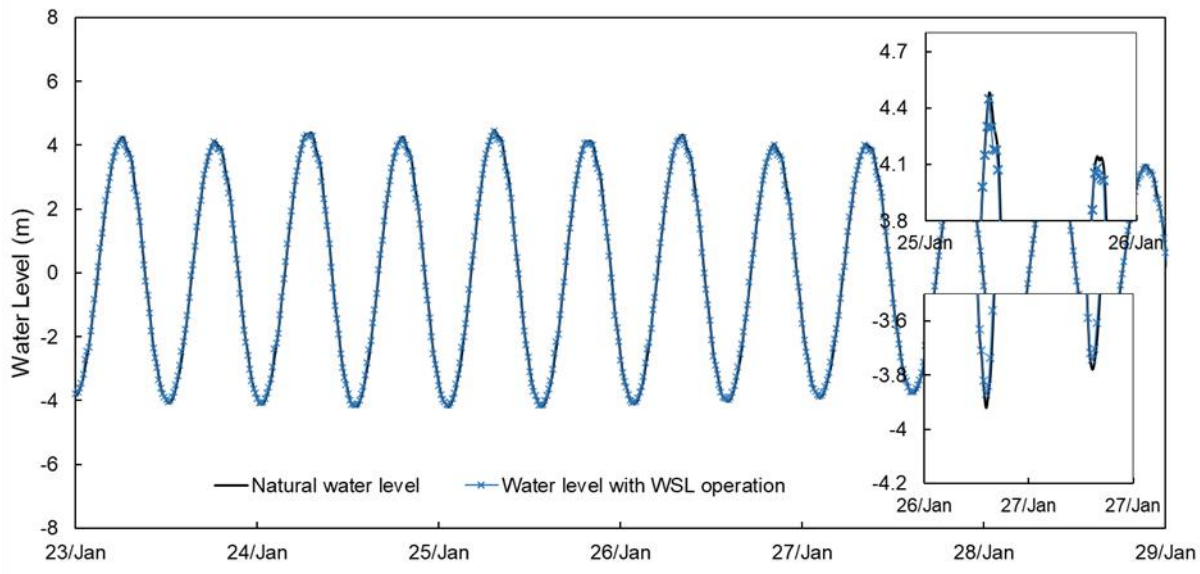

Figure 7.6: Water level change at Swansea Bay for the pre- and post-WSL conditions.

7.3 Interaction between the WSL and NWTL

7.3.1 Hydrodynamic Interaction

The NWTL and WSL are conjunctively operated in the CS model to investigate their potential interaction. The hydrodynamic changes that occurred with the conjunctive operation of WSL and NWTL are shown in Figure 7.7 and Figure 7.8. It is worth noting that the figures are focused on the area of interest of the original domain (Figure 3.18), which is extended beyond the area in the figure.

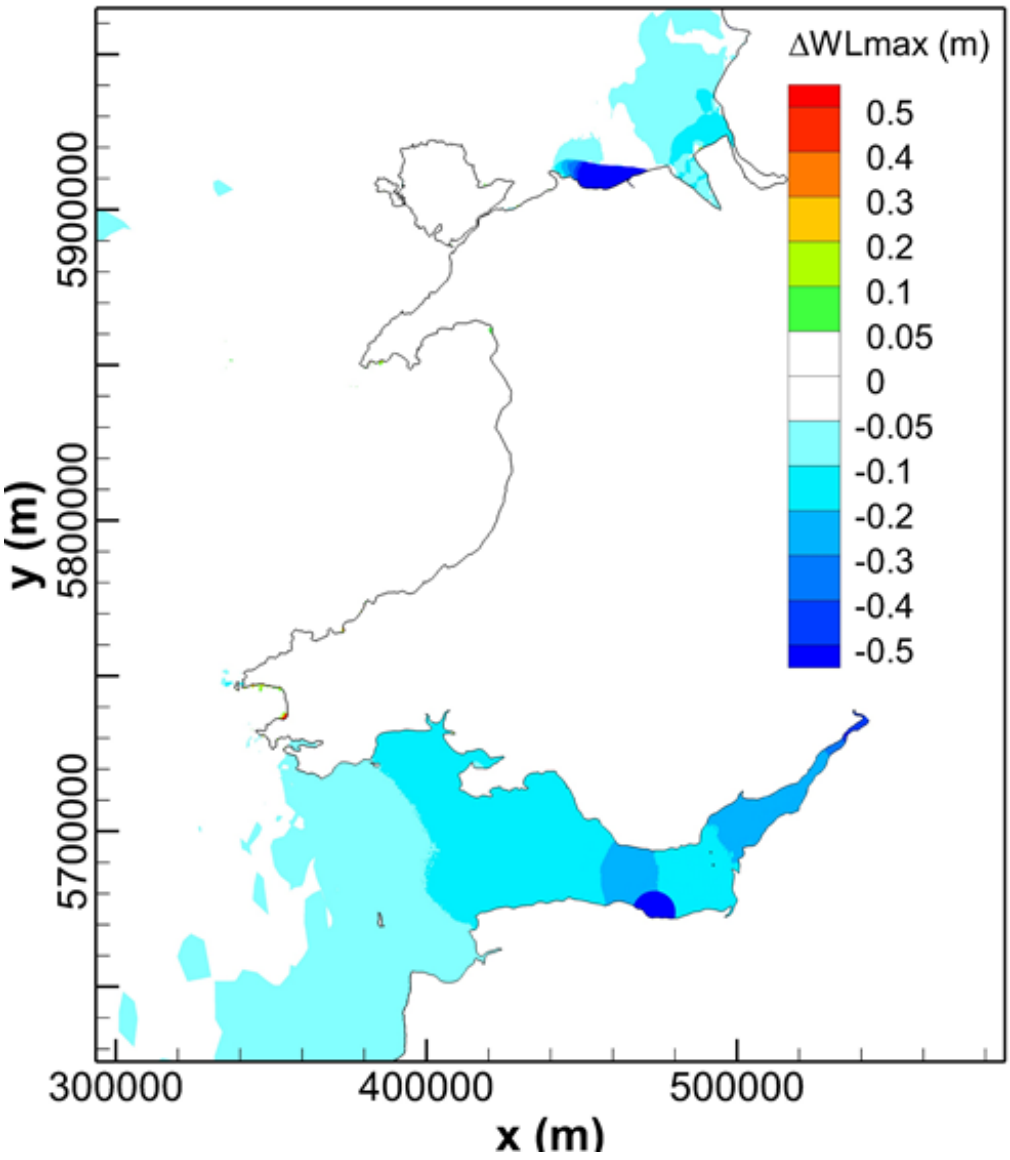

Figure 7.7: The accumulative impact of the NWTL and WSL on maximum water level during a typical spring-neap tidal cycle.

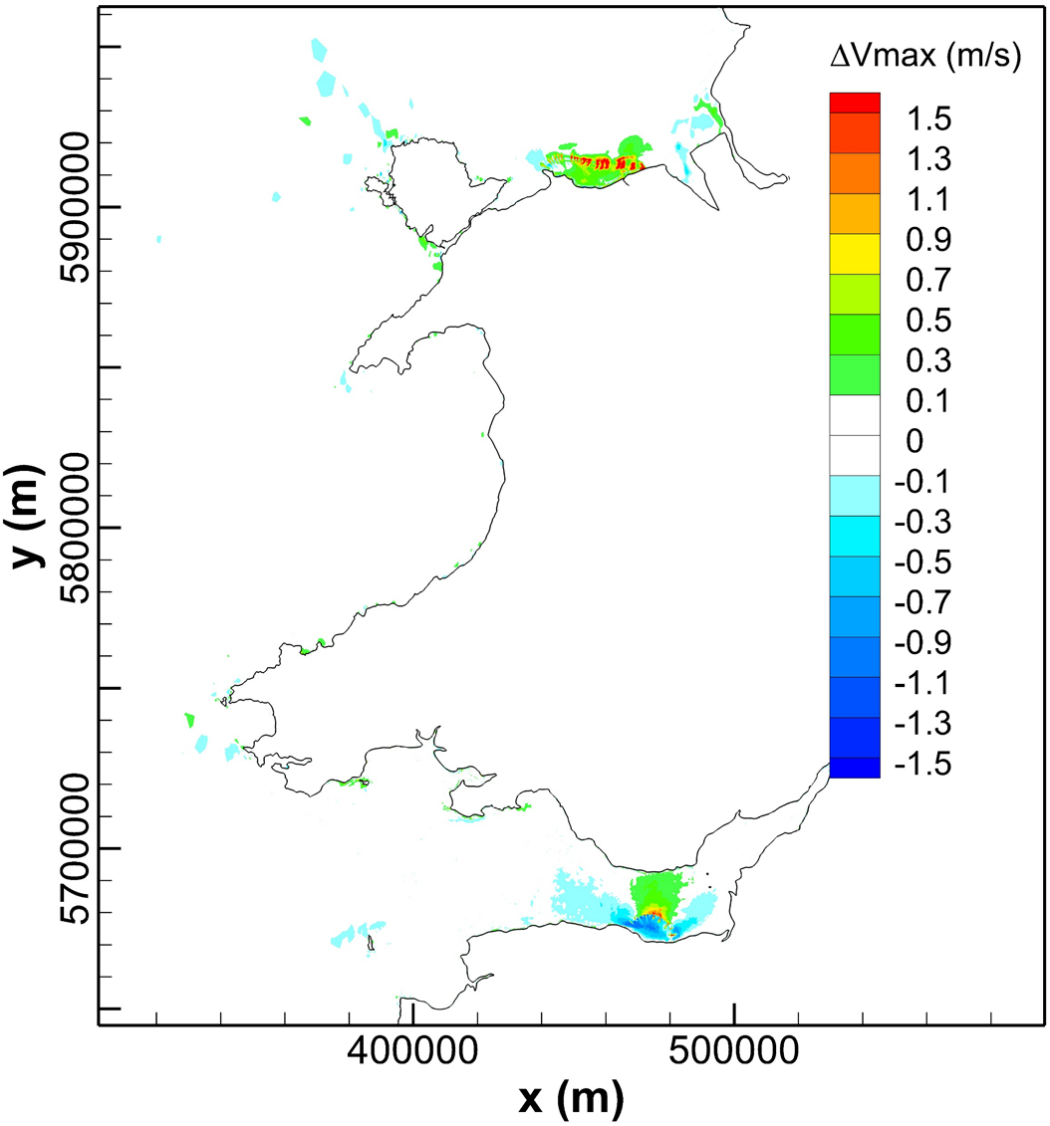

Figure 7.8: The accumulative impact of the NWTL and WSL on maximum tide speed during a typical spring-neap tidal cycle.

By comparing the high water level change between Figure 7.1, Figure 6.12 and Figure 7.7, it is observed that the water levels around each TRS are dominated by its impact. The operation of the NWTL has a negligible impact on the high water level near the WSL and vice versa. This demonstrates that the interaction between the WSL and NWTL has insignificant effects on the near-field water level predictions of the other TRS. Furthermore, although the impoundment area of NWTL is 47% larger than WSL, the hydrodynamic impact from WSL expanded further due to the funnelling effect of the basin and tidal resonance of the Bristol Channel.

However, some effects emerge from the joint operation of the schemes. The increased water level in Cardigan Bay found with the individual operation of the NWTL is mitigated under the

conjunctive operation of both lagoons, which might be a result of far-field interaction between the WSL and NWTL, as the 2-3 cm decreased high water level in Cardigan Bay caused by the WSL offset the increased water level result from the NWTL. Furthermore, in the conjunctive operation scenario, a larger area of high water level decrease between 5-10 cm appeared in Liverpool Bay. However, these values are within the model validation error (Figure B1), and therefore needs further investigations.

Similar results were found for the maximum velocity change by comparing Figure 7.2, Figure 6.18 and Figure 7.8, that negligible interactions between the NWTL and WSL were observed on maximum current speed. The impacts on tidal flows are mainly confined within the near-field of the lagoon itself.

7.3.2 Impacts on Power Generation

Slight hydrodynamic interactions of water levels were observed between the NWTL and WSL. It is important to bear in mind that even a minor change in tidal range could result in non-negligible accumulative changes in electricity generation (Angeloudis and Falconer, 2017). This is due to the non-linear relationship between power output and tidal range. Thus, any potential influence on power generation should be investigated. The changes of water level in the Colwyn Bay area, where the NWTL is located, for pre- and post-WSL construction scenarios, are presented in Table 7.2 and Figure 7.9. It was observed that the operation of the WSL slightly reduced the tidal range in the planned NWTL area by a few centimetres. However, although the same numerical settings were applied throughout models and the potential prediction deviation that origin from the mesh resolutions has been excluded by adapting the same mesh resolutions, these water level changes are relatively minor and within the validation limit.

Figure 7.10 and Table 7.2 show the water level change in the potential WSL impoundment, for pre- and post-NWTL construction scenarios. The high water level increased up to 9 cm during the spring tide while the low water level decreased by a similar value, resulting in an enlarged tidal range in the WSL impoundment area.

Table 7.2: The water level change for pre-and post-lagoon scenarios.

Water level variation	HW of spring tide	LW of spring tide	HW of neap tide	LW of spring tide
WL change in West Somerset coast with the presence of NWTL	+ 2-9 cm	- 1-7 cm	+ 1-4 cm	- 1-3 cm
WL change in North Wales coast with the presence of WSL	- 1-5 cm	+ 0-4 cm	- 0-3 cm	+ 0-2 cm

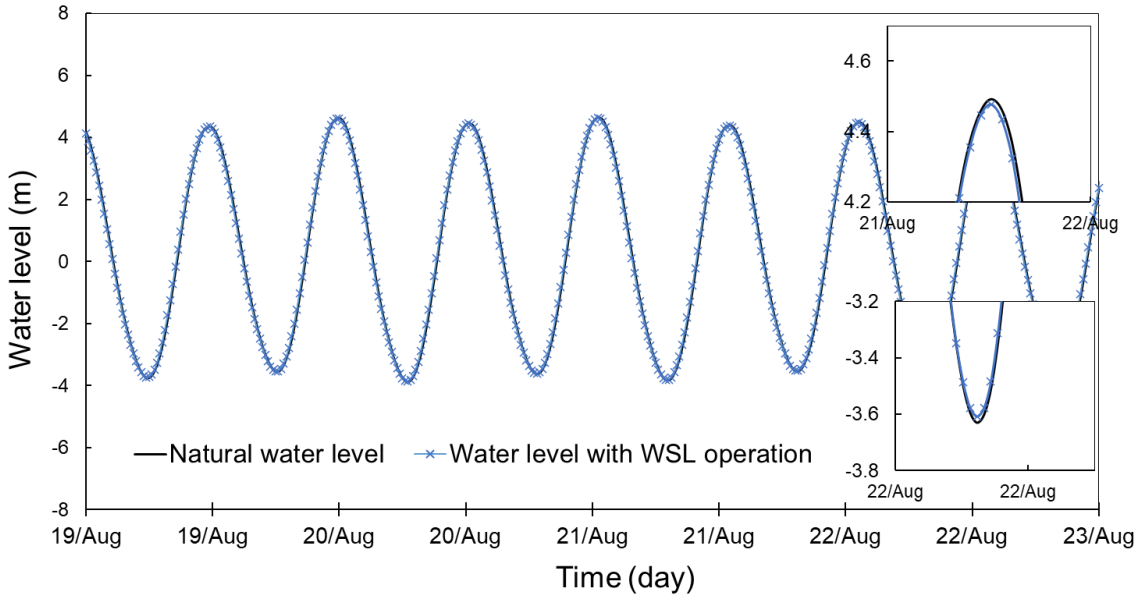

Figure 7.9: Water level change in North Wales coast area for pre- and post-WSL scenarios.

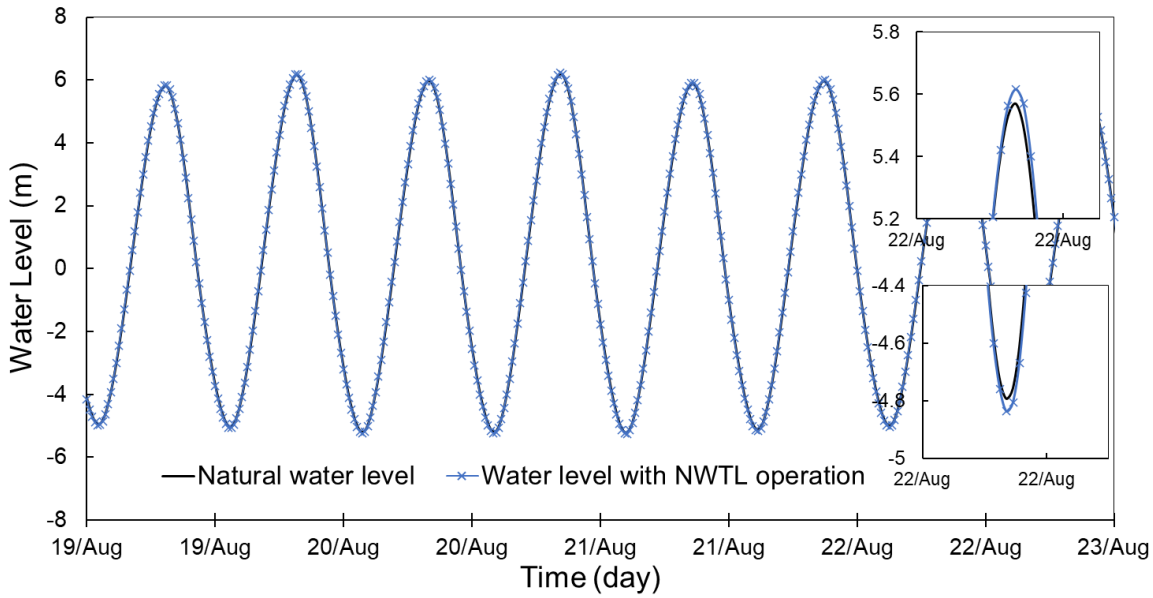

Figure 7.10: Water level change in West Somerset coast for pre- and post-NWTL scenarios.

The energy outputs of the NWTL and WSL during a typical tidal cycle for individual operation and conjunctive operation scenarios are shown in Table 7.3. It shows that the interactions between the WSL and NWTL have opposing effects on the energy output from each TRS. The operation of the WSL decreases the power output of the NWTL by 0.48% and 0.41% for flexible two-way generation without pumping and with the pumping, respectively. This result is consistent with the water level changes in the NWTL water impoundment area for pre- and post-WSL conditions. As shown in Figure 7.9, the decreased tidal range results in a slight decrease in energy output. However, the operation of NWTL could increase the energy output of the WSL by 1.6% and 1.1% for the two operation schemes as a result of the raised tidal range in the inner Bristol Channel.

Table 7.3: Energy outputs of the WSL and NWTL, respectively, with and without interaction between the two.

TRS	Condition	Flexible two-way (GWh)	Flexible two-way with pumping function (GWh)
NWTL	Without WSL	195.04	222.68
	With WSL	194.11	221.77
	Difference	-0.48%	-0.41%
WSL	Without NWTL	219.46	254.06
	With NWTL	222.97	257.77
	Difference	1.6%	1.1%

The intermittency of individual single-basin TRS is one of its noticeable disadvantages, which could increase grid congestion management costs and exacerbate electricity balancing challenges (Mackie et al., 2020). The efforts to establish a continuous power supply from TRS have been made but proved unpractical, for example, linked-basins TRS and pumped storage (MacKay, 2007; Mackie et al., 2020). However, another solution to offset the TRS power intermittency was raised, that conjunctive operating multiple TRSs by exploiting tidal phase differences (Neill et al., 2018).

The tidal phase difference between the inner Bristol Channel and Colwyn Bay could reach 4 hours, making WSL and NWTL potential conjunctive multiple TRSs system. Figure 7.11 and Figure 7.12 give the power output from WSL and NWTL with the conjunctive operating. The intermittency of power output reduced from 2.5-3.75 h to approximately 1.5 h for two-way generation, 2.5-3 h to approximately 1 h for two-way pumping generation. Furthermore, the electricity consumed in the pumping phase of NWTL could be provided by WSL, which

illustrates a potential refined pumping. The results are encouraging in proving the feasibility of continuous tidal power. However, the overlapping operation period of WSL and NWTL results in a sudden rise in power outputs, which might be a challenge for the grid to manage.

Bearing in mind that the applied operation schemes are optimised for the individual TRS energy generation maximisation rather than the systematic energy maximisation, there is a large potential improvement in the multiple-TRSs power output. Further optimisation should be thus carried on the grounds of achieving long-term continuous generation and reducing high power output peaks.

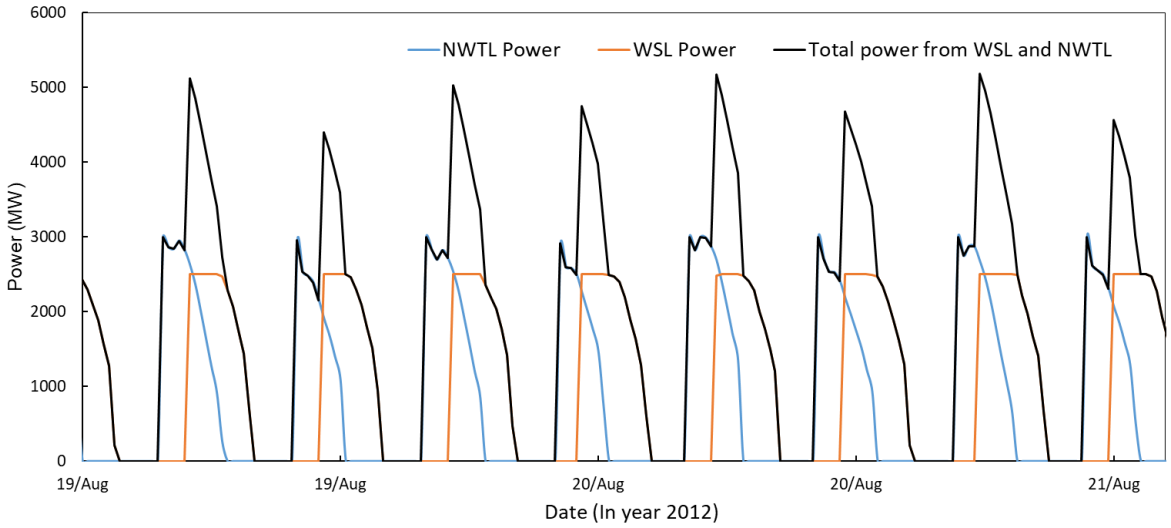

Figure 7.11: The power output of WSL and NWTL with the conjunctive two-way operation.

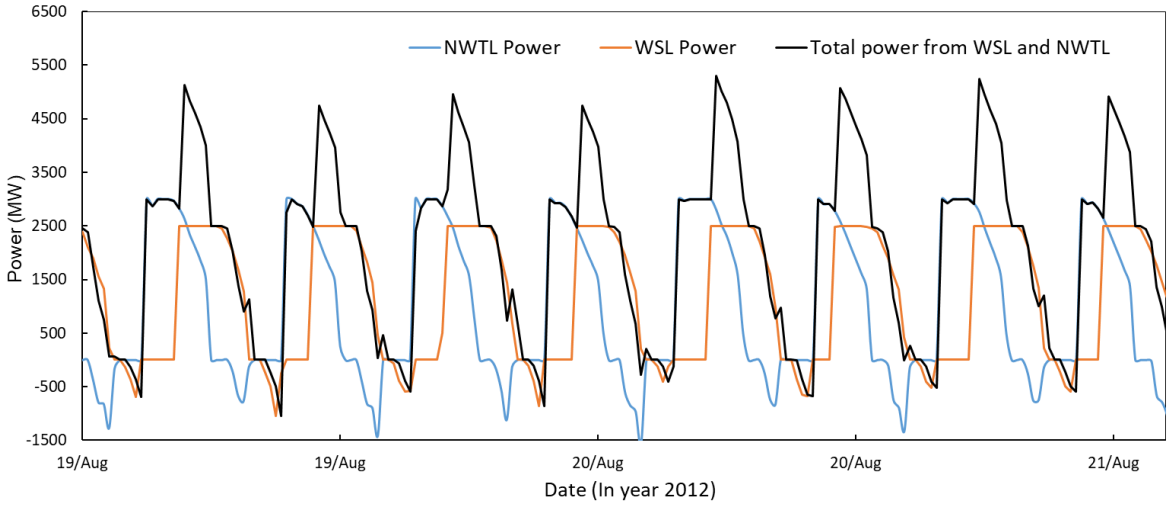

Figure 7.12: The power output of WSL and NWTL with the conjunctive operation.

7.4 Summary

A series of model predictions were compared to explore the potential interaction between TRSs. First of all, to detect accurate far-field impact from WSL operation, the effect of open boundary location on lagoon modelling is investigated by studying the impact of WSL in the CS and SEBC models, respectively. Although the hydrodynamic influences were generally consistent between CS and SEBC model, results showed the actual impact of WSL on water level extended to the outer Bristol Chanel in the CS model, with over 10 cm decrease of tidal range on the location of the open boundary of SEBC model. However, there was a limited difference in far-field velocities prediction between SEBC and CS model. Therefore, SEBC is considered suitable for early stage studies and water quality modelling of WSL while investigations on impacts of the WSL on further flood risk and intertidal mudflats need to be conducted with larger domains extended beyond the continental shelf.

WSL and SBL were then simulated jointly and it was found that the interaction between WSL and SBL on hydrodynamic is insignificant. It was found that 0.2 - 0.3 m high water level decrease zone in the Severn Estuary extended slightly towards seaward. The SBL has a negligible effect on WSL power generation due to its small scale. By contrast, the operation of WSL slightly reduces the SBL energy output. Given that the applied optimisation scheme was conducted without cumulative impacts, the power output differences can be reduced if the new water levels are used for optimisation. However, this is beyond the interest of the study.

WSL and NWTL were operated into the CS model conjunctively. The maximum velocity and maximum water level changes after including the interactions between the WSL and NWTL were studied. It was found that the hydrodynamic impacts of each lagoon were insignificant in the vicinity of the other scheme, where the local TRS itself dominated. With the combined operation of two lagoon projects, the smoothed water level change in Cardigan Bay and the 5-10 cm lower water level in Liverpool Bay showed the combined effects from the two TRSs. However, careful treatment of these small changes in water levels should be taken due to them being in the validation error range. The presence of the WSL decreased the energy output of the NWTL by 0.41% - 0.48% for the two operational schemes, while the energy output of the WSL would increase by 1.1% -1.6% with the presence of the NWTL.

Last, combined power outputs from WSL and NWTL were studied. The result showed that the intermittency of individual TRS power output was reduced from 2.5-3.75 h to less than 1.5 h

when operating conjunctively. Results showed that the conjunctive operation of multiple TRSs, i.e., WSL and NWTL, had the potential to provide less intermittent power supply by exploiting tidal phase differences.

Chapter 8 Conclusions and Recommendations

8.1 Conclusions

Despite the advantages of tidal lagoons, such as predictable renewable energy generation and flood risk reduction, the uncertainties regarding the negative environmental impacts have seriously affected its development. Thus, an accurate assessment of the marine environmental impacts of tidal lagoons is crucial in more informed decision making when designing future proposals. Hydrodynamic simulations of tidal lagoons are one of the most adaptable tools that can be used to assess the environmental risks and pave the way towards the deployment of the technology.

This thesis has focused on studying the hydro-environmental impacts and potential interaction of tidal lagoons by two-dimensional numerical modelling. The thesis studied three latest TRS projects in the UK including the West Somerset Lagoon (WSL), Swansea Bay Lagoon (SBL) and North Wales Tidal Lagoon (NWTL). The model predictions pursued include at least qualitative, and in some cases quantitative assessments of the hydrodynamic and hydro-environmental impacts.

8.1.1 Hydrodynamic Modelling of Tidal Lagoons

The establishment of a hydrodynamic model is the foundation for this research prior to simulating the operation and impact of tidal lagoons. With the considerations of the locations of tidal lagoons and their potential far-field impacts on the open boundary, two hydrodynamic models were developed and validated: the Severn Estuary and Bristol Channel (SEBC) model and the Continental Shelf (CS) model. The CS model covers the entire Irish Sea and most of the Celtic Sea, with most of its basic model settings identical to the SEBC model. However, the seaward open boundary of the CS model was driven by spatially-varying tide information from the TPXO7.2 database, while a time series of water levels was applied on the open boundary of the SEBC model. Moreover, differing from the UTM coordinates used for the SEBC model, the geographic system of the CS model was adapted in WGS84 Longitude/Latitude with spherical coordinates to adjust the Coriolis coefficient automatically. Both hydrodynamic models were calibrated and validated against tidal levels and tide current, showing good agreement between model predictions and the measurement data. The mesh

convergence has also been investigated by comparing the SEBC model prediction with different meshes. Results confirmed the independence of model prediction on the mesh grid.

Furthermore, to better understand the tidal flow structure around the tidal lagoon and to improve its hydrodynamic prediction, modelling was conducted to study the wake formed behind Flat Holm Island. Current data collected using moored Acoustic Doppler Current Profilers (ADCPs) were used to validate and refine the established SEBC model. Four different turbulence models and seven different solver options for the k-ε model were tested in this study to assess which representation could best replicate the hydrodynamics. Results show that the classic k-ε model with the conjugate residual solver was the most accurate method to simulate the wake in the lee of the island. Similarly, this modelling setting will be implanted in the lagoon modelling.

An idealised TRS model was utilised to test and validate the numerical representation of lagoon components and operation schemes. The domain decomposition method was chosen to model the TRS barrier for its numerical stability. Turbines and sluice gates were simulated as pre-programmed culverts nodes linking two sides of subdomains, with discharge through turbines described from the Hill chart and discharge through sluice gates described using the orifice equation. The conservative momentum method was applied by stimulating the external momentum term. To eliminate the influence of trivial water level oscillations on lagoon operation, water levels averaged over several points were used to determine the operation stage and the discharge. Ramp function was implemented to simulate the opening/closing process of turbines.

WSL and SBL were implanted into SEBC model for their relatively small scale, while NWTL was modelled in the CS model. Each block of turbine or sluice gate in WSL and NWTL simulation was operated independently to adapt the existence of tidal phase time lag between different turbine/sluice gate blocks. The SBL has been investigated in many previous studies, employing several different modelling tools and numerical techniques, which makes it an ideal benchmarking case study for the tidal lagoon modelling routines developed using the TELEMAC-2D model. The simulation results of SBL in this research are consistent with the past studies (Čož et al., 2019; Angeloudis et al., 2016b; Tidal Lagoon Plc, 2013) in the power prediction and the hydrodynamic impact.

A full momentum conservation approach was adopted in modelling the flow through the turbines in TRSs, and the effect of different velocity profiles at the turbine outlets was also

studied in SBL and WSL scenarios. The results show that the model without a momentum adjustment term was similar to the model with a momentum term based on the realistic velocity obtained at the end of the turbine diffusor. This indicates that the velocity at the end of the turbine diffusor might be the same as the local current velocity in this model. The turbine jet became more significant if the source velocity was taken as the simplified velocity located at the turbine blade. The results confirmed the importance of including full momentum conservation when modelling the effects of hydro-machinery in tidal impoundment schemes such as lagoons. However, the impact of momentum conservation concentrates in the local region around the lagoon, constrained to the area where dominated by the water jets through the turbine and sluice gates. The momentum term with the source velocity at the end of the turbine diffusor included was considered to be more realistic and was therefore applied in all lagoon simulations in this study.

Different operation schemes were implemented into the lagoon modellings, and the corresponding power outputs and lagoon performances were studied. The additional pumping function can contribute an 8-11%, 15.5%-26% and 12% increase in power output for the SBL, WSL and NWTL, respectively. The optimised flexible head generation significantly increases energy output compared with the traditional fixed head generation, e.g., 19% and 6.3% increase for WSL and SBL, respectively. The following environmental analysis for all the TRSs impact will be based on two-way generation with the optimised flexible head.

The optimised schemes applied in this research were achieved by a 0D model from the study of Xue et al. (2019a). The typical discrepancy in tidal lagoon energy generation between 0D and 2D models dropped from 3.8% - 30% (Neill et al., 2018) to less than 2.4% in the NWTL modelling. An even better agreement was achieved for WSL power prediction, with less than 1% differences. This thesis has achieved a high agreement between 0D model and 2D model prediction on TRS power out. This should contribute to the following improvements that were adopted in this research in close collaboration to optimisation study: independent optimisation and operation of the turbine and sluice gate blocks, and maintaining momentum conservation through the turbine housing.

8.1.2 Environmental Impact of Tidal Lagoons

This thesis studied the hydrodynamic and hydro-environmental impacts of the proposed TRSs. The operation of the TRS would absorb the tidal range energy from the surrounding water body

and consequently reduce the tidal range, i.e. a higher low-water levels and lower high-water levels for the TRS impoundment area or/and surrounding waters. The operation of WSL would generally increase the low-water levels and decrease the high water levels in the Bristol Channel and Severn Estuary. The decrease in the maximum water levels became more remarkable towards landward, which is predicted to be 0.2 - 0.3 m within the Severn Estuary. Correspondingly, with the operation of WSL, the amplitude of the M2, N2 and S2 tidal constituents decreased in the modelling area, while the phase decreased at the western side of the WSL and increased at the eastern side. The influences from SBL on the tidal constituents and water level change in Bristol Channel were similar to WSL, but were relatively insignificant and localised for its small scale. The NWTL could influence sea water levels in both near-fields and far-fields. Besides the noticeable decreased maximum water level inside the NWTL impoundment area, the water level in Liverpool Bay decreased by 5-10 cm while increased of the same value in Cardigan Bay. A minor decrease of both M2 amplitude and phase is observed in the north of NWTL, while N2 constituent increased in the east coast of Ireland and the Celtic Sea.

The change in sea surface level has both negative and/or positive impacts on the maritime environment. For example, for the WSL operation scenario, the coastal flood defences and the port access for shipping and recreational yachting could benefit from the reduced high water level and the increased low water level. The decreased maximum water level in the NWTL basin effectively reduced the flooding risk of the North Wales coastline.

Another subsequent impact of water level changes was the loss of intertidal mudflats on both the TRS impoundment coastline and the adjacent sea regions. WSL decreased the low intertidal mudflat up to 20 km^2, with the submerged mudflats are mainly located on the beach of lagoon basin, as well as Welsh Ground, Bridgewater Bay, and the Severn Beach. The SBL has little influence on the area beyond the lagoon basin, and only 1.027 km^2 loss of low-level mudflat appeared inside the SBL. For the NWTL scenario, the loss of low-level mudflats inside the lagoon is also up to 20 km^2, due to the relatively high bathymetry and the gentle slope in this area. The changes of intertidal zones might have a profound influence by affecting the biodiversity and feeding grounds for birds, mussels, and insects. The evolution of intertidal zones and the specific biota living in the affected regions need further investigation to achieve the exact ecological impact (Hooper and Austen, 2013).

Significant maximum velocity magnitude increases were observed in the wake from turbine and sluice gate for all TRSs, which could exceed 1.5 m/s. Furthermore, the operation of WSL enhanced the maximum velocity in the inner Bristol Channel by 0.25-0.75 m/s, which is due to the reduced effective cross-sectional area of tidal flow across the Bristol Channel. Moreover, decreased maximum velocity occurred inside the WSL basin, and across most of the plan-surface area. The impacts of SBL on velocity change are confined within Swansea Bay. Besides the increase of the turbine wake, the averaged velocity magnitude reduced slightly in the west side of SBL and within the impound area. Unlike WSL and SBL, the most impounded area inside NWTL shows an increased velocity ranging from 0.1-0.5 m/s. This is because of a converging water flow along the east-west direction, resulting from the split layout of turbines and sluice gates.

The change in tidal flow or newly-formed recirculation zones could consequently affect mixing and dispersion, leading to altered solute transport paths (Evans, 2017). For example, the large clockwise-rotating vortex in the centre position of the SBL during the ebb generation might contribute to the accumulation of scalar quantities, e.g., pollution and sediment, so is the recirculation zones occurred beside the turbine wake of WSL and NWTL.

To investigate such impacts, the residence time was calculated by tracking the flushing characteristics of a passive mass-conservative tracer. Modelling results demonstrate that WSL could improve the water renewal capacity in the water impoundment area by 63.8%. In contrast, SBL and NWTL decreased the water residence time by 4% and 45.7% in the lagoon basin cases study. The change of water renewal capacity inside the TRS impoundment area depended on both the natural and the post-lagoon water exchange rates. For example, despite the larger basin area of NWTL, the natural water residence time in WSL and NWTL planned areas are 22.4 and 11.36 days, respectively. The low natural water renewal rate in the WSL planned area partly contributed to the noticeable improvement of water renewal after the presence of WSL. Furthermore, the water residence times with different momentum terms indicated that stronger water jets through the turbines and sluice gates would result in shorter residence time.

The water residence time study of Swansea Bay and Porthcawl show that the SBL improved the water renewal capacity in this area by 10.45%, which should be attributed to the disturbance flow introduced by SBL. The residence times in the outer Bristol Channel, inner Bristol Channel and Severn Estuary were 113.96, 62.04 and 23.70 days in the natural condition, and

would decrease by 43%, 20% and 13% with the operation of the WSL. The reduced residence times indicated improved water renewal capacity in the whole Bristol Channel, which is a benefit of the increased tide speed in the inner Bristol Channel.

Another subsequent impact of velocity magnitude change is the suspended sediment carrying capacity. A sediment transport model, GAIA, is used to study the suspended sediment (SS) transport and bed evolution after validating model prediction with measured SS concentration. The GAIA predicted that the WSL would noticeably increase the maximum SS concentration in the inner Bristol Channel due to the markedly increased current speed, while maximum SS concentration decreased inside the WSL impoundment area. For the SBL case, the changes in SS concentration are mainly restricted within Swansea Bay for the small scale of SBL.

The noticeable increase of bed shear stress in the turbine wakes suggested scouring near the turbine and sluice gate block. Furthermore, there is a potential sedimentation area within WSL and SBL impoundment because of the decreased bed shear stress, while scouring might occur at both turbine wakes and the inside basin area of NWTL impoundment. The morphological evolution was then investigated by GAIA simulation with different values of critical shear stress for erosion (τ_{ce}) and critical shear stress for deposition (τ_{cd}). The model predictions are highly sensitive to the value of $\tau_{ce,}$ and the seabed erosion increases rapidly with the decrease of τ_{ce} in the range of 2 - 3.5 N/m^2. However, it was also found that the morphological modelling was independent of τ_{cd} values. The morphological evolution prediction of GAIA generally confirmed the results of the bed shear stress study, that the strong flow through the turbine would scour the seabed. Furthermore, the seabed degree in the inner Bristol Channel will be eroded to a certain after the presence of WSL, while siltation occurs at two sides out of WSL. As to SBL, the souring area only happened at the turbine wake area due to its limited hydrodynamic influence and low SS concentration in this area.

With the updated water exchange rate and suspended particulate matter incorporated into a screening model, the equilibrium nutrient concentrations, potential maximum phytoplankton chlorophyll and phytoplankton primary production were predicted to decrease by 1.2% - 2% after construction of WSL. The increased water exchange rate was the major reason for this decrease. Although the above determinand still exceeded the threshold limits, the risk of hyper-nutrification and eutrophication was slightly mitigated.

8.1.3 Interaction between Lagoons

Prior to studying interactions between lagoons, the effect of open boundary location on lagoon modelling has been investigated by comparing the performance of WSL in the CS and SEBC model. The hydrodynamic impact of WSL is generally consistent between CS and SEBC models. However, the oscillation of maximum water level results from the operation of WSL extended to the outer Bristol Channel in the CS model, suggesting the existence of influence of WSL operation on SEBC model open boundary. However, the influences of WSL on the maximum velocity magnitudes are almost the same. Thus, the SEBC model is regarded as a suitable hydrodynamic model for the hydro-environmental impact study of WSL.

WSL and SBL were then simulated jointly in the SEBC model, and trivial hydrodynamic interaction was found between WSL and SBL. The energy output from SBL reduced by 3.7% with the operation of WSL, while SBL has negligible influence on WSL for its small scale. The interaction study between WSL and NWTL show that hydrodynamic impacts in the vicinity of the scheme are dominated by themselves. Slight superimposed effects were found in the far-field, i.e. Cardigan Bay, where water level oscillations were mitigated. The interaction between WSL and NWTL is generally trivial on power output. Overall, the interactions between the lagoon cases in this research are relatively minor, and it wass concluded that the interactions are closely related to the lagoon scale, geographical location, tidal phase, etc. However, in the conjunctive operation of WSL and NWTL, it was found that the intermittency of individual lagoon power output was reduced from 2.5-3.75 h to less than 1.5 h with the conjunctive operation, which partially offset the disadvantage of variability in energy output from a single lagoon.

8.2 Recommendations for Future Study

Although this thesis has addressed several topics on hydro-environmental impact assessment of tidal lagoons, some areas of interest where the work here could be improved or expanded.

Morphological evolution for the operation of tidal lagoon was studied in Chapter 6. However, the calculation of net sediment flux has not been validated due to the lack of measurement calibration data. It is crucial to accurately predict the geomorphological evolution, especially inside the lagoon impoundment basin, for the bottom elevation of the impoundment basin directly determines the water storage volume and the function of the lagoon. Furthermore,

certain optimization of lagoon design could be studied to mitigate sedimentation or scour by optimising the shape of the lagoon, the layout of turbines and sluice gates, and the operation schemes.

It should also be noted that the Hill chart used to describe the discharge and power output of the specific turbines in this chapter are not publicly available at the time of the study. This uncertainty exists in all current TRS studies due to the commercial sensitivity of Hill charts. Although the general conclusions of the study will remain the same, it is expected that slight quantitative changes will occur with an update of the turbine Hill chart.

It will be important to provide a better water quality prediction, especially for the water body inside of the lagoon. The indicators of bacteria concentration, dissolved oxygen, temperature, salinity, etc., should be predicted quantitatively, which could provide guidance to designers. However, prior to this, a 3D model will be required based on the current 2D model, because the dilution and transportation of dissolved oxygen, temperature, salinity, etc., are mostly three-dimensional. Furthermore, LES can be used to better understand the flow structure in the vicinity of the turbine. This could also help to better understand the impact of the jet on the bed and potential morphological changes.

There are a number of proposals for different high tidal energy regions. For example, Tidal Lagoon Power ltd proposed a fleet of 6 tidal lagoon projects in the Bristol Channel; there are even more tidal stream energy development plans in the Irish Sea. It is argued that any potential tidal energy development scheme in this area should be evaluated holistically to avoid any future cumulative interaction issues. Thus, it is crucial to study the network of multi-TRSs and tidal stream energy projects to further explore the potential tidal energy and assess the potential far-field interactions.

Given the 120-year lifespan of a tidal lagoon, any minor long-term risk might develop into an important issue, such as sea-level rise resulting from global warming (Khojasteh et al., 2022). It would be important to include this aspect into the preliminary design for the safety of long-term management.

References

Adcock, T. A. A., Borthwick, A. G. L. and Houlsby, G. T. 2011. The open boundary problem in tidal basin modelling with energy extraction. *Proceedings of the 9th European Wave and Tidal Energy Conference*, Southampton, UK. pp.1-7.

Adcock, T. A. A., Draper, S., Houlsby, G. T., Borthwick, A. G. L. and Serhadlioglu, S. 2013. The available power from tidal stream turbines in the Pentland Firth. *Proceedings of the Royal Society A: Mathematical, Physical and Engineering Sciences,* 469(2157), pp.20130072.

Adcock, T. A. A., Draper, S. and Nishino, T. 2015. Tidal power generation - A review of hydrodynamic modelling. *Proceedings of the Institution of Mechanical Engineers, Part A: Journal of Power and Energy,* 229(7), pp.755-771.

Adcock, T. A. A., Draper, S., Willden, R. H. J. and Vogel, C. R. 2021. The fluid mechanics of tidal stream energy conversion. *Annual Review of Fluid Mechanics,* 53, pp.287-310.

Aggidis, G. 2010. Tidal range fluid machinery technology and opportunities. *Proceedings of the International Symposium on Ocean Power Fluid Machinery*, London.

Aggidis, G. and Benzon, D. 2013. Operational optimisation of a tidal barrage across the Mersey estuary using 0-D modelling. *Ocean Engineering,* 66, pp.69-81.

Aggidis, G. A. and Feather, O. 2012. Tidal range turbines and generation on the Solway Firth. *Renewable Energy,* 43, pp.9-17.

Ahmadian, R., Falconer, R. A. and Bockelmann-Evans, B. 2012. Far-field modelling of the hydro-environmental impact of tidal stream turbines. *Renewable Energy,* 38(1), pp.107-116.

Ahmadian, R., Falconer, R. A. and Bockelmann-Evans, B. 2014a. Comparison of hydro-environmental impacts for ebb-only and two-way generation for a Severn Barrage. *Computers & Geosciences,* 71, pp.11-19.

Ahmadian, R., Falconer, R. A. and Lin, B. 2010a. Hydro-environmental modelling of proposed Severn barrage, UK. *Proceedings of the Institution of Civil Engineers - Energy*, 163(3), pp.107-117.

Ahmadian, R., Morris, C. and Falconer, R. A. 2010b. Hydro-environmental modelling of off-shore and coastally attached impoundments off the North Wales Coast. *Proceedings of the 1st IAHR European Congress*, Edinburgh, UK.

Ahmadian, R., Olbert, A. I., Hartnett, M. and Falconer, R. A. 2014b. Sea level rise in the Severn Estuary and Bristol Channel and impacts of a Severn Barrage. *Computers & Geosciences*, 66, pp.94-105.

Ahn, S. H., Xiao, Y., Wang, Z., Zhou, X. and Luo, Y. 2017a. Numerical prediction on the effect of free surface vortex on intake flow characteristics for tidal power station. *Renewable Energy*, 101, pp.617-628.

Ahn, S. H., Xiao, Y., Wang, Z., Zhou, X. and Luo, Y. 2017b. Performance prediction of a prototype tidal power turbine by using a suitable numerical model. *Renewable Energy*, 113, pp.293-302.

Ahn, S. H., Zhou, X., He, L., Luo, Y. and Wang, Z. 2020. Numerical estimation of prototype hydraulic efficiency in a low head power station based on gross head conditions. *Renewable Energy*, 153, pp.175-181.

Allen, J. 1991. Fine sediment and its sources, Severn Estuary and inner Bristol Channel, southwest Britain. *Sedimentary Geology*, 75(1-2), pp.57-65.

Andre, H. 1976. Operating experience with bulb units at the Rance tidal power plant and other French hydro-power sites. *IEEE Transactions on Power Apparatus and Systems*, 95(4), pp.1038-1044.

Angeloudis, A., Ahmadian, R., Falconer, R. A. and Bockelmann-Evans, B. 2016a. Numerical model simulations for optimisation of tidal lagoon schemes. *Applied Energy*, 165, pp.522-536.

Angeloudis, A. and Falconer, R. A. 2017. Sensitivity of tidal lagoon and barrage hydrodynamic impacts and energy outputs to operational characteristics. *Renewable Energy*, 114, pp.337-351.

Angeloudis, A., Falconer, R. A., Bray, S. and Ahmadian, R. 2016b. Representation and operation of tidal energy impoundments in a coastal hydrodynamic model. *Renewable Energy*, 99, pp.1103-1115.

Angeloudis, A., Kramer, S. C., Avdis, A. and Piggott, M. D. 2018. Optimising tidal range power plant operation. *Applied Energy*, 212, pp.680-690.

Angeloudis, A., Kramer, S. C., Hawkins, N. and Piggott, M. D. 2020. On the potential of linked-basin tidal power plants: an operational and coastal modelling assessment. *Renewable Energy*, 155, pp.876-888.

Angeloudis, A., Piggott, M., Kramer, S. C., Avdis, A., Coles, D. and Christou, M. 2019. Comparison of 0-D, 1-D and 2-D model capabilities for tidal range energy resource assessments. *Proceedings of the 12th European Wave and Tidal Energy Conference (EWTEC)*, Cork, Ireland. pp.1-10.

ARCCA. 2018. Advanced Research Computing. Cardiff, UK. Available at: https://www.cardiff.ac.uk/advanced-research-computing/about-us/our-supercomputers. [Accessed: 25 November 2020].

Ashley, M. C. 2014. Ecosystem service mapping in the Severn estuary and inner Bristol Channel. *Report for NERC Marine Renewable Energy Knowledge Exchange Project*, RSPB and Plymouth Marine Laboratory, pp.1-99. Available at: https://www.pml.ac.uk/pmlsite/media/PML-Media/Images/severn%20estuary/Ecosystem_service_mapping_in_the_Severn_estuary_and_inner_Bristol_Channel,_NERC_funded_knowledge_exchange_project,_RSPB_and_Plymouth_Marine_Laboratory.pdf [Accessed: 20 November 2020].

Astariz, S., Vazquez, A. and Iglesias, G. 2015. Evaluation and comparison of the levelized cost of tidal, wave, and offshore wind energy. *Journal of Renewable and Sustainable Energy*, 7(5), pp.053112.

Atkins, W. S. 2004. Report: Tidal Electric Limited Feasibility Study for a Tidal Lagoon in Swansea Bay. Available at: http://www.tidalelectric.com/ws-atkins-feasibility-study [Accessed: 25 November 2020].

Bae, Y. H., Kim, K. O. and Choi, B. H. 2010. Lake Sihwa tidal power plant project. *Ocean Engineering,* 37(5-6), pp.454-463.

Bahaj, A. S. 2011. Generating electricity from the oceans. *Renewable and Sustainable Energy Reviews,* 15(7), pp.3399-3416.

Bakar, A. A. 2019. *Modelling of intertidal floodplains for enhanced estuarine transport and decay of faecal indicator organisms from a diffuse source.* PhD Thesis. Cardiff University.

Bakar, A. A., Ahmadian, R. and Falconer, R. A. 2017. Modelling the transport and decay processes of microbial tracers in a macro-tidal estuary. *Water Research,* 123, pp.802-824.

Baker, A. C. 1991. *Tidal Power.* Peter Peregrinus Ltd, London, United Kingdom.

Baker, A. L., Craighead, R. M., Jarvis, E. J., Stenton, H. C., Angeloudis, A., Mackie, L., Avdis, A., Piggott, M. D. and Hill, J. 2020. Modelling the impact of tidal range energy on species communities. *Ocean & Coastal Management,* 193, pp.105221.

Baldwin, E., Carley, S., Brass, J. N. and MacLean, L. M. 2017. Global renewable electricity policy: a comparative policy analysis of countries by income status. *Journal of Comparative Policy Analysis: Research and Practice,* 19(3), pp.277-298.

Bartosiewicz, Y. and Duponcheel, M. 2018. Large eddy simulation: application to liquid metal fluid flow and heat transfer, In: Thermal Hydraulics Aspects of Liquid Metal Cooled Nuclear Reactors. Elsevier, Woodhead Publishing.

BBC. 2014. Storm surge brings flooding chaos moving up Wales's coast. *BBC*. Available at: https://www.bbc.co.uk/news/uk-wales-25583295 [Accessed: 25 November 2020].

Department for Business, Energy and Industrial Strategy (BEIS). 2018a. Digest of UK Energy Statistics (DUKES), Chapter 5: Electricity. pp.111-153. Available at: https://www.gov.uk/government/uploads/system/uploads/attachment_data/file/552059/Chapter_5_web.pdf [Accessed: 25 November 2020].

Department for Business, Energy and Industrial Strategy (BEIS). 2018b. Digest of UK Energy Statistics (DUKES), Chapter 6: Renewable sources of energy. pp.1-22. Available at: https://www.gov.uk/government/statistics/renewable-sources-of-energy-chapter-6-digest-of-united-kingdom-energy-statistics-dukes [Accessed: 22 November 2020].

Department for Business, Energy and Industrial Strategy (BEIS). 2018c. Digest of UK Energy Statistics (DUKES), Main Report. Available at: https://assets.publishing.service.gov.uk/government/uploads/system/uploads/attachment_data/file/736148/DUKES_2018.pdf [Accessed: 21 November 2020].

Berenbrock, C. and Tranmer, A. W. 2008. Simulation of flow, sediment transport, and sediment mobility of the lower Coeur d'Alene River, Idaho. U.S. Geological Survey. Scientific Investigations Report: 2008-5093. Available at: https://pubs.usgs.gov/sir/2008/5093/index.html [Accessed: 01 December 2021].

Bi, Q. and Toorman, E. A. 2015. Mixed-sediment transport modelling in Scheldt estuary with a physics-based bottom friction law. *Ocean Dynamics*, 65(4), pp.555-587.

Bondi, H. 1981. Tidal power from the Severn Estuary. Volume 1. Report to the Secretary of State for Energy prepared by the Severn Barrage Committee. *Department of Energy, HMSO, London, UK*.

Bourban, S., Durand, N., Turnbull, M., Wilson, S. and Cheeseman, S. 2012. Coastal shelf model of northern European waters to inform tidal power industry decisions. *Proceedings of the XIXth TELEMAC-MASCARET User Conference*, Oxford, UK. pp.143-150.

Bray, S. 2017. *Multiscale hydro-environmental modelling of marine renewable energy devices, with particular application to the Severn Barrage.* PhD Thesis. Cardiff University.

Bray, S., Ahmadian, R. and Falconer, R. A. 2016. Impact of representation of hydraulic structures in modelling a Severn barrage. *Computers & Geosciences*, 89, pp.96-106.

British Geological Survey. 1986. Bristol Channel Sheet, 51°N–04°W. 1:250,000 Series: Sea Bed Sediments and Quaternary Geology. UK.

Buijs, F., Simm, J., Wallis, M. and Sayers, P. 2007. Performance and reliability of flood and coastal defences. Environment Agency, London, UK. Available at: http://www.pevensey-bay.org.uk/SussexTowns/Seaford/Plan/TR2%20defra.pdf [Accessed: 25 November 2020].

Bulleri, F. and Chapman, M. G. 2010. The introduction of coastal infrastructure as a driver of change in marine environments. *Journal of Applied Ecology*, 47(1), pp.26-35.

Burrows, R., Walkington, I., Yates, N., Hedges, T., Chen, D., Li, M., Zhou, J., Wolf, J., Proctor, R. and Holt, J. 2009a. Tapping the tidal power potential of the Eastern Irish Sea. *Final report of the Joule project JIRP106/03*, University of Liverpool and Proudman Oceanographic Laboratory. Available at: https://livrepository.liverpool.ac.uk/3005967/2/Joule-Tide-Final-Rpt_Dec09_inc_Appendices.pdf [Accessed: 01 December 2022].

Burrows, R., Yates, N., Hedges, T., Li, M., Zhou, J., Chen, D., Walkington, I., Wolf, J., Holt, J. and Proctor, R. 2009b. Tidal energy potential in UK waters. *Proceedings of the Institution of Civil Engineers-maritime Engineering*. Thomas Telford Ltd, pp.155-164.

Burton, N. H., Musgrove, A. J., Rehfisch, M. M. and Clark, N. A. 2010. Birds of the Severn Estuary and Bristol Channel: their current status and key environmental issues. *Marine Pollution Bulletin*, 61(1-3), pp.115-123.

Burton, N. H., Rehfisch, M. M., Clark, N. A. and Dodd, S. G. 2006. Impacts of sudden winter habitat loss on the body condition and survival of redshank Tringa totanus. *Journal of Applied Ecology*, 43(3), pp.464-473.

Cannard, P. 2016. The sediment regime of the Severn Estuary literature review. Report to Bristol City council. Available at: https://severnestuarycoastalgroup.org.uk/wp-content/uploads/sites/4/2016/02/The-Sediment-Regime-of-the-Severn-Estuary-Literature-Review.pdf [Accessed: 10 November 2020].

Carballo, R., Iglesias, G. and Castro, A. 2009. Numerical model evaluation of tidal stream energy resources in the Ría de Muros (NW Spain). *Renewable Energy*, 34(6), pp.1517-1524.

Carroll, B., Li, M., Pan, S., Wolf, J. and Burrows, R. 2009. Morphodynamic impacts of a tidal barrage in the Mersey Estuary. *Coastal Engineering 2008.* World Scientific (In Volumes 5). pp. 2743-2755.

Charlier, R. H. 2007. Forty candles for the Rance River TPP tides provide renewable and sustainable power generation. *Renewable and Sustainable Energy Reviews,* 11(9), pp.2032-2057.

Charlier, R. H. and Finkl, C. W. 2009. *Ocean energy: tide and tidal power.* Berlin, Heidelberg: Springer.

Chini, N., Stansby, P., Leake, J., Wolf, J., Roberts-Jones, J. and Lowe, J. 2010. The impact of sea level rise and climate change on inshore wave climate: A case study for East Anglia (UK). *Coastal Engineering,* 57(11-12), pp.973-984.

Cho, Y. S., Lee, J. W. and Jeong, W. 2012. The construction of a tidal power plant at Sihwa Lake, Korea. *Energy Sources, Part A: Recovery, Utilization, and Environmental Effects,* 34(14), pp.1280-1287.

Christie, E. K. 2014. *Numerical modelling of morphological impacts of offshore wind farms* PhD Thesis. University of Liverpool.

Chu, Y. J. and Chong, W. T. 2018. Numerical Study of Conventional and Biomimetic Marine Current Turbines in Tandem by Using Openfoam®. *Journal of Mechanics,* 34(5), pp.679-693.

Clark, N. A. 2006. Tidal barrages and birds. *Ibis,* 148, pp.152-157.

Cornett, A. and Cousineau, J. 2011. Hydrodynamic Impacts due to Tidal Power Lagoons in the Upper Bay of Fundy, Canada. *Proceedings of 2011 European Wave and Tidal Energy Conference (EWTEC),* Southampton, UK. pp.1-10.

Cornett, A., Cousineau, J. and Nistor, I. 2013. Assessment of hydrodynamic impacts from tidal power lagoons in the Bay of Fundy. *International Journal of Marine Energy,* 1, pp.33-54.

Cousineau, J. 2011. *Hydrodynamic impacts of tidal lagoons in the upper Bay of Fundy.* PhD Thesis. University of Ottawa.

Cousineau, J., Nistor, I. and Cornett, A. 2012. Hydrodynamic Impacts of Tidal Power Lagoons in the Bay of Fundy. *Coastal Engineering Proceedings*, 1(33), pp.69.

Čož, N. 2019. *Numerical and experimental modelling of tidal range structures with focus on conservation of momentum through hydraulic structures.* PhD Thesis. Cardiff University.

Čož, N., Ahmadian, R. and Falconer, R. A. 2019. Implementation of a Full Momentum Conservative Approach in Modelling Flow Through Tidal Structures. *Water*, 11(9), pp.1917.

Cramp, A., Coulson, M., James, A. and Berry, J. 1991. A note on the observed and predicted flow patterns around islands - Flat Holm, the Bristol Channel. *International Journal of Remote Sensing*, 12(5), pp.1111-1118.

Comprehensive Studies Task Team (CSTT). 1997. Comprehensive studies for the purposes of Article 6 of DIR 91/271 EEC, the Urban Waste Water Treatment Directive. Published for CSTT by the Department of the Environment for Northern Ireland, the Scottish Environment Agency and the Water Services Association. Edinburgh, UK.

Dabrowski, T., Hartnett, M. and Olbert, A. I. 2012. Determination of flushing characteristics of the Irish Sea: A spatial approach. *Computers & Geosciences*, 45, pp.250-260.

Department of Energy & Climate Change (DECC). 2014. UK Energy in Brief 2014. Available at: https://www.gov.uk/government/statistics/uk-energy-in-brief-2014 [Accessed: 21 November 2020].

Delta Marine Consultants. 2007. Tidal Power Plant: Bay of Fundy. Technical Feasibility Study. Available at: https://www.stantec.com/en/projects/canada-projects/b/bay-of-fundy-tidal-energy-site-feasibility-studies [Accessed: 25 November 2020].

Devlin, M., Barry, J., Mills, D., Gowen, R., Foden, J., Sivyer, D. and Tett, P. 2008. Relationships between suspended particulate material, light attenuation and Secchi depth in UK marine waters. *Estuarine, Coastal and Shelf Science*, 79(3), pp.429-439.

Dong, H., Jia, L., He, Z., Yu, M. and Shi, Y. 2020. Application of parameters and paradigms of the erosion and deposition for cohesive sediment transport modelling in the Lingdingyang Estuary, China. *Applied Ocean Research*, 94, pp.101999.

Doodson, A. T. 1921. The harmonic development of the tide-generating potential. *Proceedings of the Royal Society of London. Series A, Containing Papers of a Mathematical and Physical Character*, 100(704), pp.305-329.

Dorfmann, D. 2017. *Flow Phenomena in a Reservoir investigated by Field Measurements and Numerical Modelling.* PhD Thesis. Graz University of Technology.

Dushaw, B. D., Egbert, G. D., Worcester, P. F., Cornuelle, B. D., Howe, B. M. and Metzger, K. 1997. A TOPEX/POSEIDON global tidal model (TPXO. 2) and barotropic tidal currents determined from long-range acoustic transmissions. *Progress in Oceanography*, 40(1-4), pp.337-367.

Dyer, K. R. and Huntley, D. A. 1999. The origin, classification and modelling of sand banks and ridges. *Continental Shelf Research*, 19(10), pp.1285-1330.

Easton, M. C. 2013. *An assessment of tidal energy and the environmental response to extraction at a site in the Pentland Firth.* PhD Thesis. University of Aberdeen.

Elder, J. 1959. The dispersion of marked fluid in turbulent shear flow. *Journal of fluid mechanics*, 5(4), pp.544-560.

Elliott, K., Smith, H. C., Moore, F., van der Weijde, A. H. and Lazakis, I. 2018. Environmental interactions of tidal lagoons: A comparison of industry perspectives. *Renewable Energy*, 119, pp.309-319.

Elliott, K., Smith, H. C., Moore, F., van der Weijde, A. H. and Lazakis, I. 2019. A systematic review of transferable solution options for the environmental impacts of tidal lagoons. *Marine Policy*, 99, pp.190-200.

Estate Crown. 2012. UK Wave and Tidal Key Resource Areas Project. Summary Report. Available at: http://www.marineenergywales.co.uk/wp-content/uploads/2016/01/Summary-Report-FINAL.pdf [Accessed: 25 November 2020].

Estrade, P. and Middleton, J. H. 2010. A numerical study of island wake generated by an elliptical tidal flow. *Continental Shelf Research*, 30(9), pp.1120-1135.

Etemadi, A., Emami, Y., AsefAfshar, O. and Emdadi, A. 2011. Electricity generation by the tidal barrages. *Energy Procedia*, 12, pp.928-935.

European Commission. 2018. Renewable Energy: Moving towards a Low Carbon Economy. Brussels. Available at: https://ec.europa.eu/energy/en/topics/renewable-energy. [Accessed: 23 November 2020].

Evans, G., Mollowney, B. and Spoel, N. 1990. Two-dimensional modelling of the Bristol Channel, UK. *Proceedings of the Conference on Estuarine and Coastal Modeling*. pp.331-340.

Evans, P. 2017. Impacts of a tidal lagoon on urban drainage and pollutant dispersion in a coastal embayment. *The 12th European Wave and Tidal Energy Conference (EWTEC)*, Cork, Ireland. pp.1144.

Evans, P., Lazarus, E. D., Mason-Jones, A., O'Doherty, D. M. and O'Doherty, T. 2015. Wake characteristics of a natural submerged pinnacle and implications for tidal stream turbine installations. *Proceedings of the 11th European Wave and Tidal Energy Conference*, Nantes, France.

Fairley, I., Ahmadian, R., Falconer, R. A., Willis, M. R. and Masters, I. 2014. The effects of a Severn Barrage on wave conditions in the Bristol Channel. *Renewable Energy*, 68, pp.428-442.

Falconer, R. A., Guo, B. and Ahmadian, R. 2020. Coastal reservoirs and their potential for urban regeneration and renewable energy supply. In: Sitharam, T.G (ed). Sustainable water resource development using coastal reservoirs, pp.143-172.

Falconer, R. A., Xia, J., Lin, B. and Ahmadian, R. 2009. The Severn Barrage and other tidal energy options: Hydrodynamic and power output modeling. *Science in China Series E: Technological Sciences*, 52(11), pp.3413-3424.

Fischer, H. B., List, E. J., Koh, R. C., Imberger, J. and Brooks, N. H. 1979. *Mixing in Inland and Coastal Waters.* Academic, San Diego.

Fraenkel, P. L. 1999. New developments in tidal and wave power technologies. *Proceedings of Silver Jubilee conference: Towards a renewable future*, Brighton, UK. pp.137-145.

Frau, J. P. 1993. Tidal energy: promising projects: La Rance, a successful industrial-scale experiment. *IEEE Transactions on Energy Conversion*, 8(3), pp.552-558.

Gambhir, A., Rogelj, J., Luderer, G., Few, S. and Napp, T. 2019. Energy system changes in 1.5 °C, well below 2 °C and 2 °C scenarios. *Energy Strategy Reviews,* 23, pp.69-80.

Gao, G., Falconer, R. A. and Lin, B. 2011. Numerical Modelling Sediment-Bacteria Interaction Processes in the Severn Estuary. *Journal of Water Resource and Protection,* 03(01), pp.22-31.

Gao, G., Falconer, R. A. and Lin, B. 2013. Modeling effects of a tidal barrage on water quality indicator distribution in the Severn Estuary. *Frontiers of Environmental Science & Engineering,* 7(2), pp.211-218.

Gao, G., Xia, J., Falconer, R. A. and Wang, Y. 2020. Modelling study of transport time scales for a hyper-tidal estuary. *Water,* 12(9), pp.2434.

Garrett, C. and Greenberg, D. 1977. Predicting changes in tidal regime: the open boundary problem. *Journal of Physical Oceanography,* 7(2), pp.171-181.

Gielen, D., Boshell, F., Saygin, D., Bazilian, M. D., Wagner, N. and Gorini, R. 2019. The role of renewable energy in the global energy transformation. *Energy Strategy Reviews,* 24, pp.38-50.

Goss-Custard, J., Stillman, R., West, A., Caldow, R. and McGrorty, S. 2002. Carrying capacity in overwintering migratory birds. *Biological Conservation,* 105(1), pp.27-41.

Greaves, D. and Iglesias, G. 2018. *Wave and tidal energy*. John Wiley & Sons, Hoboken, NJ, USA.

Guerra, M., Cienfuegos, R., Thomson, J. and Suarez, L. 2017. Tidal energy resource characterization in Chacao Channel, Chile. *International journal of marine energy,* 20, pp.1-16.

Guillou, N., Thiébot, J. and Chapalain, G. 2019. Turbines' effects on water renewal within a marine tidal stream energy site. *Energy,* 189, pp.116113.

Guo, B., Ahmadian, R., Evans, P. and Falconer, R. A. 2020. Studying the Wake of an Island in a Macro-tidal Estuary. *Water,* 12(5), pp.1225.

Guo, B., Ahmadian, R. and Falconer, R. A. 2021. Refined hydro-environmental modelling for tidal energy generation: West Somerset Lagoon case study. *Renewable Energy*, 179, pp.2104-2123.

Harris, P. and Collins, M. 1991. Sand transport in the Bristol Channel: bedload parting zone or mutually evasive transport pathways? *Marine Geology*, 101(1-4), pp.209-216.

Haverson, D., Bacon, J., Smith, H. C. M., Venugopal, V. and Xiao, Q. 2017. Cumulative impact assessment of tidal stream energy extraction in the Irish Sea. *Ocean Engineering*, 137, pp.417-428.

Haverson, D., Bacon, J., Smith, H. C. M., Venugopal, V. and Xiao, Q. 2018. Modelling the hydrodynamic and morphological impacts of a tidal stream development in Ramsey Sound. *Renewable Energy*, 126, pp.876-887.

Hawkins, E., Ortega, P., Suckling, E., Schurer, A., Hegerl, G., Jones, P., Joshi, M., Osborn, T. J., Masson-Delmotte, V. and Mignot, J. 2017. Estimating changes in global temperature since the preindustrial period. *Bulletin of the American Meteorological Society*, 98(9), pp.1841-1856.

Hendry, C. 2016. The role of tidal lagoons - Final Report. Available at: https://hendryreview.files.wordpress.com/2016/08/hendry-review-final-report-english-version.pdf [Accessed: 23 November 2020].

Hervouet, J. M. 2007. *Hydrodynamics of free surface flows: modelling with the finite element method*. John Wiley & Sons Ltd, West Sussex, England.

Hooper, T. and Austen, M. 2013. Tidal barrages in the UK: Ecological and social impacts, potential mitigation, and tools to support barrage planning. *Renewable and Sustainable Energy Reviews*, 23, pp.289-298.

Intergovernmental Panel on Climate Change (IPCC). 2012. Managing the risks of extreme events and disasters to advance climate change adaptation. A Special Report of Working Groups I and II of the Intergovernmental Panel on Climate Change. Cambridge University Press, Cambridge, UK. Available at: https://www.ipcc.ch/report/managing-the-risks-of-extreme-events-and-disasters-to-advance-climate-change-adaptation/ [Accessed: 23 November 2020].

Jay, D. A., Orton, P. M., Chisholm, T., Wilson, D. J. and Fain, A. M. 2007. Particle trapping in stratified estuaries: application to observations. *Estuaries and Coasts,* 30(6), pp.1106-1125.

Jeffcoate, P., Stansby, P. and Apsley, D. 2013. Flow due to multiple jets downstream of a barrage: experiments, 3d computational fluid dynamics, and depth-averaged modeling. *Journal of Hydraulic Engineering,* 139(7), pp.754-762.

Jeffcoate, P., Stansby, P. and Apsley, D. 2017. Flow and bed-shear magnification downstream of a barrage with swirl generated in ducts by stators and rotors. *Journal of Hydraulic Engineering,* 143(2), pp.06016023.

Jeffcoate, P., Stansby, P. K. and Apsley, D. 2011. Near-field flow downstream of a barrage: experiments, 3-D, CFD and depth-averaged modelling. *International Conference on Offshore Mechanics and Arctic Engineering,* Rotterdam, Netherlands. pp.909-918.

Ji, Z. 2017. *Hydrodynamics and water quality: modeling rivers, lakes, and estuaries.* John Wiley & Sons, Hoboken, New Jerser, USA.

Jonas, P. and Millward, G. 2010. Metals and nutrients in the Severn Estuary and Bristol Channel: contemporary inputs and distributions. *Marine Pollution Bulletin,* 61(1-3), pp.52-67.

Jones, J. E. and Davies, A. M. 2008. Storm surge computations for the west coast of Britain using a finite element model (TELEMAC). *Ocean Dynamics,* 58(5-6), pp.337-363.

Jourieh, A. 2013. *Multi-dimensional numerical simulation of hydrodynamics and transport processes in surface water systems in Berlin.* PhD Thesis. Technische Universität Berlin.

Kadiri, M., Ahmadian, R., Bockelmann-Evans, B., Falconer, R. A. and Kay, D. 2014a. An assessment of the impacts of a tidal renewable energy scheme on the eutrophication potential of the Severn Estuary, UK. *Computers & Geosciences,* 71, pp.3-10.

Kadiri, M., Ahmadian, R., Bockelmann-Evans, B., Rauen, W. and Falconer, R. 2012. A review of the potential water quality impacts of tidal renewable energy systems. *Renewable and Sustainable Energy Reviews,* 16(1), pp.329-341.

Kadiri, M., Bockelmann-Evans, B. and Rauen, W. B. 2014b. Assessing the susceptibility of two UK estuaries to nutrient enrichment. *Continental Shelf Research*, 88, pp.151-160.

Kadiri, M., Zhang, H., Angeloudis, A. and Piggott, M. D. 2021. Evaluating the eutrophication risk of an artificial tidal lagoon. *Ocean & Coastal Management*, 203, pp.105490.

Kelly, K. A., McManus, M. C. and Hammond, G. P. 2012. An energy and carbon life cycle assessment of tidal power case study: The proposed Cardiff–Weston severn barrage scheme. *Energy*, 44(1), pp.692-701.

Khojasteh, D., Lewis, M., Tavakoli, S., Farzadkhoo, M., Felder, S., Iglesias, G. and Glamore, W. 2022. Sea level rise will change estuarine tidal energy: A review. *Renewable and Sustainable Energy Reviews*, 156, pp.111855.

Kim, G., Lee, M. E., Lee, K. S., Park, J. S., Jeong, W. M., Kang, S. K., Soh, J. G. and Kim, H. 2012. An overview of ocean renewable energy resources in Korea. *Renewable and Sustainable Energy Reviews*, 16(4), pp.2278-2288.

Kim, J. W., Ha, H. K. and Woo, S. B. 2017. Dynamics of sediment disturbance by periodic artificial discharges from the world's largest tidal power plant. *Estuarine, Coastal and Shelf Science*, 190, pp.69-79.

Kim, J. W., Ha, H. K., Woo, S. B., Kim, M. S. and Kwon, H. K. 2021. Unbalanced sediment transport by tidal power generation in Lake Sihwa. *Renewable Energy*, 172, pp.1133-1144.

Kirby, R. 2010. Distribution, transport and exchanges of fine sediment, with tidal power implications: Severn Estuary, UK. *Marine Pollution Bulletin*, 61(1-3), pp.21-36.

Kirby, R. and Retière, C. 2009. Comparing environmental effects of Rance and Severn barrages. *Proceedings of the Institution of Civil Engineers-Maritime Engineering*, 162(1), pp.11-26.

Langston, W., Pope, N., Jonas, P., Nikitic, C., Field, M., Dowell, B., Shillabeer, N., Swarbrick, R. and Brown, A. 2010. Contaminants in fine sediments and their consequences for biota of the Severn Estuary. *Marine Pollution Bulletin*, 61(1-3), pp.68-82.

Lewis, M., Neill, S. P., Robins, P. E. and Hashemi, M. R. 2015. Resource assessment for future generations of tidal-stream energy arrays, and comparison of TPXO and FES2012. *Energy*, 83, pp.403-415.

Lewis, M. J., Angeloudis, A., Robins, P. E., Evans, P. S. and Neill, S. P. 2017. Influence of storm surge on tidal range energy. *Energy*, 122, pp.25-36.

Li, Y. and Pan, D. 2017. The ebb and flow of tidal barrage development in Zhejiang Province, China. *Renewable and Sustainable Energy Reviews*, 80, pp.380-389.

Li, Y., Song, Z., Peng, G., Fang, X., Li, R., Chen, P. and Hong, H. 2019. Modeling Hydro-Dynamics in a Harbor Area in the Daishan Island, China. *Water*, 11(2).

LUC. 2015. National Seascape Assessment for Wales. NRW Evidence Report 80. Natural Resources Wales, Bangor (Wales), pp.78. Available at: https://naturalresources.wales/media/682028/mca-00-technical-report-summary-method-appendix.pdf [Accessed: 01 December 2020].

Ma, Q. 2020. *Impact of barrages on extreme water levels in the Bristol Channel.* PhD Thesis. University of Oxford.

Ma, Q. and Adcock, T. A. A. 2020. Modification of tidal resonance in the Severn Estuary by a barrage and lagoon. *Journal of Ocean Engineering and Marine Energy*, 6, pp.171-181.

Ma, Q., Moreira, T. M. and Adcock, T. A. A. 2019. The impact of a tidal barrage on coastal flooding due to storm surge in the Severn Estuary. *Journal of Ocean Engineering and Marine Energy*, 5(3), pp.217-226.

MacKay, D. J. C. 2007. Enhancing electrical supply by pumped storage in tidal lagoons. *Cavendish Laboratory, University of Cambridge*. Available at: https://democracy.kent.gov.uk/documents/s11499/Lagoons.pdf [Accessed: 01 November 2020].

Mackie, L., Coles, D., Piggott, M. and Angeloudis, A. 2020. The potential for tidal range energy systems to provide continuous power: a UK case study. *Journal of Marine Science and Engineering*, 8(10), pp.780.

Manning, A., Langston, W. and Jonas, P. 2010a. A review of sediment dynamics in the Severn Estuary: influence of flocculation. *Marine Pollution Bulletin,* 61(1-3), pp.37-51.

Manning, A. J., Langston, W. J. and Jonas, P. J. 2010b. A review of sediment dynamics in the Severn Estuary: influence of flocculation. *Marine Pollution Bulletin,* 61(1-3), pp.37-51.

Martin-Short, R., Hill, J., Kramer, S., Avdis, A., Allison, P. and Piggott, M. 2015. Tidal resource extraction in the Pentland Firth, UK: Potential impacts on flow regime and sediment transport in the Inner Sound of Stroma. *Renewable Energy*, 76, pp.596-607.

Matta, E. 2018. *Multi-dimensional flow and transport modeling of a surface water body in a semi-arid area.* PhD Thesis. Technische Universität Berlin.

Matta, E., Koch, H., Selge, F., Simshäuser, M. N., Rossiter, K., da Silva, G. M. N., Gunkel, G. and Hinkelmann, R. 2018. Modeling the impacts of climate extremes and multiple water uses to support water management in the Icó-Mandantes Bay, Northeast Brazil. *Journal of Water and Climate Change,* 10(4), pp.893-906.

McGrath, M. 2020. Climate change: China aims for 'carbon neutrality by 2060'. *BBC*. Available at: https://www.bbc.co.uk/news/science-environment-54256826 [Accessed: 25 November 2020].

McLaren, P., Collins, M., Gao, S. and Powys, R. 1993. Sediment dynamics of the Severn Estuary and inner Bristol Channel. *Journal of the Geological Society,* 150(3), pp.589-603.

Medeiros, S. C. and Hagen, S. C. 2013. Review of wetting and drying algorithms for numerical tidal flow models. *International journal for numerical methods in fluids,* 71(4), pp.473-487.

Mejia-Olivares, C. J., Haigh, I. D., Angeloudis, A., Lewis, M. J. and Neill, S. P. 2020. Tidal range energy resource assessment of the Gulf of California, Mexico. *Renewable Energy,* 155, pp.469-483.

Messenger, S. 2016. Swansea tidal lagoon: The environmental arguments. *BBC*. Available at: https://www.bbc.co.uk/news/uk-wales-37863807 [Accessed: 01 December 2020].

Metz, B., Davidson, O. R., Bosch, P. R., Dave, R. and Meyer, L. A. 2007. *Climate change 2007: Mitigation of climate change.* Cambridge Univiversity Press, Cambridge, UK.

Monsen, N. E., Cloern, J. E., Lucas, L. V. and Monismith, S. G. 2002. A comment on the use of flushing time, residence time, and age as transport time scales. *Limnology and Oceanography,* 47(5), pp.1545-1553.

Morison, R. 2018. Climate changed: Britain has gone nine days without wind power. *Bloomberg*. Available at: https://www.bloomberg.com/news/articles/2018-06-07/u-k-wind-drought-heads-into-9th-day-with-no-relief-for-weeks [Accessed: 01 December 2020].

Morris, C. and Jungjohann, A. 2017. Energizing the people. *Nature,* 551(7682), pp.138-140.

Morris, J. E. 2006. *Organically bound tritium in sediments from the Severn estuary, UK*. PhD Thesis. University of Southampton.

Nash, S., Hartnett, M. and Dabrowski, T. 2011. Modelling phytoplankton dynamics in a complex estuarine system. *Proceedings of the Institution of Civil Engineers-Water Management*, 164(1), pp.35-54.

National Oceanograhic Centre. 2011. Continental Shelf Model: Fine Grid (CS3 and CS3-3D). Available at: https://www.adrena-software.com/wp-content/uploads/2012/03/ATLAS-DE-COURANTS_NOC_ModelDetails_CS3_CS3D.pdf [Accessed: 25 November 2020].

National Development and Reform Commission (NDRC). 2016. The 13th Five-Year Plan for Energy Development, NDRC, Beijing. Available at: http://www.ndrc.gov.cn/zcfb/zcfbghwb/201701/W020170117350627940556.pdf. [Accessed: 20 November 2020].

Nedwell, D., Dong, L., Sage, A. and Underwood, G. 2002. Variations of the nutrients loads to the mainland UK estuaries: correlation with catchment areas, urbanization and coastal eutrophication. *Estuarine, Coastal and Shelf Science,* 54(6), pp.951-970.

Neill, S. P., Angeloudis, A., Robins, P. E., Walkington, I., Ward, S. L., Masters, I., Lewis, M. J., Piano, M., Avdis, A., Piggott, M. D., Aggidis, G., Evans, P., Adcock, T. A. A., Židonis, A., Ahmadian, R. and Falconer, R. 2018. Tidal range energy resource and optimization – Past perspectives and future challenges. *Renewable Energy*, 127, pp.763-778.

Neill, S. P. and Elliott, A. J. 2004. Observations and simulations of an unsteady island wake in the Firth of Forth, Scotland. *Ocean Dynamics,* 54(3-4), pp.324-332.

Neill, S. P., Hashemi, M. R. and Lewis, M. J. 2016. Tidal energy leasing and tidal phasing. *Renewable Energy*, 85, pp.580-587.

Neill, S. P., Litt, E. J., Couch, S. J. and Davies, A. G. 2009. The impact of tidal stream turbines on large-scale sediment dynamics. *Renewable Energy,* 34(12), pp.2803-2812.

Neill, S. P. and Scourse, J. D. 2009. The formation of headland/island sandbanks. *Continental Shelf Research,* 29(18), pp.2167-2177.

Nixon, S., Ammerman, J., Atkinson, L., Berounsky, V., Billen, G., Boicourt, W., Boynton, W., Church, T., Ditoro, D. and Elmgren, R. 1996. The fate of nitrogen and phosphorus at the land-sea margin of the North Atlantic Ocean. *Biogeochemistry,* 35(1), pp.141-180.

North Wales Tidal Energy. 2020. North Wales presents a world-class site for a tidal lagoon. Available at: https://www.northwalestidalenergy.com/concept [Accessed: 25 November 2020].

Otto, S. 1998. Off-shore sand banks and their role in coastal sedimentary processes: the Welsh coast of the outer Severn Estuary, SW Britain, In: Bennet, M. R. and Doyle, P. (ed.). *Issues in Environmental Geology: a British Perspective, Geological Society. Bath, UK.*

Owens, M. 1984. Severn Estuary - an appraisal of water quality. *Marine Pollution Bulletin,* 15(2), pp.41-47.

Painting, S., Devlin, M., Malcolm, S., Parker, E., Mills, D., Mills, C., Tett, P., Wither, A., Burt, J. and Jones, R. 2007. Assessing the impact of nutrient enrichment in estuaries: susceptibility to eutrophication. *Marine Pollution Bulletin,* 55(1-6), pp.74-90.

Park, K., Wang, H. V., Kim, S. C. and Oh, J. H. 2008. A model study of the estuarine turbidity maximum along the main channel of the upper Chesapeake Bay. *Estuaries and Coasts,* 31(1), pp.115-133.

Park, N. 2007. Sihwa Tidal Power Plant: a success of environment and energy policy in Korea. Korea University. Available at: https://eer.wustl.edu/McDonnellMayWorkshop/Presentation_files/Saturday/Saturday/Park.pdf [Accessed: 01 Janurary 2021].

Parker, W. R. and Kirby, R. 1982. Sources and transport patterns of sediment in the inner Bristol Channel and Severn Estuary. In: Institution of Civil Engineers (Eds.), Severn Barrage, Thomas Telford, London, pp. 181–194.

Parsons Brinckerhoff Ltd. 2008a. Analysis of Options for Tidal Power Development in the Severn Estuary - Interim Options Analysis Report. Volume 1. Report for the Department for Energy and Climate Change (DECC). pp.1-81. Available at: https://archive.uea.ac.uk/~e680/energy/pdf_files/OptionsforTidalPowerReportVolume1.pdf [Accessed: 23 November 2020].

Parsons Brinckerhoff Ltd. 2008b. Severn tidal power - scoping topic paper, Hydraulics and geomorphology. Report prepared for the Department for Energy and Climate Change. pp.1-81. Available at: https://assets.publishing.service.gov.uk/government/uploads/system/uploads/attachment_data/file/69902/39._Hydraulics_and_Geomorphology_-_NTS.pdf [Accessed: 01 December 2021].

Parsons Brinckerhoff Ltd. 2008c. Severn Tidal Power - Scoping Topic Paper. Marine and Estuarine Water Quality. Report for the Department for Energy and Climate Change (DECC). pp.1-120. Available at: https://assets.publishing.service.gov.uk/government/uploads/system/uploads/attachment_data/file/69903/40._Marine_Water_Quality_-_NTS.pdf [Accessed: 22 November 2020].

Parsons Brinckerhoff Ltd. 2010. Severn tidal power - Sea topic paper: Hydraulics and Geomorphology Annex 13, Geo 9: Sediment budget. Report for Deapartment of Energy and Climate Change (DECC). pp.1-73. Available at: http://severnestuarycoastalgroup.org.uk/files/2016/03/DECC-STP-SEA-HG-Annex-13-Geo-9-April-2010.pdf [Accessed: 01 December 2020].

Pawlowicz, R., Beardsley, B. and Lentz, S. 2002. Classical tidal harmonic analysis including error estimates in MATLAB using T_TIDE. *Computers & Geosciences*, 28(8), pp.929-937.

Payne, G. 2008. Guidance for the experimental tank testing of wave energy converters. *SuperGen Marine Report*, University of Edinburgh. Available at: https://home.hvl.no/ansatte/gste/ftp/MarinLab_files/Litteratur/WEC_tank_testing.pdf [Accessed: 25 November 2020].

Pelc, R. and Fujita, R. M. 2002. Renewable energy from the ocean. *Marine Policy*, 26(6), pp.471-479.

Pethick, J. S., Morris, R. K. and Evans, D. H. 2009. Nature conservation implications of a Severn tidal barrage – A preliminary assessment of geomorphological change. *Journal for Nature Conservation,* 17(4), pp.183-198.

Petley, S. and Aggidis, G. 2016. Swansea Bay tidal lagoon annual energy estimation. *Ocean Engineering,* 111, pp.348-357.

Pingree, R. 1978. The formation of the Shambles and other banks by tidal stirring of the seas. *Journal of the Marine Biological Association of the United Kingdom,* 58(1), pp.211-226.

Poyry Consultants. 2014. Levelised costs of power from tidal lagoons. A report to Tidal Lagoon Power plc. Available at: https://docplayer.net/11766490-Levelised-costs-of-power-from-tidal-lagoons-levelised-costs-of-power-from-tidal-lagoons-a-report-to-tidal-lagoon-power-plc.html.

Prandle, D. 1984. Simple theory for designing tidal power schemes. *Advances in water resources,* 7(1), pp.21-27.

Prandle, D. 2009. Design of tidal barrage power schemes. *Proceedings of the Institution of Civil Engineers-maritime Engineering,* 162(4), pp.147-153.

Pugh, D. T. 1996. *Tides, surges and mean sea-level: a handbook for engineers and scientists.* Chichester, John Wiley & Sons Ltd.

Pye, K. and Blott, S. 2014. Tidal Lagoon Swansea Bay: Sediment Sources and Depositional Processes in Swansea Bay. Report to Natural Resources Wales. Kenneth Pye Associates Ltd.

Radford, P. 1987. The impact of a barrage on water quality and ecosystem performance. *Proceedings on Conference on Barrages and Coastal Technology, South Glamorgan County Council*. pp.18-33.

Radford, P. 1994. Pre-and post-barrage scenarios of the relative productivity of benthic and pelagic subsystems of the Bristol Channel and Severn estuary. *Biological Journal of the Linnean Society,* 51(1-2), pp.5-16.

Rahimi, R., Penesis, I., Hemer, M., Mason, L. and Thomas, G. 2014. Characterization of the tidal current resource in Tasmania. *Proceedings of the Asian Wave and Tidal Energy Conference, Tokyo, Japan, 28–30 July 2014*.

Rainey, R. C. T. 2009. The optimum position for a tidal power barrage in the Severn estuary. *Journal of fluid mechanics*, 636, pp.497-507.

Ranjbar, M. H., Etemad-Shahidi, A. and Kamranzad, B. 2020. Modeling the combined impact of climate change and sea-level rise on general circulation and residence time in a semi-enclosed sea. *Science of The Total Environment*, 740, pp.140073.

Rastogi, A. K. and Rodi, W. 1978. Predictions of heat and mass transfer in open channels. *Journal of the Hydraulics Division*, 104(3), pp.397-420.

Renn, O. and Marshall, J. P. 2016. Coal, nuclear and renewable energy policies in Germany: From the 1950s to the "Energiewende". *Energy Policy*, 99, pp.224-232.

Roberts, A., Thomas, B., Sewell, P., Khan, Z., Balmain, S. and Gillman, J. 2016. Current tidal power technologies and their suitability for applications in coastal and marine areas. *Journal of Ocean Engineering and Marine Energy*, 2(2), pp.227-245.

Robins, P. E., Neill, S. P., Lewis, M. J. and Ward, S. L. 2015. Characterising the spatial and temporal variability of the tidal-stream energy resource over the northwest European shelf seas. *Applied Energy*, 147, pp.510-522.

Rogers, C. S. 1990. Responses of coral reefs and reef organisms to sedimentation. *Marine Ecology Progress Series*, 62(1), pp.185-202.

Rourke, F. O., Boyle, F. and Reynolds, A. 2010. Tidal energy update 2009. *Applied Energy*, 87(2), pp.398-409.

Rtimi, R., Sottolichio, A. and Tassi, P. 2021. Hydrodynamics of a hyper-tidal estuary influenced by the world's second largest tidal power station (Rance estuary, France). *Estuarine, Coastal and Shelf Science*, 250, pp.107143.

Sanders, B. F. 2002. Non-reflecting boundary flux function for finite volume shallow-water models. *Advances in Water Resources*, 25(2), pp.195-202.

Sanford, L. P. and Halka, J. P. 1993. Assessing the paradigm of mutually exclusive erosion and deposition of mud, with examples from upper Chesapeake Bay. *Marine Geology*, 114(1-2), pp.37-57.

Schnabl, A. M., Moreira, T. M., Wood, D., Kubatko, E. J., Houlsby, G. T., McAdam, R. A. and Adcock, T. A. A. 2019. Implementation of tidal stream turbines and tidal barrage structures in DG-SWEM. *Proceedings of the 38th International Conference on Ocean, Offshore and Arctic Engineering*, Glasgow, UK.

Serhadlıoğlu, S., Adcock, T. A. A., Houlsby, G. T., Draper, S. and Borthwick, A. G. 2013. Tidal stream energy resource assessment of the Anglesey Skerries. *International Journal of Marine Energy*, 3, pp.98-111.

Severn Estuary Partnership. 2011. State of the Severn Estuary Report. Cardiff. Available at: https://severnestuarypartnership.org.uk/wp-content/uploads/sites/2/2015/10/SOSER.pdf [Accessed: 01 November 2021].

Severn Tidal Power Group. 1989. The Severn Barrage Project: General Report. Department of Energy, HMSO, London, pp.1-116.

Shewchuk, J. R. 1994. An introduction to the conjugate gradient method without the agonizing pain. Techical Report. Carnegie Mellon University. Pittsburgh, PA, USA. Available at: https://www.cs.cmu.edu/~quake-papers/painless-conjugate-gradient.pdf [Accessed: 25 November 2020].

Shi, B., Wang, Y. P., Yang, Y., Li, M., Li, P., Ni, W. and Gao, J. 2015. Determination of critical shear stresses for erosion and deposition based on in situ measurements of currents and waves over an intertidal mudflat. *Journal of Coastal Research*, 31(6), pp.1344-1356.

Shi, W., Wang, C. and Shen, J. 2011. Utilisation and prospect of ocean energy resource in China. *Acta Energiae Solaris Sinica*, 32(6), pp.913-923.

Short, F. T. and Wyllie-Echeverria, S. 1996. Natural and human-induced disturbance of seagrasses. *Environmental Conservation*, 23(1), pp.17-27.

Simons, R. K., Canali, G. E., Anderson-Newton, G. and Cotton, G. 2000. Sediment transport modeling: Calibration, verification, and evaluation. *Soil and Sediment Contamination*, 9(3), pp.261-289.

Smith, J. and Shackley, S. E. 2006. Effects of the closure of a major sewage outfall on sublittoral, soft sediment benthic communities. *Marine Pollution Bulletin*, 52(6), pp.645-658.

Spiteri, C., Maren, B. v., Kessel, T. v. and Dijkstra, J. 2011. Effect chain modelling to support ems-dollard management. *Journal of Coastal Research*, 61, pp.226-233.

Stansby, P., Chini, N. and Lloyd, P. 2016. Oscillatory flows around a headland by 3D modelling with hydrostatic pressure and implicit bed shear stress comparing with experiment and depth-averaged modelling. *Coastal Engineering*, 116, pp.1-14.

Stansby, P. K. 2003. A mixing-length model for shallow turbulent wakes. *Journal of Fluid Mechanics*, 495, pp.369-384.

Stapleton, C. M., Wyer, M. D., Kay, D., Bradford, M., Humphrey, N., Wilkinson, J., Lin, B. L., Yang, L., Falconer, R. A. and Watkins, J. 2007. Fate and transport of particles in estuaries - Volume IV: Numerical modelling for bathing water enterococci estimation in the Severn Estuary. Environment Agency Science Report SC000002/SR2, Bristol, UK. Available at: https://assets.publishing.service.gov.uk/government/uploads/system/uploads/attachment_data/file/291098/scho0307bmef-e-e.pdf [Accessed: 25 November 2020].

Steffler, P. and Blackburn, J. 2002. Two-dimensional depth averaged model of river hydrodynamics and fish habitat. *River2D user's manual, University of Alberta, Canada*. Available at: https://citeseerx.ist.psu.edu/viewdoc/download?doi=10.1.1.499.1928&rep=rep1&type=pdf [Accessed: 23 November 2020].

Stoesser, T. 2014. Large-eddy simulation in hydraulics: Quo Vadis? *Journal of Hydraulic Research*, 52(4), pp.441-452.

Supercomputing Wales. 2018. The national supercomputing research facility for wales. Available at: https://www.supercomputing.wales/ [Accessed: 25 November 2020].

Sustainable Development Commission. 2007a. Tidal Power in the UK. Research Report 3 - Review of Severn barrage proposals. pp.1-251. Available at: http://www.sd-commission.org.uk/data/files/publications/TidalPowerUK3-Severn_barrage_proposals.pdf.

Sustainable Development Commission. 2007b. Turning the tide: Tidal power in the UK. Whitehall, London. Available at: http://www.sd-commission.org.uk/data/files/publications/Tidal_Power_in_the_UK_Oct07.pdf [Accessed: 20 November 2020].

Tidal Engineering and Environmental Services Ltd (TEES Ltd). 2018. Engineering Design and Construction of West Somerset Lagoon. Available at: https://tidalengineering.co.uk/west-somerset-lagoon/engineering-design-and-construction/.

TELEMAC. 2020a. GAIA user manual version v8p2. Available at: http://wiki.opentelemac.org/doku.php?id=documentation_v8p2r1 [Accessed: 01 March 2021].

TELEMAC. 2020b. TELEMAC-2D user manual version v8p2. Available at: http://wiki.opentelemac.org/doku.php?id=documentation_v8p2r1 [Accessed: 01 March 2021].

Tett, P., Gilpin, L., Svendsen, H., Erlandsson, C. P., Larsson, U., Kratzer, S., Fouilland, E., Janzen, C., Lee, J.-Y. and Grenz, C. 2003a. Eutrophication and some European waters of restricted exchange. *Continental Shelf Research*, 23(17-19), pp.1635-1671.

Tett, P., Gilpin, L., Svendsen, H., Erlandsson, C. P., Larsson, U., Kratzer, S., Fouilland, E., Janzen, C., Lee, J. Y. and Grenz, C. 2003b. Eutrophication and some European waters of restricted exchange. *Continental Shelf Research*, 23(17-19), pp.1635-1671.

The Robert Gordon University. 2002. A scoping study for an environmental impact field programme in tidal current energy. Technical Report. pp.1-68. Available at: https://www.osti.gov/etdeweb/servlets/purl/20295312 [Accessed: 20 November 2020].

Thiébot, J., Bailly du Bois, P. and Guillou, S. 2015. Numerical modeling of the effect of tidal stream turbines on the hydrodynamics and the sediment transport – Application to the Alderney Race (Raz Blanchard), France. *Renewable Energy*, 75, pp.356-365.

Thomson, R. E. and Emery, W. J. 2014. *Data analysis methods in physical oceanography.* Elsevier Science.

Tidal Lagoon Plc. 2013. Application for Development Consent. Available at: http://www.tidallagoonpower.com/application-for-development-consent/ [Accessed: 10 November 2020].

Tidal Lagoon Plc. 2016. Key Statistics - Tidal Lagoon. Available at: http://www.tidallagoonpower.com/projects/swansea-bay/ [Accessed: 22 November 2020].

Todeschini, G. 2017. Review of tidal lagoon technology and opportunities for integration within the UK energy system. *Inventions,* 2(3), pp.14.

Tomczak, M. 1988. Island wakes in deep and shallow water. *Journal of Geophysical Research: Oceans,* 93(C5), pp.5153-5154.

Tousif, S. M. R. and Taslim, S. M. B. 2011. Tidal power: an effective method of generating power. *International Journal of Scientific & Engineering Research,* 2(5), pp.1-5.

UK Government. 2019a. UK becomes first major economy to pass net zero emissions law. New target will require the UK to bring all greenhouse gas emissions to net zero by 2050. Available at: https://www.gov.uk/government/news/uk-becomes-first-major-economy-to-pass-net-zero-emissions-law [Accessed: 23 November 2020].

UK Government. 2019b. The Uk's Draft Integrated National Energy and Climate Plan (NECP). Available at: https://www.gov.uk/government/publications/uk-national-energy-and-climate-plan-necp [Accessed: 21 November 2020].

Uncles, R. 2010. Physical properties and processes in the Bristol Channel and Severn Estuary. *Marine Pollution Bulletin,* 61(1-3), pp.5-20.

Uncles, R. and Radford, P. 1980. Seasonal and spring-neap tidal dependence of axial dispersion coefficients in the Severn-a wide, vertically mixed estuary. *Journal of Fluid Mechanics,* 98(4), pp.703-726.

Underwood, G. J. 2010. Microphytobenthos and phytoplankton in the Severn estuary, UK: present situation and possible consequences of a tidal energy barrage. *Marine Pollution Bulletin,* 61(1-3), pp.83-91.

United Nations. 2012. Cancun Agreements. Cancún, Mexico. Available at: http://unfccc.int/key_steps/cancun_agreements/items/6132.php [Accessed: 20 November 2020].

Uqaili, M. A. and Harijan, K. 2011. *Energy, environment and sustainable development.* Vienna, Austria, Springer Science & Business Media.

Urban Waste Water Treatment Directive (UWWTD). 1991. Concerning Urban Waste WaterTreatment (91/271/EEC), Council of the European communities. Available at: https://www.eea.europa.eu/policy-documents/council-directive-91-271-eec [Accessed: 15 November 2020].

Vaughan, A. 2018. UK summer wind drought puts green revolution into reverse. The Guardian. Available at: https://www.theguardian.com/environment/2018/aug/27/uk-summer-wind-drought-puts-green-revolution-into-reverse [Accessed: 25 November 2020].

Vazquez, A. and Iglesias, G. 2015. Device interactions in reducing the cost of tidal stream energy. *Energy Conversion and Management,* 97, pp.428-438.

Visser, P. M., Verspagen, J. M., Sandrini, G., Stal, L. J., Matthijs, H. C., Davis, T. W., Paerl, H. W. and Huisman, J. 2016. How rising CO_2 and global warming may stimulate harmful cyanobacterial blooms. *Harmful Algae,* 54, pp.145-159.

Wadey, M. P., Brown, J. M., Haigh, I. D., Dolphin, T. and Wisse, P. 2015. Assessment and comparison of extreme sea levels and waves during the 2013/2014 storm season in two UK coastal regions. *Natural Hazards and Earth System Sciences,* 15(10), pp.2209-2225.

Wadey, M. P., Haigh, I. D. and Brown, J. M. 2014. A century of sea level data and the UK's 2013/14 storm surges: an assessment of extremes and clustering using the Newlyn tide gauge record. *Ocean Science,* 10(6), pp.1031-1045.

Walstra, L. C., Van Rijn, L. C., Blogg, H. and Van Ormondt, M. 2001. Evaluation of a hydrodynamic area model based on the COAST3D data at Teignmouth 1999. *Report TR121-ECMAST Project No. MAS3-CT97-0086,* HR Wallingford, UK.

Wang, S., Yuan, P., Li, D. and Jiao, Y. 2011. An overview of ocean renewable energy in China. *Renewable and Sustainable Energy Reviews,* 15(1), pp.91-111.

Warwick, R. and Somerfield, P. 2010. The structure and functioning of the benthic macrofauna of the Bristol Channel and Severn Estuary, with predicted effects of a tidal barrage. *Marine Pollution Bulletin,* 61(1-3), pp.92-99.

Waters, S. and Aggidis, G. 2016a. Tidal range technologies and state of the art in review. *Renewable and Sustainable Energy Reviews,* 59, pp.514-529.

Waters, S. and Aggidis, G. 2016b. A World First: Swansea Bay Tidal lagoon in review. *Renewable and Sustainable Energy Reviews,* 56, pp.916-921.

Wikipedia. 2021. Rance Tidal Power Station. Available at: https://en.wikipedia.org/wiki/Rance_Tidal_Power_Station [Accessed: 01 December 2020].

Wilhelm, S., Balarac, G., Métais, O. and Ségoufin, C. 2016. Analysis of Head Losses in a Turbine Draft Tube by Means of 3D Unsteady Simulations. *Flow, Turbulence and Combustion,* 97(4), pp.1255-1280.

Wilson, S., Bourban, S. and Couch, S. 2012. Understanding the interactions of tidal power projects across the UK Continental Shelf. *Proceedings of the 4th International Conference on Ocean Energy, Dublin.*

Winterwerp, J. C. and Van Kesteren, W. G. 2004. *Introduction to the physics of cohesive sediment dynamics in the marine environment.* Amsterdam, The Netherlands, Elsevier.

Wolanski, E., Imberger, J. and Heron, M. L. 1984. Island wakes in shallow coastal waters. *Journal of Geophysical Research,* 89(C6), pp.10553-10569.

Wolf, J., Walkington, I. A., Holt, J. and Burrows, R. 2009. Environmental impacts of tidal power schemes. *Proceedings of the Institution of Civil Engineers-Maritime Engineering,* 162(4), pp.165-177.

Woodworth, P., Teferle, F. N., Bingley, R., Shennan, I. and Williams, S. 2009. Trends in UK mean sea level revisited. *Geophysical Journal International,* 176(1), pp.19-30.

Wu, W., Wang, P. and Chiba, N. 2004. Comparison of five depth-averaged 2-D turbulence models for river flows. *Archives of Hydro-Engineering and Environmental Mechanics,* 51(2), pp.183-200.

Xia, J., Falconer, R. A. and Lin, B. 2010a. Hydrodynamic impact of a tidal barrage in the Severn Estuary, UK. *Renewable Energy,* 35(7), pp.1455-1468.

Xia, J., Falconer, R. A. and Lin, B. 2010b. Impact of different operating modes for a Severn Barrage on the tidal power and flood inundation in the Severn Estuary, UK. *Applied Energy,* 87(7), pp.2374-2391.

Xia, J., Falconer, R. A. and Lin, B. 2010c. Impact of different tidal renewable energy projects on the hydrodynamic processes in the Severn Estuary, UK. *Ocean Modelling,* 32(1-2), pp.86-104.

Xie, Z., Lin, B., Falconer, R. A., Nichols, A., Tait, S. J. and Horoshenkov, K. V. 2021. Large-eddy simulation of turbulent free surface flow over a gravel bed. *Journal of Hydraulic Research*), pp.1-15.

Xue, J. 2021. *Optimisation of Tidal Range Schemes.* PhD Thesis. Cardiff University.

Xue, J., Ahmadian, R. and Falconer, R. A. 2019a. Optimising the Operation of Tidal Range Schemes. *Energies,* 12(15), pp.2870.

Xue, J., Ahmadian, R. and Jones, O. 2019b. Optimisation of Tidal Lagoon using Genetic Algorithm. *Proceedings of the 13th European Wave and Tidal Energy Conference,* Naples, Italy. pp.1764.

Xue, J., Ahmadian, R. and Jones, O. 2020. Genetic Algorithm in Tidal Range Schemes' optimisation. *Energy,* 200, pp.117496.

Yates, N. and Tatlock, B. 2017. Optimising Tidal Lagoons. *Proceedings of the European Wave and Tidal Energy Conference*, Cork, Republic of Ireland.

Yates, N., Walkington, I., Burrows, R. and Wolf, J. 2013a. Appraising the extractable tidal energy resource of the UK's western coastal waters. *Philosophical Transactions of the Royal Society A: Mathematical, Physical and Engineering Sciences,* 371(1985), pp.20120181.

Yates, N., Walkington, I., Burrows, R. and Wolf, J. 2013b. The energy gains realisable through pumping for tidal range energy schemes. *Renewable Energy,* 58, pp.79-84.

Young, E., Aldridge, J. and Brown, J. 2000. Development and validation of a three-dimensional curvilinear model for the study of fluxes through the North Channel of the Irish Sea. *Continental Shelf Research*, 20(9), pp.997-1035.

Zhang, Y. L., Lin, Z. and Liu, Q. L. 2014. Marine renewable energy in China: Current status and perspectives. *Water Science and Engineering*, 7(3), pp.288-305.

Zhou, J., Falconer, R. A. and Lin, B. 2014a. Refinements to the EFDC model for predicting the hydro-environmental impacts of a barrage across the Severn Estuary. *Renewable Energy*, 62, pp.490-505.

Zhou, J., Pan, S. and Falconer, R. A. 2014b. Effects of open boundary location on the far-field hydrodynamics of a Severn Barrage. *Ocean Modelling*, 73, pp.19-29.

Zhou, J., Pan, S. and Falconer, R. A. 2014c. Optimization modelling of the impacts of a Severn Barrage for a two-way generation scheme using a Continental Shelf model. *Renewable Energy*, 72, pp.415-427.

Appendix A: TELEMAC Settings for Hydrodynamic Model and TRS Modelling

A.1 Telemac Steering File for SEBC hydrodynamic model

```
/-------------------------------------------------------------------------------
/ TELEMAC-2D  Version v8p2
/-------------------------------------------------------------------------------
/ TITLE OF MODEL, INFORMATION
/-------------------------------------------------------------------------------
TITLE = 'Severn Estuary and Bristol Channel'
/-------------------------------------------------------------------------------
/ PARAMETERS SETTING
/-------------------------------------------------------------------------------
AIR PRESSURE                                                =true
LAW OF BOTTOM FRICTION                                      =4
ROUGHNESS COEFFICIENT OF BOUNDARIES                         =0.025
FRICTION COEFFICIENT                                        =0.025
BOTTOM SMOOTHINGS                                           =1
TURBULENCE MODEL                                            =3
CORIOLIS COEFFICIENT                                        =0.000128523
CORIOLIS                                                    =YES
/-------------------------------------------------------------------------------
/ SOURCE POINTS, BOUNDARY CONDITIONS
/-------------------------------------------------------------------------------
OPTION FOR LIQUID BOUNDARIES                                =1
GLOBAL NUMBERS OF SOURCE NODES
= 123312;123300;122593;122585;120368;117421;118868;101916
/Above points are the location of river discharge input
WATER DISCHARGE OF SOURCES
=19.1;6.35;38.1;14.18;52;52;36;36;28;21;10;12.5
VALUES OF THE TRACERS AT THE SOURCES                        =0;0;0;0;0;0;0;0
STAGE-DISCHARGE CURVES                                      =0
MAXIMUM NUMBER OF SOURCES                                   =300
MASS-LUMPING ON H                                           =1
/-------------------------------------------------------------------------------
/ INITIAL CONDITIONS
/-------------------------------------------------------------------------------
INITIAL CONDITIONS                                            ='CONSTANT ELEVATION'
INITIAL ELEVATION                                             =1.49
/-------------------------------------------------------------------------------
/ INPUT-OUTPUT, FILES
/-------------------------------------------------------------------------------
```

```
GEOMETRY FILE                                    ='SEBC_hydrodynamic.slf'
RESULTS FILE                                     ='SEBC_hydrodynamic.slf'
LIQUID BOUNDARIES FILE                           ='t2d-11.08.2012.liq'
BOUNDARY CONDITIONS FILE                         ='SEBC_hydrodynamic.cli'
FORTRAN FILE                                     = 'user_fortran'
/-------------------------------------------------------------------------------
/ INPUT-OUTPUT, GRAPHICS AND LISTING
/-------------------------------------------------------------------------------
MASS-BALANCE                                      =true
VARIABLES FOR GRAPHIC PRINTOUTS                   =U,V,B,H,L,S
LISTING PRINTOUT PERIOD                           =30
GRAPHIC PRINTOUT PERIOD                           =450
INFORMATION ABOUT SOLVER                          =true
/-------------------------------------------------------------------------------
/ NUMERICAL PARAMETERS
/-------------------------------------------------------------------------------
DISCRETIZATIONS IN SPACE                          =12;11
CONTINUITY CORRECTION                             =true
ORIGINAL DATE OF TIME                             =2012;08;11
ORIGINAL HOUR OF TIME                             =13;00;00
NUMBER OF PRIVATE ARRAYS                          =1
TREATMENT OF THE LINEAR SYSTEM                    =2
NUMBER OF TIME STEPS                              =134280
FINITE VOLUME SCHEME                              =0
TIME STEP                                         =10
DURATION                                          =1342800
SUPG OPTION                                       =1;1;1;1
PARALLEL PROCESSORS                               =40
/-------------------------------------------------------------------------------
/ ACCURACY AND SOLVERS
/-------------------------------------------------------------------------------
TIDAL FLATS                                      =YES
OPTION FOR THE TREATMENT OF TIDAL FLATS          =1
TIDE GENERATING FORCE                            =NO
TREATMENT OF NEGATIVE DEPTHS                     =1
TREATMENT OF THE LINEAR SYSTEM                   =2
ACCURACY OF EPSILON                              =1.E-9
ACCURACY OF K                                    =1.E-9
CONTINUITY CORRECTION                            =YES
C-U PRECONDITIONING                              =YES
INITIAL GUESS FOR H                              =1
INITIAL GUESS FOR U                              =1
MAXIMUM NUMBER OF ITERATIONS FOR K AND EPSILON   =50
MAXIMUM NUMBER OF ITERATIONS FOR SOLVER          =100
OPTION FOR THE SOLVER FOR K-EPSILON MODEL        =2
```

```
PRECONDITIONING                                          =2
PRECONDITIONING FOR K-EPSILON MODEL                      =2
SOLVER                                                   =3
SOLVER ACCURACY                                          =1.E-6
SOLVER FOR K-EPSILON MODEL                               =1
SOLVER OPTION                                            =2
/-----------------------------------------------------------------------
/ NUMERICAL PARAMETERS, VELOCITY-CELERITY-HIGHT
/-----------------------------------------------------------------------
IMPLICITATION FOR VELOCITY                               =0.6
IMPLICITATION FOR DEPTH                                  =0.6
/-----------------------------------------------------------------------
```

A2: Locations and discharges of 7 rivers in the SEBC model.

River	UTM coordinate		Discharge (m^3/s)
	Easting	Northing	
Taff	488696.406	5698899.500	21
Usk	501844.130	5712116.578	28
Wye	523458.259	5719377.726	72
Severn	538274.416	5738830.358	104
Avon	496179.256	5670299.499	20.46
Parrett	496104.844	5670209.000	10
Tawe	435701.250	5718797.000	12.5

A3: Flexible generation head for SBL.

Number of the tidal loop	Starting time	Ending time	Ending head	Starting head
1	26	32.6	2.4	4.6
2	32.6	38.6	1.5	4
3	38.6	44.9	1.4	3.8
4	44.9	51.2	1.6	4.3
5	51.2	57.8	1.4	4.2
6	57.8	63.8	1.7	4.6
7	63.8	70.4	1.4	4.5
8	70.4	76.4	1.7	4.7
9	76.4	82.7	1.6	4.5
10	82.7	89	1.8	5.2
11	89	95.6	1.6	5
12	95.6	101.3	2	5.2
13	101.3	107.6	1.6	4.6
14	107.6	113.9	2.2	5.9
15	113.9	119.9	1.8	5.2
16	119.9	126.2	2.2	5.9
17	126.2	132.5	1.9	5
18	132.5	138.5	2.2	5.9
19	138.5	144.8	2	4.8
20	144.8	150.8	2.5	5.9
21	150.8	157.4	2.2	5.9

22	157.4	163.4	2.7	5.9
23	163.4	169.7	2	5.2
24	169.7	175.7	2.5	5.8
25	175.7	181.7	2.4	5.9
26	181.7	188	2.6	5.9
27	188	194.3	2.2	5.9
28	194.3	200	2.4	5.9
29	200	206.6	1.9	5.2
30	206.6	212.6	2.4	5.9
31	212.6	218.6	1.8	4.7
32	218.6	224.6	2.3	5.9
33	224.6	230.9	1.7	4.3
34	230.9	236.9	2.4	5.9
35	236.9	243.5	2	5.1
36	243.5	248.9	2.3	5.9
37	248.9	255.5	1.6	4.7
38	255.5	261.5	2.2	5.9
39	261.5	267.8	1.7	4.5
40	267.8	273.8	2	5.2
41	273.8	279.8	1.6	4.7
42	279.8	285.8	1.8	4.7
43	285.8	292.7	1.6	4.6
44	292.7	298.4	1.6	4.5
45	298.4	304.7	1.4	4.2
46	304.7	310.7	1.5	4.5
47	310.7	317	1.4	3.8
48	317	323	1.7	4.1
49	323	329.6	1.3	3.7
50	329.6	335.6	1.4	3.8
51	335.6	341.9	1.4	3.5
52	341.9	347.9	1.4	3.5
53	347.9	354.5	1.3	3.2
54	354.5	360.5	1.5	3.2
55	360.5	366.8	0.5	3.2
56	366.8	373.1	1.4	3
57	373.1	379.7	0.5	3.1

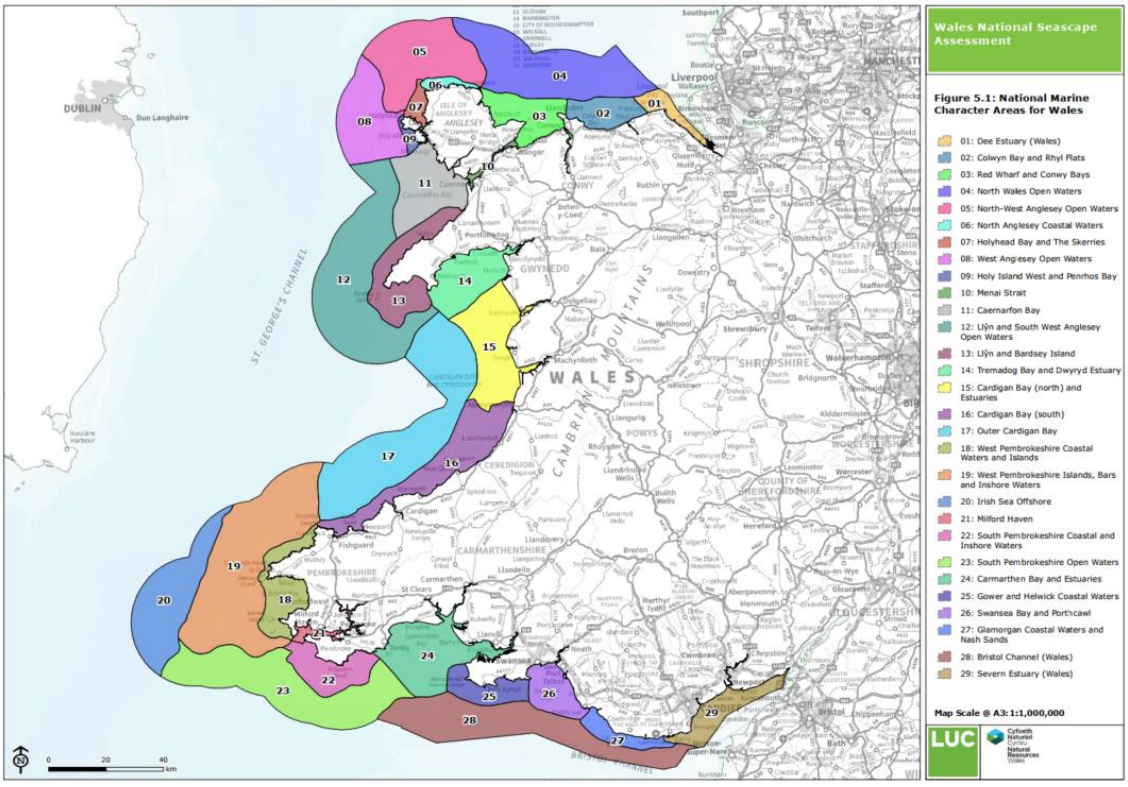

Figure A1: The national marine character areas for Wales (LUC, 2015).

Appendix B: Validation Result for Continental Shelf Model

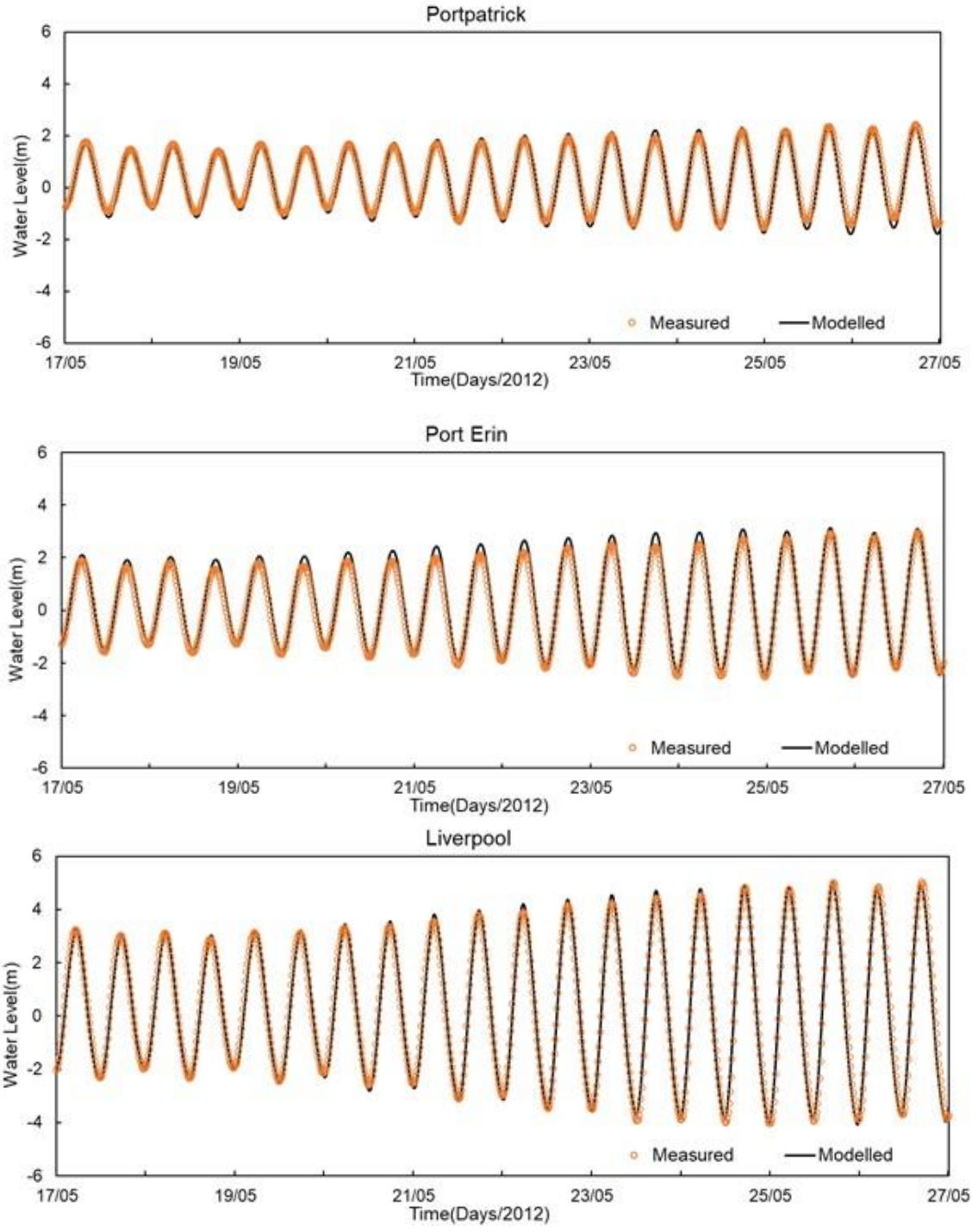

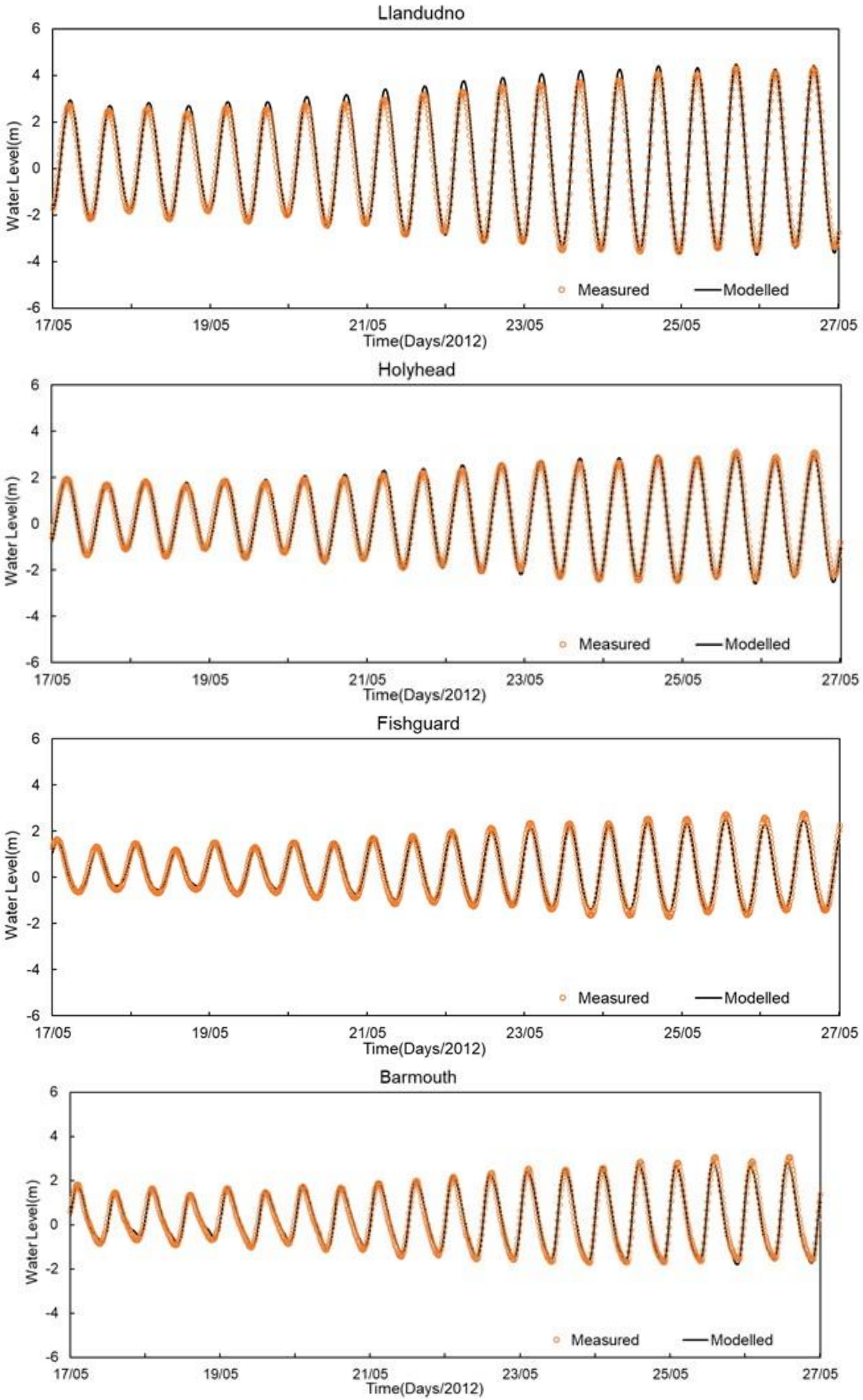
Llandudno
Water Level(m)
6
4
2
0
-2
-4
-6
Measured
Modelled
17/05
19/05
21/05
23/05
25/05
27/05
Time(Days/2012)
Holyhead
Water Level(m)
Measured
Modelled
Time(Days/2012)
Fishguard
Water Level(m)
Measured
Modelled
Time(Days/2012)
Barmouth
Water Level(m)
Measured
Modelled
Time(Days/2012)

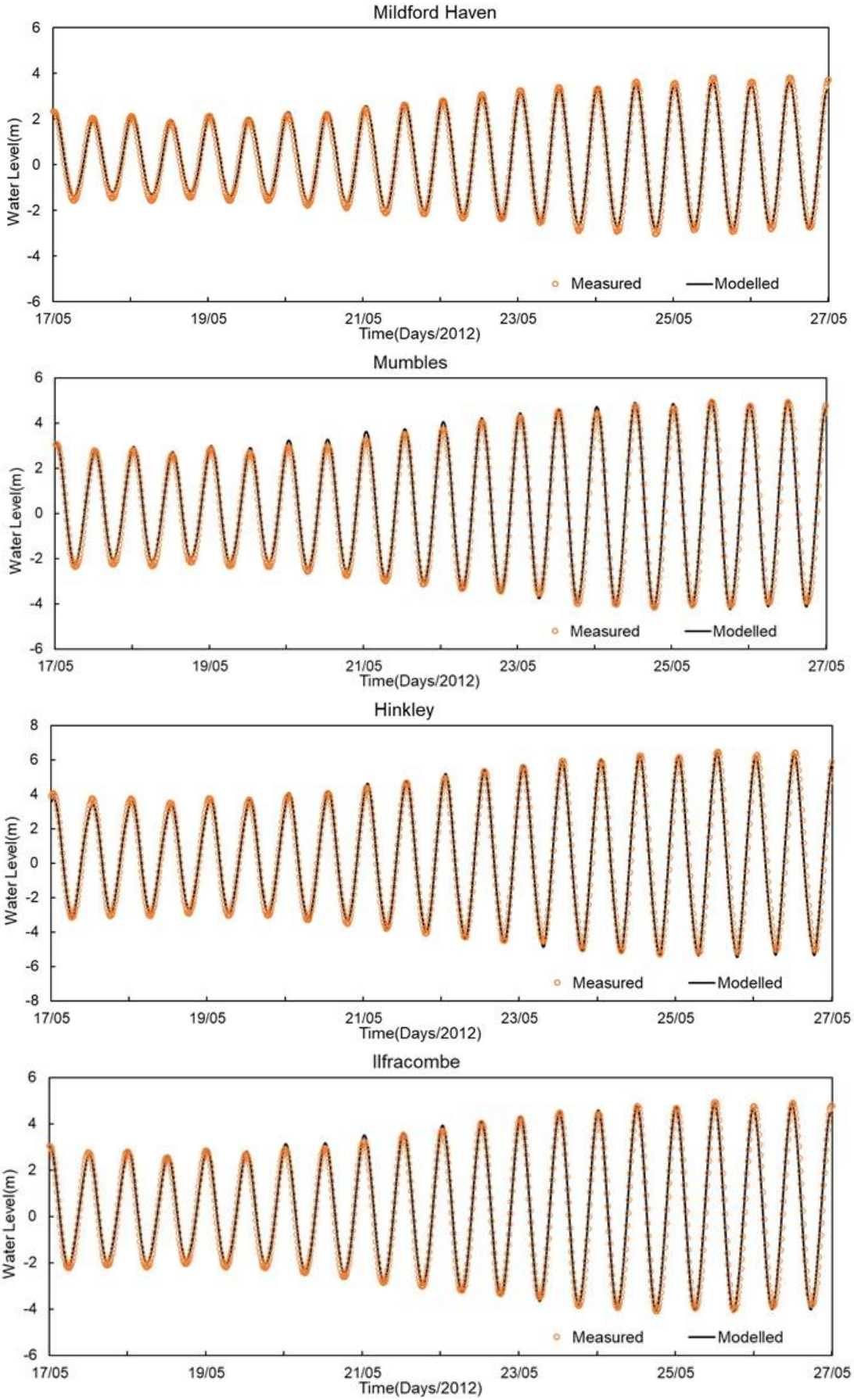
Mildford Haven
Water Level(m)
6
4
2
0
-2
-4
-6
Measured
Modelled
17/05
19/05
21/05
23/05
25/05
27/05
Time(Days/2012)
Mumbles
Water Level(m)
6
4
2
0
-2
-4
-6
Measured
Modelled
17/05
19/05
21/05
23/05
25/05
27/05
Time(Days/2012)
Hinkley
Water Level(m)
8
6
4
2
0
-2
-4
-6
-8
Measured
Modelled
17/05
19/05
21/05
23/05
25/05
27/05
Time(Days/2012)
Ilfracombe
Water Level(m)
6
4
2
0
-2
-4
-6
Measured
Modelled
17/05
19/05
21/05
23/05
25/05
27/05
Time(Days/2012)

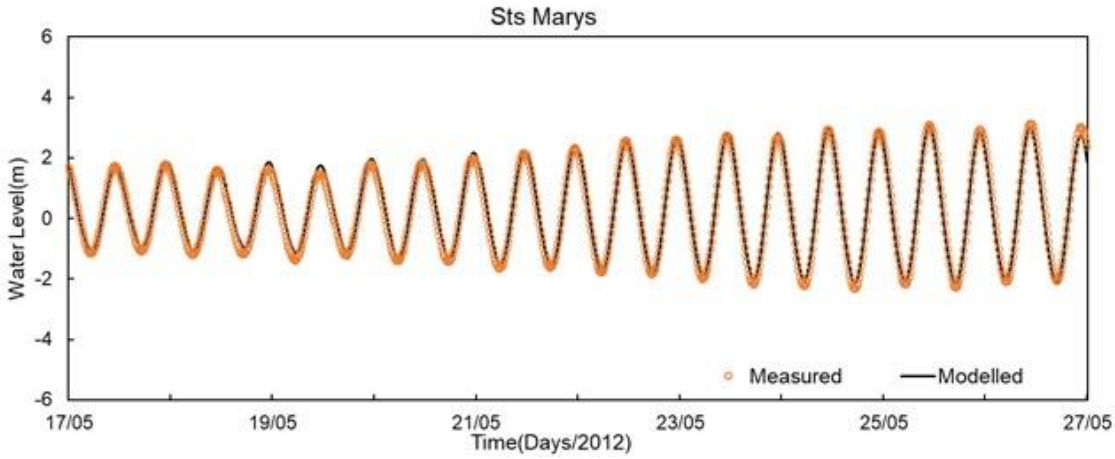

Figure B1: Water level comparisons at 11 BODC tidal gauges for the CS model.

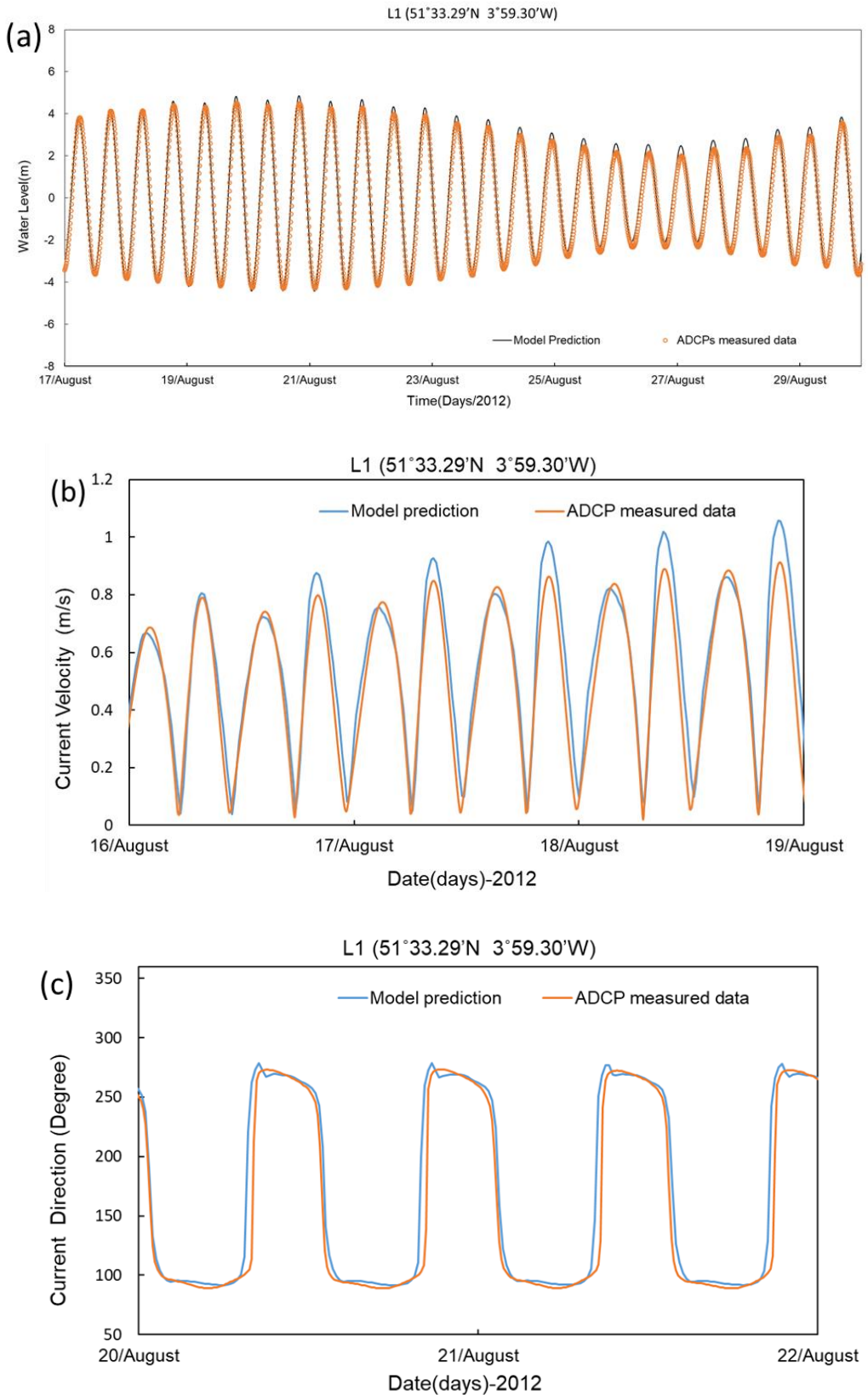

Figure B4: Model prediction of CS model and the validation on Swansea Bay ADCP L1 measurement point, (a) Water level; (b) Tide spped; (c) Current direction.

Appendix C: Typical Mesh Resolution Presentation

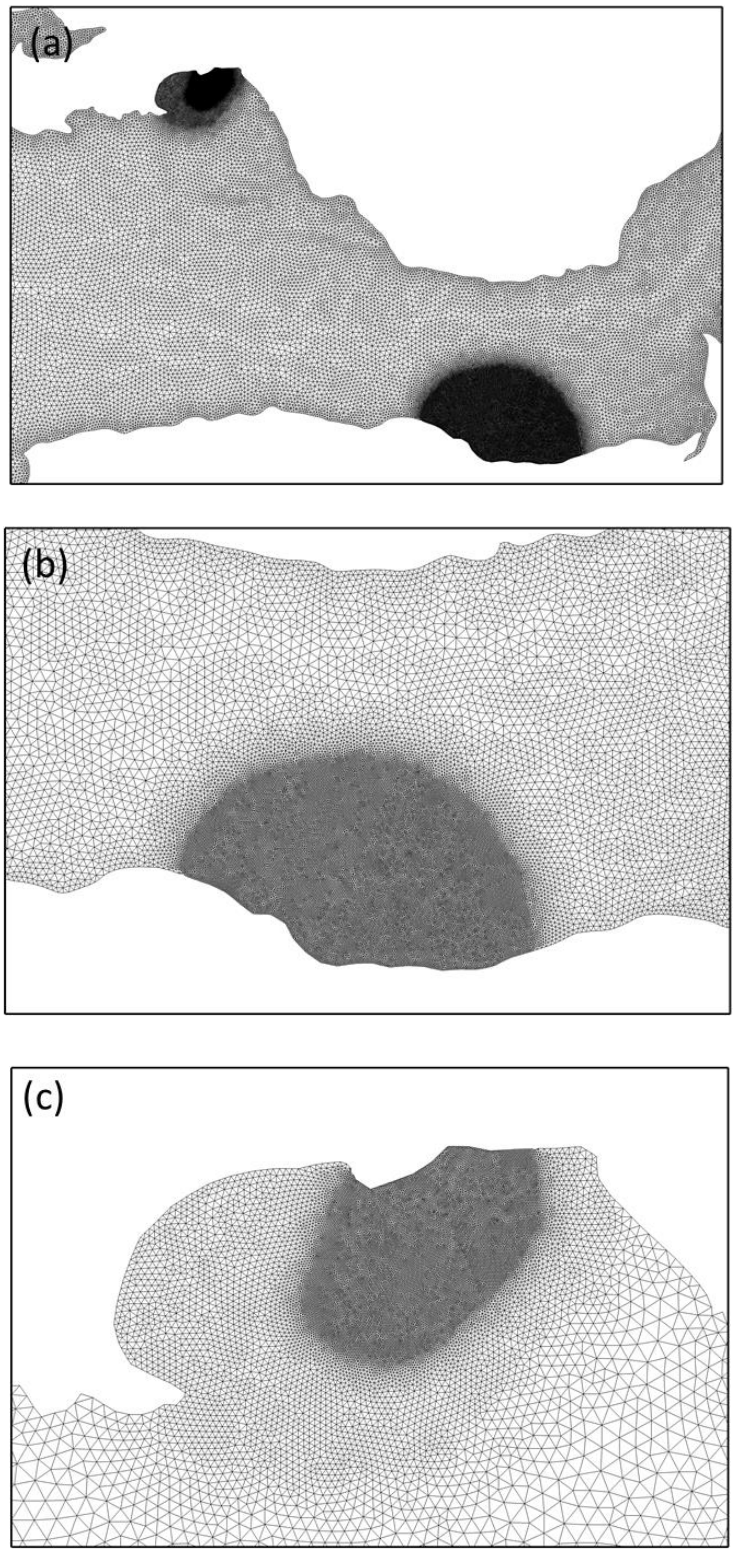

Figure C1: The mesh resolution of model that used to compare the influence of WSL and SBL joint operation, mesh resolution for (a) The whole computational domain;(b) West somerset coast for pre-lagoon condition; (c) Swansea Bay for pre-lagoon condition.

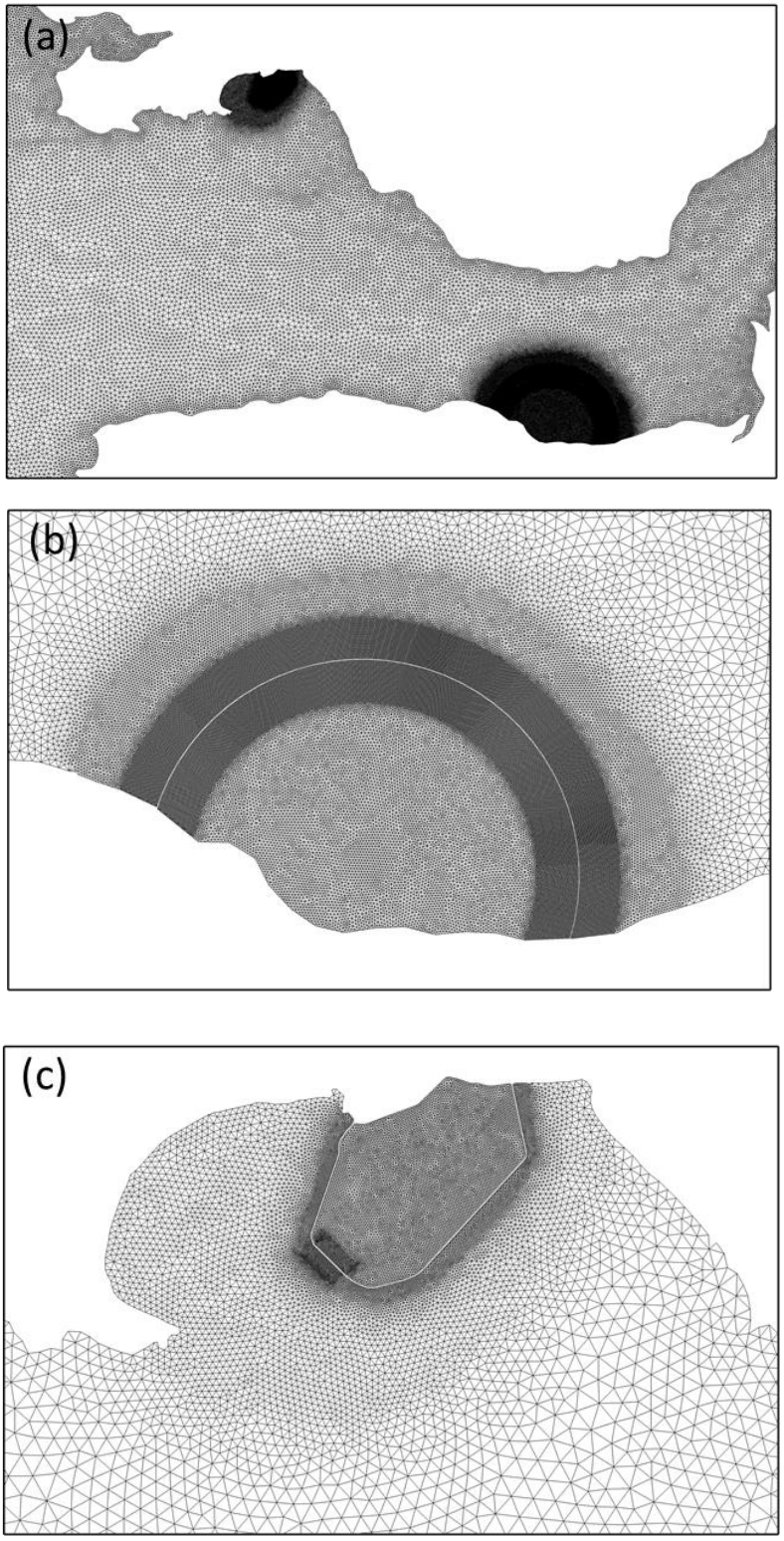

Figure C1: The grid resolution of model that used to study the influence of WSL and SBL joint operation, mesh resolution for (a) The whole computational domain;(b) West somerset lagoon; (c) Swansea Bay lagoon

Appendix D: Morphological Evolution Modelling

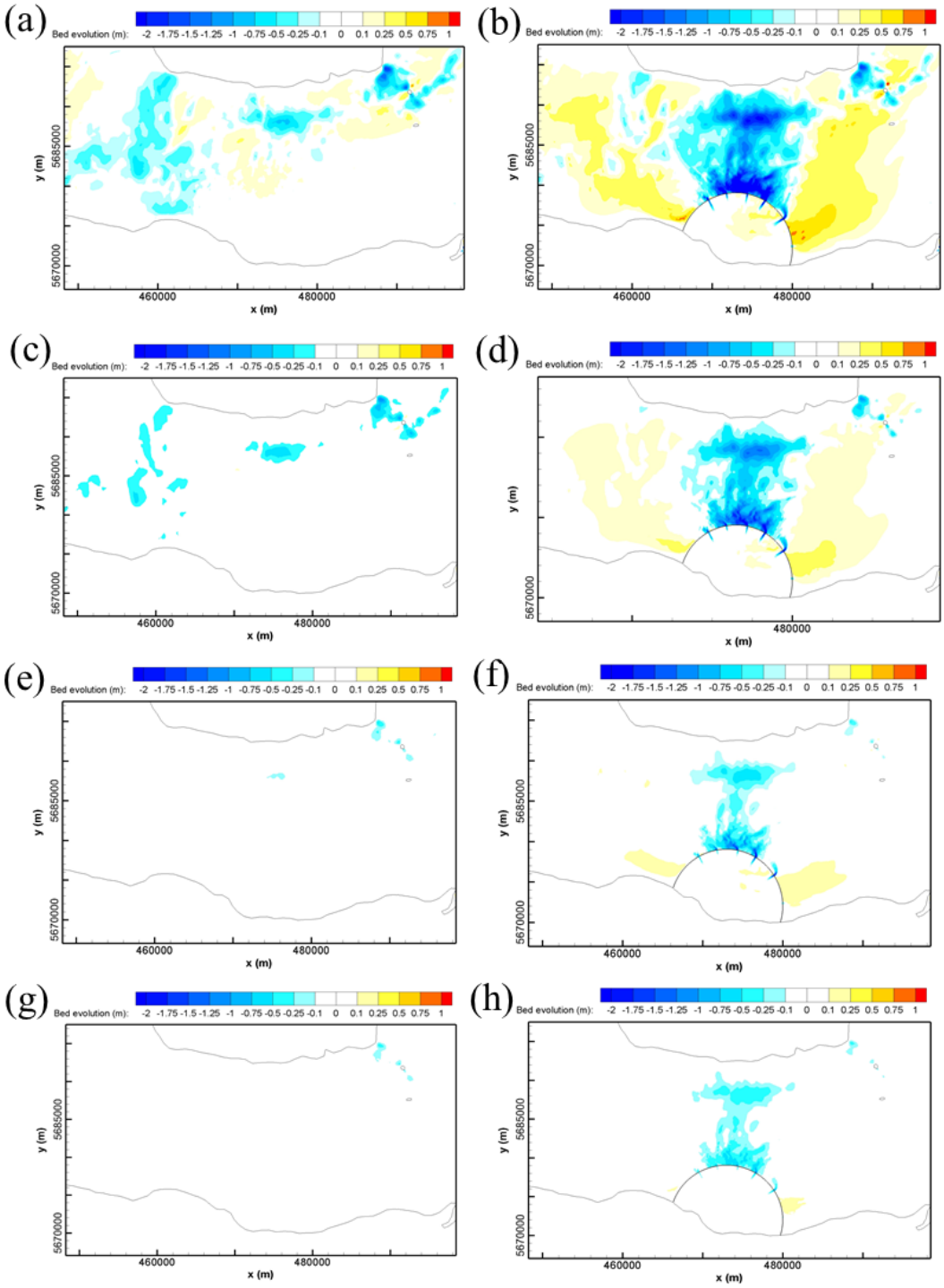

Figure D1: Morphological evolution in the inner Bristol channel for the pre- and post-WSL scenarios after a spring-neap cycle, with the critical deposition shear stress (τ_{cd}) equal to 0.05 N/m^2 and the critical erosion shear stress (τ_{ce}) equal to (a) (b) 2 N/m^2; (c) (d) 2.5 N/m^2; (e) (f) 3 N/m^2; (g) (h) 3.5 N/m^2.

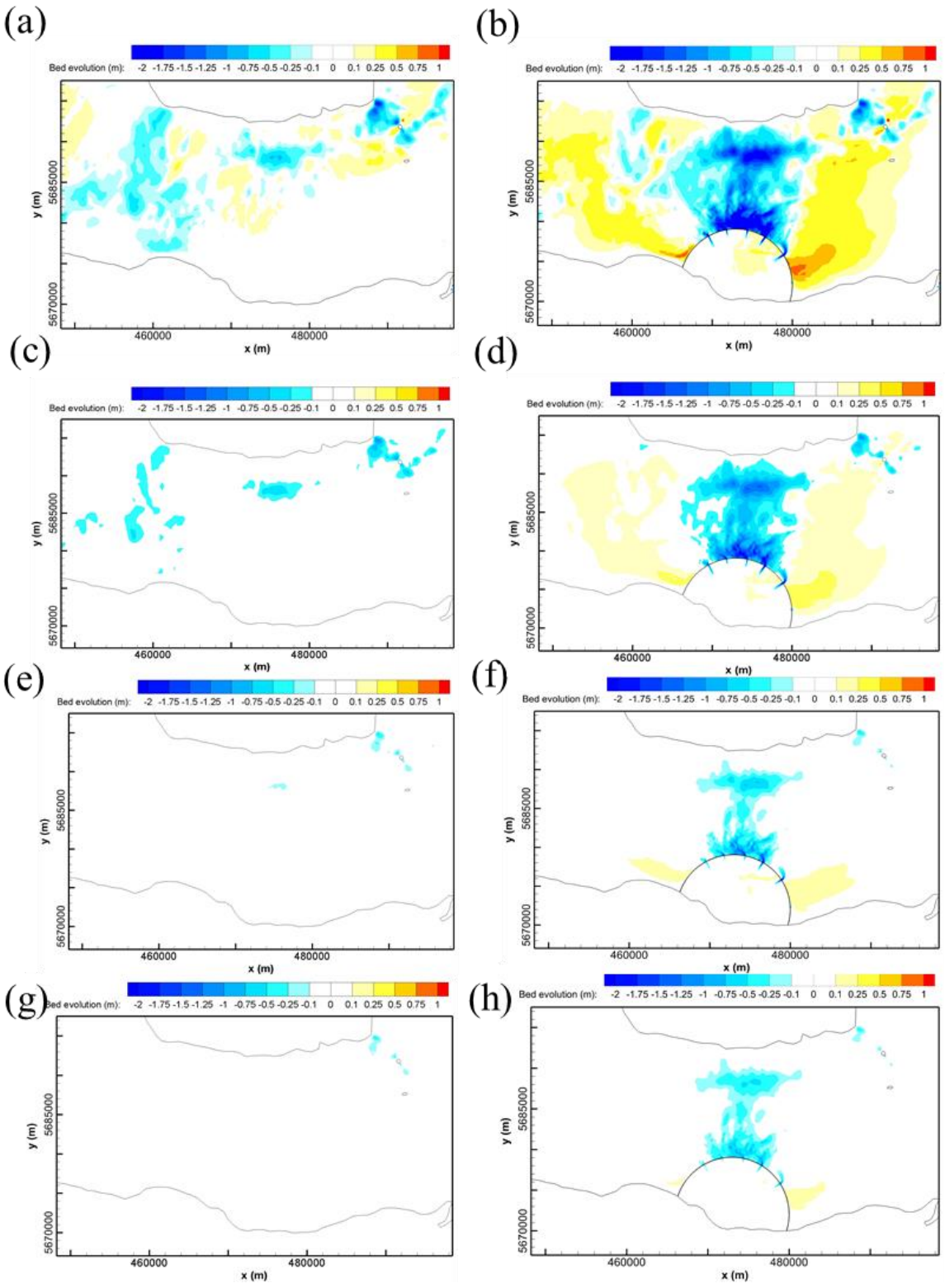

Figure D2: Morphological evolution in the inner Bristol channel for the pre- and post-WSL scenarios after a spring-neap cycle, with the critical deposition shear stress (τ_{cd}) equal to 0.15 N/m^2 and the critical erosion shear stress (τ_{ce}) equal to (a) (b) 2 N/m^2; (c) (d) 2.5 N/m^2; (e) (f) 3 N/m^2; (g) (h) 3.5 N/m^2.